A thesis entitled

Innovative, Robust Nanostructures for SERS-based Hazardous Materials Sensing Realized Using Ultrafast Gaussian/Bessel/Vortex Beams

Submitted to the

University of Hyderabad

Towards partial fulfillment for the degree of

Doctor of Philosophy

in

Physics

by

Dipanjan Banerjee (19ACPP02)

Prime Minister Research Fellow (PMRF)

प्रतिष्ठित संस्थान
INSTITUTION OF EMINENCE
राष्ट्रीय अपेक्षाएँ, वैश्विक मानक
National Needs, Global Standards
हैदराबाद विश्वविद्यालय
UNIVERSITY OF HYDERABAD

सत्यमेव जयते

Prime Minister's Research Fellowship scheme for Ph.D. students

under the supervision of

Prof. Soma Venugopal Rao

School of Physics, Advanced Centre for Research in High Energy Materials (ACRHEM),
DRDO Industry Academia − Centre of Excellence (DIA-COE), University of Hyderabad, Hyderabad 500046, Telangana, India

July 2024

Certificate

This is to certify that the thesis entitled **"Innovative, Robust Nanostructures for SERS-based Hazardous Materials Sensing Realized Using Ultrafast Gaussian/Bessel/Vortex Beams"** being submitted to the University of Hyderabad by **Dipanjan Banerjee** (UoH Reg. No. 19ACPP02), a Prime Minister Research Fellow (PMRF, ID - 3700692), for the award of the degree of Doctor of Philosophy in Physics, is a record of *bonafide* work carried out by him under my supervision and is free of plagiarism.

The matter embodied in this report has not been submitted to any other University or Institution for the award of any degree or diploma.

S Venugopal Rao 18/07/2024

Prof. Soma Venugopal Rao
(PhD Supervisor)

Soma Venugopal Rao
Senior Professor
FSPIE, F.N.A.Sc., FRSC,F.Inst.Phys., FIAAM, FTAS
School of Physics & ACRHEM, DIA-CoE
University of Hyderabad
Hyderabad-500 046. Telangana, India.

D C Bhattacharyya 18/7/24

Director,
DIA-COE,
Formerly ACRHEM

Director
DIA-CoE, UoH

19/7/2024

Dean
School of Physics

DEAN
School of Physics
University of Hyderabad
HYDERABAD - 500 046.

Certificate

This is to certify that the thesis entitled " **Innovative, Robust Nanostructures for SERS-based Hazardous Materials Sensing Realized Using Ultrafast Gaussian/Bessel/Vortex Beams,"** submitted by **Dipanjan Banerjee** bearing registration number **19ACPP02** in partial fulfillment of the requirements for the award of Doctor of Philosophy in Physics at **ACRHEM, DIA-COE, School of Physics, University of Hyderabad** is a bonafide work carried out by him under my supervision and guidance. This thesis is free from plagiarism and has not been submitted previously in part or in full to this or any other University or Institution for the award of any degree or diploma.

Further, the student has the following publications before submission of the thesis for adjudication.

Published Journal articles

1. **Dipanjan Banerjee**, M Akkanaboina, RK Kanaka, VR Soma, Femtosecond Bessel beam induced ladder-like LIPSS on the trimetallic surface for SERS-based sensing of Tetryl and PETN, Applied Surface Science, 616, 156561, 2023.
2. **Dipanjan Banerjee,** S. S. B. Moram; C. Byram; J. Rathod; T. Jena; G. K. Podagatlapalli, V. R. Soma, Plasmon-enhanced Ultrafast and Tunable Thermo-Optic Nonlinear Optical Properties of Femtosecond Laser Ablated TiO_2 and Silver-doped TiO_2 Nanoparticles, Applied Surface Science, 569, 151070, 2021.
3. **Dipanjan Banerjee,** A. Mangababu, Ravi Kumar Kanaka, Venugopal Rao Soma, Nanotubular Arrayed LIPSS Achieved with Femtosecond Bessel Beam on Silver Surface for SERS-based Multiple Explosives Sensing, Journal of Physical Chemistry C, 128 (11), 4655–4665.
4. **Dipanjan Banerjee,** A. Mangababu, Ravi Kumar Kanaka, Venugopal Rao Soma, Plasmonic Alloy Nanocolloids Fabricated via Femtosecond Bessel Beam for Photonic and SERS-based Sensing Applications, Optical Materials, 154, 115668, 2024.

International Conference Proceedings Published

1. **Dipanjan Banerjee,** Mangababu Akkanaboina, Ravi Kumar Kanaka, Venugopal Rao Soma, Ag-Au bimetallic ladder-like nanostructures achieved with femtosecond Bessel beam for real-time sensing of tetryl and ammonium nitrate, SPIE Photonics West, Laser-based Micro-and Nanoprocessing XVII, **Proc. SPIE** 255-260, San Francisco California United States, 17 March 2023.
2. **Dipanjan Banerjee,** Akkanaboina Mangababu, Supriya Pradhan, and Venugopal Rao Soma, Uniform LIPSS on copper created using zeroth-order femtosecond Bessel beam for SERS-based applications, **Proc. SPIE** 13069, International Conference on Optical and Photonic Engineering (icOPEN), 130691F, 15 February 2024, Singapore.

3. **Dipanjan Banerjee,** SSB Moram, VR Soma, Ag-doped TiO2 Nanoparticles Generated with Femtosecond Laser Ablation for Sensing RDX and Ammonium Nitrate, **Laser Science,** JM7A. 1, **OSA,** Laser Science 2023, Tacoma, Washington United States, 9–12 October 2023.
4. MSS Bharathi, **Dipanjan Banerjee**, VR Soma, Femtosecond Laser Ablation Assisted Single-step Fabrication of Metal-semiconductor Interfaced SERS-active Substrate, Laser Applications Conference, JW2A. 7, **Laser Applications Conference 2023, OSA,** Tacoma, Washington United States, 8–12 October 2023.

The student has passed the following courses towards fulfilling the course requirement of the Ph.D.

S. No.	Course ID	Course Name	Credit	Results
1	PY801	Research Methodology	4	Pass
2	PY802	Advanced Quantum Mechanics	4	Pass
3	PY803	Advanced Experimental Techniques	4	Pass
4	PY819	Non-equilibrium Statistical Mechanics	2	Pass

Venugopal Rao 18/7/2024

Supervisor:

Prof. Soma Venugopal Rao,
ACRHEM, School of Physics,
University of Hyderabad,
Hyderabad, India

Soma Venugopal Rao
Senior Professor
FSPIE, F.N.A.Sc., FRSC,F.Inst.Phys., FIAAM, FTAS
School of Physics & ACRHEM, DIA-CoE
University of Hyderabad
Hyderabad-500 046. Telangana, India.

S C Bhattacharyya 18/7/24

Director:

DIA-CoE
Formerly ACRHEM,
University of Hyderabad,
Hyderabad, India

Director
DIA-CoE, UoH

19/7/2024

Dean:

School of Physics,
University of Hyderabad,
Hyderabad, India

DEAN
School of Physics
University of Hyderabad
HYDERABAD - 500 046.

Declaration

I hereby declare that the thesis titled **"Innovative, Robust Nanostructures for SERS-based Hazardous Materials Sensing Realized Using Ultrafast Gaussian/Bessel/Vortex Beams,"** submitted by me under the guidance and supervision of **Prof. Soma Venugopal Rao,** is a bonafide research work and is free from plagiarism. I also declare that it has not been submitted previously, in part or in whole, to this university or any other university or institution for the award of any degree or diploma. I hereby agree that my thesis can be deposited in Shodhganga/INFLIBNET.

A report on plagiarism statistics from the university librarian is enclosed.

Dipanjan Banerjee

Dipanjan Banerjee
(19ACPP02)

Hyderabad, India
Date: 18.07.2024

Dedicated to

My Parents and My PhD Supervisor

Acknowledgments

First and foremost, I would like to express my profound gratitude and appreciation towards my **mother, Surupa Banerjee, and Father, Dipayan Banerjee,** for everything great that has happened in my life. I want my mother to know how grateful I am for all the work she has put into raising me. When I was in school, she used to run behind me from Birati to Baranagore (~ 10 km) to watch out for me. She also offered strong support for my decision to pursue a research career. I recall my childhood days when my father took me to 'Science City,' Kolkata, at least once in two weeks. As a small kid, I used to feel mesmerized by exploring different sections of that science park. From the impressive display of life-sized replicas of ancient dinosaurs to the wide variety of fish, snakes, and amphibians in the biodiversity park, culminating in engaging activities centered on various scientific phenomena, time passed swiftly. As I remember them, those days undoubtedly shaped an enduring mark of absolute bliss in a child's memory. My father nurtured the habit of watching many fascinating science fiction movies and TV shows in me as I grew up. 'Jurassic Park', 'The Day After Tomorrow', 'Indiana Jones', 'Hirak Rajar Deshe', 'Char Murti', 'Sonar Kella 'The Discovery Channel', and 'Animal Planet' are a few among many movies which my father made me watch sitting beside me. These days, as I realize now after 15 years, shaped the mental framework of a growing kid with uncountable purely charmful experiences.

I take this opportunity to thank my supervisor, **Prof. Venugopal Rao Soma**, especially for providing me with the platform to do research under his efficient guidance. I feel lucky to have him as my research mentor. In addition to research skills, I also tried to learn several qualities from his personality. Aside from providing competent research suggestions, he always helped us to develop several other significant life skills, saying - 'Listen to the question properly; half of the answer hides in that' and 'Never keep work pending for tomorrow.' I shall strive to carry these qualities within in the future.

Furthermore, I would like to take this opportunity to say how grateful I am for my school, Baranagore Ramakrishna Mission Ashrama High School. The environment and educators at this institution have undoubtedly influenced not only my own life but also the lives of many other students in many ways. In my B.Sc. at Vidyasagar College, Prof. Saugata Bhattacharya was the guide. I feel utmost humbled and privileged even to write his name now. He was the first to show many of us how physics should be studied. Throughout my

master's studies, Dr. GK became an essential mentor and advisor. I am extremely thankful to him. Regarding the duration of my research career, I am grateful to the University of Hyderabad, but words fail to express my gratitude fully. At UoH, I have gained valuable knowledge about many facets of life and the vast range of Indian culture, in addition to studying ultrafast optics. I would also like to thank my school, and colony friends, remembering our funny, mischievous group name 'World Heritage Group' at Birati. I would also like to mention about my bike, being my constant companion in HCU campus.

I genuinely thank my DRC members Prof. A. K. Chaudhary (ACRHEM, UoH), Prof. Suneel Singh (School of Physics, UoH), Prof. Sai Santosh Kumar Ravi (IIT Hyderabad-PMRF External member). Thanks to the present/former Directors of DIA-CoE (fommerly ACRHEM), Dr. S.C. Bhattacharya/Dr. Vepa Kameswara Rao, Dean SoP Prof. James Raju, and former Directors, ACRHEM, Deans School of Physics. I am also grateful to the UoH administration and all the nonteaching staff, especially Sashikala madam, Sudarshan sir, Nagaraj sir, for addressing our concerns throughout the Ph.D. I thank all my Seniors and colleagues of ACRHEM Dr. GK, Dr. Hamad, Dr. Kalam, Dr. Bharathi, Dr. Chandu, Dr. Lingamurthy, Dr. KK, Dr. Somdatta, Dr. Samuel, Dr. Reshma, Dr. Kaushik, Dr. Rajendar, Dr. Mani, Dr. Naga, Dr. Ganesh, Jagannath, Chandan, Naveen, Arjun, Menchu, Rajesh, Arun, Supratik, Subhashree, Mitali, Dr. Chinmoy, Soif, Sudhanshu, Rahul, Supriyo, Niharika, Dr Abhinash, Dr. Tara for always supporting me. Hearty Thanks to my numerous seniors, colleagues, and friends from the School of Physics and other UoH and IIT Hyderabad departments. Again, thanks to my family and childhood friends who always trusted me. Finally, I thank DRDO, PMRF, IOE- UoH India, and OPTICA (OSA) USA for providing funding on various occasions.

Abbreviations

Abbreviations	Description
a.u.	Arbitrary unit
AN	Ammonium nitrate
BB	Bessel Beam
CE	Chemical enhancement
CV	Crystal violet
DNT	2,4 di-nitro-toluene
DI water	Deionized water
EDX	Energy dispersive X-ray spectroscopy
EF	Enhancement factor
EM	Electromagnetic
ESA	Excited state absorption
FESEM	Field emission electron microscopy
Fs	Femtosecond
FP	Filter paper
FWHM	Full-width at half maxima
GSB	Ground state bleaching
HAZ	Heat affected zone
He-Ne laser	Helium-neon laser
HMX	1,3,5,7-Tetranitro-1,3,5,7-tetrazocane
HRTEM	High-resolution transmission electron microscopy
HSFL	High spatial frequency LIPSS
IR	Infrared
kHz	kilo hertz
LAA	Laser ablation in air
LAL	Laser ablation in liquids
LASER	Light Amplification by stimulated emission of radiation
LIBS	laser-induced breakdown spectroscopy
LIPSS	Laser induced periodic surface structures
LSPR	Localized surface plasmon resonance
LSFL	Low spatial frequency LIPSS
MB	Methylene blue
MG	Malachite green
MS	Methyl salicylate
NB	Nile blue
NIR	Near-infrared,
NLO	Nonlinear optical
NPs	Nanoparticles
nm	nanometers
NS/NSs	Nanostructure/s
OA	Open aperture
OAM	Orbital angular momentum
CA	Closed Aperture
PA	Picric acid
RDX	1,3,5-Trinitroperhydro-1,3,5-triazine

RSD	Relative standard deviation
SAED	Selected Area Electron Diffraction
SEM	Scanning electron microscopy
SERS	surface-enhanced Raman spectroscopy/scattering
SPR	Surface plasmon resonances
TAS	Transient absorption spectroscopy
TEM	Transmission electron microscopy
TNT	trinitrotoluene, 2-Methyl-1,3,5-trinitrobenzene
ULAL	Ultrafast laser ablation in liquids
UV	Ultraviolet
VB	Vortex Beam
VPP	Vortex phase plate
XRD	X-ray diffraction

Table of Contents

Chapter 1 - Introduction & Outline of The Thesis

Abstract 2

1.1. Introduction and Motivation 3

1.2. Explosives Trace Detection 8

1.3. Localized Surface Plasmon 9

1.4. SERS Enhancement Mechanism 13

1.4.1. Electromagnetic Enhancement 15

1.4.1.1. Local Field Enhancement 15

1.4.1.2. Re-radiation Enhancement 16

1.4.2. Chemical Enhancement 17

1.5. Ultrafast Laser Ablation 17

1.5.1. Ultrafast Laser Ablation in Air (ULAA) 18

1.5.2. Ultrafast Laser Ablation in Liquid (ULAL) 20

1.6. Ultrafast Time-resolved Dynamics in Plasmonic Metal Nanoparticles 22

1.7. Overview of thesis - Chapter-wise summary 24

Chapter 2 - Experimental Techniques & Characterization Studies

Abstract 50

2.1. Introduction 51

2.2. Mode-locking: Important Mechanisms Involved 51

2.2.1 Kerr-lens Mode Locking 53

2.2.2 Self-Phase Modulation 54

2.2.3 Group Velocity Dispersion 54

2.2.4 Chirped Pulse Amplification (CPA) 54

2.2.5 Regenerative Amplification 55

2.3. Libra, Ultrafast laser system from M/s Coherent 57

2.3.1. Vitesse (Oscillator) 58

2.3.2 Evolution-HE (Pump laser): 60

2.4 Optical Parametric Amplification (OPA) 60

2.4.1 TOPAS-C 61

2.5 Characterization of Ultrashort Pulses 63

2.5.1 Single shot autocorrelator (SSA) for pulse-width measurements 63

2.6 Femtosecond laser ablation experimental details 65

2.6.1 Axicon lens for the generation of fs Bessel beam 66

2.6.2 Optical Vortex Phase Plate (OVPP) for the generation of fs Vortex beam 67

2.7 Characterization & Measurement Techniques Involving Nanoentities 67
2.7.1 UV-Visible absorption 67
2.7.2 X-ray diffraction.....69
2.7.3 Transmission Electron Microscopy (TEM).....69
2.7.4 Field Emission Scanning Electron Microscope (FESEM) 70
2.7.5 Atomic Force Microscopy (AFM) 72
2.7.6 Horiba μ-Raman spectrometer 74
2.7.7 Portable Raman spectrometer.....74
2.8 Optical Nonlinearity Measurement via Z-scan Technique.....76
2.9 Transient Absorption Spectroscopy 78
2.9.1 Principle of TAS.....80
2.9.2 HELIOS.....81
2.9.3 Chirp correction…… 83

Chapter 3 - Femtosecond Gaussian Beam Laser Ablated Ag-TiO_2 Nanoentities for SERS

Abstract 92
3.1. Introduction 93
3.2. Experimental Details.....95
3.2.1. Fabrication of TiO_2 and Ag-TiO_2 NPs by femtosecond laser ablation.....95
3.3. Results & Discussion 97
3.3.1. XRD Characterization 97
3.3.2. UV-Visible Absorption Spectroscopy 99
3.3.3. Transmission Electron Microscope (TEM) studies 100
3.3.4. SERS-based sensing studies engaging the nanoparticles and nanostructures ……..104
3.4. Conclusions 107

Chapter 4 - Bessel Beam Generated LIPSS on Trimetallic, Bimetallic, Pure Metal Surfaces for SERS

Abstract (4A).....117
4A.1. Introduction 119
4A.2. Experimental details 121
4A.3. Results & Discussion.....122
4A.3.1 Nanoscale topographies designed under Bessel beam contact.....122
4A.3.1.1. Ablation on a single spot 123

4A.3.1.2. Large area Bessel beam overlapping 124
4A.3.1.3. Trimetallic nanostructures having ladder-like periodicity 125
4A.3.2. Bessel beam interacted LIPSS formation mechanism 128
4A.3.3. Differences in structural formation between Gaussian beam ablation 130
4A.3.4. Sensing studies based on SERS 133
4A.3.5. In-depth understanding of the trimetallic nano-system 139
4A.3.6. LIPSS formation on Ag-Au bimetallic surface and its SERS response 140
4A.4. Conclusions 143
Abstract (4B) 154
4B.1. Introduction 156
4B.2. Experimental and characterization details: 158
4B.3. Results & Discussion 159
4B.3.1. Enhanced efficiency in structuring surfaces by the interplay of Bessel beams 159
4B.3.1.1. Comparative analysis of BB and GB line ablation 159
4B.3.2. Bessel beam structured nanostructures 162
4B.3.3. Nanotubular arrayed LIPSS nanostructures 162
4B.3.4. Principle mechanisms of nanotubular LIPSS generation using Bessel beam 166
4B.3.5. Contrast with fluence using Gaussian beam ablation 168
4B.3.6. SERS-based detection of multiple explosives 170
4B.3.7. Uniform LIPSS on Copper Created Using Zeroth-Order Femtosecond Bessel Beam for SERS-based Applications 180
4B.4. Conclusions 185

Chapter 5 - Plasmonic Alloy Nanocolloids Fabricated via Femtosecond Bessel Beam & Preliminary Studies Involving Femtosecond Vortex Beam

Abstract (5A) 195
5A.1. Introduction 197
5A.2. Experimental Details 200
5A.3. Results & Discussion 202
5A.3.1. Synthesis of multi-metal nanoalloys by femtosecond Bessel beam ablation 202
5A.3.2. Detection of explosives using the SERS technique 210
5A.3.3. Superior three-photon absorption under femtosecond NLO excitation 213
5A.3.3.1. Central understandings of the MM NAPs' higher NLO response 216
5A.3.4. Transient absorption dynamics under femtosecond laser excitation 218
5A.4. Conclusions 222

Abstract (5B) 234
5B.1. Introduction 236
5B.2. Experimental details 238
5B.3. Results & Discussion 239
5B.3.1 Single spot ablation imprint using femtosecond vortex beam 239
5B.3.2 Nanostructure prepared using large area raster scan 240
5B.3.3. Sensing studies based on SERS 241
5B.4. Conclusions 244

Chapter 6 - Conclusions & Future scope

6.1 Conclusions 250
6.2. Future scope of our research 255

Table of Figures

Figure 1. 1 Diagram of the Jablonski energy levels illustrating the transitions involved in Rayleigh, Raman Stokes, anti-Stokes, and Resonance Raman scattering. Image adapted from Ref. [148]. **.....10**

Figure 1. 2 Different techniques of explosives detection **.....11**

Figure 1. 3 Schematic diagrams illustrating localized surface plasmon. Image adapted from Ref. [149]. **.....12**

Figure 1. 4 The real (Re) and imaginary (Im) parts of the dielectric functions for different metals. Image adapted from Ref. [153]. **.....13**

Figure 1. 5 Schematic of the electromagnetic enhancement phenomena involving a nanoparticle, depicting enhanced local field (1,2) and re-radiation process (3-5). Image adapted from Ref. [159]. **.....16**

Figure 1. 6 Overview of surface-enhanced Raman spectroscopy: fundamentals of the process, versatility in application and future scope. Image adapted from Ref. [153]**. 18**

Figure 1. 7 Potential applications of laser-assisted colloid synthesis. (a) The number of citations per year in the last ten years was calculated by searching the ISI Web of Science using the keywords "laser" and "nanoparticle". (b) The evolution of the attainable mean power of pulsed laser systems throughout time. The solid lines serve as visual aids to direct the eye by fitting to the data points. (c) Diagram depicting the process of creating colloids using lasers, which relies on two important technologies: photonics and nanotechnology (d) Summary of the subdisciplines of chemistry and related fields engaged in laser synthesis research. Image adapted from Ref. [160]**.....19**

Figure 1. 8 (a) Timescales of various processes involved in fs laser ablation in liquid (b) schematic of laser ablation in liquid and generation of nanoparticles. Image adapted from Ref [171]. **.....21**

Figure 1. 9 Illustration of the band structure of metals with a filled d-band, a partially filled s-p band, and the possibility of inter-band, intraband transitions. **.....23**

Figure 1. 10 A schematic of the complete thesis. **.....25**

Figure 1. 11 Summary of the complete research work **.....31**

Figure 2. 1 Frequency and time domain parameters of mode-locked pulses. **.....52**

Figure 2. 2 Schematic of the CPA process, adapted from Ref. [8]**.....55**

Figure 2. 3 Schematic of the regenerative amplifier. **.....56**

Figure 2. 4 The top view of the Femtosecond amplifier system (LIBRA) shows the essential modules (i) Vitesse (seed) (ii) Evolution (Pump) (iii) RGA cavity (iv) Stretcher/compressor region. (Image adapted from Coherent, Operator's manual for Libra Ultrafast amplifier laser System). **.....57**

Figure 2. 5 Layout of the Vitesse laser **58**

Figure 2. 6 Internal schematic layouts of (a) Vitesse seed laser and (b) Verdi laser layouts. Image adapted from Ref. [11]. **59**

Figure 2. 7 The flow of pump energy to the signal beam in OPA (b) stimulated the emission of signal photons from the virtual level created by the pump beam. Image adapted from Ref. [14]. **61**

Figure 2. 8 Optical layout of the TOPAS-C. (Image adapted from TOPAS – C, Light Conversion Manual).....**61**

Figure 2. 9 Optical layout of the single-shot autocorrelator. (a) optical path inside the SSA (b) schematic of the optical components inside (Image adapted from Coherent, Single Shot Autocorrelation manual). **63**

Figure 2. 10 SSA signal from the oscilloscope. **64**

Figure 2. 11 Photographs of (a) laboratory setup of laser ablation in air (LAA) setup using axicon lens, generating Bessel beam (b) laser ablation in liquid (LAL) setup using axicon lens (c) laser ablation in air (LAA) setup using conventional plano-convex lens, generating Gaussian beam (d) LAA setup engaging a vortex beam, generated using a phase plate along with conventional plano-convex lens. **66**

Figure 2. 12 Photograph of the TEM available at the School of Chemistry, University of Hyderabad. **71**

Figure 2. 13 Photograph of the FESEM available at the School of Physics, University of Hyderabad. **72**

Figure 2. 14 (a) Photograph of the LabRAM HR Evolution Raman spectrometer (available at ACRHEM, University of Hyderabad) (b) Optical path inside LabRAM HR Evolution, image adapted from Horiba Scientific, LabRAM HR evolution user manual. **73**

Figure 2. 15 Schematic and photograph of portable Raman spectrometer (available at ACRHEM, University of Hyderabad) (b) large variation in typical SERS and Raman spectra of the Tetryl. **75**

Figure 2. 16 (a) Schematic of the fs Z-scan experimental setup (b) Actual experimental setup of fs Z-scan utilized for the experiment. **77**

Figure 2. 17 (a) Typical transient absorption spectra (ESA; excited-state absorption, PA; product absorption, GSB; ground state bleach, SE; stimulated emission). Image adapted from Ref. [11] **78**

Figure 2. 18 Experimental layout of the HELIOS transient absorption spectrometer. **81**

Figure 2. 19 The TAS spectra of Ag-Au-Cu trimetallic alloy NPs visible on Surface Xplorer software graphical layout. The top left panel shows the $\Delta A(t, \lambda)$ surface; it contains several transient spectra at closely spaced probe time delays. The below-left corner shows the transient spectra at successive probe delays. The top right corner displays the individual kinetic profile with a probe delay. The lower right corner contains

experimental details during the measurement. **.....82**

Figure 2. 20 Chirp corrected 3D surface panel data. Image adapted from Surface Xploreroperation manual, Ultrafast Systems. Here the Y-axis (ΔA) is a function of time as well as broadband probe wavelength.**.....83**

Figure 2. 21 (a) Typical fs transient absorption spectra of Ag-Au-Cu trimetallic alloy NPs at a time delay increased from 0 to 20 ps for a pump wavelength of 400 nm. Image adapted from Ref. [46] **…… 84**

Figure 3. 1 XRD spectra of the synthesized (a) Ag-TiO_2 NPs (b) TiO_2 NPs. **.....98**

Figure 3. 2 UV-visible absorption spectra of pure TiO2 NPs prepared by fs laser ablation (red) and Ag-doped TiO_2 NPs prepared by reduction (blue). The inset shows the pictures of the prepared nanoparticles.**.....99**

Figure 3. 3 TEM images of (a) TiO_2 NPs synthesized in deionized water and its (b) magnified view. Inset lying at the intersection of Figures (a) and (b) is the histogram constructed by the number density of TiO_2 NPs (c) SAED pattern of the TiO_2 NPs demonstrate a polycrystalline nature (d) HRTEM image of a single TiO_2 NP exhibiting a clear shell structure. **.....101**

Figure 3. 4 TEM images of (a) Ag-doped TiO_2 NPs in deionized water and its (b) magnified view. Inset of Figure (a) is the histogram constructed by the number density of TiO_2 NPs (c) SAED pattern of the Ag-TiO_2 NPs demonstrating the polycrystalline nature (d) HRTEM image of a single Ag-TiO_2 nanoparticle (represented by a blue dotted circle) indicating the presence of embedded Ag nanoparticle (shown inside the red circles). **..102**

Figure 3. 5 FESEM-EDX elemental mapping images of Ag-doped TiO2 NPs (a) Electron microscopic image of Ag-TiO2 (b) Single particle colored mix-map of Ag-TiO_2 containing each constituent (c) EDS spectra inset depicting the atomic % and weight% of individual elements. (d, e, f) clarifies the presence and distribution of Oxygen (blue), Titanium (green), and Silver (red), respectively. [magnification bar of all images is 1 µm]**.....103**

Figure 3. 6 (a) UV-Vis-IR absorption spectra of Ag-doped TiO_2 NPs (b) SERS spectrum of RDX traces (100 µM) sensed employing Ag-doped TiO_2 NPs (c) SERS spectrum of AN traces (20 µM) sensed employing Ag-doped TiO_2 NPs.**.....104**

Figure 3. 7 Lower and higher magnification FESEM images of (a and b) Ti NSs (c and d) Ti-Ag NSs. FESEM EDX spectra of Ti (e) and Ti-Ag NS (f), with elemental composition table inside.**.....105**

Figure 3. 8 (a) SERS of MB 1 µM using Ti and Ti-Ag NSs (b) Concentration SERS spectra of MB from 10^{-5} to 10^{-9} M using Ti-Ag NS. **.....106**

Figure 4A. 1 (a) FESEM image of single spot fs BB ablation producing BB profiled ablation imprint on TM substrate surface, red arrow depicts the laser polarization direction, (b) Spatial periodic profile analysis of the concentric rings surrounding the central lobe portion. (c) MATLAB simulated intensity beam profile of generalized zeroth order BB from Bessel function J_0 (x) term……..……**123**

Figure 4A. 2 (a) Large area overlapping of BB ablated zones, leading to the formation of the complete raster scanned NS, (b) 700X magnified portion from Figure 4A.2(a), (c) overlapping between two consecutive BB profiled laser ablated region, with 1500X magnification. The square-marked (3) region displays the region of overlap. The red arrow depicts the laser polarization direction. **.....124**

Figure 4A. 3 (a) Region of overlap, 4 kX magnified (b) magnified region from Figure 4A.3(a), revealing ladder-like periodic NSs, having nano growths on the ladder steps. The red arrow depicts the laser polarization direction. **.....124**

Figure 4A. 4 The image on the left-most side portrays the physical outlook of the BB ablated TM NS substrate (a) FESEM image (50 kX magnification) of the large area NS (b) FESEM image of BB ablated TM NS, under 2.5 kX magnification (c) lower magnification image corresponding to the yellow square-dashed position in Figure 4A.4(b), 4A.4(d), (e) 50 X magnified images from separate, correspondingly identified positions of the image (c), (f) exhibits the ladder-like NS, with 100 kX magnification. Yellow dashed boxes with arrow lines indicate the region that has been magnified in the subsequent image. The red arrow depicts the laser polarization direction. **.....126**

Figure 4A. 5 (a) FESEM image of BB central lobe ablated lines in 2.5 kX magnification, (b) and (c) central lobe ablated line regions in higher magnifications, 4.6 kX, 20 kX respectively. Yellow dashed boxes, with arrow lines, indicate the region that has been magnified in the subsequent image. Sand dune-like periodicity is observed around the walls of the central lobe ablated line. The red arrow depicts the laser polarization direction. **.....126**

Figure 4A. 6 EDX mapping data of BB patterned TM NS. (a) the region under EDX mapping, (b) overlay mapping data exhibiting the existence of all the elements. Individual exhibition of EDX mapping data for all the elements found- (b1) Au, (b2) Ag, (b3) Cu, (b4) O, (c) and (d) show elemental peaks and weight percentages of each element found respectively. **.....127**

Figure 4A. 7 (a) AFM data corresponding to the BB ablated ladder-like periodic NS, the average depth within the periodic ladder step-like NSs is estimated to be ~95 nm. (b) the maximum depth between two ladder-like structures was ~900 nm, extracted from the AFM image and shown on the right. **.....128**

Figure 4A. 8 (a) Bessel beam induced SPP generation and propagation towards counter-direction along TM surface-air interface. (b) A periodic modulated intensity profile was developed following the interference of a scattered field with the incident beam**……..** **.....130**

Figure 4A. 9 The image on the left-most side portrays the physical outlook of the GB ablated TM NS substrate (a), (b) depict lower magnification (300 X, 500 X correspondingly) images of fs GB fabricated TM NS, (c) and (d) exhibit 10 kX magnification images of corresponding sections marked in light, dark blue dashed boxes in Figure 4A.9(b). Similarly, (e), and (f) present 50 kX magnified regions identified with dark red- and purple-colored dashed boxes, respectively, in Figure 4A.9(d). **.....132**

Figure 4A. 10 EDX mapping data of Gaussian beam patterned TM NS. (a) the region under EDX mapping, (b) overlay mapping data exhibiting the existence of all the elements.

Individual exhibition of EDX mapping data for all the elements found- (b1) O, (b2) Cu, (b3) Ag, (b4) Au, (c) and (d) depict elemental peaks and weight percentages of each element found respectively. **132**

Figure 4A. 11 (a) FESEM image of unablated, pristine TM substrate surface. (b) EDX data was collected from the unablated, pristine TM substrate surface, confirming the presence of three metals, Ag, Au, and Cu. **133**

Figure 4A. 12 (a) Concentration-dependent SERS spectra of CE using BB ablated TM NS, along with pure Raman spectrum (in orange color) of CE (50 mM) collected from unablated TM pristine, (b) Reproducibility spectra (with ~12% RSD) of CE (100 μM), (c) Concentration-dependent SERS spectra of PETN using recycled BB ablated TM NS, along with pure Raman spectrum (in orange color) of PETN (50 mM) collected from unablated TM pristine, (d) Reproducibility spectra (with ~14% RSD) of PETN (5 mM). The portable Raman acquired the complete SERS data in this Figure, with the same acquisition parameters mentioned in the experimental details. **134**

Figure 4A. 13 (a) Concentration-dependent SERS spectra of CE collected by GB ablated TM NS, along with pure Raman spectrum (in orange colour) of CE (50 mM) collected from unablated TM pristine, (b) Reproducibility spectra (with ~16% RSD) of CE (500 μM), (c) Concentration-dependent SERS spectra of PETN using recycled GB ablated TM NS, along with pure Raman spectrum (in orange colour) of PETN (50 mM) collected from unablated TM pristine, (d) Reproducibility spectra (with ~17% RSD) of PETN (5 mM). The portable Raman acquired the complete SERS data in this Figure, with the same acquisition parameters mentioned in the experimental details section. **136**

Figure 4A. 14 (a) Comparison of EFs between BB patterned TM NS and GB patterned TM NS, for the detection of Tetryl (CE), (b) similar comparative data of EFs between BB patterned TM NS and GB patterned TM NS, for the detection of PETN. **137**

Figure 4A. 15 (a) SERS mapping data of CE (0.5 mM), corresponding to 1357 cm^{-1} peak. (b) overlay the SERS mapping data representation with TM NS under the 10X objective. **138**

Figure 4A. 16 (a) SERS mapping data of PETN (5 mM), corresponding to 1292 cm^{-1} peak. (b) overlay representation of the aforementioned SERS mapping data with TM NS under the 10X objective. **139**

Figure 4A. 17 A complete picture of charge transition in TM nano-system. (a) incident photon-assisted interband transition in Cu NS, (b) photon-excited interband transition in Au NS (c) photon-induced intraband charge excitation in Ag NS. **139**

Figure 4A. 18 Schematic of BB induced laser ablation in air, engaging 50 fs, 800 nm BB generated using an axicon (a) FESEM image of the overlap of two consecutive BB profile ablation imprints on BM alloy surface (b) lower magnification image of the BB patterned surface (c) ladder-like LIPSS formed in nanoscale topography due to BB interaction (d) higher magnification image of BM NS revealing ladder-like steps with various nano growths all over. **141**

Figure 4A. 19 (a) EDX spectrum of fs BB ablated Ag-Au BM LIPSS NS. The elemental weight percentage table has been provided as an inset. **142**

Figure 4A. 20 (a) SERS data of trace concentration of AN (10 µM), with its signature peak at 1043 cm^{-1} (b) SERS spectrum of TETRYL (5 µM), displaying its signature peak at 1353 cm^{-1}……**143**

Figure 4B. 1 (a) Schematic diagram explaining the laser ablation process to prepare the NS substrate and the subsequent SERS-based detection process. (b) Simulated intensity beam profile on MATLAB for the zeroth order BB from Bessel function J_0 (x) term (c) FESEM image of BB ablated single line forming NSs both sides (d) Line profile plot corresponding to the navy-blue line over the BB imprint on the starting point in figure 4B.1(c). The plot reveals the central lobe ablated portion surrounded by periodic concentric rings. (e) FESEM image of GB ablated single line forming NSs within the line**…… 160**

Figure 4B. 2 (a) FESEM image of overlapping two Bessel beam profiled ablation zones causing periodic structures. FESEM images of the fabricated complete NS with different magnifications, (b) 92X (c) 300X (d) 1kX (e) 2.5 kX. The red arrow depicts the direction of laser polarization. The ablation parameters are 0.3 mm/sec scan speed, an inter-line spacing of 55 µm, and 13 J/cm^2 central peak fluence.**.....161**

Figure 4B. 3 (a) FESEM image of column-wise periodic NSs on Ag surface, with 10 kX magnification (b) FESEM image of nanotubular LIPSS, with 50 kX magnification (c), (d) Higher (100 kX) magnification image of the same nanotubular LIPSS in a different region (e) AFM image of the column-wise LIPSS. The ablation parameters used were 0.3 mm/sec scan speed and 13 J/cm^2 peak fluence. **.....163**

Figure 4B. 4 FESEM images of central ablation line for (a) 12 kX and (b) 40 kX magnification. The ablation parameters are 0.3 mm/sec scan speed and 13 J/cm^2 central peak fluence. **.....165**

Figure 4B. 5 (a) FESEM image of pristine, unablated Ag surface and (b), (c) its corresponding EDX data revealing Ag and O elemental weight percentage**.....166**

Figure 4B. 6 (a) FESEM image of BB-ablated Ag nanostructure and (b), (c) its corresponding EDX data revealing Ag and O elemental weight percentage**.....166**

Figure 4B. 7 FESEM images of Gaussian beam ablated NSs for (a) 79 kX, (b) 1 kX, (c) 4 kX, and (d) 50 kX magnifications, respectively. The red arrow depicts the direction of laser polarization. The ablation parameters, such as BB ablation, were kept unchanged, as mentioned in Figure 4B.3. **.....169**

Figure 4B. 8 (a) FESEM image of GB-ablated Ag nanostructure and (b), (c) its corresponding EDX data revealing Ag and O elemental weight percentage**.....170**

Figure 4B. 9 (a) Concentration-dependent SERS spectra of TNT using BB ablated Ag NS, along with pure Raman spectrum (in black color) of TNT (50 mM) collected from unablated Ag pristine, (b) Reproducibility spectra (with ~15% RSD) of TNT (5 mM), (c) Concentration-dependent SERS spectra of Tetryl using recycled BB ablated Ag NS, along with pure Raman spectrum (in black color) of Tetryl (50 mM) collected from unablated Ag pristine, (d) Reproducibility spectra (with ~17% RSD) of Tetryl (5 µM). The portable Raman acquired the complete SERS data in this figure, with the same acquisition parameters mentioned in the experimental details.**.....172**

Figure 4B. 10 (a) Concentration-dependent SERS spectra of RDX using BB ablated Ag NS, along with pure Raman spectrum (in black color) of RDX (50 mM) collected from unablated Ag pristine, (b) Reproducibility spectra (with ~16% RSD) of RDX (50 µM), (c) Concentration-dependent SERS spectra of HMX using recycled BB ablated Ag NS, along with pure Raman spectrum (in black color) of HMX (50 mM) collected from unablated Ag pristine, (d) Reproducibility spectra (with ~20% RSD) of HMX (5 mM). The complete SERS data in this figure has been acquired by the portable Raman, with the same acquisition parameters mentioned in experimental details. **173**

Figure 4B. 11 (a) Concentration-dependent SERS spectra of TNT using GB ablated Ag NS, along with pure Raman spectrum (in black colour) of TNT (50 mM) collected from unablated Ag pristine, (b) Reproducibility spectra (with ~28% RSD) of TNT (5 mM), (c) Concentration-dependent SERS spectra of Tetryl using recycled GB ablated Ag NS, along with pure Raman spectrum (in black colour) of Tetryl (50 mM) collected from unablated Ag pristine, (d) Reproducibility spectra (with ~22% RSD) of Tetryl (5 µM). The portable Raman acquired the complete SERS data in this figure, with the same acquisition parameters mentioned in the experimental details. **175**

Figure 4B. 12 SERS performance comparison plot of the BB-engineered Ag NS, with GB-structured Ag NS, regarding EFs and signal consistency (RSD). (a) Comparison of RSDs between BB patterned Ag NS and GB patterned Ag NS, for the detection of TNT. The inset bar plot shows the EFs comparison. (b) Comparison of the RSDs between BB patterned Ag NS and GB patterned Ag NS, for the detection of Tetryl. The inset bar plot shows the EFs comparison. **176**

Figure 4B. 13 Large area mapping image data, 8(a)- TNT (corresponding peak 821 cm^{-1}, 5 mM concentration), 8(b)- Tetryl (corresponding peak 1357 cm^{-1}, 5 mM concentration), 8(c)- RDX (corresponding peak 875 cm^{-1}, 5 mM concentration), and 8(d)-HMX (corresponding peak 881 cm^{-1}, 5 mM concentration), covering more than 2500 μm^2 area for each image. **177**

Figure 4B. 14 (a) Reflectivity spectra for BB structured LIPSS Ag NS, GB structured Ag NS, and pristine Ag surface at 45^0 angle of incidence (b) Signal strength stability data for the sensing of TNT (5 mM) molecule, unveiling the presence of 1355 cm^{-1} peak signature. The SERS data was collected for up to 90 days. **179**

Figure 4B. 15 Schematic of BB generated laser ablation in air, with a 50 fs, 800 nm BB generated using an axicon (a) FESEM image of the spatial overlap of two consecutive BB profile ablation imprints on Cu surface (b) lower magnification image of the BB patterned Cu surface (c) ladder-like LIPSS formed in nanoscale topography due to BB interaction (d) higher magnification image of Cu NS revealing ladder-like steps with numerous nano growths on them. **181**

Figure 4B. 16 (a-c) FESEM EDX elemental analysis data for the ladder-like LIPSS region, depicting the amount of O, and Cu in the same region. (d-f) FESEM EDX elemental analysis data for the larger NS region, depicting the amount of O, and Cu present. **182**

Figure 4B. 17 (a) SERS data of trace concentration of Tetryl (5 µM), with its signature peak at 1357 cm^{-1} (b) SERS spectrum of PETN (1 mM), displaying its signature peak at 1292 cm^{-1}. **183**

Figure 5A. 1 (a) FESEM image of the surface of the pristine, unablated MM (Ag-Au-Cu) substrate (b) EDX spectra of the surface of the pristine, unablated MM (Ag-Au-Cu) substrate. **203**

Figure 5A. 2 (a)-(c) TEM images of the MM NAPs from lower to higher magnification, (d) UV-Visible-IR absorption data of the MM NAPs. Inset (1) in Figure 5A.2(d) depicts the axicon lens and (2) shows stored colloidal NPs. (e)-(f) Higher magnification TEM images for the MM NAPs. (g) Overlay image of the EDX mapping. (h)-(j) TEM EDX mapping data of the same. (k) Elemental composition of the MM alloy NPs. **205**

Figure 5A. 3 (a) EDX spectra of the multimetal (MM) nanoalloy particles. **206**

Figure 5A. 4 (a) HRTEM image of MM NAPs, (b) 2DFFT performed at an area indicated with a rectangular box. The Inset of Figure 5A.4(b) presents the XRD spectrum. Bottom panel, images [1]-[5] represent IFFT at locations [1]-[5] shown in (b)], and (c) SAED patterns recorded from the MM NAPs. **207**

Figure 5A. 5 (a) Concentration-dependent SERS spectra of RDX using MM NAPs drop cast on unablated Ag pristine, along with pure Raman spectrum (in grey colour) of RDX (50 mM) collected from only unablated Ag pristine, (b) Reproducibility spectra (with ~29% RSD) of RDX (50 µM), (c) Concentration-dependent SERS spectra of PA using MM NAPs drop cast on unablated Ag pristine, along with pure Raman spectrum (in pink colour) of PA (50 mM) collected from unablated Ag pristine, (d) Reproducibility spectra (with ~24% RSD) of HMX (50 mM). The portable Raman acquired the complete SERS data in this figure, with the same acquisition parameters mentioned in the experimental details. **211**

Figure 5A. 6 (a) Open aperture Z-scan curves of MM NAPs in deionized water performed with ~50 fs amplifier pulses,1 kHz, and 800 nm excitation. 3d spheres in blue represent the experimental data, whereas the solid red curve is the theoretical fit corresponding to 3PA. The yellow solid line depicts the theoretical fit for 2PA, which does not fit with the experimental data. (b) Closed aperture Z-scan data of the MM NAPs reveal the n2 value. Similarly, 3d spheres in blue represent the experimental data, whereas the solid red curve is the theoretical fit. (c) The TEM image shows different alloyed portions of the MM NAPs. (d) Schematic energy level diagram of MM NAPs in NLO regime. **213**

Figure 5A. 7 (a) fs transient absorption spectra of MM NAPs at a time delay increased from 0 to 20 ps for a pump wavelength of 400 nm. (b) Transient absorption time profiles of the same MM NAPs at 675 nm central peak of the ESA band with the corresponding triple-exponential fit. **221**

Figure 5A. 8 (a) Transient absorption time profile of the MM NAPs, corresponding to the bleach central peak at 550 nm. **221**

Figure 5B. 1 (a) Experimental setup engaging vortex phase plate and a plano-convex lens (b) VB profile captured in a beam profiler. **239**

Figure 5B. 2 (a) Single spot ablation with fs VB engaging 2000 pulses for 2 seconds of exposure time (b1) 2D map of the theoretically simulated VB profile (b2) normalized intensity profiles along the diameter for the VB beam. The (b1, b2) images are adapted from Ref. 33. ..... **240**

Figure 5B. 3 FESEM images of the VB ablated Ag NSs. (a) Image of the complete structure (b) lower magnification (1.5 kX) images of the NS showing the laser ablated lines. (c, d) higher magnification (4 kX, 10 kX) images showing immature LIPSS formation..... **242**

Figure 5B. 4 EDX data of the fabricated Ag NS (a, b) EDX spectra of the same showing Ag and O peaks (c) Table showing the elemental analysis. **..... 243**

Figure 5B. 5 (a) Concentration-dependent SERS spectra of Tetryl collected by VB ablated Ag NS, along with pure Raman spectrum (in dark yellow colour) of Tetryl (50 mM) collected from unablated pristine Ag surface, (b) Reproducibility spectra (with ~26% RSD) of Tetryl (5 μM), (c) Concentration-dependent SERS spectra of AN using VB ablated Ag NS, along with pure Raman spectrum (in black colour) of AN (50 mM) collected from unablated Ag pristine, (d) Reproducibility spectra (with ~23% RSD) of AN (5 mM). The portable Raman acquired the complete SERS data in this Figure, with the same acquisition parameters mentioned in the experimental details**. 243**

Figure 6.1 Summary of different segments of the complete thesis work **……257**

List of Tables

Table 1.1 Performance of the SERS substrates prepared in this thesis ……. 29
Table 2.1 Specifications of Vitesse and LIBRA systems ……... 60
Table 2.2 Various parameters about the Axicon lens mentioned on Thorlab's official website ……...…...66
Table 4B.1 Raman modes corresponding to significant Raman peaks ……...……...184
Table 4B.2 Lowest trace and EFs comparison of BB fabricated LIPSS NSs ……...… 184

Intentional Blank Page

Intentional Blank Page

Chapter 1

Introduction & Outline of The Thesis

Abstract

First and foremost, this chapter provides an overview of high-energy materials (HEM) and their most notable characteristics. Secondly, a historical perspective of the effectiveness of near-field detection by surface-enhanced Raman scattering (SERS), the remarkable properties of localized surface plasmon resonances (LSPR), and the applications of these resonances in science and industry is provided. In addition, the chapter discusses the mechanisms that are responsible for the SERS technique, such as electromagnetic and chemical enhancement processes. In the subsequent sections, a comprehensive explanation of SERS active elements, including nanoparticles (NPs) and nanostructures (NSs), as well as the manufacturing of these elements using ultrafast laser ablation in liquids (ULAL) and ultrafast laser ablation in air (ULAA), is presented. The last section of this chapter describes the dynamics of the excited states of the plasmonic nanoentities investigated using ultrafast lasers.

1.1. Introduction and Motivation

The phrase "nano" is derived from the Greek word [1] meaning "extremely small," and Nanoscience is the field of research that focuses on systems with extremely small dimensions. Despite Richard Feynman's recognition as the pioneer of modern nanoscience and nanotechnology (N&N) [2], nanomaterials were already used for many purposes before his time. Michael Faraday conducted a study in 1857 on the production and characteristics of colloidal suspensions of gold known as "Ruby" gold [1,3]. Due to their distinctive optical and electrical characteristics, these nanoparticles are considered very intriguing. Faraday illustrated the phenomenon of gold nanoparticles generating solutions of varying colours when exposed to certain illumination conditions. John Utynam [2] obtained a patent for a glass containing gold nanoparticles in 1449. During the 16th century, Paracelsus, a Swiss physician known as Theophrastus von Hohenheim, used gold nanoparticles to treat patients afflicted with many illnesses [1,2]. Richard Zsigmondy [2] pioneered the notion of the nanometer and was awarded the Nobel Prize in Chemistry in 1925 for his groundbreaking work in measuring the size of particles, including gold colloidal particles, using a microscope. However, in 1959, Feynman did provide significant elucidation on the same topic during his *iconic lecture* [4] at a conference held at the California Institute of Technology. During this lecture, Feynman demonstrated to the audience that nanotechnology could impact modern science significantly. Feynman proposed, “Why cannot we write the entire 24 volumes of the Encyclopedia Britannica on the head of a pin?” [1,4]. In 1974, after fifteen years, Norio Taniguchi, a Japanese scientist, coined and provided the first definition for the word "nanotechnology" [5]. Before the advancements of the contemporary period, people in the fourth century AD, namely the Romans, used nanoparticles and architecture to create the *Lycurgus cup* [6]. The observed dichroism, characterized by the existence of two distinct colours, could be attributed to the nanoparticles that have a diameter ranging from 50 nm to 100 nm. According to the findings of the X-ray analysis, the nanoparticles were made up of an alloy of silver (Ag) and gold (Au), with the proportion of silver to gold being around seven parts to three parts. For more information, the nanoparticles include around ten percent copper (Cu) dispersed across a glass matrix [1,6]. The incorporation of nanoparticles of gold (Au) and silver (Ag) into the glasses of late medieval church windows [1] resulted in the creation of a fantastic display of red and yellow colors. Beginning in the ninth century and continuing until the seventeenth century, ceramic glazes referred to as "lustre" were used throughout

the Islamic world and, later, in Europe. NPs of silver (Ag), copper (Cu), or other elements were incorporated in these glazes [7], which resulted in a bright and dazzling look. Also, the Italians are credited for using nanoparticles in producing Renaissance pottery around the 16th century [8]. Over the last half-century, certain branches of nanophotonics and nanotechnology have thrived in the contemporary "nanoworld," built on the pillars of ultrafast laser-matter interaction. Similarly, ultrafast laser-induced periodic surface structure (LIPSS) has become a prominent area of study in laser-matter interaction. It has exciting potential uses in areas such as photochemical water splitting, hydrogen evolution [9], biomedicine, surface chemistry [10], photodetectors, solar thermal conversion [11], and storage of data [12,13]. Nanopatterning is a rapidly growing field of study essential to contemporary photocatalysis, microelectronics, and semiconductors [14]. Many other procedures have developed alongside laser-based approaches for doing surface changes. There are many well-established techniques for surface change, including surface chemistry, catalysis-assisted modification of surfaces [15], ion beam irradiation created waveguide surfaces [16,17], ion beam milling, electron beam irradiation [18], and co-catalysis [19]. One of the most effective methods for creating surface micro/nanostructures as well as colloidal nanoentities is laser ablation, which may be performed in either liquid or air and termed laser ablation in the air (LAA) and laser ablation in liquid (LAL) techniques. Several reports have provided meticulous discussions on important mechanisms, models [20,21], and other aspects underlying the femtosecond (fs) LAA [22–27] and LAL [28–30] processes. These techniques are also significantly useful to fabricate periodic surface structures. In biosensing, in particular, periodic hierarchical topographies have outstanding biomimetic mechano-bactericidal [31] properties. Several seminal investigations have extensively and methodically uncovered the complex physics underlying the creation of different LIPSS topographies [32,33]. Ultrafast laser-fabricated LIPSS production [34–36] is among the most intriguing methods that have proved organized and effective. Over the last 20 years, Bonse and co-workers [12,37–41] have conducted extensive research to construe the intricate processes of LIPSS development. Senegacnik et al. [41] recently created diffraction-assisted laser structuring using cavitation bubbles created through ablation. This technology effectively creates beam-guiding pattern-structured arc-shaped concentric microgroove channels using thermo-optical tweezers powered by thermocapillary forces. Chang et al. [41] recently achieved fs laser-induced periodic structures on a copper surface. The experimental results were well-

matched with the numerical model of the high repetition rate ablation experiment, which used a two-temperature model (TTM). In another study, Taher et al. [42] demonstrated the wavelength-dependent production of LIPSS on the surface of stainless steel using an excitation wavelength ranging from 400 nm to 2200 nm. Both high spatial frequency LIPSS (termed HSFL) and low spatial frequency LIPSS (termed LSFL) have been noted to have achieved regulated periodicity. Liu and colleagues researched creating ~100 nm deep-subwavelength ripples on a ZnO surface [43] using fs laser structuring with the help of a metal film. A significant reduction in damage threshold was noted, revealing a novel method to generate LIPSS in wide-bandgap materials. Using suitable contact-angle measurements, observing the water's intriguing anisotropic wetting behavior was also possible. The intriguing work of Elshorbagy et al. [44] on polarization state conversion at infrared radiation and subsequent reflecting interaction on LIPSS was presented. To clarify where the incoming light's polarization state alteration originates, the research examined the LIPSS's birefringence. By acting as a retarded, the subwavelength grating structure changes the polarization of light from linear to circular. The popularity of laser ablation in liquid (LAL) [45–47] has significantly improved in recent years due to its ability to produce nanoparticles of various materials such as metals, semiconductors, glasses, ceramics, and more. This approach has facilitated the production of numerous novel functional nanomaterials in colloidal state. One of the main benefits of LAL is its ability to synthesize colloidal nanoparticles and solid nanostructures on the target surface simultaneously in a single experiment. This also aids in fabricating novel nanostructures on the substrates submerged in liquid [48–50]. This concurrent production of nanoentities reveals exciting new possibilities for a wide range of nanophotonic and optoelectronic applications. The pulsed LAL technology is now recognized as a green chemistry method for producing pure or alloyed ligand-free nanoparticles in different sizes and shapes. Therefore, this way of rapidly interacting lasers with matter has been extensively utilized over the past two decades to create a wide range of nanostructures. Amendola’s group [45,51–54], a leading research group in nanophotonics, has investigated the synthesis, modelling, features, and diverse applications of newly created plasmonic pure and alloy nanoparticles [45,46,51]. The NPs generated using the LAL approach have gained widespread recognition for their diverse applications. These objects have been discovered to possess optical, magnetic, or catalytic properties [55,56]. They are utilized in several fields, such as photonics, hydrogen evolution [11], photocatalysis [57,58], sensing [59–

61], magneto-optics applications [47,62–64], and many more [65,66].

Recent developments in structured light have shown various new light patterns, such as non-diffracting beams like the Bessel beam (BB), vector vortex beam, and Mathew beam. These innovative investigations have expanded the possibilities for the fundamental research and practical applications of the LAL and LAA methods for fabricating solid and colloidal nanoentities via surface structuring. [67–70] The self-healing optical profile [71,72], higher depth of focus (DOF) [73], orbital angular momentum [74], and invariance of intensity profile along the propagation length are some of the fantastic advantages of these beams. These properties make them appropriate optical tools for investigations of laser-matter interaction, [75,76] surface engineering, [77,78] optical trapping, optical coherence tomography [71], and other fields [12]. Another example of this type is the BB produced by an Axicon, which yields an intensity profile that is self-healing and distance-invariant while offering an improved depth of field. Surprisingly, neither LAA nor LAL has had many investigations upon fs BB interactions with metals.

In light of the perturbing circumstances for homeland security, advancements in research regarding trace detection of high energy materials (HEMs)/explosives have emerged as a need of the hour for several nations due to the sustained and collective terrorist/warfare activities over the past two decades. High energy materials (HEMs) [79,80], sometimes known as explosives, consist of energetic groups that release a significant amount of energy (in the form of light and heat) when exposed to spark, shock, or friction. Based on their sensitivity and detonation criteria, explosives are classified as primary and secondary. Primary explosives have high sensitivity and may generate significant energy, even in response to little shocks or collisions. Consequently, managing the primary explosives is challenging, but it enhances or activates the detonation of secondary explosives. Lead azide and mercury fulminate are classified as significant explosives, whereas TNT (2,4,6-Trinitrotoluene, $C_7H_5N_3O_6$), Tetryl (2,4,6-Trinitrophenylmethylnitramine, $C_7H_5N_5O_8$), RDX (1,3,5-Trinitroperhydro-1,3,5-triazine, $C_3H_6N_6O_6$) and others are classified as secondary explosives [79,80]. A limited number of homemade explosives are used in the creation of improvised explosive devices (IEDs). They can be readily produced in a laboratory setting using essential compounds such as ammonium nitrate (AN), picric acid (PA), and 2,4,6-trinitrotoluene (TNT), and its manufacturing impurities, including 2,4-DNT (2,4-Dinitrotoluene), 2,6-DNT, and 1,3-dinitrobenzene (1,3-DNB) [81]. Multiple

analytical techniques are available for the molecular identification of HEMs, whether in residual form or concealed in hidden locations and for analyzing samples collected from regions affected by detonations. Several detection approaches include photo-acoustic, Raman spectroscopy, terahertz spectroscopy (THz), laser-induced breakdown spectroscopy, ion-mobility spectroscopy (IMS), and gas chromatography [82–89]. Some of these procedures either result in sample destruction or require sample separation. Additionally, they may not be suitable for handling low-quantity samples or need a qualified individual for instrument calibration. In addition, the high water absorption, lack of specificity, and challenges in equipment restrict the use of these approaches for on-field explosive sensing [90,91]. Raman spectroscopy is a straightforward, expeditious, and non-invasive technology for sensing a variety of analytes based on the signatures of their vibrational modes. The Raman spectrum is a reliable method for obtaining precise chemical and structural information on explosives, whether in their pure form or mixed with other substances. This method may be used for explosives in many states, including liquid, solid, powder, and gas [92]. Nevertheless, the limited Raman scattering intensity of low-concentration molecules restricts their employment. Consequently, many Raman spectroscopic methods have been developed, including surface-enhanced Raman scattering (SERS) [93,94]. Over time, SERS has become one of the highly efficient techniques for sensing, biomedical, and pharmaceutical applications [95–99].

Ultra-high signal amplification characteristic of metal (plasmonic) nanostructures (NSs) and the high molecular specificity of Raman spectra combine to create SERS, a highly sensitive, nondestructive, and label-free vibrational spectroscopic molecular identification technique [100–107]. In 1974, pyridine molecules adsorbed on an electrochemically roughened silver (Ag) surface revealed increased Raman signals, which Martin Fleischmann and colleagues [100] described as a *lucky finding*. They found an enhancement factor (a mathematical estimation of the augmentation in the SERS signal, taking into account specific parameters such as the concentration of the analyte, corresponding to the Raman signal of a high-concentration analyte molecule and SERS signal of the same molecule in the lowest traced concentration) of ~10^6 in the pyridine vibrations' Raman cross-section. SERS refers to this amplification of the Raman signal in the area of the metal nanostructure. Improved Raman signals from the metal surface were described by the Van Duyne and Albrecht groups [103,108] in 1977. Maskovits [109], in 1985, provided an overview of the main theories behind enhancement processes, including

chemical (CM) and electromagnetic (EM) enhancement. The short-range chemical enhancement results from the charge transfer process (between the substrate and the analyte molecule), whereas the long-range electromagnetic (EM) enhancement is attributed to the localized surface plasmon resonance (termed LSPR) in the near-field metallic surface. The difference between CM and EM is at least three orders of magnitude. Over the last 20 years, several scientists have researched the influential factors that affect the SERS signal's augmentation. Many factors, including shape, material, size [110–117], inter-nanoentities spacing [118–120], molecular Raman scattering cross-section [121], and excitation probing wavelength [122–124], contribute to the Raman signal increase. The SERS approach has significant potential in several domains, such as biosensing, single-molecule detection, and gas-phase chemical detection [125–129]. Desirable SERS substrates [130,131] must have a high and spatially uniform enhancement factor (EF), as well as chemical stability, repeatability, accuracy, and speedy production in vast regions [132–134] with tiny debris. Ultrasensitive SERS substrates with lower analyte detection limits [120,135–137] may be fabricated using fs laser-based techniques. Laser-assisted periodic nanostructures, in contrast to wet chemical synthesis processes, provide homogeneity, flexibility, and repeatability. Plasmonic LIPSS structures may function as sensitive SERS substrates [138–141], exhibiting the necessary unpredictability and roughness to support a high hotspot density [142].

1.2. Explosives Trace Detection

High energy materials (HEMs), regularly known as explosives, are energetic groups that release significant energy in light and heat when exposed to external triggers such as a spark, shock, or friction. According to their detonation characteristics and sensitivity, explosives are classified as main and secondary. Primary explosives have high sensitivity and may release significant amounts of energy even when subjected to little stress or impact. Consequently, managing the high/secondary explosives takes much work. They serve as catalysts or triggers for igniting secondary explosives. Primary explosives, such as lead azide and mercury fulminate, are very sensitive and may be easily detonated. On the other hand, secondary explosives [79,143], ammonium nitrate (AN), picric acid (PA), and 2,4,6-trinitrotoluene (TNT), 2,4-DNT (2,4-Dinitrotoluene) are more stable and need a primary explosive to initiate their detonation. Nevertheless, there exists a limited number of homemade explosives that are used in the creation of improvised explosive devices

(IEDs). These explosives may be readily produced in a laboratory setting using basic compounds like ammonium nitrate (AN), dinitrotoluene (DNT), picric acid (PA), and so on. Identifying and detecting these materials is a paramount issue for several nations and is of utmost importance for homeland security. Many analytical techniques are available for detecting high-energy materials/explosives, either in the form of residue or in concealed locations (such as surface offset Raman spectroscopy), as well as samples taken from regions after an explosion. Several approaches that have been investigated include ion-mobility spectroscopy (IMS), terahertz spectroscopy (THz), laser-induced breakdown spectroscopy (LIBS) [144–146], Raman spectroscopy, Light Detection and Ranging, or Laser Imaging, Detection, and Ranging (LIDAR), Differential absorption lidar (DIAL), Coherent anti-Stokes Raman spectroscopy (CARS), Mass spectrometry (MS), Chemiluminescence (CL), mass spectroscopy (MS), photoacoustic spectroscopy (PAS), Fourier Transform Infrared Spectroscopy (FTIR) and gas chromatography (GC) [82–89]. Some of these procedures either result in sample destruction or the isolation of the sample, while others may not support the analysis of low-amount samples. Additionally, some approaches may need a qualified individual for equipment calibration. In addition, the high water absorption, lack of specificity, and challenges in equipment restrict the use of these approaches for on-field explosive detection. [90,91] Raman spectroscopy is a straightforward, rapid, and nondestructive method for analyzing molecule spectra. The Raman spectrum is a reliable method for obtaining precise chemical and structural information on explosives, whether in a pure form or mixed with other substances. This technique may be used for solid, liquid, powder, or gas explosives [92,147]. A Jablonski energy-level diagram from the work of Saletnik et al. [148] illustrating the transitions involved in Rayleigh, Raman Stokes, anti-Stokes, and resonance Raman scattering has been depicted in Figure 1.1. Further, various techniques for detecting hazardous materials have been summarized in Figure 1.2.

1.3. Localized Surface Plasmon

Understanding localized surface plasmon resonance (LSPR) [149,150] is essential to comprehend SERS and the variables that affect its improvement. SERS mainly employs (LSPR) to amplify the Raman signal via techniques that will be explained in subsequent sections. The research conducted in this thesis has only concentrated on using LSPR-based SERS due to the benefits outlined in the introduction. To comprehend the LSPR

phenomenon, examining how electromagnetic radiation interacts with metal nanoparticles smaller than light's wavelength is necessary.

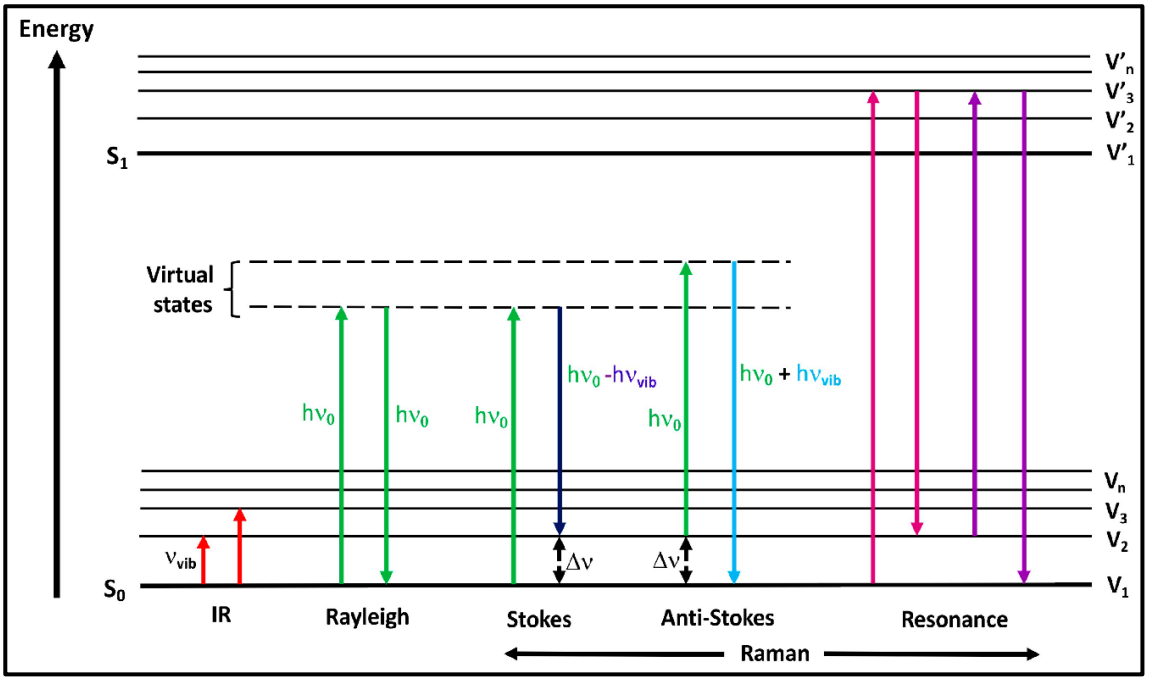

Figure 1. 1 Jablonski diagram of the energy levels illustrating the transitions involved in IR, Rayleigh, Raman Stokes, anti-Stokes, and resonance Raman scattering. Image adapted from Ref. [148].

This interaction is often approached as an electrostatic issue. When metal nanoparticles are exposed to electromagnetic radiation, the conduction electrons are displaced from the positive ions, resulting in the system's polarization. However, the phenomenon of Columbic attraction leads to the convergence of the separated negative and positive charges, resulting in the generation of a restoring force. The conduction electrons in the nanoparticle undergo coherent oscillation due to the periodic electric field and the restoring force resulting from the Columbic attraction between the positive and negative charges, as seen in the picture. The phenomenon of coherent oscillations in metal nanoparticles is often known as localized surface plasmon resonance (LSPR) [schematically presented in Figure 1.3]. The term "localized" is used because the electron oscillations are confined inside a specific region in three-dimensional space. To establish a theoretical explanation for the genesis of LSPR, the most straightforward approach is to use a model that involves a metallic nanoparticle with a spherical shape. Let's examine a metallic sphere with a radius, R, and a dielectric function positioned in a medium with a dielectric constant, ε_m.

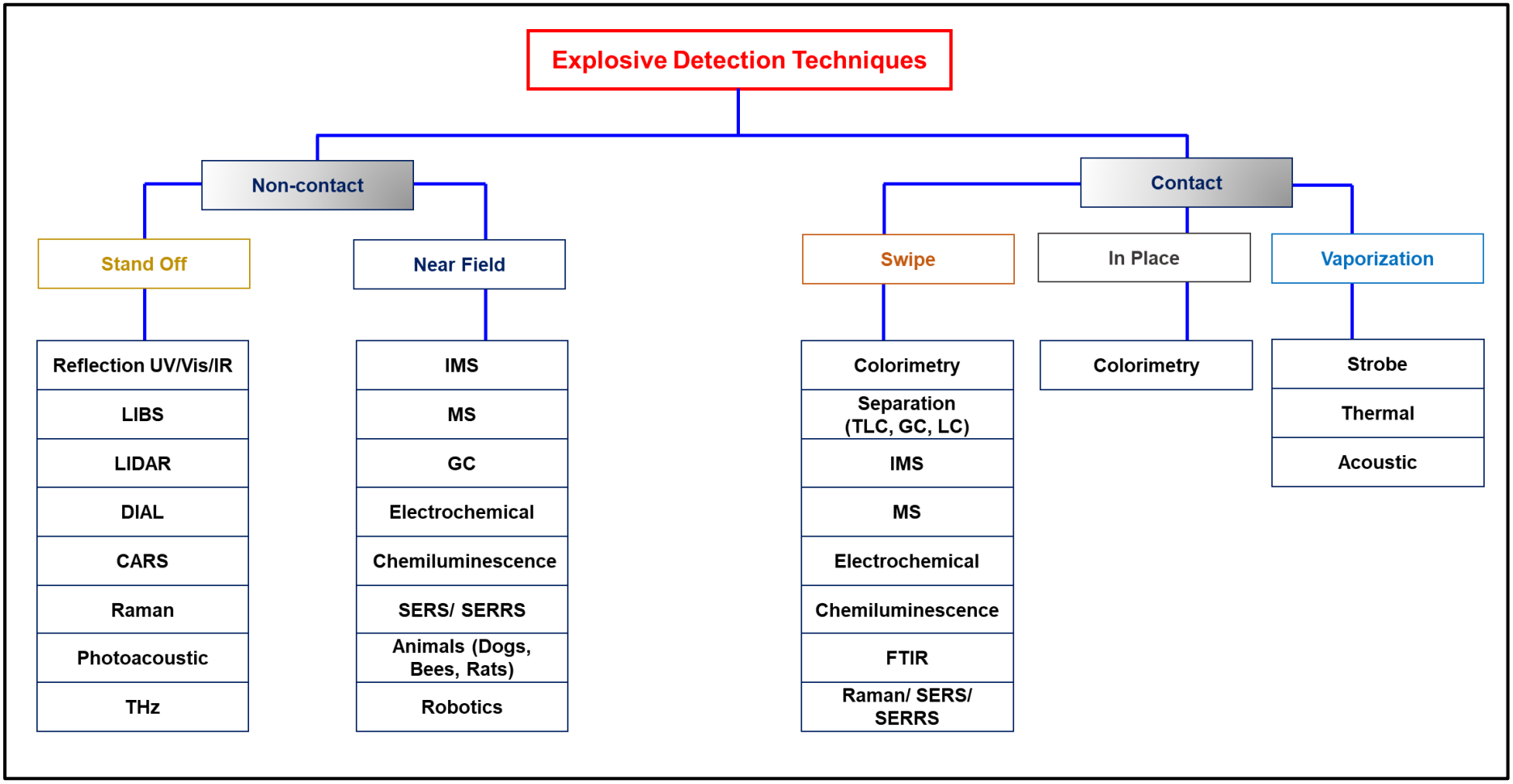

Figure 1. 2 Different techniques reported in the literature used for explosives detection

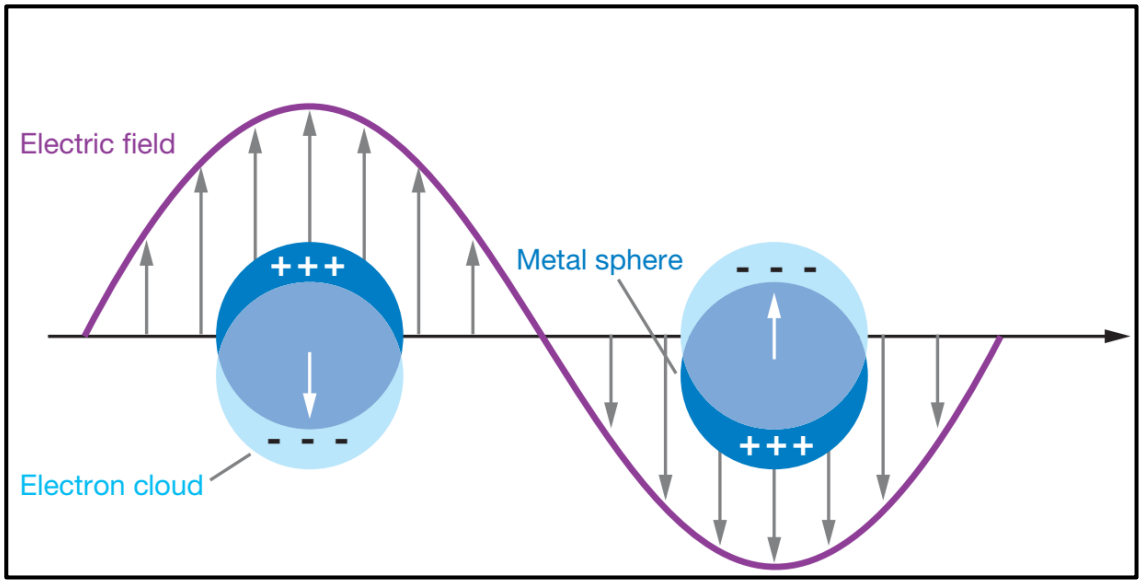

Figure 1. 3 Schematic diagrams illustrating localized surface plasmon. Image adapted from Ref. [149].

The electric potential inside (V_{in}) and outside (V_{out}) of this metallic sphere in the presence of an external electromagnetic field, E_{Inc}. When expressed in spherical coordinates, the solution to the Laplace equation for a potential V may be represented as a sequence of Legendre polynomials. The mathematical approach has been explained elsewhere. [151,152] Finally, we arrive at the expression of the potential inside and beyond the sphere that may be expressed as,

$$V_{in} = \frac{-3\varepsilon_m}{\varepsilon+2\varepsilon_m} E_{Inc} r\cos\theta \tag{1.1}$$

$$V_{out} = -E_{Inc} r\cos\theta + \frac{\varepsilon-\varepsilon_m}{\varepsilon+2\varepsilon_m} R^3 E_{Inc} \frac{\cos\theta}{r^2} \tag{1.2}$$

The electric field within the metallic sphere may be determined based on its potential as,

$$E_{In} = \frac{3\varepsilon_m}{\varepsilon+2\varepsilon_m} E_{Inc} \tag{1.3}$$

It is important to acknowledge that the dielectric function for metals is a complex function that may be expressed as the sum of real and imaginary components, given by,

$$\varepsilon \approx \varepsilon(\lambda) = \mathrm{Re}\varepsilon(\lambda) + i\mathrm{Im}\varepsilon(\lambda) \tag{1.4}$$

When Im[ε(λ)] is small, which means Im[ε(λ)] is approximately equal to zero, and Re[ε(λ)] is approximately equal to ($-2\varepsilon_m$), the denominator in equation 1.3 becomes infinitely large [151]. The resonance occurs when the metallic sphere exhibits a significant optical response, known as Localized Surface Plasmon Resonance (LSPR). The field created, and hence the denominator in equation 1.3, is highly influenced by the form of the metal nanostructure. In this case, the resonance condition is solely a result of the sphere's geometry and the boundary conditions used in the derivation.

- The characteristics and excellence of LSPR are contingent upon certain parameters.
- First and foremost is the dielectric function of the metal, ε(λ). The imaginary and real parts of the dielectric function have a significant role in the excitation of LSP. In Figure 1.4, wavelength-dependent plots of the real and imaginary parts of the ε have been presented from the report of Ma et al. [153]
- The nanoparticle's shape affects the resonance condition in the denominator of the electric field.
- Wavelength of excitation.
- Additional nanoparticles in the surrounding medium are also accounted for.

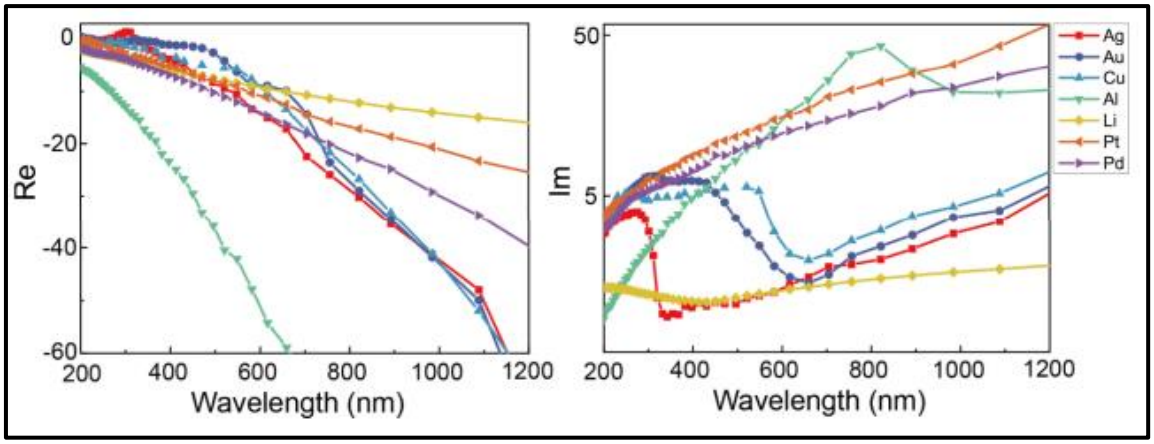

Figure 1. 4 The real (Re) and imaginary (Im) parts of the dielectric functions for different metals. Image adapted from Ref. [153].

1.4. SERS Enhancement Mechanism

Before delving into the process of SERS, it is essential first to understand Raman Scattering thoroughly. [92] SERS is a Raman scattering that amplifies the signal using plasmonic nanostructures. Raman scattering is the phenomenon of light being scattered by materials, causing a change in the frequency of the incoming light. The change in

frequency is referred to as the 'Raman shift' and serves as a distinctive indication of the vibrational characteristics of the materials being examined. The phenomenon is known as "Stokes Raman" (down conversion) when the frequency of the scattered light is lower than the incident frequency and as "anti-Stokes Raman" (upconversion) when it is higher. The Anti-Stokes scenario arises when the molecules are already excited, which is not frequent at ambient temperature. This thesis only focuses on the phenomenon known as Stokes shift. Raman spectroscopy offers significant promise for several applications due to its label-free nature, rapidity, and ability to provide fingerprint spectra, allowing for the distinct identification of studied items. The Raman scattering phenomenon may be described by considering the oscillating electric dipole, where the scattered radiation is regarded as radiation released by the dipole. One can express the mathematical form of the induced dipole moment as [154,155]

$$p_{induced} = \alpha_0 E_0 \cos(2\pi\nu_0 t) + q_0 E_0 \left(\frac{d\alpha}{dq}\right)_{q=0} [\cos\{2\pi(\nu_0 - \nu_m)t\} + \cos\{2\pi(\nu_0 + \nu_m)t\}] + \cdots \quad (1.5)$$

The induced dipole moment, denoted as $p_{induced}$, is directly proportional to the input electromagnetic field, E_{inc}. The proportionality constant that relates them is called polarizability, represented by the symbol α. ν_m represents the frequency of the vibration relative to the average location. It is influenced by both the bond strength and the decreased mass of the atoms, where q is total displacement following Hook's law model. The equation demonstrates the presence of anti-Stokes and Stokes frequencies in the Raman scattering event, as shown by the sum and difference frequencies created. It is crucial to emphasize that in the Raman scattering case, the polarizability's derivative concerning the normal coordinate ($d\alpha/dq$) must not be zero. This implies that only the vibrational modes that cause a change in polarizability are considered Raman active. The Raman signal's strength is directly related to the molecule's Raman cross-section and the incoming light's power density. In the case of SERS, the situation remains the same, except that there is an increase in the enhancement factor due to both electromagnetic and chemical enhancement. In the context of SERS, the output power, P_{SERS}, is directly proportional to the Raman power. Additionally, P_{SERS} is further enhanced by a factor called G_{SERS}, which is the product of two factors: electromagnetic enhancement (G_{EM}) and chemical enhancement (G_{CM})[94,151,156].

$$P_{SERS} = G_{SERS} P_{Raman} = G_{EM} G_{CM} P_{Raman} \quad (1.6)$$

1.4.1. Electromagnetic Enhancement

The primary cause of the electromagnetic enhancement (EME) in the SERS is the characteristics of LSPR and its impact on the proximity of probe molecules. Like any other LSPR approach, this one relies on near-field enhancement and is influenced by several variables that affect the quality of LSPR. The probe molecules in SERS substrates adhere to the surface of metal nanoparticles/nanostructures by physisorption or chemisorption. The amplification is achieved by solving the electric field around the probe molecules in the presence of the metal NPs. The EME may be comprehended about two occurrences.

1.4.1.1. Local Field Enhancement

The preceding sections have shown that metal nanoparticles undergo field amplification in their proximity under certain circumstances. The electric field amplification with nanoparticles is called LFE (localized field enhancement). Field enhancement occurs specifically in the proximity of the nanoparticle, resulting in regions of high electric field density, sometimes referred to as "hotspots" [157,158] in surface-enhanced Raman spectroscopy (SERS). As previously discussed, the field enhancement in this scenario may be comprehended using the classical dipole approximation. The power of dipole radiation from the oscillating Raman dipole can be expressed as [94,151,156],

$$P_{Raman} = \frac{\omega^4}{12\pi\varepsilon_0 c^3}|P_{induced}|^2 = \frac{\omega^4}{12\pi\varepsilon_0 c^3}|\alpha E_{inc}|^2 \quad (1.7)$$

The equation implies that the power is directly proportional to the square of the incident field intensity. This allows us to construct an LF intensity enhancement factor (LFIEF) and an M_{LFIE} for a local field of $E_{Loc}(\omega_L)$, where ω_L represents the frequency of the incoming radiation.

$$M_{LFIE} = \frac{|E_{Loc}(\omega_L)|^2}{|E_{inc}(\omega_L)|^2} \quad (1.8)$$

The augmentation of the local field is influenced by several variables that arise from the dependency of LSPR on different parameters. The intensity is often concentrated at the tips, sharp edges, and crevices, resembling the well-known phenomenon of the lightning rod effect in metals. The phenomenon is also influenced by the molecule's orientation, probing wavelength, and the polarization of the input field.

1.4.1.2. Re-radiation Enhancement

The LFE refers to the phenomenon seen from the viewpoint of the metal nanoparticle and its related LSPR. On the other hand, the reradiation effect is observed from the molecule's perspective. This is due to the dependence of the power released by an oscillating dipole on its surrounding environment, as shown by equation 1.7. The amount of energy a given oscillating dipole amplitude extracts varies depending on its electromagnetic surroundings. The phenomena have been demonstrated schematically in Figure 1.5. Suppose a dipole oscillates close to a metal surface with a frequency of ω_R. In that case, its power may be much higher than if it were radiated in free space, perhaps differing by several orders of magnitude. The power emitted by the molecule, P_{rad}, is amplified in the presence of metal nanoparticles and the local field enhancement. The radiation enhancement factor, M_{REF}, relative to the space, P_0, may be calculated as follows,

$$M_{REF} = \frac{P_{rad}}{P_0} = \frac{|E_{Loc}(\omega_L)|^2}{|E_{inc}(\omega_L)|^2} \quad (1.9)$$

The overall EM enhancement in the SERS, denoted as G_{EM}, is determined by the multiplication of the local field intensity enhancement factor (LFIE) [94,151,156] and the enhancement factor due to the re-radiation (REF). This combined effect is often referred to as the $|E|^4$ approximation of SERS enhancement [94,156].

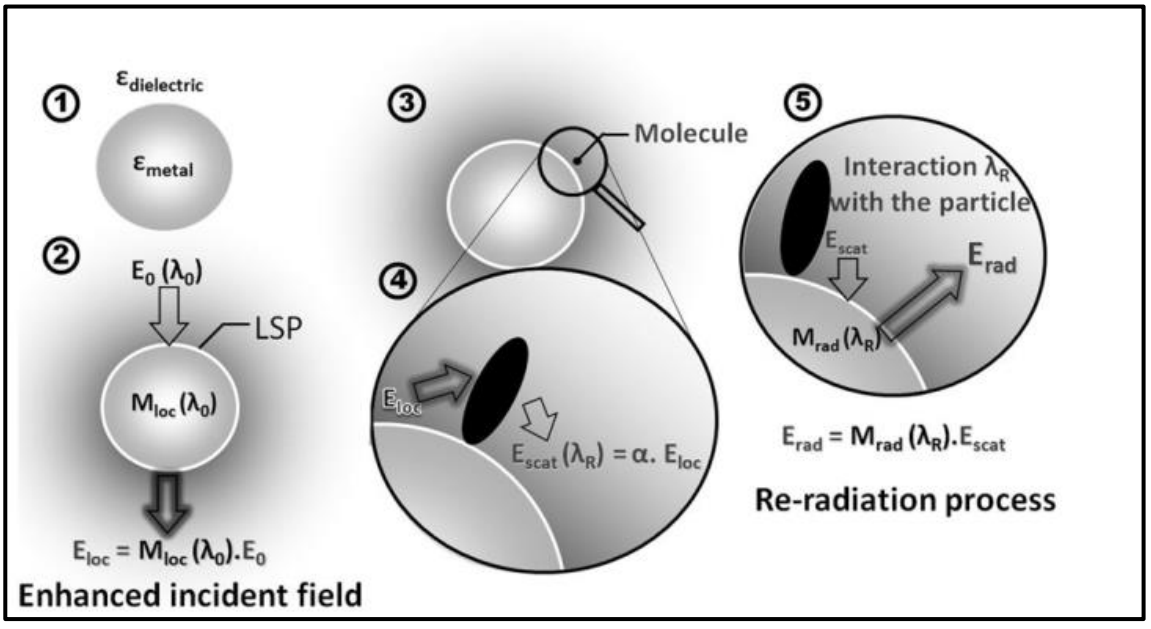

Figure 1. 5 Schematic of the electromagnetic enhancement phenomena involving a nanoparticle, depicting enhanced local field (1,2) and re-radiation process (3-5). Image adapted from Ref. [159].

1.4.2. Chemical Enhancement

EME is a characteristic of metal nanostructures. On the other hand, CME, or chemical enhancement, relies on the interaction between molecules and nanostructures, making the enhancement level subjective. The cause of CME in SERS is thought to be the change in the molecule's polarizability resulting from chemical or physical modifications after its contact with the plasmonic material. The specific degree of this improvement, known as G_{CME}, varies depending on the combination of the molecule and metal and typically falls within the range of 10^2-10^4 in magnitude. While the contribution may be minimal compared to EME, it is vital in SERS since it often leads to abnormalities, such as changes in predicted Raman modes and the strengthening of some modes while suppressing others. These processes are often referred to as 'charge transfer mechanisms,' [94] where the electrical charge distribution of the molecule is somewhat altered in the presence of the nanostructure. Following the discussion, the complete overview of SERS and its versatile applications are demonstrated in Figure 1.6.

1.5. Ultrafast Laser Ablation

Laser ablation of plasmonic metal targets in liquid/air media is very effective for simultaneously producing both NPs and nanospheres (NSs) [12,160–162]. Ablation refers to eliminating fragments from a substance upon exposure to a high-intensity laser pulse. Fragments include atoms, ions, and molecular clusters, among other entities. The interaction of ultrashort pulses with materials is of great interest because their pulse length is much shorter than the period necessary for several relaxation processes, such as energy transfer between electron and lattice systems and heat diffusion [29,163–166]. Short pulse durations result in the deposition of larger energy densities, specifically higher peak intensities when they are focused on or below a bulk target surface. As a result, the impact will cause the material to experience increased pressures and temperatures, resulting in changes to its surface and easy fragmentation. The temporary condition of the material following the exposure to a concentrated and intermittent laser beam can be estimated as a phase change that happens under conditions where equilibrium is not reached. This is because the absorption of the electron gas, which has a high energy density, in the target material, causes the remaining target (lattice) to remain at its original temperature while the electron gas transitions to a higher temperature state. The restoration of the system to

a state of equilibrium relies on the specific parameters of the laser pulses used for ablation, as well as the inherent characteristics of the target. Ultrafast laser ablation (ULA) reduces the random unevenness of the target by using very short pulse durations and providing a heat-affected zone (HAZ) much smaller than the HAZ produced by longer laser pulses.

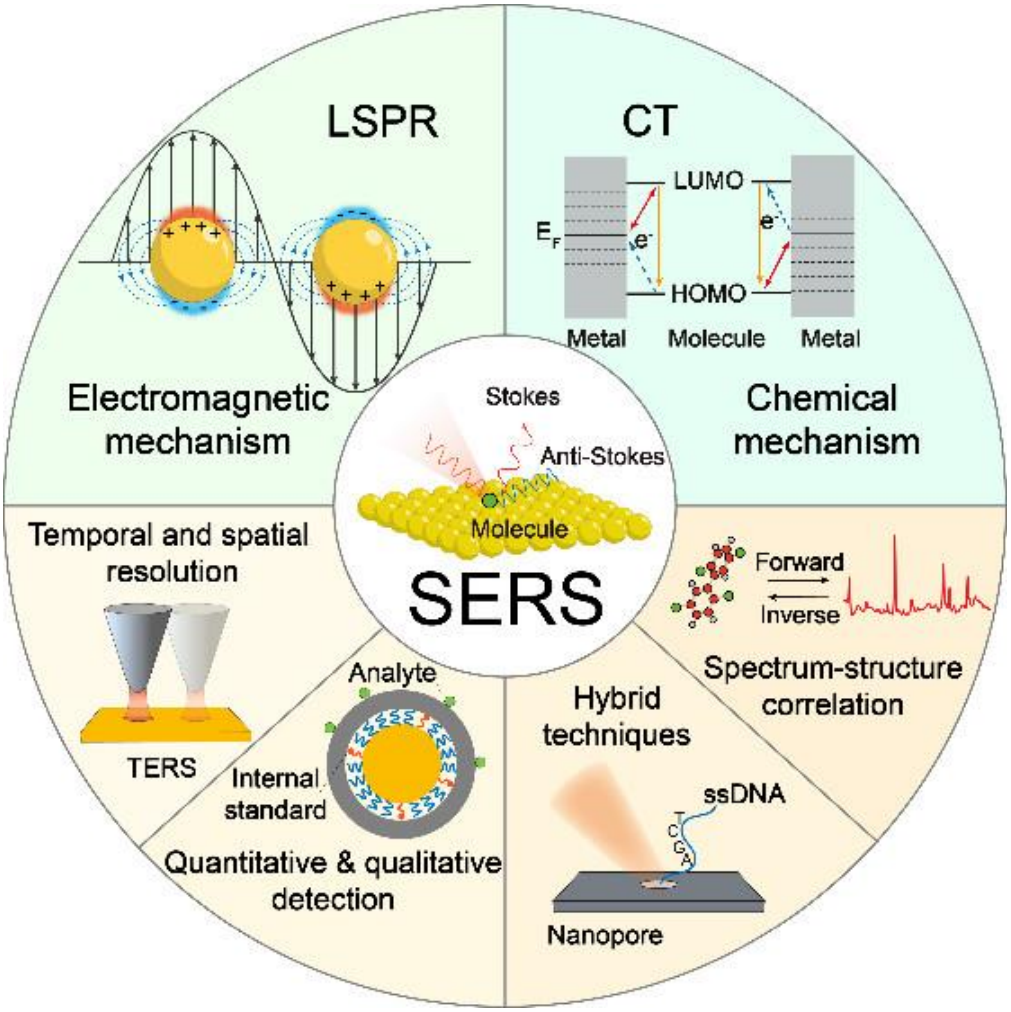

Figure 1. 6 Overview of surface-enhanced Raman spectroscopy: the process's fundamentals, application versatility, and future scope. Image adapted from Ref. [153].

1.5.1. Ultrafast Laser Ablation in Air (ULAA)

Laser ablation refers to removing material fragments from a surface by exposing them to intense irradiation from a concentrated laser beam. Laser ablation of solid objects is a procedure that involves the removal of material from the surface using a laser. This approach has greatly interested the scientific community over the last 50 years [160]. The complete picture can be observed in Figure 1.7. In the case of LAA, when the focused laser interacts directly with the target in ambient air, the electric field generated by the laser pulse impact appears to be strong enough to cause the expulsion of electrons, ions,

molecule clusters, and other intermediate products and is controlled by two significant nonlinear processes, namely multi-photon absorption and cascade ionization. These systems rely only on the length of the pulse. At first, the electrons on the material's surface absorb laser energy by inverse-Bremsstrahlung and gain increased kinetic energies. As a result, they sustain a temperature far greater than that of the surrounding lattice. The temperature gradient between the hot electrons and the lattice may be described using a two-temperature model [20,167–169], which is regulated by the following set of equations,

$$C_e \frac{\partial T_e}{\partial t} = \frac{\partial Q(z)}{\partial t} - \gamma(T_e - T_l) + S$$

$$C_e \frac{\partial T_l}{\partial t} = \gamma(T_e - T_l) + S$$

$$Q(z) = -k_e \frac{\partial T_e}{\partial z}$$

$$S = I(t)\alpha e^{-(\alpha z)} \qquad (1.10)$$

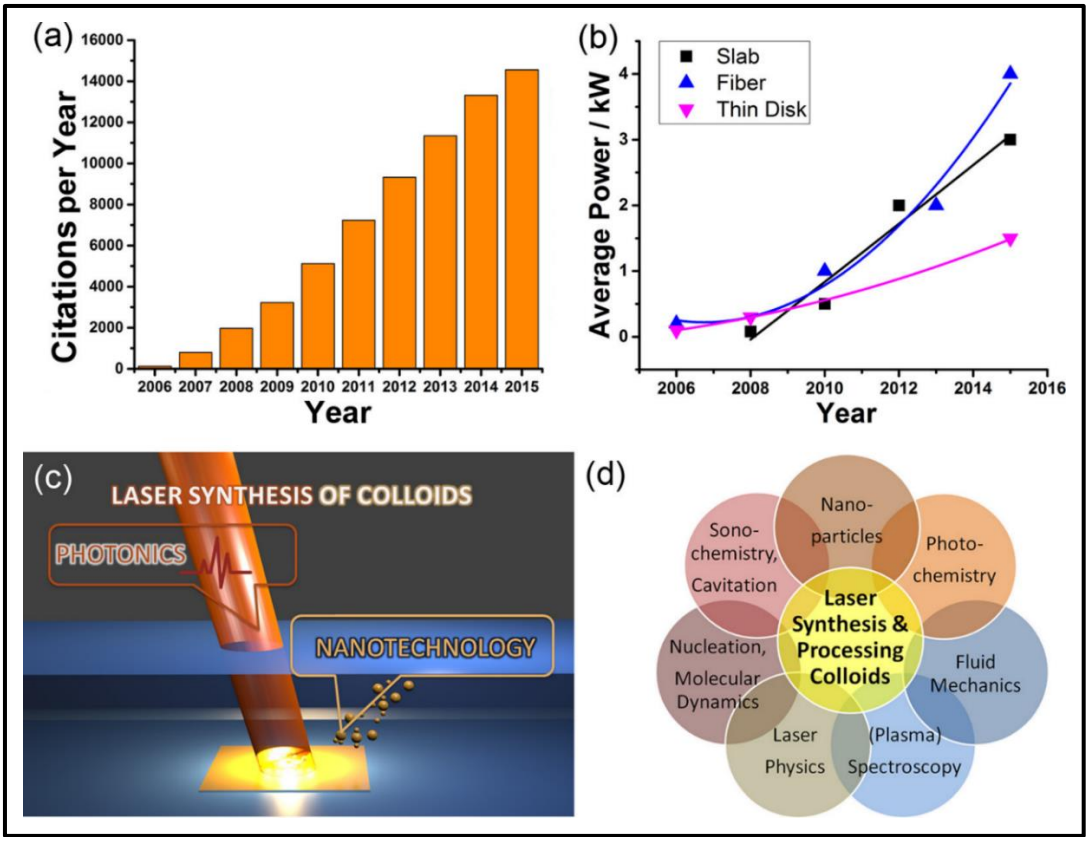

Figure 1. 7 Potential applications of laser-assisted colloid synthesis. (a) The number of citations per year in the last ten years was calculated by searching the ISI Web of Science using the keywords "laser" and "nanoparticle" (b) The evolution of the attainable mean power of pulsed laser systems throughout time. The solid lines serve as visual aids to direct the eye by fitting to the data points. (c) Diagram depicting the process of creating colloids using lasers, which relies on two important technologies: photonics and nanotechnology (d) Summary of the subdisciplines of chemistry and related fields engaged in laser synthesis research. Image adapted from Ref. [160].

The variables in the equation are as follows: T_e signifies the temperature of the electrons in the particular material, T_l denotes to the temperature of the atomic lattice/ phonons in the particular material, Q(z) represents the heat flux, I(t) represents the input laser intensity, α represents the materials absorption coefficient, C_e represents the electron heat capacity per unit volume, C_e represents the lattice heat capacity per unit volume, γ represents the electron-phonon coupling constant, and κ_e represents the electron thermal conductivity, S denotes the heat flux from electrons to phonons per unit volume [29,46,160]. Typically, the temperatures for ultrafast laser ablation are about 10^3 K, and the pressures of the plasma plume are around ~10^9 Pa. [170] The high-energy electrons in the conduction band dissipate the surplus thermal energy through collisions with the electron lattice, which typically takes a few picoseconds. [170] After thermalization, the whole system attains a condition of equilibrium. At this point, if the temperature reaches a level higher than the melting threshold of the material, then the material in the area where the laser beam is incident begins to melt. The complete process has a duration of many picoseconds. NPs are expelled from the surface of the target within a few microseconds.

1.5.2. Ultrafast Laser Ablation in Liquid (ULAL)

The ablation dynamics grow quite complex if an aqueous medium surrounds the target. [45–47,51]. When the laser beam is concentrated on the surface of a target material covered by a liquid layer, it causes the metal target to melt in that specific area. Consequently, the metal area the laser beam hits undergoes a phase change and melts. The neighboring liquid layer of molten metal absorbs some thermal energy and reaches a greater temperature. The liquid cannot maintain its phase at this temperature and undergoes evaporation. During evaporation, the liquid layer applies a rebound pressure on the underlying melt. Nevertheless, the surface tension inside the molten substance strives to maintain its spherical form. Due to the increased rebound pressures caused by the evaporation of the liquid layer, the metallic melt splinters into nano-sized particles that disperse into the surrounding liquid medium. The metallic melt undergoes redistribution at high rebound pressure levels before condensing to produce various nanoscale structures and nanoparticles. Time scales of the various processes involved have been demonstrated in Figure 1.8(a), and subsequently, a schematic of the ULAL process is presented in Figure 1.8(b). Furthermore, it is crucial to briefly address the fundamental distinctions between

short pulse ablation (ns/ps) and ultrafast (fs) laser ablation in a liquid medium within this particular context. When performing ns ablation, due to longer pulse width, slower heating might result in increased thermal effects and potential damage to nearby material owing to heat diffusion. On the other hand, for fs LAL, ultrafast heating induces nonlinear optical effects and greatly lowers thermal damage to surrounding material [47-50]. Ablation in liquid using ns pulses largely occurs through thermal mechanisms, such as boiling, evaporation. whereas fs ablation is mostly driven by nonthermal processes, such as direct breaking of chemical bonds and multiphoton ionization. Due to thermal impacts and debris development, ns ablation typically results in rougher surface textures; in contrast, fs laser ablation produces finer NSs with a smaller heat impacted zone [45-49].

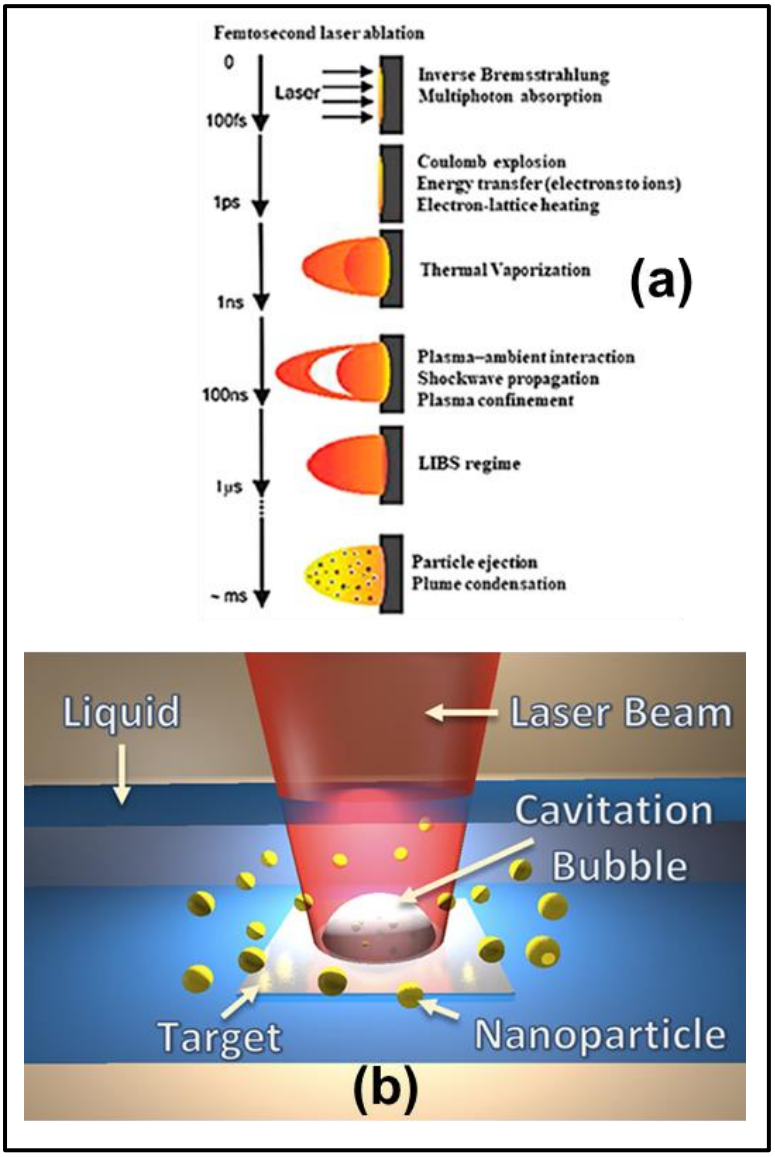

Figure 1. 8 (a) Timescales of various processes involved in fs laser ablation in liquid (b) schematic of laser ablation in liquid and generation of nanoparticles. Image adapted from Ref. [171].

1.6. Ultrafast Time-resolved Dynamics in Plasmonic Metal Nanoparticles

The noble metals (Au, Ag, Cu) comprise monovalent atoms with a comparable electrical structure. The atomic d-orbitals are completely occupied, forming the d-band, while the hybridized s-p orbitals are partly occupied, forming the p-band [172,173]. The electrons in these partly filled orbitals exhibit delocalization, resulting in the formation of a conduction band. These electrons are influenced by both thermal and electrical characteristics. On the other hand, the filled d-orbitals, known as the valence band, have a lesser impact on both properties. Figure 1.9 illustrates the band structure of metals, with E_f representing the Fermi level. The Fermi level corresponds to the highest occupied electronic state at absolute zero temperature. The decrease in the size of metals leads to the emergence of a notable phenomenon known as surface plasmon resonance (SPR), characterized by electrons' collective motion. The attribute of metals referred to here is the ability to generate spatial localization and augment electromagnetic fields in metal nanoparticles. The metallic nanoparticles are stimulated by either interband or intraband transitions, depending on the wavelength of the pump. Electron scattering occurs within a few femtoseconds after photoexcitation. [150,174] The electron has a lower heat capacity than the lattice, allowing us to selectively stimulate and observe the electron's behavior in real time. After being excited by a laser pulse, the electrons undergo relaxation by internal thermalization, which involves collisions between electrons and subsequent coupling with phonons to achieve exterior thermalization. When interband excitation occurs, the electron-hole pairs produced recombine within a very short period, often a few femtoseconds. NPs are efficient light absorbers that may generate highly energized electron-hole pairs. These energetic charge carriers are used in many applications, such as photocatalysis, biology, and solar energy conversion. [175,176] The gold nanoparticles (Au NPs) display surface plasmon modes in the visible area due to the oscillations of conduction electrons. The plasmon peak is primarily influenced by the morphology and dimensions of the NPs. As the size of the NPs rises, the peak shifts towards longer wavelengths (redshift) and becomes broader. [152,177] The exceptional performance of optical switching systems based on metal nanostructures relies on the entanglement of ultrafast electron relaxation processes with localized surface plasmonic phenomena. The electron dynamics and third-order nonlinear optical (NLO) characteristics of metal and metal-alloy NPs have been extensively investigated using various spectroscopic methods. Metal and metal alloy nanoparticles, or colloids, exhibit unique physical and electrical

characteristics influenced by their form and size. These qualities make them very valuable in catalytic processes and the development of plasmonic lasers. The NLO characteristics of gold (Au) and gold-silver (Au-Ag) alloy NPs have garnered considerable attention in several sectors due to their diverse uses [178]. Doping metal nanoparticles with semiconductors or metals allows for precise adjustment of the intrinsic plasmon band over the visible and near-infrared (NIR) spectrum, providing a distinct advantage. Several researchers have examined the electron dynamics of gold (Au) and gold-silver (Au-Ag) alloy NPs manufactured using diverse methods. These investigations were conducted in both solution form (colloids) and in a thin film using femtosecond time-resolved absorption spectroscopy (fs-TAS) [179,180].

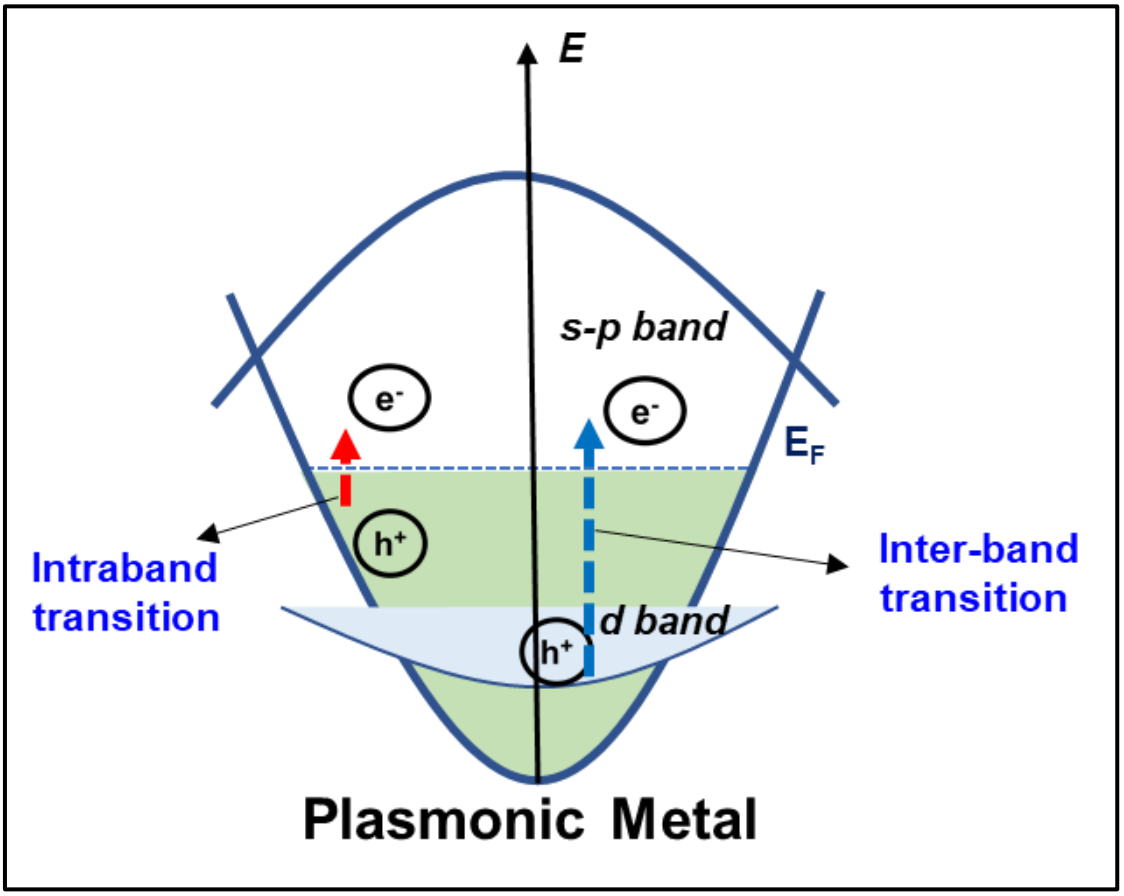

Figure 1. 9 Illustration of the band structure of metals with a filled d-band, a partially filled s-p band, and the possibility of inter-band, intraband transitions.

The NPs' shape impacts the NLO characteristics and the related ultrafast electron dynamics in the excited states. [181] After being excited by the laser pulse, the electrons undergo internal thermalization by collisions with other electrons, followed by exterior thermalization through coupling with phonons. [182,183] Various laser-based approaches

have been used to investigate the electron distribution above the Fermi level after strong, non-thermal, non-Fermi stimulation. The kinetics of electron thermalization in mixed metal nanoparticles in intraband and interband excitation have not been extensively studied. Zhang and his colleagues [184] have recently investigated the impact of interband and intraband effects on localized surface plasmon oscillations in pure gold nanoparticles (Au NPs). They discovered a redshifted-induced localized surface plasmon resonance (LSPR) characteristic when the nanoparticles were pumped with light at 400 nm. When the energy is increased over the threshold of 2.38 eV, it causes the electronic transition from the 5d band to the 6sp band, leading to a temporary rise in the population of the conduction band. A recent study has shown that the energetic 5d electrons transition into plasmonic oscillation with a temporal delay of 1 picosecond.

Considering the above-stated segments of the thesis, we have outlined the main goals of this thesis work and provided further details for each of them.

1. Nanoparticles and solid nanostructures synthesized using ultrafast Gaussian beam and the LAL technique. Subsequently, we employ those nanoentities in SERS-based sensing studies.
2. Study the fs Bessel beam interaction with plasmonic, pure, and alloy metal substrates and the consequent fabrication of LIPSS.
3. Investigate the performance of the novel LIPSS substrates in SERS-based sensing of hazardous compounds.
4. Develop a fs BB-engaged novel LAL technique for the synthesis of multi-metal nanocolloids
5. Study the electron dynamics of the synthesized nano alloys involving transient absorption spectroscopy.
6. Studies on fs vortex beam interaction with metal surfaces.

1.7. Overview of thesis - Chapter-wise summary

This thesis contains six chapters in which the schematic representation of working chapters is illustrated below.

Chapter 1

The history of nanoscience and nanotechnology, high-energy materials and different detection methods, the fundamentals of Raman spectroscopy, and the evolution of surface-

enhanced Raman scattering enhancement processes are briefly covered in the opening chapter of this thesis. The laser ablation method (in air and liquid) and the processes behind the production of nanoparticles and nanostructures using fs pulses will be introduced in this chapter. Further, we will discuss the transition from Gaussian beam to Bessel beam ablation technology and the benefits involved. The importance of transient absorption spectroscopy in examining the time-resolved electron dynamics of plasmonic metal nanoparticles is highlighted. Figure 1.10. shows a chapter-wise schematic of the various works involved in this thesis.

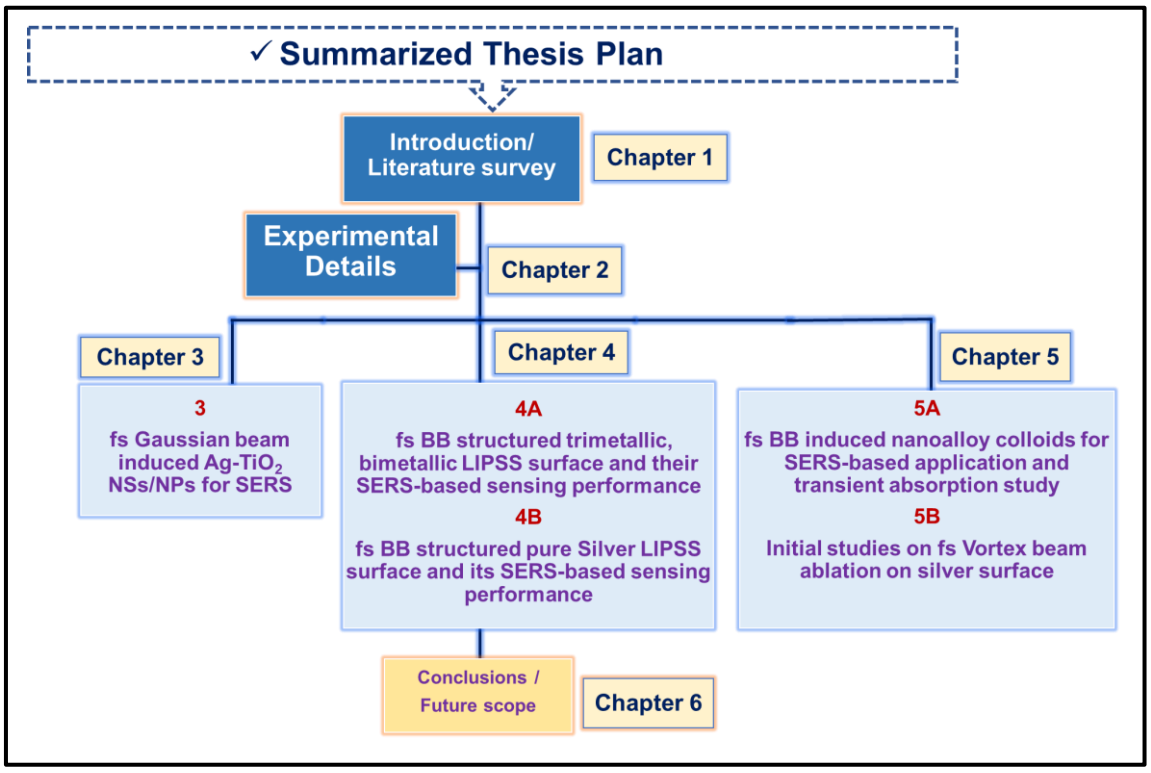

Figure 1. 10 A schematic of the complete thesis.

Chapter 2

An overview of the characterization methods and experimental information is provided in this chapter. Specifications of the fs laser used in the ablation tests include pulse width measurements using a single-shot auto-correlator. Detailed experimental protocols are also provided for creating LIPSS surfaces using Bessel beams and nanoparticles and nanostructures using Gaussian beams. Furthermore, the vortex phase plate for the vortex beam-metal surface interaction is explored. Moreover, X-ray diffraction (XRD), field emission electron microscope (FESEM) with energy dispersive spectroscopy (EDAX), transmission electron microscopy (TEM), and UV-visible absorption spectroscopy were

used to characterize synthesized colloidal NPs and solid substrates. The details of the transient absorption spectroscopy experiment have also been covered. Lastly, a short discussion of the specifics of the portable and micro-Raman spectrometers employed for different SERS measurements is given.

Chapter 3

In this chapter, we present the outcomes of our fs LAL followed by the production of nanoparticle nanoparticles of titanium dioxide (TiO_2) and Ag-doped TiO_2 (Ag-TiO_2). Specifically, fs laser ablation and simultaneous laser pulses-induced chemical reduction by irradiation were used to create TiO_2 and Ag-TiO_2 NPs in deionized water, respectively. After careful investigations, the results related to the characterization of the NPs using XRD, TEM, FESEM with EDAX, and UV-visible absorption spectroscopy have been provided. Following synthesis, SERS analysis was conducted on Ag-TiO_2 NPs and the solid Ag-decorated Ti nanostructured surface (produced as a result of LAL). Using fs laser ablation in liquid technique, a hybrid semiconductor-metal SERS substrate was created in a single step. SERS investigations using the Ag-TiO_2 nanostructure (NS) revealed a signal that was 16 times better than that of pure TiO_2 NS. Additionally, surface-enhanced Raman scattering-based RDX, and ammonium nitrate trace detection were performed using Ag-TiO_2 NPs.

Chapter 4

This chapter comprises two sections as follows:

4A

In this chapter, surface structuring of an alloy substrate was performed using fs BB generated by an axicon, considering the benefits of non-diffracting light. This chapter demonstrates the mechanism to create unique ladder-like trimetallic (Ag-Au-Cu alloyed) LIPSS in the presence of a fs Bessel beam. A wide-ranging overlapping raster scan and single spot ablation were used to carefully analyze the BB profile imprint on the surface and the broad area ablation process. It was noted that an interesting ladder-like periodicity emerged across the NS. Using FESEM and AFM, the NSs' intrinsic nanoscale topographical characteristics were methodically explored. The creation of LSFL type I LIPSS [period (Λ) of 540±12 nm] was understood to be primarily caused by the interference of BB-induced SPP with the incoming pulses at several areas, which resulted in the periodic variation of the input fluence at the surface. The following comparison

analysis, using a fs Gaussian beam with the same fluence, revealed that both the NSs produced with altered beam profiles had an intriguing structural difference. The BB-induced TM LIPSS NS was also more effective as a SERS-active plasmonic substrate for explosive real-time sensing. One exciting result was the trace detection of Tetryl (the lowest detected concentration was 200 nM), with an estimated enhancement factor of ~10^5. SERS mapping was used to collect the plasmonic responses from several sub-micron sections throughout a broad area of the TM NS. Additionally, we tried to understand the TM nano-systems charge excitation and decay mechanisms that control the LSP intensity, which is closely linked to an amplified Raman signal. Furthermore, we used BB ablation to create ladder-like periodic surface structures with sub-20 nm growths on the ladder steps for a bimetallic alloy (50% gold, 50% silver). These plasmonic nanostructures were then used as surface-enhanced Raman scattering (SERS) platforms to find explosives, tetryl (TL), and ammonium nitrate (AN) residues. For AN and TL, the lowest detectable levels were 10 µM and 5 µM, respectively.

4B

The development of a new nanotubular arrayed silver (Ag) LIPSS with an fs Bessel beam generated by an axicon is presented in this chapter. A thorough investigation has elucidated the process of Bessel beam-induced LIPSS creation, demonstrating the critical role that ablation fluence profile variation plays in conjunction with photon-induced surface plasmon polariton (SPP) interaction with the incident pulses. The Bessel beam profile and the SPP decay duration have created such unique nanostructures. The artificial low spatial frequency LIPSS is expected to have a period (Λ) of 575±10 nm. We also describe the unique topographical properties of Ag nanostructures produced with the same fluence Gaussian beam. Moreover, these plasmonic nanostructures demonstrated remarkable effectiveness and adaptability as active substrates for sensing applications based on SERS. It has been possible to find traces of common explosives such as Tetryl, RDX, TNT, and HMX. The lowest concentrations detected were in the range of 50-500 nM. The enhancement factors achieved were ~10^6, which makes these substrates very useful for practical uses. Furthermore, our study of the BB ablation technique revealed its potential uses in fabricating anti-reflection surfaces. This work dramatically advances our understanding of the hitherto unknown field of Bessel beam-metal interaction, which results in the creation of novel nanotubular LIPSS and offers a variety of SERS-based sensing applications. Also, in this chapter, we have successfully created uniform LIPSS

nano-structures on a Copper (Cu) surface utilizing the fs BB LAA method. The same was engaged in SERS studies for detecting Tetryl and PETN, revealing EFs ~10^3.

Chapter 5

This chapter comprises two sections as follows:

5A

This chapter describes our successful creation of a new plasmonic multi-metal nanoalloy colloid using a less-used but highly effective fs Bessel beam ablation approach. EDX studies, TEM, and high-resolution TEM have been used to conduct an extensive morphological and elemental analysis. Through SERS-based sensing experiments, the nanoalloys effectively identified traces of the explosive chemicals PA (500 nM) and RDX (5 µM). The results showed that PA and RDX calculated enhancement factor (EF) values were 2.4×10^5 and 1.7×10^4, respectively. Moreover, fs pulses were used to investigate the nanoalloy particles (NAPs), and the open aperture Z-scan measurements demonstrated a dominant three-photon absorption (3PA) phenomenon. The nonlinear refraction (NLR) coefficient n_2 value was found to be 1.1×10^{-15} cm^2/W, while the 3PA coefficient (γ) value was retrieved to be 1.8×10^{-22} cm^3/W^2. Moreover, an estimated 1.9×10^{-75} cm^6/s^2 has been made for the 3PA cross-section ($\sigma3$). We have also shown that these nanoalloys are capable of optical limitation. To understand the time-resolved behavior of the photoexcited electrons in this nanoalloy system, we also conducted fs transient absorption spectroscopy (fs TAS). From the TAS data, the photoexcited processes of electron-phonon ($\tau_{e\text{-}ph}$ = 1.2±0.05 ps), electron-electron/thermalization ($\tau_{e\text{-}e}$ = 0.7±0.1 ps), and phonon-phonon scattering ($\tau_{ph\text{-}ph}$ = 47.5±8 ps) were extracted and fit. Through the TAS measurements, many other features of the nanoalloy system, including bleach splitting, delayed ESA band duration, and interband-excitation-induced plasmon (EIP), were thoroughly understood. These findings support the benefits of the fs BB-induced ablation approach in creating new, multi-metal plasmonic nanoalloys and demonstrate its potential uses in various industries, such as photonics, optical limiting, and sensors.

5B

This part presents our initial experimental findings on the interaction of fs Vortex beams with silver surfaces. We have also summarized preliminary findings from SERS research employing the Vortex beam-interacted nanostructures. Two explosive compounds have been detected at the trace levels. We have also summarized (see Table 1.1) the

performance of the SERS substrates prepared in this thesis to detect eight hazardous compounds (seven explosives and one food-contaminating dye). The same compounds have been mentioned as follows- Tetryl, PETN (pentaerythritol tetranitrate), TNT, RDX, HMX, AN (ammonium nitrate), PA (2,4,6-trinitrophenol), and MB (methylene blue).

Chapter 6

This chapter provides a concise overview of the findings derived from the data acquired in this thesis. A summary of the achievements is presented in Figure 1.11. This chapter presents the potential future applications of this research, including (i) identifying explosive vapors and (ii) enhancing the SERS response of the nanostructured substrates by applying plasmonic nanoentities as a coating. Additional investigations are scheduled to employ fs BB for surface engineering on gold. This thesis presents preliminary findings on Vortex beam ablation, with further investigations still to be undertaken. SERS response of the vortex beam ablated structures is to be examined in the future. The plasmonic LIPSS nanostructures will be investigated using reflection geometry transient absorption investigations to explore the excited state's dynamics.

Table 1.1 Performance of the SERS substrates prepared in this thesis.

S. No.	SERS Substrate	Molecules	Lowest Concentration detected	Remarks
1	Femtosecond Bessel beam structured trimetallic (Ag-Au-Cu) ladder-like LIPSS surface	Tetryl, PETN	200 nM, 500 µM	Novel SERS-active substrate with good recyclability and reproducibility (< 20 %), SERS mapping data collected
2	Gaussian beam structured trimetallic (Ag-Au-Cu) nanostructures	Tetryl, PETN	500 nM, 500 µM	The robust, solid substrate with a moderate practical trace detection limit
3	Ag-doped TiO_2 Nanoparticles generated via fs Gaussian beam LAL	RDX, AN	100 µM, 20 µM	Colloidal NPs with a lower trace detection limit for AN
4	Ag decorated Ti solid nanostructures fabricated via Gaussian beam LAL	Methylene Blue	1 nM	Single-step fabricated hybrid SERS-active substrate
5	Nanotubular Arrayed LIPSS on Ag surface produced via fs BB	TNT, Tetryl RDX, HMX	50 nM, 50 nM, 500 nM, 5 µM	Novel LIPSS substrate with high versatility, enhancement factor, recyclability, reproducibility (< 15%), Signal stability studies carried out up to 90 days
6	Ag-Au bimetallic ladder-like nanostructures achieved with fs BB	AN, Tetryl	10 µM, 5 µM	Novel LIPSS substrate with robust, practical application
7	LIPSS on Copper via fs BB	Tetryl, PETN	5 µM, 1 mM	Low-cost, novel SERS-active substrate
8	Multi-metal nanoalloy colloids fabricated via fs BB LAL	RDX, PA	5 µM, 500 nM	Novel nanoalloy with acceptable SERS activity
9	fs VB structured Ag substrate	Tetryl, AN	500 nM, 5 µM	Further optimization required

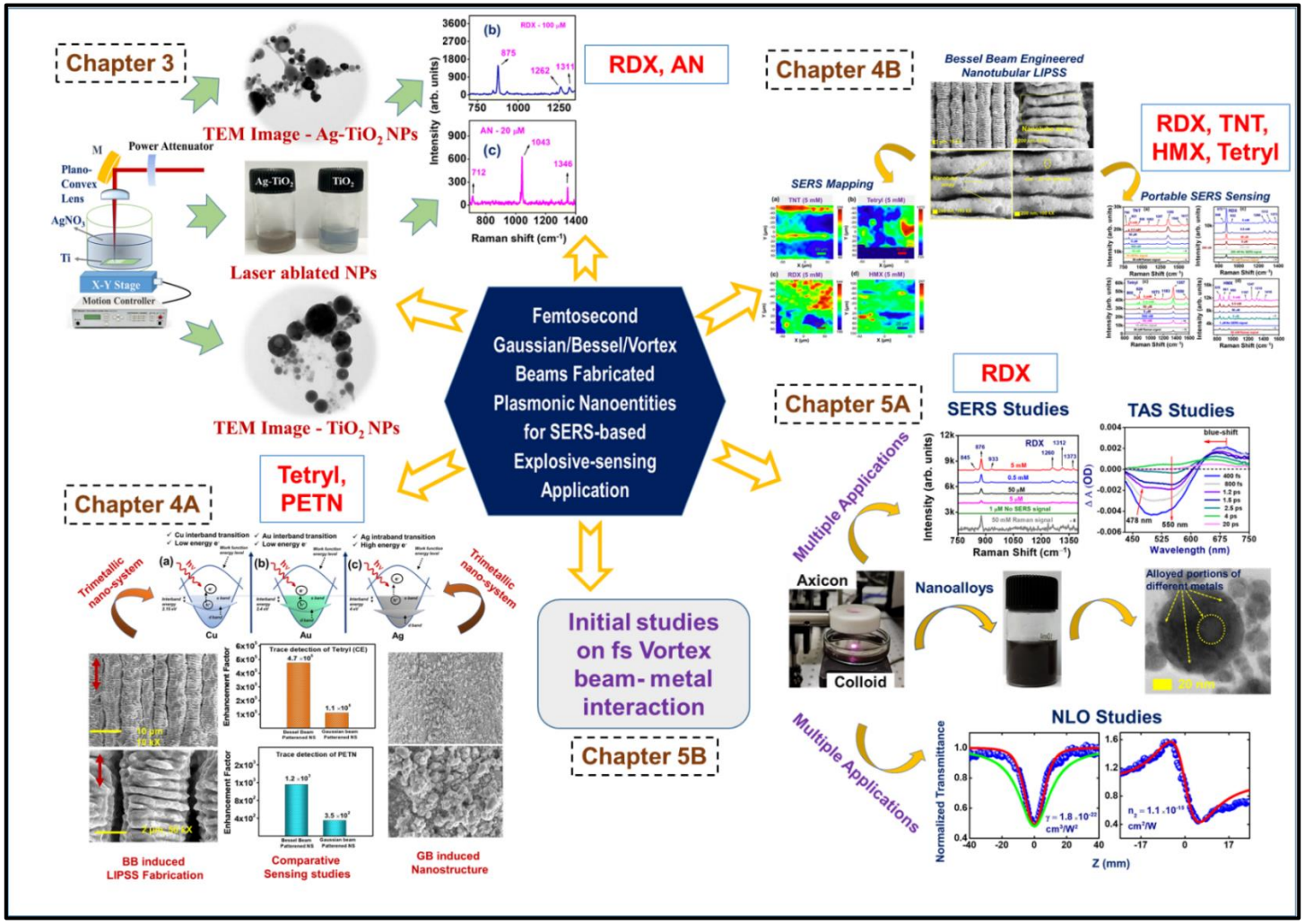

Figure 1. 11 Summary of the complete research work

References:

[1] S. Bayda, M. Adeel, T. Tuccinardi, M. Cordani, F. Rizzolio, The History of Nanoscience and Nanotechnology: From Chemical–Physical Applications to Nanomedicine, Molecules. 25 (2019) 112. https://doi.org/10.3390/molecules25010112.

[2] M. Rafique, M.B. Tahir, M.S. Rafique, M. Hamza, History and fundamentals of nanoscience and nanotechnology, in: Nanotechnol. Photocatal. Environ. Appl., Elsevier, 2020: pp. 1–25. https://doi.org/10.1016/B978-0-12-821192-2.00001-2.

[3] M. Faraday, X. The Bakerian Lecture.—Experimental relations of gold (and other metals) to light, Philos. Trans. R. Soc. London. (1857) 145–181.

[4] W.G. Eberhard, W.T. Wcislo, Plenty of room at the bottom? Tiny animals solve problems of housing and maintaining oversized brains, shedding new light on nervous-system evolution, Am. Sci. 100 (2012) 226.

[5] N. Taniguchi, On the basic concept of'nano-technology', in: Proc. Intl. Conf. Prod. Eng. Tokyo, Part II, 1974, Japan Society of Precision Engineering, 1974.

[6] I. Freestone, N. Meeks, M. Sax, C. Higgitt, The Lycurgus cup—a roman nanotechnology, Gold Bull. 40 (2007) 270–277.

[7] T. Pradell, A. Climent-Font, J. Molera, A. Zucchiatti, M.D. Ynsa, P. Roura, D. Crespo, Metallic and nonmetallic shine in luster: An elastic ion backscattering study, J. Appl. Phys. 101 (2007) 103518. https://doi.org/10.1063/1.2734944.

[8] C.P. Poole, F.J. Owens, Introduction to Nanotechnology, Wiley, 2003. https://books.google.co.in/books?id=gPK-DwAAQBAJ.

[9] M. Valenti, A. Venugopal, D. Tordera, M.P. Jonsson, G. Biskos, A. Schmidt-Ott, W.A. Smith, Hot Carrier Generation and Extraction of Plasmonic Alloy Nanoparticles, ACS Photonics. 4 (2017) 1146–1152. https://doi.org/10.1021/acsphotonics.6b01048.

[10] N.J. Halas, S. Lal, W.S. Chang, S. Link, P. Nordlander, Plasmons in strongly coupled metallic nanostructures, Chem. Rev. 111 (2011) 3913–3961. https://doi.org/10.1021/cr200061k.

[11] S.A. Jalil, B. Lai, M. ElKabbash, J. Zhang, E.M. Garcell, S. Singh, C. Guo, Spectral absorption control of femtosecond laser-treated metals and application in solar-thermal devices, Light Sci. Appl. 9 (2020) 14. https://doi.org/10.1038/s41377-020-0242-y.

[12] J. Bonse, S. V. Kirner, J. Krüger, Laser-Induced Periodic Surface Structures (LIPSS), in: Handb. Laser Micro- Nano-Engineering, Springer International Publishing, Cham, 2021: pp. 1–59. https://doi.org/10.1007/978-3-319-69537-2_17-2.

[13] J. Zhang, Y. Wang, D. Li, Y. Sun, L. Jiang, Engineering Surface Plasmons in Metal/Nonmetal Structures for Highly Desirable Plasmonic Photodetectors, ACS Mater. Lett. 4 (2022) 343–355. https://doi.org/10.1021/acsmaterialslett.1c00768.

[14] J. Geng, L. Shi, X. Sun, W. Yan, M. Qiu, Artificial Seeds-Regulated Femtosecond Laser Plasmonic Nanopatterning, Laser Photon. Rev. 16 (2022) 2200232.

https://doi.org/10.1002/lpor.202200232.

[15] S.Y. Chae, N. Yoon, E.D. Park, O.S. Joo, Surface modification of CuInS2 photocathodes with ruthenium co-catalysts for efficient solar water splitting, Appl. Surf. Sci. 612 (2023) 155856. https://doi.org/10.1016/j.apsusc.2022.155856.

[16] D.S. Chezganov, E.O. Vlasov, L.V. Gimadeeva, M.M. Neradovskiy, A.R. Akhmatkhanov, M.A. Chuvakova, D.O. Alikin, H. Tronche, F. Doutre, P. Baldi, V.Y. Shur, Short-period domain patterning by ion beam irradiation in lithium niobate waveguides produced by soft proton exchange, Opt. Laser Technol. 158 (2023) 108813. https://doi.org/10.1016/j.optlastec.2022.108813.

[17] L. Huang, Q. Wang, H. Liu, Y. Wu, Y. Yang, G. Ma, Z. Lei, S. Ren, N+ irradiation regulates surface defects and doping towards efficient hydrogen evolution reaction on Sb2Te3, Appl. Surf. Sci. 609 (2023) 155347. https://doi.org/10.1016/j.apsusc.2022.155347.

[18] X. Ge, Y. Hu, H. Shen, W. Liang, Z. Sun, X. Zhang, G. Ospankulova, M. Muratkhan, K.Z. Kh, W. Li, Electron beam irradiation application for improving the multiscale structure and enhancing physicochemical and digestive properties of acetylated naked barley, Food Chem. 404 (2023) 134674. https://doi.org/10.1016/j.foodchem.2022.134674.

[19] M. Jaworski, A. Chudzyńska, P. Mrowiński, G. Sęk, Efficient Emission in the Telecom Range from Quantum Dots Embedded in Photonic Structures Fabricated by Focused Ion Beam Milling, Acta Phys. Pol. A. 142 (2022) 662–667. https://doi.org/10.12693/APhysPolA.142.662.

[20] S. Song, Q. Lu, P. Zhang, H. Yan, H. Shi, Z. Yu, T. Sun, Z. Luo, Y. Tian, A critical review on the simulation of ultra-short pulse laser-metal interactions based on a two-temperature model (TTM), Opt. Laser Technol. 159 (2023) 109001. https://doi.org/10.1016/j.optlastec.2022.109001.

[21] L. V Zhigilei, E. Leveugle, B.J. Garrison, Y.G. Yingling, M.I. Zeifman, Computer simulations of laser ablation of molecular substrates, Chem. Rev. 103 (2003) 321–348.

[22] P.A. Danilov, E.A. Drozdova, A.A. Ionin, S.I. Kudryashov, S.B. Odinokov, A.A. Rudenko, V.I. Yurovskikh, D.A. Zayarny, Single-shot front-side nanoscale femtosecond laser ablation of a thin silver film, Appl. Phys. A. 117 (2014) 981–985. https://doi.org/10.1007/s00339-014-8741-4.

[23] A.A. Ionin, S.I. Kudryashov, S.V. Makarov, A.A. Rudenko, P.N. Saltuganov, L.V. Seleznev, D.V. Sinitsyn, E.S. Sunchugasheva, Femtosecond laser fabrication of sub-diffraction nanoripples on wet Al surface in multi-filamentation regime: High optical harmonics effects?, Appl. Surf. Sci. 292 (2014) 678–681.

https://doi.org/10.1016/j.apsusc.2013.12.032.

[24] S.I. Kudryashov, P.A. Danilov, A.P. Porfirev, I.N. Saraeva, T.H.T. Nguyen, A.A. Rudenko, R.A. Khmelnitskii, D.A. Zayarny, A.A. Ionin, A.A. Kuchmizhak, S.N. Khonina, O.B. Vitrik, High-throughput micropatterning of plasmonic surfaces by multiplexed femtosecond laser pulses for advanced IR-sensing applications, Appl. Surf. Sci. 484 (2019) 948–956. https://doi.org/10.1016/j.apsusc.2019.04.048.

[25] S.I. Kudryashov, I.N. Saraeva, V.N. Lednev, S.M. Pershin, A.A. Rudenko, A.A. Ionin, Single-shot femtosecond laser ablation of gold surface in air and isopropyl alcohol, Appl. Phys. Lett. 112 (2018) 3101. https://doi.org/10.1063/1.5026591.

[26] A. Naghilou, M. He, J.S. Schubert, L. V Zhigilei, W. Kautek, Femtosecond laser generation of microbumps and nanojets on single and bilayer Cu/Ag thin films, Phys. Chem. Chem. Phys. 21 (2019) 11846–11860. https://doi.org/10.1039/C9CP02174D.

[27] A.A. Ionin, S.I. Kudryashov, S. V Makarov, L. V Seleznev, D. V Sinitsyn, E. V Golosov, O.A. Golosova, Y.R. Kolobov, A.E. Ligachev, Femtosecond laser color marking of metal and semiconductor surfaces, Appl. Phys. A. 107 (2012) 301–305. https://doi.org/10.1007/s00339-012-6849-y.

[28] W. Ming, S. Hu, Z. Xie, F. Zhang, G. Zhang, X. Guo, H. Huang, Recent advances in molecular dynamics of metal laser-processed nanoparticles: A review, Opt. Laser Technol. 174 (2024) 110618. https://doi.org/10.1016/j.optlastec.2024.110618.

[29] D. Zhang, Z. Li, K. Sugioka, Laser ablation in liquids for nanomaterial synthesis: diversities of targets and liquids, J. Phys. Photonics. 3 (2021) 042002. https://doi.org/10.1088/2515-7647/ac0bfd.

[30] D. Zhang, Z. Li, C. Liang, Diverse nanomaterials synthesized by laser ablation of pure metals in liquids, Sci. China Physics, Mech. Astron. 65 (2022) 274203.

[31] A. Nakhoul, A. Rudenko, C. Maurice, S. Reynaud, F. Garrelie, F. Pigeon, J. Colombier, Boosted Spontaneous Formation of High-Aspect Ratio Nanopeaks on Ultrafast Laser-Irradiated Ni Surface, Adv. Sci. 9 (2022) 2200761. https://doi.org/10.1002/advs.202200761.

[32] V.S. Vendamani, S. Rao, A.P. Pathak, V.R. Soma, Robust and cost-effective silver dendritic nanostructures for SERS-based trace detection of RDX and ammonium nitrate, RSC Adv. 10 (2020) 44747–44755. https://doi.org/10.1039/d0ra08834j.

[33] F. Nyenhuis, P.N. Terekhin, T. Menold, B. Rethfeld, A. Michalowski, J.A. L'huillier, Fundamentals of Scanning Surface Structuring by Ultrashort Laser Pulses: From Electron Diffusion to Final Morphology, Adv. Photonics Res. 3 (2022) 2200045. https://doi.org/10.1002/adpr.202200045.

[34] Y. Zhang, Q. Jiang, M. Long, R. Han, K. Cao, S. Zhang, D. Feng, T. Jia, Z. Sun, J.

Qiu, H. Xu, Femtosecond laser-induced periodic structures: mechanisms, techniques, and applications, Opto-Electronic Sci. 1 (2022) 220005–220005. https://doi.org/10.29026/oes.2022.220005.

[35] D. Zhang, K. Sugioka, Hierarchical microstructures with high spatial frequency laser induced periodic surface structures possessing different orientations created by femtosecond laser ablation of silicon in liquids, Opto-Electronic Adv. 2 (2019) 190002.

[36] H. Zhang, J.P. Colombier, C. Li, N. Faure, G. Cheng, R. Stoian, Coherence in ultrafast laser-induced periodic surface structures, Phys. Rev. B - Condens. Matter Mater. Phys. 92 (2015) 174109. https://doi.org/10.1103/PhysRevB.92.174109.

[37] J. Bonse, Quo Vadis LIPSS?—Recent and Future Trends on Laser-Induced Periodic Surface Structures, Nanomaterials. 10 (2020) 1950. https://doi.org/10.3390/nano10101950.

[38] J. Bonse, S. Gräf, Maxwell Meets Marangoni—A Review of Theories on Laser-Induced Periodic Surface Structures, Laser Photon. Rev. 14 (2020) 2000215. https://doi.org/10.1002/lpor.202000215.

[39] J. Bonse, J. Krüger, Pulse number dependence of laser-induced periodic surface structures for femtosecond laser irradiation of silicon, J. Appl. Phys. 108 (2010) 034903. https://doi.org/10.1063/1.3456501.

[40] J. Bonse, J. Krüger, S. Höhm, A. Rosenfeld, Femtosecond laser-induced periodic surface structures, J. Laser Appl. 24 (2012) 572–579. https://doi.org/10.2351/1.4712658.

[41] J. Bonse, A. Rosenfeld, J. Krüger, On the role of surface plasmon polaritons in the formation of laser-induced periodic surface structures upon irradiation of silicon by femtosecond-laser pulses, J. Appl. Phys. 106 (2009) 104910. https://doi.org/10.1063/1.3261734.

[42] M.A. Taher, N. Chaudhary, K. Thirunaukkarasu, V.K. Rajput, S.R.G. Naraharisetty, Controlled periodicities of ladder-like structures via femtosecond laser of wavelength from 400 nm to 2200 nm, Surfaces and Interfaces. 28 (2022) 101622. https://doi.org/10.1016/j.surfin.2021.101622.

[43] Y. Liu, Y. Wang, M. Yang, Q. Wu, Z. Li, C. Zhang, J. Zhang, J. Yao, J. Xu, Deep-subwavelength ripples on the ZnO surface obtained via metal-film-assisted femtosecond laser processing, Appl. Surf. Sci. 573 (2022) 151576. https://doi.org/10.1016/j.apsusc.2021.151576.

[44] M.H. Elshorbagy, L.M. Sánchez-Brea, J. Buencuerpo, J. del Hoyo, Á. Soria-García, V. Pastor-Villarrubia, A. San-Blas, A. Rodríguez, S.M. Olaizola, J. Alda, Polarization conversion using customized subwavelength laser-induced periodic

surface structures on stainless steel, Photonics Res. 10 (2022) 2024. https://doi.org/10.1364/PRJ.454451.

[45] V. Amendola, Laser-Assisted Synthesis of Non-Equilibrium Nanoalloys, ChemPhysChem. 22 (2021) 622–624. https://doi.org/10.1002/cphc.202000987.

[46] V. Amendola, S. Scaramuzza, F. Carraro, E. Cattaruzza, Formation of alloy nanoparticles by laser ablation of Au/Fe multilayer films in liquid environment, J. Colloid Interface Sci. 489 (2017) 18–27. https://doi.org/10.1016/j.jcis.2016.10.023.

[47] V. Coviello, D. Forrer, V. Amendola, Recent Developments in Plasmonic Alloy Nanoparticles: Synthesis, Modelling, Properties and Applications, ChemPhysChem. 23 (2022) e202200136. https://doi.org/10.1002/cphc.202200136.

[48] J. Yong, F. Chen, Q. Yang, D. Zhang, U. Farooq, G. Du, X. Hou, Bioinspired underwater superoleophobic surface with ultralow oil-adhesion achieved by femtosecond laser microfabrication, J. Mater. Chem. A. 2 (2014) 8790–8795.

[49] D. Zhang, B. Ranjan, T. Tanaka, K. Sugioka, Underwater persistent bubble-assisted femtosecond laser ablation for hierarchical micro/nanostructuring, Int. J. Extrem. Manuf. 2 (2020) 15001.

[50] D. Zhang, J. Liu, P. Li, Z. Tian, C. Liang, Recent Advances in Surfactant-Free, Surface-Charged, and Defect-Rich Catalysts Developed by Laser Ablation and Processing in Liquids, ChemNanoMat. 3 (2017) 512–533.

[51] V. Amendola, M. Meneghetti, What controls the composition and the structure of nanomaterials generated by laser ablation in liquid solution?, Phys. Chem. Chem. Phys. 15 (2013) 3027–3046. https://doi.org/10.1039/C2CP42895D.

[52] V. Amendola, M. Meneghetti, Laser ablation synthesis in solution and size manipulation of noble metal nanoparticles, Phys. Chem. Chem. Phys. 11 (2009) 3805–3821.

[53] V. Amendola, D. Amans, Y. Ishikawa, N. Koshizaki, S. Scirè, G. Compagnini, S. Reichenberger, S. Barcikowski, Room-temperature laser synthesis in liquid of oxide, metal-oxide core-shells, and doped oxide nanoparticles, Chem. Eur. J. 26 (2020) 9206–9242.

[54] V. Amendola, R. Pilot, M. Frasconi, O.M. Maragò, M.A. Iatì, Surface plasmon resonance in gold nanoparticles: a review, J. Phys. Condens. Matter. 29 (2017) 203002.

[55] H. Chen, L. Shao, Q. Li, J. Wang, Gold nanorods and their plasmonic properties, Chem. Soc. Rev. 42 (2013) 2679–2724. https://doi.org/10.1039/C2CS35367A.

[56] Y. Yao, Q. Dong, A. Brozena, J. Luo, J. Miao, M. Chi, C. Wang, I.G. Kevrekidis, Z.J. Ren, J. Greeley, G. Wang, A. Anapolsky, L. Hu, High-entropy nanoparticles: Synthesis-structure-property relationships and data-driven discovery, Science (80-.

). 376 (2022) eabn3103. https://doi.org/10.1126/science.abn3103.

[57] L.R. Buddiga, G.R. Gajula, B.B.V. Sailaja, M.L.V.P. Ch, Visible light photocatalytic exploit of P/Zr doped TiO2 nano particles for dye degradation of rose Bengal, Appl. Surf. Sci. Adv. 18 (2023) 100492. https://doi.org/10.1016/j.apsadv.2023.100492.

[58] W. Tang, L. Zhang, G. Henkelman, Catalytic Activity of Pd/Cu Random Alloy Nanoparticles for Oxygen Reduction, J. Phys. Chem. Lett. 2 (2011) 1328–1331. https://doi.org/10.1021/jz2004717.

[59] C. Byram, S.S.B. Moram, D. Banerjee, R. Beeram, J. Rathod, V.R. Soma, Review of ultrafast laser ablation for sensing and photonic applications, J. Opt. 25 (2023) 043001. https://doi.org/10.1088/2040-8986/acbc31.

[60] M. Haribabu, B. Dipanjan, M.S.S. Bharati, J. Chelsea, A. Chandrasekhar, P. Kanaka raju, S. Venugopal Rao, S. Hamad, G. Krishna Podagatlapalli, Exciton-mediated surface-enhanced Raman studies of Aluminum doped platinum nano colloids, Opt. Mater. (Amst). 133 (2022) 113013. https://doi.org/10.1016/j.optmat.2022.113013.

[61] J. Rathod, C. Byram, R.K. Kanaka, M. Sree Satya Bharati, D. Banerjee, M. Akkanaboina, V.R. Soma, Hybrid Surface-Enhanced Raman Scattering Substrates for the Trace Detection of Ammonium Nitrate, Thiram, and Nile Blue, ACS Omega. 7 (2022) 15969–15981. https://doi.org/10.1021/acsomega.2c01095.

[62] M.B. Cortie, A.M. McDonagh, Synthesis and Optical Properties of Hybrid and Alloy Plasmonic Nanoparticles, Chem. Rev. 111 (2011) 3713–3735. https://doi.org/10.1021/cr1002529.

[63] G. V Hartland, Optical Studies of Dynamics in Noble Metal Nanostructures, Chem. Rev. 111 (2011) 3858–3887. https://doi.org/10.1021/cr1002547.

[64] J. Zhang, J. Claverie, M. Chaker, D. Ma, Colloidal Metal Nanoparticles Prepared by Laser Ablation and their Applications, ChemPhysChem. 18 (2017) 986–1006. https://doi.org/10.1002/cphc.201601220.

[65] J.N. ANKER, W.P. HALL, O. LYANDRES, N.C. SHAH, J. ZHAO, R.P. VAN DUYNE, Biosensing with plasmonic nanosensors, in: Nanosci. Technol., Co-Published with Macmillan Publishers Ltd, UK, 2009: pp. 308–319. https://doi.org/10.1142/9789814287005_0032.

[66] A.N. Koya, J. Cunha, T.-L. Guo, A. Toma, D. Garoli, T. Wang, S. Juodkazis, D. Cojoc, R. Proietti Zaccaria, Novel Plasmonic Nanocavities for Optical Trapping-Assisted Biosensing Applications, Adv. Opt. Mater. 8 (2020) 1901481. https://doi.org/10.1002/adom.201901481.

[67] R. Stoian, M. Boyle, A. Thoss, A. Rosenfeld, G. Korn, I. V. Hertel, Dynamic temporal pulse shaping in advanced ultrafast laser material processing, Appl. Phys.

A Mater. Sci. Process. 77 (2003) 265–269. https://doi.org/10.1007/s00339-003-2112-x.

[68] H.D. Nguyen, E. Moreno, A. Rudenko, N. Faure, X. Sedao, C. Mauclair, J.P. Colombier, R. Stoian, Super-efficient drilling of metals with ultrafast non diffractive laser beams, Sci. Rep. 12 (2022) 1–14. https://doi.org/10.1038/s41598-022-05967-5.

[69] D. Pallarés-Aldeiturriaga, A. Abou Khalil, J.P. Colombier, R. Stoian, X. Sedao, Ultrafast Cylindrical Vector Beams for Improved Energy Feedthrough and Low Roughness Surface Ablation of Metals, Materials (Basel). 16 (2023) 1–8. https://doi.org/10.3390/ma16010176.

[70] R. Stoian, Ultrafast laser volume nanostructuring; a limitless perspective, Adv. Opt. Technol. 12 (2023) 1237524. https://doi.org/10.3389/aot.2023.1237524.

[71] S.N. Khonina, N.L. Kazanskiy, S.V. Karpeev, M.A. Butt, Bessel Beam: Significance and Applications—A Progressive Review, Micromachines. 11 (2020) 997. https://doi.org/10.3390/mi11110997.

[72] Y. Shen, S. Pidishety, I. Nape, A. Dudley, Self-healing of structured light: a review, J. Opt. 24 (2022) 103001. https://doi.org/10.1088/2040-8986/ac8888.

[73] G.K. Podagatlapalli, S. Hamad, M.A. Mohiddon, S.V. Rao, Fabrication of nanoparticles and nanostructures using ultrafast laser ablation of silver with Bessel beams, Laser Phys. Lett. 12 (2015) 036003. https://doi.org/10.1088/1612-2011/12/3/036003.

[74] G. Kontenis, D. Gailevičius, N. Jiménez, K. Staliunas, Optical Drills by Dynamic High-Order Bessel Beam Mixing, Phys. Rev. Appl. 17 (2022) 034059. https://doi.org/10.1103/PhysRevApplied.17.034059.

[75] T. Chen, G. Zhang, H. Zhang, J. Lv, Y. Wang, P. Qu, R. Stoian, G. Cheng, Nano-spheroid formation on YAG surfaces induced by single ultrafast Bessel laser pulses, Appl. Surf. Sci. 604 (2022) 154360. https://doi.org/10.1016/j.apsusc.2022.154360.

[76] R. Stoian, M.K. Bhuyan, A. Rudenko, J.-P. Colombier, G. Cheng, High-resolution material structuring using ultrafast laser non-diffractive beams, Adv. Phys. X. 4 (2019) 1659180. https://doi.org/10.1080/23746149.2019.1659180.

[77] F. Courvoisier, P.-A. Lacourt, M. Jacquot, M.K. Bhuyan, L. Furfaro, J.M. Dudley, Surface nanoprocessing with nondiffracting femtosecond Bessel beams, Opt. Lett. 34 (2009) 3163. https://doi.org/10.1364/ol.34.003163.

[78] F. Courvoisier, J. Zhang, M.K. Bhuyan, M. Jacquot, J.M. Dudley, Applications of femtosecond Bessel beams to laser ablation, Appl. Phys. A. 112 (2013) 29–34. https://doi.org/10.1007/s00339-012-7201-2.

[79] J. Yinon, J.C. Hoffsommer, Analysis of Explosives, C R C Crit. Rev. Anal. Chem.

7 (1977) 1–35. https://doi.org/10.1080/10408347708542697.

[80] F. Zapata, M. López-López, C. García-Ruiz, Detection and identification of explosives by surface enhanced Raman scattering, Appl. Spectrosc. Rev. 51 (2016) 227–262. https://doi.org/10.1080/05704928.2015.1118637.

[81] Y. Huang, W. Liu, Z. Gong, W. Wu, M. Fan, D. Wang, A.G. Brolo, Detection of Buried Explosives Using a Surface-Enhanced Raman Scattering (SERS) Substrate Tailored for Miniaturized Spectrometers, ACS Sensors. 5 (2020) 2933–2939. https://doi.org/10.1021/acssensors.0c01412.

[82] A.G. Davies, A.D. Burnett, W. Fan, E.H. Linfield, J.E. Cunningham, Terahertz spectroscopy of explosives and drugs, Mater. Today. 11 (2008) 18–26. https://doi.org/10.1016/S1369-7021(08)70016-6.

[83] K. Konstantynovski, G. Njio, F. Börner, A. Lepcha, T. Fischer, G. Holl, S. Mathur, Bulk detection of explosives and development of customized metal oxide semiconductor gas sensors for the identification of energetic materials, Sensors Actuators B Chem. 258 (2018) 1252–1266. https://doi.org/10.1016/j.snb.2017.11.116.

[84] L. Mokalled, M. Al-Husseini, K.Y. Kabalan, A. El-Hajj, Sensor review for trace detection of explosives, Int. J. Sci. Eng. Res. 5 (2014) 337–350.

[85] S. Ruan, Y. Chen, P. Zhang, X. Pan, C. Fang, A. Qin, H. Ebendorff-Heidepriem, B.Z. Tang, Y. Tang, Y. Ruan, Online remote monitoring of explosives by optical fibres, RSC Adv. 6 (2016) 103324–103327. https://doi.org/10.1039/C6RA24080A.

[86] S. Singh, Sensors—An effective approach for the detection of explosives, J. Hazard. Mater. 144 (2007) 15–28. https://doi.org/10.1016/j.jhazmat.2007.02.018.

[87] S. Wallin, A. Pettersson, H. Östmark, A. Hobro, Laser-based standoff detection of explosives: a critical review, Anal. Bioanal. Chem. 395 (2009) 259–274. https://doi.org/10.1007/s00216-009-2844-3.

[88] P. Wen, M. Amin, W.D. Herzog, R.R. Kunz, Key challenges and prospects for optical standoff trace detection of explosives, TrAC Trends Anal. Chem. 100 (2018) 136–144. https://doi.org/10.1016/j.trac.2017.12.014.

[89] J. Yinon, Counterterrorist detection techniques of explosives, Elsevier, 2011.

[90] S.D. Christesen, J.A. Guicheteau, J.M. Curtiss, A.W. Fountain III, Handheld dual-wavelength Raman instrument for the detection of chemical agents and explosives, Opt. Eng. 55 (2016) 074103–074103.

[91] D.S. Moore, R.J. Scharff, Portable Raman explosives detection, Anal. Bioanal. Chem. 393 (2009) 1571–1578. https://doi.org/10.1007/s00216-008-2499-5.

[92] D.J. Gardiner, H.J. Bowley, P.R. Graves, D.L. Gerrard, J.D. Louden, G. Turrell, Practical Raman Spectroscopy, Springer Berlin Heidelberg, 2012.

https://books.google.co.in/books?id=58nqCAAAQBAJ.

[93] X. Wang, G. Liu, R. Hu, M. Cao, S. Yan, Y. Bao, B. Ren, Principles of surface-enhanced Raman spectroscopy, in: Princ. Clin. Diagnostic Appl. Surface-Enhanced Raman Spectrosc., Elsevier, 2022: pp. 1–32.

[94] E. Le Ru, P. Etchegoin, Principles of Surface-Enhanced Raman Spectroscopy: and related plasmonic effects, Elsevier, 2008.

[95] J. Mun, D. Lee, S. So, T. Badloe, J. Rho, Surface-enhanced spectroscopy: Toward practical analysis probe, Appl. Spectrosc. Rev. 54 (2019) 142–175. https://doi.org/10.1080/05704928.2018.1467438.

[96] V.A. Tran, T.T.V. Tran, V.T. Le, V.D. Doan, G.N.L. Vo, V.H. Tran, H. Jeong, T.T.T. Vo, Advanced nano engineering of surface-enhanced Raman scattering technologies for sensing applications, Appl. Mater. Today. 38 (2024) 102217. https://doi.org/10.1016/j.apmt.2024.102217.

[97] S.R. Balasubramani, K. Nagappan, L.S. Ewe, K. Viswanathan, W.K. Yew, S.G. Thiraviam, S. Sadana, T.K.D. Samuel, K. Kamalakannan, Recent developments in surface-enhanced Raman spectroscopy in the field of chemical, biochemical and clinical application– a critical review, Int. J. Environ. Anal. Chem. 00 (2024) 1–27. https://doi.org/10.1080/03067319.2024.2339453.

[98] N. Eshbekova, A. Sowndarya, T.D. Thangadurai, Y.I. Lee, Recent advancements in Raman instrumentation and capabilities for pharmaceutical and biomedical applications, Appl. Spectrosc. Rev. 0 (2024) 1–52. https://doi.org/10.1080/05704928.2024.2355193.

[99] A. Balčytis, Y. Nishijima, S. Krishnamoorthy, A. Kuchmizhak, P.R. Stoddart, R. Petruškevičius, S. Juodkazis, From Fundamental toward Applied SERS: Shared Principles and Divergent Approaches, Adv. Opt. Mater. 6 (2018) 1–29. https://doi.org/10.1002/adom.201800292.

[100] M. Fleischmann, P.J. Hendra, A.J. McQuillan, Raman spectra of pyridine adsorbed at a silver electrode, Chem. Phys. Lett. 26 (1974) 163–166.

[101] A.R. Bizzarri, S. Cannistraro, Temporal Fluctuations in Single-Molecule SERS Spectra, in: Surface-Enhanced Raman Scatt. – Phys. Appl., Springer Berlin Heidelberg, 2006: pp. 279–296. https://doi.org/10.1007/11663898_14.

[102] N. Chen, T.-H. Xiao, Z. Luo, Y. Kitahama, K. Hiramatsu, N. Kishimoto, T. Itoh, Z. Cheng, K. Goda, Porous carbon nanowire array for surface-enhanced Raman spectroscopy, Nat. Commun. 11 (2020) 4772. https://doi.org/10.1038/s41467-020-18590-7.

[103] D.L. Jeanmaire, R.P. Van Duyne, Surface Raman spectroelectrochemistry: Part I. Heterocyclic, aromatic, and aliphatic amines adsorbed on the anodized silver

electrode, J. Electroanal. Chem. Interfacial Electrochem. 84 (1977) 1–20.
[104] J. Langer, D.J. de Aberasturi, J. Aizpurua, R.A. Alvarez-Puebla, B. Auguié, J.J. Baumberg, G.C. Bazan, S.E.J. Bell, A. Boisen, A.G. Brolo, J. Choo, D. Cialla-May, V. Deckert, L. Fabris, K. Faulds, F. Javier García de Abajo, R. Goodacre, D. Graham, A.J. Haes, C.L. Haynes, C. Huck, T. Itoh, M. Käll, J. Kneipp, N.A. Kotov, H. Kuang, E.C. Le Ru, H.K. Lee, J.F. Li, X.Y. Ling, S.A. Maier, T. Mayerhöfer, M. Moskovits, K. Murakoshi, J.M. Nam, S. Nie, Y. Ozaki, I. Pastoriza-Santos, J. Perez-Juste, J. Popp, A. Pucci, S. Reich, B. Ren, G.C. Schatz, T. Shegai, S. Schlücker, L.L. Tay, K. George Thomas, Z.Q. Tian, R.P. van Duyne, T. Vo-Dinh, Y. Wang, K.A. Willets, C. Xu, H. Xu, Y. Xu, Y.S. Yamamoto, B. Zhao, L.M. Liz-Marzán, Present and future of surface-enhanced Raman scattering, ACS Nano. 14 (2020) 28–117. https://doi.org/10.1021/acsnano.9b04224.
[105] A.I. Pérez-Jiménez, D. Lyu, Z. Lu, G. Liu, B. Ren, Surface-enhanced Raman spectroscopy: benefits, trade-offs and future developments, Chem. Sci. 11 (2020) 4563–4577. https://doi.org/10.1039/D0SC00809E.
[106] S. Schlücker, Surface-Enhanced raman spectroscopy: Concepts and chemical applications, Angew. Chemie Int. Ed. 53 (2014) 4756–4795.
[107] L. Yang, Y. Peng, Y. Yang, J. Liu, H. Huang, B. Yu, J. Zhao, Y. Lu, Z. Huang, Z. Li, J.R. Lombardi, A Novel Ultra-Sensitive Semiconductor SERS Substrate Boosted by the Coupled Resonance Effect, Adv. Sci. 6 (2019) 1900310. https://doi.org/10.1002/advs.201900310.
[108] M.G. Albrecht, J.A. Creighton, Anomalously intense Raman spectra of pyridine at a silver electrode, J. Am. Chem. Soc. 99 (1977) 5215–5217. https://doi.org/10.1021/ja00457a071.
[109] M. Moskovits, Surface roughness and the enhanced intensity of Raman scattering by molecules adsorbed on metals, J. Chem. Phys. 69 (1978) 4159–4161.
[110] M.R. McCourt, A. Stewart, S.E.J. Bell, P.M. Champion, L.D. Ziegler, SERS Enhancements by Aggregated Au Colloids: Effect of Particle Size, in: AIP Conf. Proc., 2010: pp. 936–937. https://doi.org/10.1063/1.3482900.
[111] M.G. Blaber, M.D. Arnold, M.J. Ford, A review of the optical properties of alloys and intermetallics for plasmonics, J. Phys. Condens. Matter. 22 (2010) 143201. https://doi.org/10.1088/0953-8984/22/14/143201.
[112] K.-Q. Lin, J. Yi, S. Hu, B.-J. Liu, J.-Y. Liu, X. Wang, B. Ren, Size Effect on SERS of Gold Nanorods Demonstrated via Single Nanoparticle Spectroscopy, J. Phys. Chem. C. 120 (2016) 20806–20813. https://doi.org/10.1021/acs.jpcc.6b02098.
[113] Y. Lin, Y.-J. Zhang, W.-M. Yang, J.-C. Dong, F.-R. Fan, Y. Zhao, H. Zhang, N. Bodappa, X.-D. Tian, Z.-L. Yang, G.D. Stucky, Z.-Q. Tian, J.-F. Li, Size and

dimension dependent surface-enhanced Raman scattering properties of well-defined Ag nanocubes, Appl. Mater. Today. 14 (2019) 224–232. https://doi.org/10.1016/j.apmt.2018.12.012.

[114] W.Y. Ma, H. Yang, J.P. Hilton, Q. Lin, J.Y. Liu, L.X. Huang, J. Yao, A numerical investigation of the effect of vertex geometry on localized surface plasmon resonance of nanostructures, Opt. Express. 18 (2010) 843. https://doi.org/10.1364/OE.18.000843.

[115] K.G. Stamplecoskie, J.C. Scaiano, V.S. Tiwari, H. Anis, Optimal Size of Silver Nanoparticles for Surface-Enhanced Raman Spectroscopy, J. Phys. Chem. C. 115 (2011) 1403–1409. https://doi.org/10.1021/jp106666t.

[116] F. Tian, F. Bonnier, A. Casey, A.E. Shanahan, H.J. Byrne, Surface enhanced Raman scattering with gold nanoparticles: effect of particle shape, Anal. Methods. 6 (2014) 9116–9123. https://doi.org/10.1039/C4AY02112F.

[117] H. You, Y. Ji, L. Wang, S. Yang, Z. Yang, J. Fang, X. Song, B. Ding, Interface synthesis of gold mesocrystals with highly roughened surfaces for surface-enhanced Raman spectroscopy, J. Mater. Chem. 22 (2012) 1998–2006. https://doi.org/10.1039/C1JM13211C.

[118] L.B. He, Y.L. Wang, X. Xie, M. Han, F.Q. Song, B.J. Wang, W.L. Chen, H.X. Xu, L.T. Sun, Systematic investigation of the SERS efficiency and SERS hotspots in gas-phase deposited Ag nanoparticle assemblies, Phys. Chem. Chem. Phys. 19 (2017) 5091–5101. https://doi.org/10.1039/C6CP08513J.

[119] S.L. Kleinman, R.R. Frontiera, A.-I. Henry, J.A. Dieringer, R.P. Van Duyne, Creating, characterizing, and controlling chemistry with SERS hot spots, Phys. Chem. Chem. Phys. 15 (2013) 21–36. https://doi.org/10.1039/C2CP42598J.

[120] G. Kumari, J. Kandula, C. Narayana, How Far Can We Probe by SERS?, J. Phys. Chem. C. 119 (2015) 20057–20064. https://doi.org/10.1021/acs.jpcc.5b07556.

[121] K. Kneipp, Surface-enhanced Raman scattering, Phys. Today. 60 (2007) 40–46.

[122] R.A. Alvarez-Puebla, D.J. Ross, G.-A. Nazri, R.F. Aroca, Surface-Enhanced Raman Scattering on Nanoshells with Tunable Surface Plasmon Resonance, Langmuir. 21 (2005) 10504–10508. https://doi.org/10.1021/la051645l.

[123] R.A. Álvarez-Puebla, Effects of the Excitation Wavelength on the SERS Spectrum, J. Phys. Chem. Lett. 3 (2012) 857–866. https://doi.org/10.1021/jz201625j.

[124] H.K. Lee, Y.H. Lee, C.S.L. Koh, G.C. Phan-Quang, X. Han, C.L. Lay, H.Y.F. Sim, Y.-C. Kao, Q. An, X.Y. Ling, Designing surface-enhanced Raman scattering (SERS) platforms beyond hotspot engineering: emerging opportunities in analyte manipulations and hybrid materials, Chem. Soc. Rev. 48 (2019) 731–756. https://doi.org/10.1039/C7CS00786H.

[125] K. Kneipp, H. Kneipp, H.G. Bohr, Single-molecule SERS spectroscopy, Surface-Enhanced Raman Scattering, Springer Berlin Heidelberg, 2006. https://doi.org/10.1007/3-540-33567-6.

[126] S. Nie, S.R. Emory, Probing single molecules and single nanoparticles by surface-enhanced Raman scattering, Science (80-.). 275 (1997) 1102–1106.

[127] F. Saviñon-Flores, E. Méndez, M. López-Castaños, A. Carabarin-Lima, K.A. López-Castaños, M.A. González-Fuentes, A. Méndez-Albores, A Review on SERS-Based Detection of Human Virus Infections: Influenza and Coronavirus, Biosensors. 11 (2021) 66. https://doi.org/10.3390/bios11030066.

[128] D.A. Stuart, K.B. Biggs, R.P. Van Duyne, Surface-enhanced Raman spectroscopy of half-mustard agent, Analyst. 131 (2006) 568. https://doi.org/10.1039/b513326b.

[129] K. Xu, R. Zhou, K. Takei, M. Hong, Toward Flexible Surface-Enhanced Raman Scattering (SERS) Sensors for Point-of-Care Diagnostics, Adv. Sci. 6 (2019) 1900925. https://doi.org/10.1002/advs.201900925.

[130] Y. Li, K. Zhang, J. Zhao, J. Ji, C. Ji, B. Liu, A three-dimensional silver nanoparticles decorated plasmonic paper strip for SERS detection of low-abundance molecules, Talanta. 147 (2016) 493–500. https://doi.org/10.1016/j.talanta.2015.10.025.

[131] T. Vo-Dinh, F. Yan, M.B. Wabuyele, Surface-Enhanced Raman Scattering for Biomedical Diagnostics and Molecular Imaging, in: Surface-Enhanced Raman Scatt., Springer Berlin Heidelberg, 2006: pp. 409–426. https://doi.org/10.1007/3-540-33567-6_22.

[132] N.K. Gushiken, G.T. Paganoto, M.L.A. Temperini, F.S. Teixeira, M.C. Salvadori, Substrate for surface-enhanced Raman spectroscopy formed by gold nanoparticles buried in poly (methyl methacrylate), ACS Omega. 5 (2020) 10366–10373.

[133] Y. Hu, J. Liao, D. Wang, G. Li, Fabrication of gold nanoparticle-embedded metal–organic framework for highly sensitive surface-enhanced Raman scattering detection, Anal. Chem. 86 (2014) 3955–3963.

[134] V.K. Rao, T.P. Radhakrishnan, Tuning the SERS response with Ag-Au nanoparticle-embedded polymer thin film substrates, ACS Appl. Mater. Interfaces. 7 (2015) 12767–12773.

[135] R. Buividas, P.R. Stoddart, S. Juodkazis, Laser fabricated ripple substrates for surface-enhanced Raman scattering, Ann. Phys. 524 (2012) L5–L10. https://doi.org/10.1002/andp.201200140.

[136] H.-W. Chang, Y.-C. Tsai, C.-W. Cheng, C.-Y. Lin, Y.-W. Lin, T.-M. Wu, Nanostructured Ag surface fabricated by femtosecond laser for surface-enhanced Raman scattering, J. Colloid Interface Sci. 360 (2011) 305–308. https://doi.org/10.1016/j.jcis.2011.04.005.

[137] I. Izquierdo-Lorenzo, S. Jradi, P.-M. Adam, Direct laser writing of random Au nanoparticle three-dimensional structures for highly reproducible micro-SERS measurements, RSC Adv. 4 (2014) 4128–4133.
[138] M. Akkanaboina, D. Banerjee, K.R. Kumar, R.S.P. Goud, V.R. Soma, S.V.S.N. Rao, Gold nanoparticles coated LIPSS on GaAs for trace detection of RDX and Tetryl, Surfaces and Interfaces. 36 (2023) 102563. https://doi.org/10.1016/j.surfin.2022.102563.
[139] M. Akkanaboina, D. Banerjee, K. Ravi Kumar, R. Sai Prasad Goud, V.R. Soma, S.V.S. Nageswara Rao, Sub-70 nm surface structures on femtosecond laser irradiated GaAs in distilled water and sensing application, Opt. Lett. 48 (2023) 5539. https://doi.org/10.1364/OL.502527.
[140] D. Banerjee, M. Akkanaboina, R. Kumar Kanaka, V. Rao Soma, Femtosecond Bessel beam induced ladder-like LIPSS on trimetallic surface for SERS-based sensing of Tetryl and PETN, Appl. Surf. Sci. 616 (2023) 156561. https://doi.org/10.1016/j.apsusc.2023.156561.
[141] D. Banerjee, M. Akkanaboina, R.K. Kanaka, B. Ghose, V.R. Soma, Nanotubular Arrayed LIPSS Achieved with Femtosecond Bessel Beam on Silver Surface for SERS-Based Multiple Explosive Sensing, J. Phys. Chem. C. 128 (2024) 4655–4665. https://doi.org/10.1021/acs.jpcc.4c00160.
[142] S.N. Erkızan, F. İdikut, Ö. Demirtaş, A. Goodarzi, A.K. Demir, M. Borra, I. Pavlov, A. Bek, LIPSS for SERS: Metal coated direct laser written periodic nanostructures for surface enhanced Raman spectroscopy, Adv. Opt. Mater. 10 (2022) 2200233.
[143] F. Zapata, M. López-López, C. García-Ruiz, Detection and identification of explosives by surface enhanced Raman scattering, Appl. Spectrosc. Rev. 51 (2016) 207–242. https://doi.org/10.1080/05704928.2015.1118637.
[144] T. Paul, D. Roy Choudhury, D. Ghosh, C. Saha, Advancements in optical sensors for explosive materials Identification: A comprehensive review, Results Chem. 8 (2024) 101602. https://doi.org/10.1016/j.rechem.2024.101602.
[145] W. Zhang, Y. Tang, A. Shi, L. Bao, Y. Shen, R. Shen, Y. Ye, Recent developments in spectroscopic techniques for the detection of explosives, Materials (Basel). 11 (2018). https://doi.org/10.3390/ma11081364.
[146] K.L. Gares, K.T. Hufziger, S. V. Bykov, S.A. Asher, Review of explosive detection methodologies and the emergence of standoff deep UV resonance Raman, J. Raman Spectrosc. 47 (2016) 124–141. https://doi.org/10.1002/jrs.4868.
[147] S. Adhikari, E.K. Ampadu, M. Kim, D. Noh, E. Oh, D. Lee, Detection of explosives by SERS platform using metal nanogap substrates, Sensors. 21 (2021). https://doi.org/10.3390/s21165567.

[148] A. Saletnik, B. Saletnik, C. Puchalski, Overview of popular techniques of raman spectroscopy and their potential in the study of plant tissues, Molecules. 26 (2021) 1537. https://doi.org/10.3390/molecules26061537.
[149] K.A. Willets, R.P. Van Duyne, Localized surface plasmon resonance spectroscopy and sensing, Annu. Rev. Phys. Chem. 58 (2007) 267–297. https://doi.org/10.1146/annurev.physchem.58.032806.104607.
[150] E. Petryayeva, U.J. Krull, Localized surface plasmon resonance: Nanostructures, bioassays and biosensing-A review, Anal. Chim. Acta. 706 (2011) 8–24. https://doi.org/10.1016/j.aca.2011.08.020.
[151] P.G. Etchegoin, E.C.L. Ru, Basic Electromagnetic Theory of SERS, Surf. Enhanc. Raman Spectrosc. Anal. Biophys. Life Sci. Appl. (2010) 1–37. https://doi.org/10.1002/9783527632756.ch1.
[152] C.F. Bohren, D.R. Huffman, Absorption and scattering of light by small particles, John Wiley & Sons, 1983. https://doi.org/10.1088/0031-9112/35/3/025.
[153] H. Ma, S.Q. Pan, W.L. Wang, X. Yue, X.H. Xi, S. Yan, D.Y. Wu, X. Wang, G. Liu, B. Ren, Surface-Enhanced Raman Spectroscopy: Current Understanding, Challenges, and Opportunities, ACS Nano. 18 (2024) 14000-14019. https://doi.org/10.1021/acsnano.4c02670.
[154] H.A. Szymanski, Raman spectroscopy: theory and practice, Springer Science & Business Media, 2012.
[155] D.A. Long, Raman spectroscopy, New York. 1 (1977) 310.
[156] E.C. Le Ru, B. Auguié, Enhancement Factors: A Central Concept during 50 Years of Surface-Enhanced Raman Spectroscopy, ACS Nano. 18 (2024) 9773–9783. https://doi.org/10.1021/acsnano.4c01474.
[157] H. Wang, Y. Liu, G. Rao, Y. Wang, X. Du, A. Hu, Y. Hu, C. Gong, X. Wang, J. Xiong, Coupling enhancement mechanisms, materials, and strategies for surface-enhanced Raman scattering devices, Analyst. 146 (2021) 5008–5032. https://doi.org/10.1039/d1an00624j.
[158] M. Hardy, P. Goldberg Oppenheimer, ‘When is a hotspot a good nanospot’ - review of analytical and hotspot-dominated surface enhanced Raman spectroscopy nanoplatforms, Nanoscale. 14 (2024) 3293–3323. https://doi.org/10.1039/d3nr05332f.
[159] N. Guillot, M.L. de la Chapelle, The electromagnetic effect in surface enhanced Raman scattering: Enhancement optimization using precisely controlled nanostructures, J. Quant. Spectrosc. Radiat. Transf. 113 (2012) 2321–2333. https://doi.org/10.1016/j.jqsrt.2012.04.025.
[160] D. Zhang, B. Gökce, S. Barcikowski, Laser Synthesis and Processing of Colloids:

Fundamentals and Applications, Chem. Rev. 117 (2017) 3990–4103. https://doi.org/10.1021/acs.chemrev.6b00468.

[161] S. Barcikowski, Handbook of laser synthesis of colloids, (2016).

[162] S. Barcikowski, A. Hahn, A. V. Kabashin, B.N. Chichkov, Properties of nanoparticles generated during femtosecond laser machining in air and water, Appl. Phys. A Mater. Sci. Process. 87 (2007) 47–55. https://doi.org/10.1007/s00339-006-3852-1.

[163] J. Zhang, M. Chaker, D. Ma, Pulsed laser ablation based synthesis of colloidal metal nanoparticles for catalytic applications, J Colloid Interface Sci. 489 (2017) 138–149. https://doi.org/10.1016/j.jcis.2016.07.050.

[164] N.N. Nedialkov, S.E. Imamova, P.A. Atanasov, Ablation of metals by ultrashort laser pulses, J. Phys. D. Appl. Phys. 37 (2004) 638–643. https://doi.org/10.1088/0022-3727/37/4/016.

[165] A. V Simakin, V. V Voronov, N.A. Kirichenko, G.A. Shafeev, Nanoparticles produced by laser ablation of solids in liquid environment, Appl. Phys. a-Materials Sci. Process. 79 (2004) 1127–1132. https://doi.org/10.1007/s00339-004-2660-8.

[166] A.Y. Vorobyev, C. Guo, Femtosecond laser nanostructuring of metals, Opt. Express. 14 (2006) 2164. https://doi.org/10.1364/OE.14.002164.

[167] V. Schmidt, W. Husinsky, G. Betz, Dynamics of laser desorption and ablation of metals at the threshold on the femtosecond time scale, Phys. Rev. Lett. 85 (2000) 3516–3519. https://doi.org/10.1103/PhysRevLett.85.3516.

[168] R. Fang, A. Vorobyev, C. Guo, Direct visualization of the complete evolution of femtosecond laser-induced surface structural dynamics of metals, Light Sci. Appl. 6 (2017) e16256-7. https://doi.org/10.1038/lsa.2016.256.

[169] L. Chen, Z. Chen, K. Shimada, M. Mizutani, T. Kuriyagawa, Electric field analysis coupled with the two-temperature model to elucidate the generation process of laser-induced periodic surface structure, J. Mater. Process. Technol. 305 (2022) 117601. https://doi.org/10.1016/j.jmatprotec.2022.117601.

[170] S.V. Rao, G.K. Podagatlapalli, S. Hamad, Ultrafast laser ablation in liquids for nanomaterials and applications, J. Nanosci. Nanotechnol. 14 (2014) 1364–1388. https://doi.org/10.1166/jnn.2014.9138.

[171] N.L. Lahaye, S.S. Harilal, P.K. Diwakar, A. Hassanein, The effect of laser pulse duration on ICP-MS signal intensity, elemental fractionation, and detection limits in fs-LA-ICP-MS, J. Anal. At. Spectrom. 28 (2013) 1781–1787. https://doi.org/10.1039/c3ja50200g.

[172] P.B. Johnson, R.-Wjp. Christy, Optical constants of the noble metals, Phys. Rev. B. 6 (1972) 4370.

[173] N.W. Ashcroft, N.D. Mermin, Solid state, Phys. (New York Holt, Rinehart Winston) Append. C. (1976).
[174] C. Voisin, D. Christofilos, P.A. Loukakos, N. Del Fatti, F. Vallée, J. Lermé, M. Gaudry, E. Cottancin, M. Pellarin, M. Broyer, Ultrafast electron-electron scattering and energy exchanges in noble-metal nanoparticles, Phys. Rev. B. 69 (2004). https://doi.org/10.1103/PhysRevB.69.195416.
[175] G. V. Hartland, L. V. Besteiro, P. Johns, A.O. Govorov, What's so Hot about Electrons in Metal Nanoparticles?, ACS Energy Lett. 2 (2017) 1641–1653. https://doi.org/10.1021/acsenergylett.7b00333.
[176] A. Rana, N. Gupta, A. Lochan, G.D. Sharma, S. Chand, M. Kumar, R.K. Singh, Charge carrier dynamics and surface plasmon interaction in gold nanorod-blended organic solar cell, J. Appl. Phys. 120 (2016).
[177] M. Kerker, The scattering of light and other electromagnetic radiation, Elsevier, 2016.
[178] E.J. Heilweil, R.M. Hochstrasser, Nonlinear spectroscopy and picosecond transient grating study of colloidal gold, J. Chem. Phys. 82 (1985) 4762–4770.
[179] S. Link, C. Burda, Z.L. Wang, M.A. El-Sayed, Electron dynamics in gold and gold-silver alloy nanoparticles: The influence of a nonequilibrium electron distribution and the size dependence of the electron-phonon relaxation, J. Chem. Phys. 111 (1999) 1255–1264. https://doi.org/10.1063/1.479310.
[180] Y. Lin, X. Zhang, Ultrafast multipolar plasmon for unidirectional optical switching in a hemisphere-nanoshell array, Adv. Opt. Mater. 5 (2017) 1601088.
[181] T.E. Karam, H.T. Smith, L.H. Haber, Enhanced Photothermal Effects and Excited-State Dynamics of Plasmonic Size-Controlled Gold-Silver-Gold Core-Shell-Shell Nanoparticles, J. Phys. Chem. C. 119 (2015) 18573–18580. https://doi.org/10.1021/acs.jpcc.5b05110.
[182] O.B. Wright, Ultrafast nonequilibrium stress generation in gold and silver, Phys. Rev. B. 49 (1994) 9985–9988. https://doi.org/10.1103/PhysRevB.49.9985.
[183] C.K. Sun, F. Vallée, L.H. Acioli, E.P. Ippen, J.G. Fujimoto, Femtosecond-tunable measurement of electron thermalization in gold, Phys. Rev. B. 50 (1994) 15337–15348. https://doi.org/10.1103/PhysRevB.50.15337.
[184] X. Zhang, C. Huang, M. Wang, P. Huang, X. He, Z. Wei, Transient localized surface plasmon induced by femtosecond interband excitation in gold nanoparticles, Sci Rep. 8 (2018) 10499. https://doi.org/10.1038/s41598-018-28909-6.

Intentional Blank Page

Chapter 2

Experimental Techniques & Characterization Studies

Abstract

This chapter examines the strategies used in producing colloidal nanoparticles (NPs) and nanostructures (NSs) utilized in all the experiments conducted in this thesis. The information provided details on the femtosecond (fs) laser system utilized in laser ablation studies. This chapter also presents the measurements of pulse width of fs amplifier pulses. A detailed discussion of the techniques for generating multi-metal alloy nanoparticles (NPs) and fabricating LIPSS on plasmonic surfaces is provided. Additionally, this chapter offers detailed information about the characterization tools used to analyze the obtained NPS and NSs. These tools include UV-visible absorption spectroscopy, X-ray diffractometer (XRD), Transmission electron microscopy (TEM) with selected area diffraction (SAED) technique, atomic force microscopy (AFM) and Field emission scanning electron microscope equipped with energy-dispersive X-ray spectroscopy (FESEM-EDS). The chapter also discusses the specifications of the micro- and portable Raman spectrometers used for different surface-enhanced Raman scattering experiments. It also offers an overview of the experimental techniques, including Z-scan and fs transient absorption spectroscopy.

2.1. Introduction

This thesis explores the fs laser-matter interaction leading to the generation of LIPSS and colloidal alloy NPs. Further, it also deals with SERS-based sensing applications and transient absorption spectroscopic studies. Several experimental approaches have been undertaken in these investigations. We have attempted to summarize all of them in this chapter. The femtosecond (fs) laser system used in laser ablation investigations is described here. The chapter then elaborates on the methods used to make colloidal nanoparticles (NPs) and nanostructures (NSs) for all thesis experiments. This section explains the process of making multi-metal alloy nanoparticles (NPs) and LIPSS on plasmonic surfaces. We have also elaborated on the characterization techniques used to examine NPS and NSs. These tools include UV-visible absorption spectroscopy, XRD, TEM with SAED, AFM, and FESEM-EDS. SERS studies employ micro- and portable Raman spectrometers. It describes experimental methods, including Z-scan and transient absorption spectroscopy.

Firstly, the femtosecond (fs) laser system used in laser ablation investigations is described here, starting with the Mode-locking technique utilized to generate the fs pulses.

2.2. Mode-locking: Important Mechanisms Involved

A gain medium and an optical resonator are the two main components of any laser. The range of frequencies where gain exceeds resonator losses is the range across which the laser is found to oscillate. In general, this oscillation-band consists of several resonator cavity modes. Therefore, the laser's output comprises many tightly spaced frequencies. Finally, the output of these laser frequencies in terms of time [ω(t)] will depend on their respective frequencies, amplitudes, and phases, respectively. These settings can be adjusted to prevent random oscillations and nonlinear effects in the laser medium. The output as a function of time will change in a managed way if all the oscillating frequencies have identical frequency spacing and a fixed phase to one another. This kind of laser is known as a mode-locked [1,2] laser. We can observe continuous light and periodic pulse as an output. Considering there are n modes of amplitude E_0 and frequency ω_n, then we can express the total field,

$$E(t) = \sum_n e^{i[\omega_n + \varphi_n]} \quad (1)$$

where φ_n is the phase. Now, $I(t)=NE_0^2$ gives the resulting intensity as the N times the intensity of the different modes. If $\varphi_n = \varphi_0$, $\omega_n = \omega_{n-1} - n\Delta\omega$ and $\Delta\omega = 2\pi(c/2L)$, then

$$E(t)=E_0\, e^{i\varphi_0}\{\sum_n e^{i[\omega_{n-1}-n\Delta\omega]t}\} \quad (2)$$

And we get total intensity as

$$I(e) = E_0^2 \frac{\sin^2(N\Delta\omega t/2)}{\sin^2(\Delta\omega t/2)}, \text{ where } \frac{\Delta\omega t}{2} = 0, \pi, 2\pi, \ldots, n\pi \quad (3)$$

The time being taken by a pulse to complete one whole round in the cavity is $\Delta t_p = \frac{1}{\Delta\upsilon_{sep}} = \frac{2L}{C}$, displayed in Figure. 2.1. As a result, total intensity is indicated by $I(t) = N^2E_0^2$ raised by a factor N when it is $\varphi_n = \varphi_0$. Passive and active mode locking are two categories for the mode-locking process. When active mode-locking is used, an externally driven device is inserted into the laser cavity to control the intra-cavity frequency or amplitude at the cavity rate of repetition frequency. Adding the saturable absorber (SA) leads to the passive ML. Consequently, the leading part of the laser pulse becomes saturated with absorption, and the main pulse will experience zero loss. This enables high-intensity light owing to SA; continuous waves will experience absorption loss. SA functions as a shutter. Because, compared to electrical shutters, the pulse activates with a considerably quicker modulation.

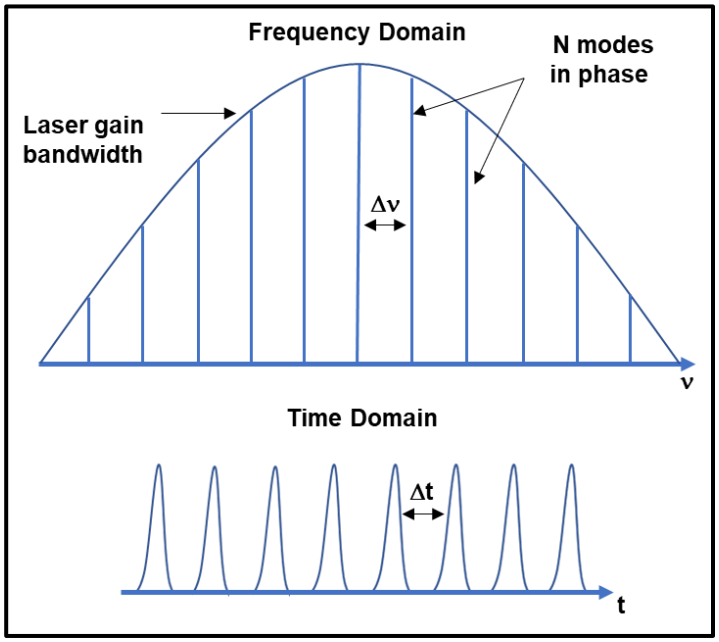

Figure 2. 1 Frequency and time domain parameters of mode-locked pulses.

2.2.1 Kerr-lens Mode Locking

The basis of Kerr-lens mode-locking (KLM), also known as self-focusing, is the change in the nonlinear refractive index. This procedure is based on a material's refractive index changing depending on the intensity [3,4]. Equation $n = n_0+n_2\times I$ (where n_0 refers to refractive index, n_2 denotes nonlinear refractive index) predicts that Gaussian-shaped pulses moving within an area with a higher intensity at the middle portion than the borders will experience a greater change in refractive index at the middle than the borders, resulting in the formation of a lens that directs the beam of light within the substance. The degree of concentration depends on the intensity and route length. An aperture is positioned at one side of the mirror in the KLM technique; in the CW situation, the beam experiences significant loss as the intensity grows owing to self-focusing. Consequently, beam size decreases, and less loss may be accomplished than in CW mode. We can alter the aperture by pumping with a reduced beam diameter. The benefit of the focusing effect in the material is that it enhances self-phase modulation (SPM), expands the pulse's frequency range, and shortens the pulse's length.

2.2.2 Self-Phase Modulation

The self-focusing phenomenon, which happens when an optical pulse that is time-dependent interacts with a material's intensity-dependent refractive index, causes self-phase modulation [5,6]. The pulse gains the extra frequency components during its nonlinear medium propagation. Because of the intensity-dependent refractive index, it concentrates on the substance when a laser pulse travels within a material at a high enough intensity. When a pulse travels through this material and contacts an SPM, the source pulse's frequency spectrum is widened. The leading edge of the laser pulse experiences a significant change in refractive index as it travels through the material, which results in a drop in beam velocity. The drop in velocity represents the delay in the rising edge electromagnetic waves reaching the material's exit side, resulting in a narrowing of the frequency spectra. The index of refraction drops on the trailing end of the pulse, boosting the beam's velocity and, consequently, the trailing edge's frequency. Pulse chirping or frequency chirping are the names for this mechanism.

2.2.3 Group Velocity Dispersion

Group velocity dispersion (GVD) is a method for reducing or increasing pulse duration. [6] Assume a wave having frequency ω_0 and width of $\Delta\omega$, then we can express variation of propagation constant k_0 as

$$k = k_0 + \left(\frac{dk}{d\omega}\right)_{\omega=\omega_0} (\omega - \omega_0) + \dots \quad (4)$$

The Fourier expansion of the electric field

$$E(z,t) = \int E(\omega) e^{-i(kz-\omega)}\, d\omega \quad (5)$$

Put the above equation

$$E(z,t) = e^{-i(kz-\omega)} \int_{-\Delta\omega/2}^{+\Delta\omega/2} \exp\{-i[\left(\frac{dk}{d\omega}\right)_{\omega_0} z - t]\Delta\omega\} d\Delta\omega \quad (6)$$

Where $\Delta\omega = \omega - \omega_0$. We can obtain the modulated wave's velocity from $[(dk/d\omega)z - t] = \text{constant}$; therefore,$dz/dt = V_G = d\omega/dk$. Where V_G is the group velocity. The variation in velocity with various wavelengths is shown by a finite amount of V_G. A media having these characteristics is referred to as a dispersive medium. We have $d\omega/dk = 0$ for nondispersive medium and one way to express group velocity dispersion is,

$$GVD = \frac{d^2k}{d\omega^2} = \frac{d}{d\omega}\left(\frac{1}{V_G}\right) = \frac{-1}{V_G^2}\frac{dV_G}{d\omega} \quad (7)$$

The frequency-dependent dispersion inside the medium can compress or extend a brief optical pulse as it travels through a medium with considerable GVD. The group velocity falls as the frequency components of the pulse increase for positive GVD (V_G red >V_G blue), Which causes the pulse to expand. The pulse starts to shorten [1] in negative GVD (V_G blue >V_G red).

2.2.4 Chirped Pulse Amplification (CPA)

The chirped pulse amplification (CPA) method of generating powerful ultrafast laser pulses from a solid medium has made it possible to produce terawatt or higher laser peak powers [7]. The CPA technique is frequently employed in all kinds of solid-state lasers to increase the output power of the laser. Figure 2.2 illustrates the CPA process. The seed laser's

low energy pulses (100 fs) are sent to a dispersive pulse stretcher, where they become highly chirped stretched pulses that are broadened up to 200 ps or more for that time to prevent optical damage and self-focusing effects without influencing bandwidth. Either single-stage or multi-stage amplifiers are used to amplify the stretcher's pulse. The stretched and amplified pulse then travels into an opposing (i.e., stretcher) dispersive medium, which is compressed according to the bandwidth constraint. The amplified pulse's chirp may be regulated by adding the group delay dispersion of various signs. The wavelength-dependent latency is created by the angular dispersion of the diffraction gratings or prism pairs used in typical CPA lasers for pulse stretching and compressing [1,7]. In the case of our laser (LIBRA), the starting pulses (100 fs, 80 MHz) are extended up to 200 ps, decreasing the peak strength, which is further boosted in the regenerative amplifier before compression. Seed pulses are switched to the amplifier by Pockels cell (PC), which is tuned to the seed laser. As a result, nJ energy in the seed pulses increases to mJ in the amplified pulses.

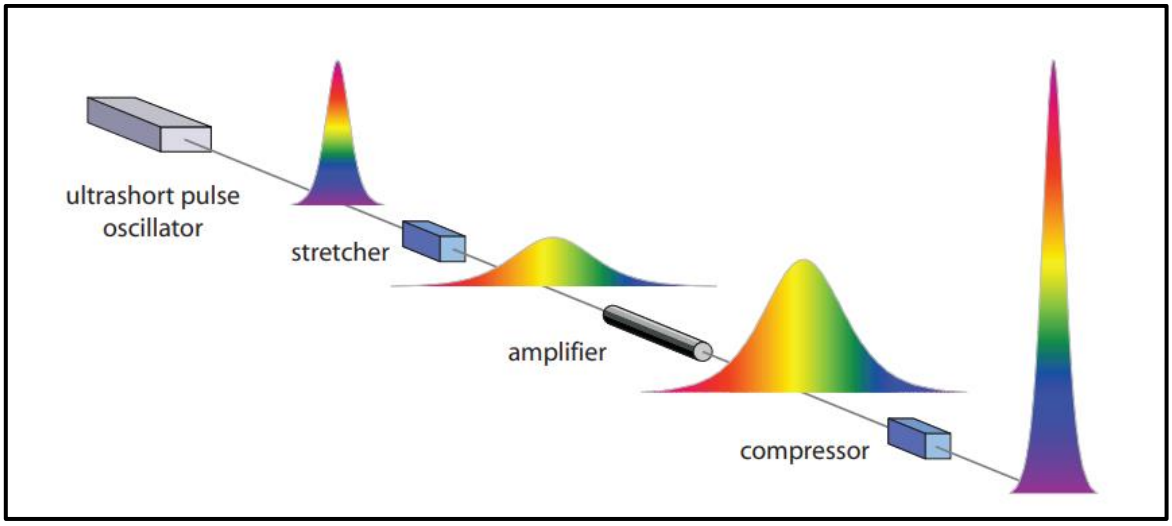

Figure 2. 2 Schematic of the CPA process, adapted from Ref. [8]

2.2.5 Regenerative Amplification

The pulse that needs to be amplified is trapped inside the cavity during the regenerative amplification process (RGA) using a technique called polarization gating [9]. As seen in Figure 2.3, any light produced by spontaneous emission (SE) that enters the resonator while pumping the gain medium is reduced by polarizing the SE travelling via a thin sheet. When V=0, resulting in zero polarization change, the polarizer turns by 90^0 in a double pass across

the wave plate and the Pockels cell, causing enhanced SE to be projected out of the cavity [10]. The pulse to be amplified first goes into the cavity via a polarizer at a particular polarization, causing it to reflect inside the cavity. The polarization changes following a second pass through the wave plate, and then the beam is directed through the polarizer toward the gain medium. A voltage is supplied to the PC before the pulse returns to the polarizer. It behaves like a wave plate and prevents any net polarization change from occurring after reflection from the cavity side mirrors. To prevent the pulse from escaping the cavity and enable several passes through the gain medium. Last but not least, the PC voltage is disabled throughout the pulse emission from the cavity; therefore, to take the pulse out of the cavity, the polarization is shifted by 90^0 at the polarizer after crossing twice within the wave plate. The overall amplification factor, or number of passes across the gain medium, determines additional PC time adjustments. An RGA has greater benefits for multi-pass amplifiers since it allows several passes over the gain medium and excellent signal and pump beam overlap. The RGA technique does have a drawback for ultrafast applications, namely longer material route lengths that result in significant dispersion effects. As a result, it is more challenging to compress the amplified pulse in RGA devices fully.

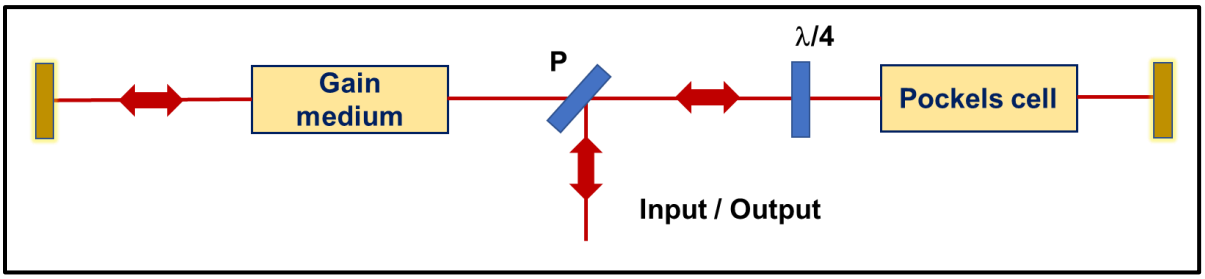

Figure 2. 3 Schematic of the regenerative amplifier.

The LIBRA amplifier technology operates on the same theory. The (Vitesse) laser has an 80 MHz repetition rate. Vertically polarized seed pulses are initially injected into the RGA cavity. The crystal and polarizer can pass on horizontally polarized light while preventing vertically polarized light at the Brewster angle; however, after two passes through the wave plate, the polarization shifts by 90^0 (i.e., from S to P). The wave plate voltage is provided to PC1 (HV1) twice, traveling through PC1 after the pulse has ended, and the wave plate produces zero shift in polarization. The pulse continues to be p-polarized while it travels across an active medium (Ti: Sapphire) several times (about 15 times) and gets amplified with a high-Q cavity at this

period. The cavity reflects every other seed pulse with S-polarization. After several rounds, the amplified pulse returns to S-polarization when a higher voltage is supplied to the PC2 (HV2). This causes more reflection from the active medium and lowers the cavity Q. The average time interval between seed pulses is 13 ns.

2.3. Libra, Ultrafast laser system from M/s Coherent

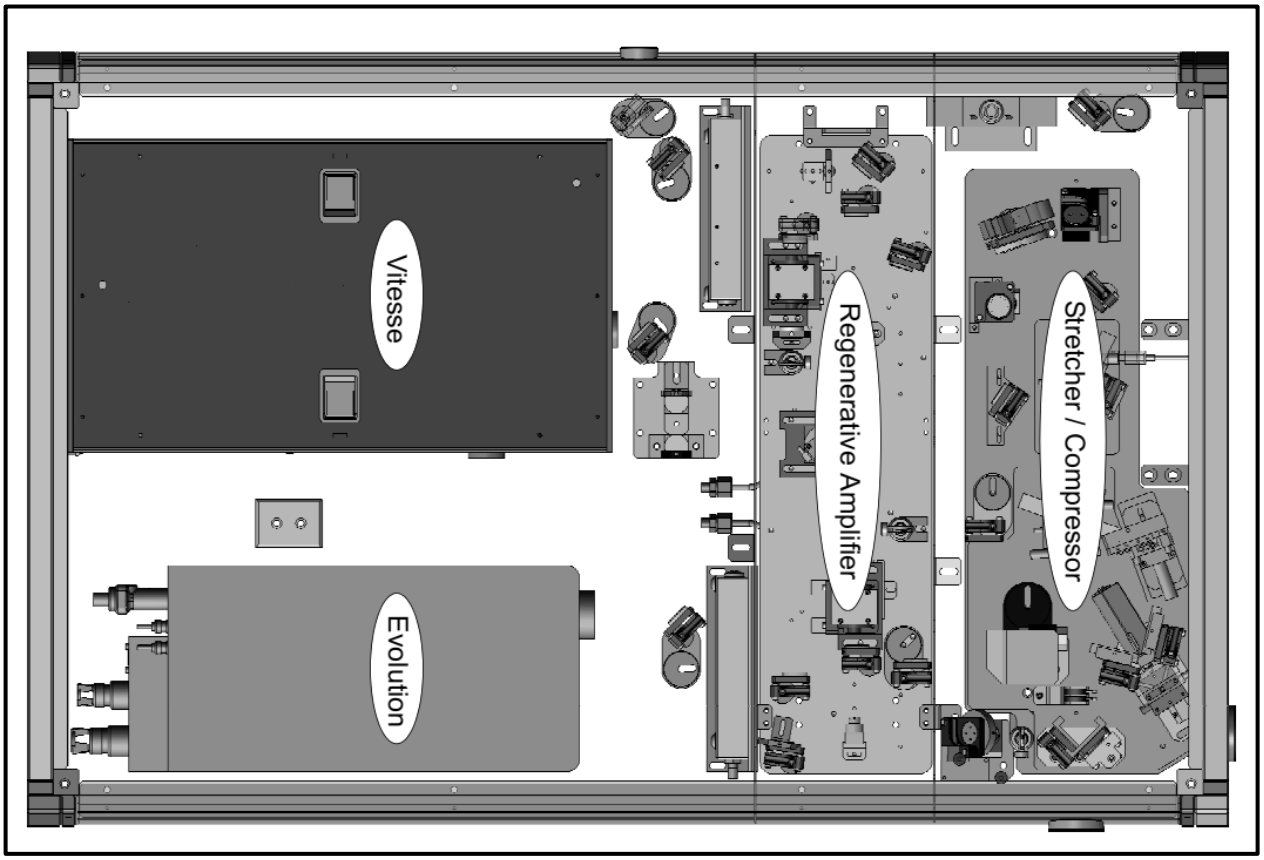

Figure 2. 4 The top view of the Femtosecond amplifier system (LIBRA) shows the essential modules (i) Vitesse (seed) (ii) Evolution (Pump) (iii) RGA cavity (iv) Stretcher/compressor region. (Image adapted from Coherent, operator's manual for Libra ultrafast amplifier laser system).

Scientific and commercial-grade magnified Ti: Sapphire laser, the Libra laser system (50 fs pulse duration, working at 1 kHz, 4 mJ of maximum pulse energy, M/s Coherent) operated with a central wavelength of 797 nm. The beam we get as output has a diameter of around 9 mm ($1/e^2$). Figure 2.4 depicts the Libra assembly's optical architecture. It is primarily made up of four modules: (i) a Vitesse (Oscillator) seed laser; (ii) evolution as a pump laser; (iii) RGA; and (iv) a compressor followed by a stretcher portion merged and placed in a single box.

2.3.1. Vitesse (Oscillator)

According to European community standards EN-60825-1, the Vitesse laser is categorized as a Class IV laser. The seed laser (also known as the oscillator) in the Libra system is a Verdi-pumped mode-locked laser that generates sub-100 fs pulses at an 80 MHz repetition rate with an average power greater than 250 mW at 800 nm. At a central wavelength of 800 nm, it provides a bandwidth of between 30 and 100 nm. Figure 2.5 illustrates the components of the Vitesse laser: (1) Verdi laser (2) Verdi Pumped Ultra-Fast (VPUF) laser (3) power track mirror. To reduce environmental contamination, each component is enclosed in isolation.

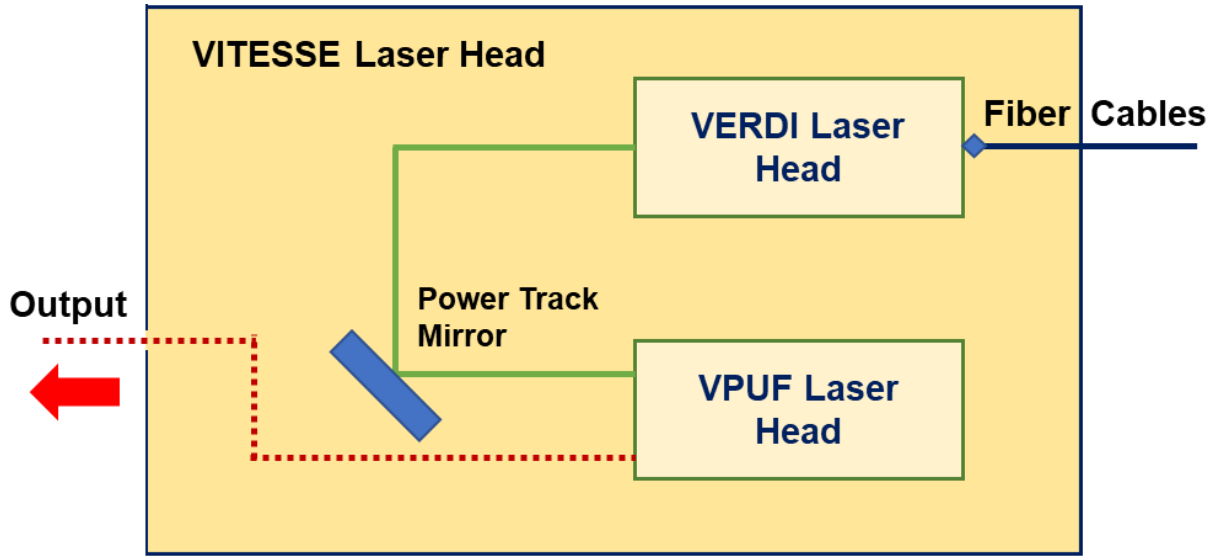

Figure 2. 5 Layout of the Vitesse laser.

For the Vitesse laser, the Verdi laser serves as a pump laser. As shown in figure 2.6 (a), it is composed of Nd: YVO4 (Vanadate) gain material that is pumped using two diodes (5 Watt) lasers, delivering a continuous laser of 1064 nm with 2 W average power. The output of the diode lasers (808 nm wavelength) is linked to the Verdi using cables made of optical fiber after being installed in the Vitesse laser head. The main optical components of the Verdi laser are lithium triborate (also known as LiB_3O_5 or LBO), a frequency filtering etalon, two end mirrors, a stigmatic compensator, two pump mirrors, and an optical diode. The pump laser is positioned into the cavity of the VPUF laser head using a piezo-driven mirror. A negative

dispersion mirror (NDM) and a gain medium (Ti: Sapphire crystal) make up the VPUF laser head. The 532 nm Verdi laser output pumps the gain medium (Ti: Sapphire crystal) within the VPUF laser head. Figure 2.6 (b) illustrates how negative dispersion mirrors (NDMs), which provide the negative dispersion and repeated reflections from NDMs to correct the ND, are required to create pulses that last for around 100 fs. A passive mode-locking technique, Kerr-lens Mode locking (KLM), was used to achieve ML in Vitesse. As a result, low-noise ultrashort pulses with a repetition rate of 80 MHz, a bandwidth of 35 nm, and a mean power of about 300 mW are generated.

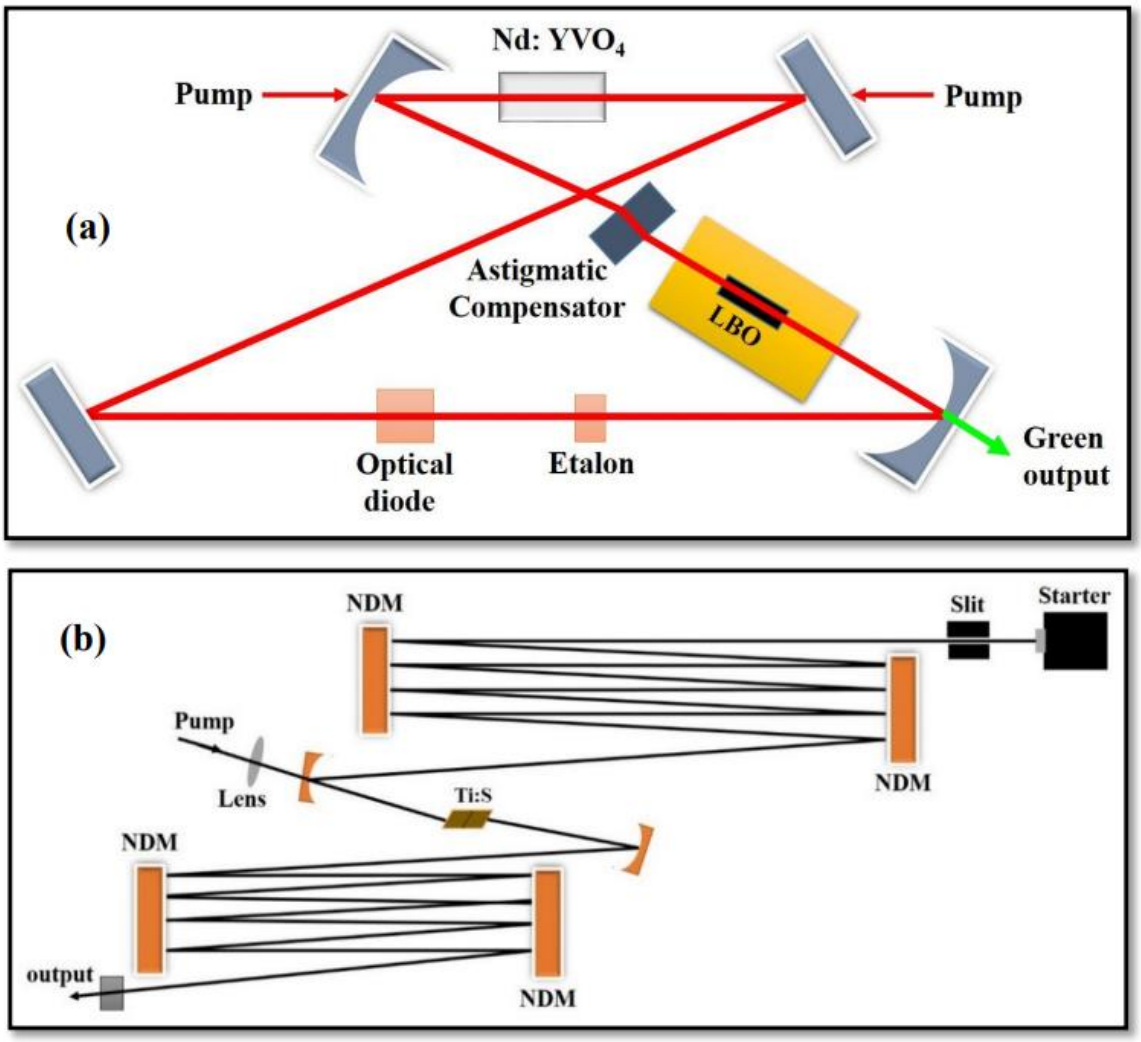

Figure 2. 6 Internal schematic layouts of (a) Vitesse seed laser and (b) Verdi laser layouts. Image adapted from Ref. [11].

2.3.2 Evolution-HE (Pump laser):

Evolution-HE is a diode-pumped, Q-switched Nd: YLiF4, yttrium lithium fluoride (Nd: YLF), a laser that generates a pulse of energy >45 mJ at 1 kHz and 45 W of average output. It runs at a wavelength of 527 nm, the second harmonic from 1053 nm, and is perfect for pumping extremely rapid, high-power titanium sapphire amplifiers. With the Evolution-HE, you get a very effective and high-quality beam. Which consists mostly of four components (a) electrical, optomechanical, and cooling components are included in the optical laser bench assembly, along with (b) a closed-loop chiller, (c) a power supply to operate the laser diodes and keep the LBO crystal at the proper temperature, and (d) computer control. Table (2.1) contains the specs for the LIBRA and Vitesse oscillators.

Table 2.1 Specifications of Vitesse and LIBRA systems

S. No.	Parameters	Vitesse oscillator	Libra fs amplifier
1	Average power	300 mW @ 2 W Verdi	4 W
2	Pulse duration	<100 fs	~35 fs
3	Bandwidth	~25 nm	~30 nm
4	Max output energy	~3-5 nJ	~4 mJ
5	Repetition rate	~80 MHz	1 kHz
6	Beam diameter	~1.25 mm	~9 mm
7	Polarisation	Horizontal	Horizontal

2.4 Optical Parametric Amplification (OPA)

OPA is a well-known nonlinear optical (NLO) mechanism that occurs in second-order nonlinear substances and involves energy exchange from higher to lower-frequency pump beams. Another beam, known as the idler, is formed during energy transfer. [12,13] The energy conversion formula for higher pump frequency is $\omega_P + \omega_S = \omega_I$. OPA is frequently followed by optical parametric generation (OPG). One light beam at a frequency ω_P serves as the input for OPG, while two beams at frequencies ω_S and ω_I serve as the output. Phase-

matching establishes the output beams' wavelength. After OPG, the generated beams are often dispersed in a direction and are fairly weak. OPA is used as a second step to resolve this problem; with OPA, two input beams of frequency ω_P and ω_S are used, as illustrated in Figure 2.7, adapted from the report of [14]. As a result, the OPA weakens the pump beam (ω_P) to strengthen the signal beam (ω_S). It also creates an additional beam at a frequency (ω_I) known as the idler frequency.

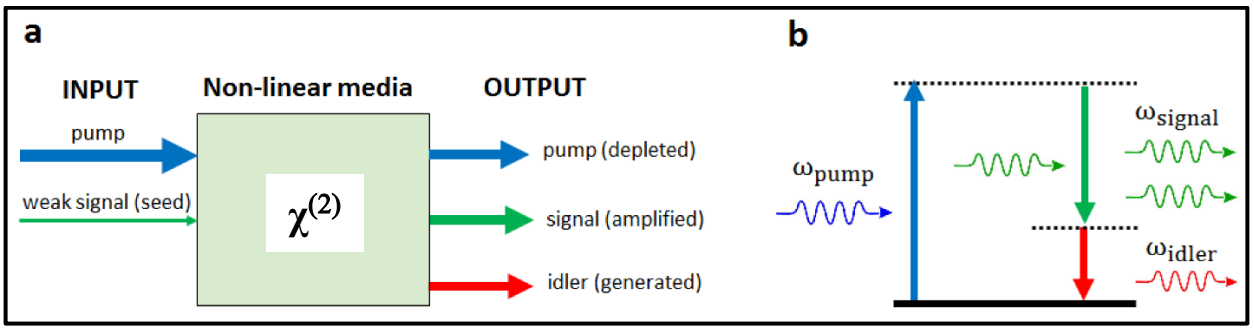

Figure 2. 7 The flow of pump energy to the signal beam in OPA (b) stimulated the emission of signal photons from the virtual level created by the pump beam. Image adapted from Ref. [14].

2.4.1 TOPAS-C

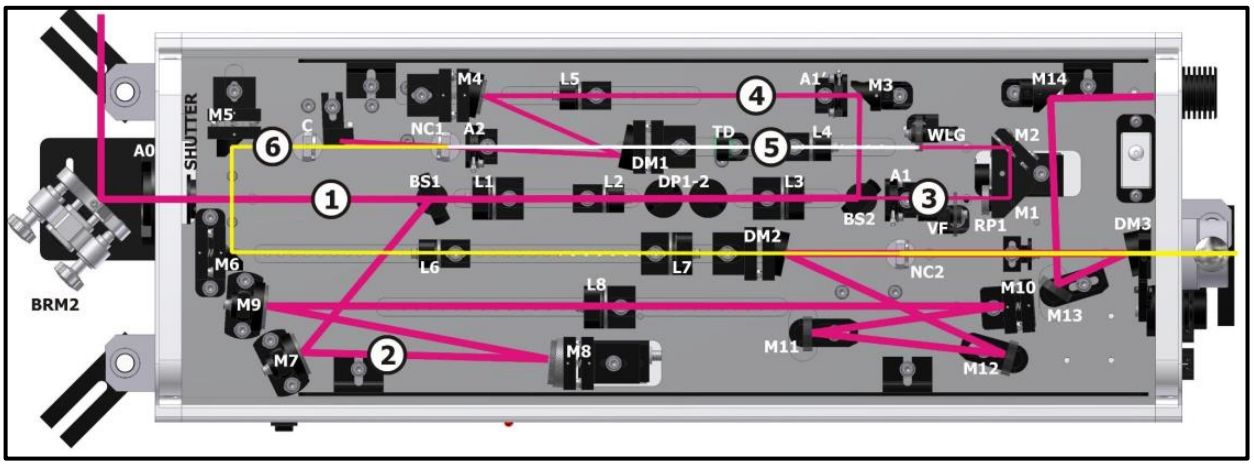

Figure 2. 8 Optical layout of the TOPAS-C. (Image adapted from TOPAS – C, Light Conversion Manual)

The output of LIBRA at 800 nm pumps a two-stage amplifier called TOPAS (Traveling Wave Optical Parametric Amplifier). With further frequency mixers, this offers a wavelength range of 1100 nm–1600 nm, which may be expanded to 260 nm–2600 nm. Its fundamental configuration comprises numerous subunits, including a power amplifier (PA2), a pre-

amplifier (PA1) stage, a signal beam collimator and expander (SE), and a pump beam guiding and white light continuum generating (WLC) component. All of these components are organized into a single, small unit. A program accurately controls every element of this device, like the mirrors, translation stages, rotation of the crystals, and tuning of the output wavelength offered by WinTopas, Ultrafast Systems, USA. Figure 2.8 illustrates the TOPAS-C's entire configuration. A sapphire plate creates WLC utilizing a modest portion of the input pump beam (1.3 μJ, from BS1) at 800 nm wavelength. The pre-amplifier crystal (NC1), where the parametric amplification happens, receives the other portion of the pump beam at 800 nm (30–50 J) and WLC by non-collinear collimation. Non-collinear geometry makes distinguishing amplified signals from the residual idler and pumped beams simple. Following the pre-amplification (PA1) of the signal, a telescopic lens collimates the beam before it is translated to the power-amplification (PA2) step. The residual high-energy pumping beam is further collimated to the power amplification stage. A second nonlinear crystal (NC2) is collinearly mixed with the amplified signal and a high-power pump beam. As a result, signal beams and well-collimated collinear idler are produced by the TOPAS-C. The TOPAS output can be utilized with the supplementary frequency mixer to increase the tuning spectrum from UV to NIR. By modifying the angle of the crystal for ideal phase-matching and changing the delay between the WLC and the first pump beam, the wavelength tuning in the PA1 stage may be accomplished. Additionally, the second crystal angle and the time delay between the amplified signal and the second pump beam are modified after optimizing the wavelength at the PA1 step. WinTOPAS is a specialized computer program that can alter the wavelength.

2.5 Characterization of Ultrashort Pulses

Due to the short reaction times of electrical equipment, measuring ultrafast pulses with a duration of less than 20 ps is challenging. Numerous methods, namely intensity autocorrelation [1] and frequency-resolved optical gating (FROG) were found. The intensity autocorrelation approach is one of the most used methods for determining the pulse width of fast pulses. However, we do not know the phases of using this technique. It is the pulse that is utilized for time-domain self-measurement.

2.5.1 Single shot autocorrelator (SSA) for pulse-width measurements

An exhaustive description of ultrashort pulses may be obtained from single-shot autocorrelator (SSA, coherent M/S) data. The input wavelength of 800 nm (the output of the LIBRA amplifier) is split into two halves within the SSA. It overlaps non-collinearly onto a nonlinear crystal called KDP (potassium dihydrogen phosphate). The second harmonic pulse experiences a space-dependent time delay due to the comparative tilt of the wavefront, which produces autocorrelation in the ultrafast pulse's time variable intensity profile. The autocorrelation pulse is often monitored using a CCD array coupled to an oscilloscope (Tektronix 1320B), as shown in Figure 2.9, which illustrates the optical configuration of SSA. A configurable delay line is supplied to guarantee that the input pulses overlap spatially.

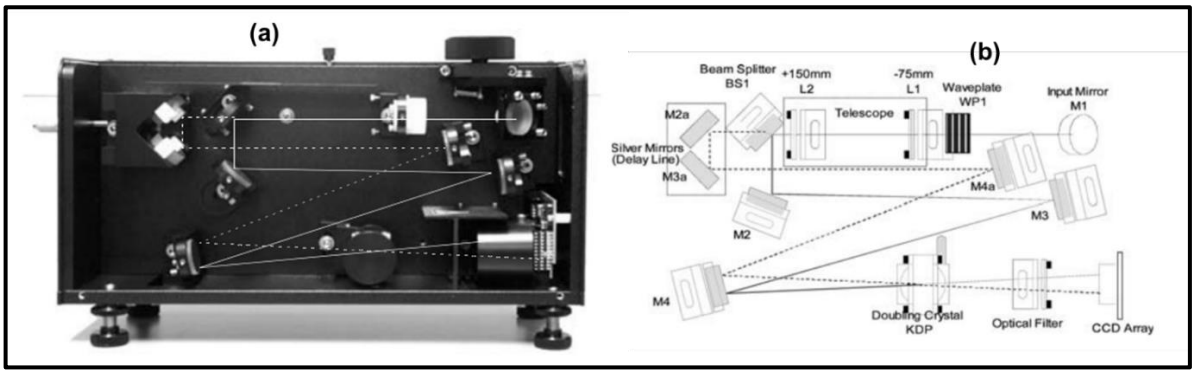

Figure 2. 9 Optical layout of the single-shot autocorrelator. (a) optical path inside the SSA (b) schematic of the optical components inside (Image adapted from Coherent, Single Shot Autocorrelation manual).

The oscilloscope-recoded SSA signal, the second harmonic (SH) beam intensity, produced at the greatest overlap among two pulses in KDP is displayed in Figure 2.10. We can see the full calculation [15,16] of pulse duration below,

The FWHM of the SSA signal is $\approx 2.34\times10^{-4} \approx 0.234$ ms

Delay stage movement = 0.04 mm, Optical path length = 0.08 mm

Change in optical delay = 0.08 mm / 3×10^{8} m/s = 266 fs

Amount of peak shift in oscilloscope ≈ 550 μs

Calibration = 266 fs /550 μs = 0.483 fs/μs

So, the actual pulse duration, Gaussian waveform, is to be found as

= (0.483 fs/μs × 0.234 ms) / √2 = 113/√2 = 79 fs.

Temporal broadening is the reason why there is a difference between the observed pulse length (79 fs) and the given pulse length (50 fs), and this temporal broadening [17,18] is due to the travelling of the input laser pulse through the dispersive medium like KDP and ND filters.

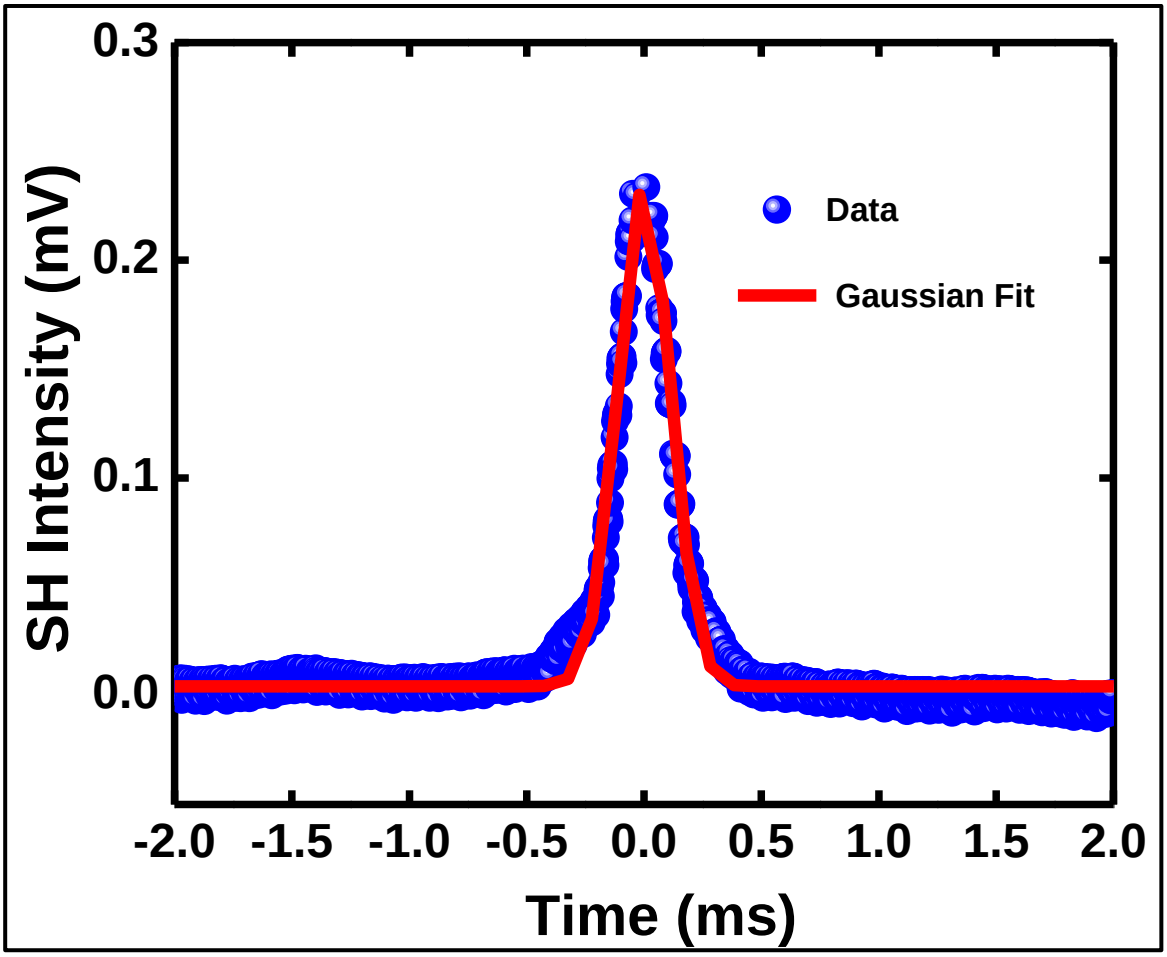

Figure 2. 10 SSA signal of the femtosecond pulses from the oscilloscope.

2.6 Femtosecond laser ablation experimental details

Figure 2.11 shows the arrangement to produce nanostructure and nanoparticles using the fs laser ablation [19] system. A Ti: Sapphire fs laser having a pulse length of 50 fs and peak wavelength of 800 nm is used to produce nanoparticles (NPs). Therefore, the amplifier produced a mean output of power 4 W. The energy of the input pulse was adjusted by passing

the laser beam across a half-wave plate (H) and a Brewster polarizer (B). The half-wave plate, which was placed in a revolving polarizer holder, is essentially a polarization rotator. We can adjust the intensity ratio (I/I_0) by adjusting the half-wave plate, according to Malus law intensity $I=I_0 \cos 2\theta$. Again, the Brewster's polarizer is kept at Brewster's angle so that it reflects only s-polarized light and transmits p-polarized light when a beam passes through it. Three mirrors, M1, M2, M3, and M4, were utilized to direct the polarized beam according to the required pulse energy. The laser beam was focused on the sample using an axicon lens and plano-convex lens. We also produced NPs through axicon-generated fs BB ablation in liquid. A Vortex phase plate was also used in another configuration. Observing the strong plasma plume and hearing the sound it created changed the focus on the sample's surface. An X-Y stage controlled by a computer was used to scan the target/beaker. Sample movement was often employed to prevent ablation on a single point and produce various morphologies. The produced NPs/NSs were stored for further use following the ablation. Figure 2.11 (a) shows a laboratory setup of laser ablation in the air (LAA) using an axicon lens, generating a Bessel beam. Figure 2.11 (b) displays laser ablation in a liquid (LAL) setup using an axicon lens. Figure 2.11 (c) depicts a laser ablation in the air (LAA) setup using the conventional plano-convex lens, generating a Gaussian beam. Also, in Figure 2.11 (d), an LAA setup engages a vortex beam generated using a phase plate and a conventional plano-convex lens.

2.6.1 Axicon lens for the generation of fs Bessel beam

An axicon lens has been used in this work to transform a Gaussian beam into a zeroth-order Bessel beam. An axicon, or rotationally symmetric prism, is a lens with a conical and flat surface. They often generate a beam exhibiting a Bessel intensity profile or a conical, non-diverging beam. Position the plano side of the axicon towards the collimated source to transform a collimated beam into a ring. The axicon lens utilized in this thesis work has the following specifications: a diameter of 1/2" (Ø12.7 mm), a physical angle (α) of 10^0, a deflection angle (β) of 4.6°, a center thickness (t_c) of 6.1 mm, an edge thickness (t_e) of 5 mm, a substrate material made of UV fused silica, an operation wavelength range of 650 - 1050 nm. The specific details of the axicon lens have been mentioned in Table 2.2.

Table 2.2: Various parameters about the Axicon lens mentioned on Thorlab's official website

Substrate Material	UV Fused Silica
Diameter	1/2" (12.7 mm) or 1" (25.4 mm)
Diameter Tolerance	+0.0 / -0.1 mm
Apex Rounding Diameter (S1)	<1.5 mm
Surface Quality (S1, S2)	40-20 Scratch-Dig
Surface Flatness (S2)	<λ/10 at 633 nm
Surface Deviation (RMS) (S1)	<0.05 µm
Surface Roughness (RMS) (S1)	<6 Å
Clear Aperture (S1, S2)	>90% of Diameter
Edge Thickness	5.0 mm
Edge Thickness Tolerance	+0.1/-0.0 mm
Center Thickness Tolerance	+0.1/-0.0 mm
Angular Tolerance	±0.01°

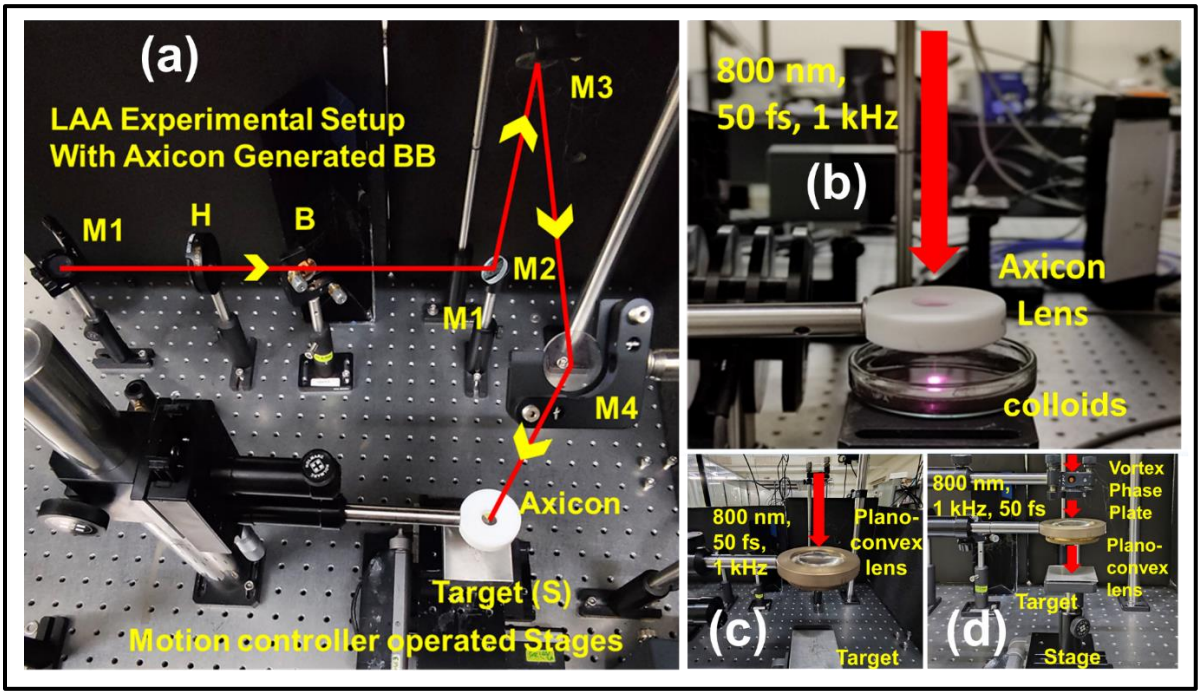

Figure 2. 11 Photographs of (a) laboratory setup of laser ablation in air (LAA) setup using axicon lens, generating Bessel beam (b) laser ablation in liquid (LAL) setup using axicon lens (c) laser ablation in air (LAA) setup using conventional plano-convex lens, generating Gaussian beam (d) LAA setup engaging a vortex beam, generated using a phase plate along with conventional plano-convex lens.

2.6.2 Optical Vortex Phase Plate (OVPP) for the generation of fs Vortex beam

The optical Vortex phase plate (OVPP) transforms a Gaussian laser beam into a donut-shaped energy ring. The optical Vortex phase plate is a distinctive optical device comprising a helix or spiral phase steps. Its main function is to regulate the phase of the transmitted beam. The overall depth of the etching, measured from the highest point to the lowest point of the "staircase" structure, depends on the design's wavelength and the substrate's refractive index. Typically, this depth is about equal to the design wavelength. Consequently, every optical Vortex phase plate is particular to a certain wavelength. The topological charge, often represented as m in the literature, quantifies the number of 2π cycles ("staircases") that encircle a 360-degree rotation of a diffractive surface. A single "staircase" cycle encompasses a complete 360° surface rotation, resulting in a value of m=1 for the vortex phase plate. An elevated topological charge leads to a proportional augmentation in the angular momentum of the vortex beam with a factor of m. We have used a vortex phase plate to transform a Gaussian input profile into a toroidal energy distribution with no energy at the centre. Its primary function is to regulate the beam's phase that passes through it. The phase plate has the following specifications: serial number VL-209-800-Y-A, a compatible wavelength of 800 nm, a topological charge of 1, AR coating, and a thickness of 3 mm. The material utilized is Fused Silica, and the element size was 25.4 mm.

2.7 Characterization & Measurement Techniques Involving Nanoentities

Various approaches are available to describe the NPs or provide direct proof that they are present in the produced sample. UV-visible absorption spectroscopy is a quick and simple method to establish if nanoparticles are present in a liquid media. NP may be analyzed for size and form using electron microscopes, such as FESEM and TEM. This section summarizes the fundamental ideas behind the methods utilized in this thesis to characterize artificially produced NPs.

2.7.1 UV-Visible absorption

The most straightforward and rapid technique to confirm the presence of nanoparticles (NPs) in a liquid media and the concentration of an element in the fluid is absorption spectroscopy.

This method does not use just one particle. It offers the standard absorption of NPs [20] dissolved in the liquid. UV-visible absorption spectroscopy gives us the wavelength of absorbed light by the nanoparticles [21]. With two cuvettes made of a quartz path length of about one centimetre, the Perkin Elmer Lambda 750 UV-visible absorption spectrometer was utilized to collect the UV-visible absorption spectra for this study. Three millilitres of liquid were utilized for the experiments.

Instrumentation:

(a) A Tungsten-halogen lamp produces radiation of 375 nm to 3300 nm, and a Deuterium lamp gives radiation of 165 nm to 375 nm. These two lamps were used to power the UV-visible spectrometer.

(b) The monochromator creates one wavelength from the light source's vast spectrum, which is subsequently distributed by spinning prisms and chosen by the slits. It makes straightforward data recording possible by offering a continuous wavelength increase. The beam splits into a pair of beams of the same intensity.

(c) A single segmented beam traverses the sample cell that holds nanoparticles colloidal solution.

(d) The other goes via a reference cell made of solvent. Because glass cuvettes absorb UV light, they are not useful for some measurements. Typically, quartz or silica cuvettes are employed to gather sample data. To detect it, we used a series of photodiodes and photomultipliers.

(e) These transform the incoming light into electricity; a greater current corresponds to a perceived intensity. The measurement of light intensity was done concerning wavelength for both the reference material and sample [21].

A solution within a cuvette is exposed to a light beam with wavelengths ranging from UV to near-infrared. Transmission of the radiation by the sample in the cuvette depends on how much of the radiation is absorbed. The transmittance of the specimen (T) is the percentage of photons that flow through it relative to the incoming photon count. Beer-Lambert's law [22,23] $A = \log(T) = -\log\left(\frac{I_0}{I_T}\right)$ is used to calculate the quantity of light absorbed as it passes through the specimen. Here, I_0 = intensity of incoming light and I_T = intensity of transmission.

2.7.2 X-ray diffraction

A popular method for determining atomic spacing and crystalline structures is X-ray diffraction (XRD) [24]. X-rays are diffracted by the crystalline planes, and this diffraction is governed by Bragg's condition, which is as $2d \times \sin\theta = n\lambda$, where n is diffraction order, d is interplanar spacing, λ is the wavelength of the incident ray, θ is the angle of incidence. A secondary spherical wavefront is produced when the X-ray interacts with the crystal's atoms, forming the diffraction pattern. Acquiring all conceivable lattice diffraction directions is feasible by changing the incidence angle θ across a large range. It is possible to identify various crystal structures by comparing them to the common reference patterns. The intensity of the scattered X-rays is measured vs the angle to determine the X-ray diffraction image. It is a widely used characterization technique for determining the chemical composition, particle size, and lattice stresses caused by flaws, alloying, doping, and other sample factors. Specific peaks are produced by each metal nanostructure based on the atom kind or lattice constant. On the other hand, the peak of XRD in alloy-type nanoscale structures varies based on the amount of every metal atom. Cu K_α 1.54 Å radiation was used in this XRD measurement of the thesis work, which was done on the materials using a BRUKER D8 X-ray diffractometer with an accuracy of 8×10^{-3} degrees. Thick layers of all the synthesized nanoparticle solutions were created using a straightforward drop-casting technique and then deposited on a glass slide or Si. After the sample was dried, the XRD patterns were recorded. The sample's peaks were determined by analysis utilizing the Joint Committee on Powder Diffraction Standards (JCPDS) data. [24]

2.7.3 Transmission Electron Microscopy (TEM)

Similar in operation to an optical microscope, a transmission electron microscope (TEM) [25] employs electrons rather than photons or light. Because electrons have a considerably smaller wavelength than photons, TEM pictures may achieve resolutions of several orders of magnitude greater than those from optical microscopes. Using an electromagnetic lens (condenser aperture, objective aperture), the electron source's stream of high energy electrons—typically a tungsten filament producing thermionic emission - is directed toward the object being examined within an elevated vacuum. Information is carried by the electron beam when it enters the object being studied and strikes the fluorescent screen. The sample's

various portions are shown in the contrast of colours in a shadow picture created by differences in density within the sample locations. The TEM picture has a resolution of a few nm. As such, it can make NPs visible for analysis of their size, shape, distribution, etc. Additionally, it offers the selected area electron diffraction (SAED) pattern [25] derived from the energy of electron and X-ray examination. From the atomic plane, electron beams diffracted when Bragg's condition was filled. There, we observe a ring pattern of concentric rings, and the spacing of the lattice plane of the material is described by the diameter of each ring. A JEM-F200 multi-purpose electron microscope (JEOL) operated at an accelerating voltage of 200 kV was used in the present work to take TEM observations for the produced NPs; a picture of the instrument is included in Figure 2.12. To create the TEM samples, a copper grid covered with copper is coated with 5 µl of nanoparticle suspension, which is then allowed to dry at room temperature. The TEM micrographs were analyzed using the openly available Image-J program. The average diameter of the collected nanoparticles was usually determined using more than 250 nanoparticles. The Gaussian curve of the acquired data was used to determine the average size and the size distribution. The crystal planes and structure were examined using high-resolution TEM (HRTEM) and SAED structures.

2.7.4 Field Emission Scanning Electron Microscope (FESEM)

Using a focused high-intensity electron beam, the FESEM [demonstrated in Figure 2.13] creates a picture of the specimen by scanning its surface [26]. The taken samples are put in a sample container and sealed in a vacuum system to prevent the electrons from colliding with the gas molecules. The beam of electrons is produced by the field emission electron cannon. The electron beam was focused on the sample by the lens (electromagnetic and electrostatic lens). The sample's atoms' valance/conduction band is where the secondary electrons are expelled from. The detectors pick up on all of these, creating a digital picture in the form of an electrical signal. The in-lens sensor provides a high-resolution picture at extremely low accelerating potential within its electron section. Low-resolution pictures at high accelerating

potentials are obtained using an additional electron detector (secondary electron detector SE2), and the backscattered electrons are the primary electrons that have deviated due to their contact with the nuclei. A detector of backscattered electrons produces a greater contrast in atomic number. Generally speaking, heavier elements look brighter than lighter ones because they have larger nuclei, which aggressively deflect electrons. The electron is ejected from the inner shell of the atom of the sample and creates an electron hole. This ejection is due to an incident of the high-energy beam on the sample's surface. The hole created in the inner shell is then filled by an electron from an outer shell with greater energy. An X-ray is released due to the difference in energy between higher and lower energy levels. [26]

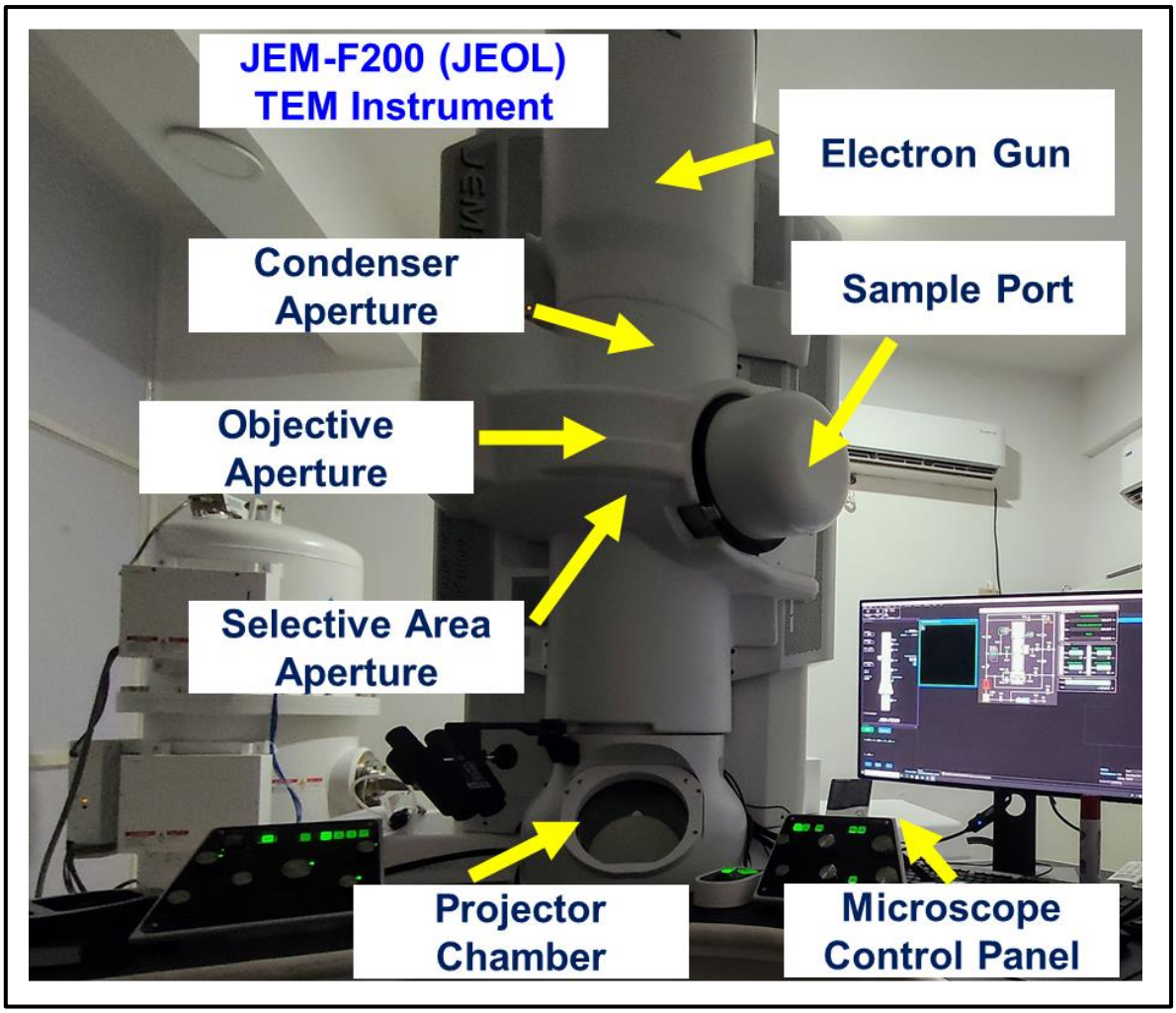

Figure 2. 12 A photograph of the TEM is available at the School of Chemistry, University of Hyderabad.

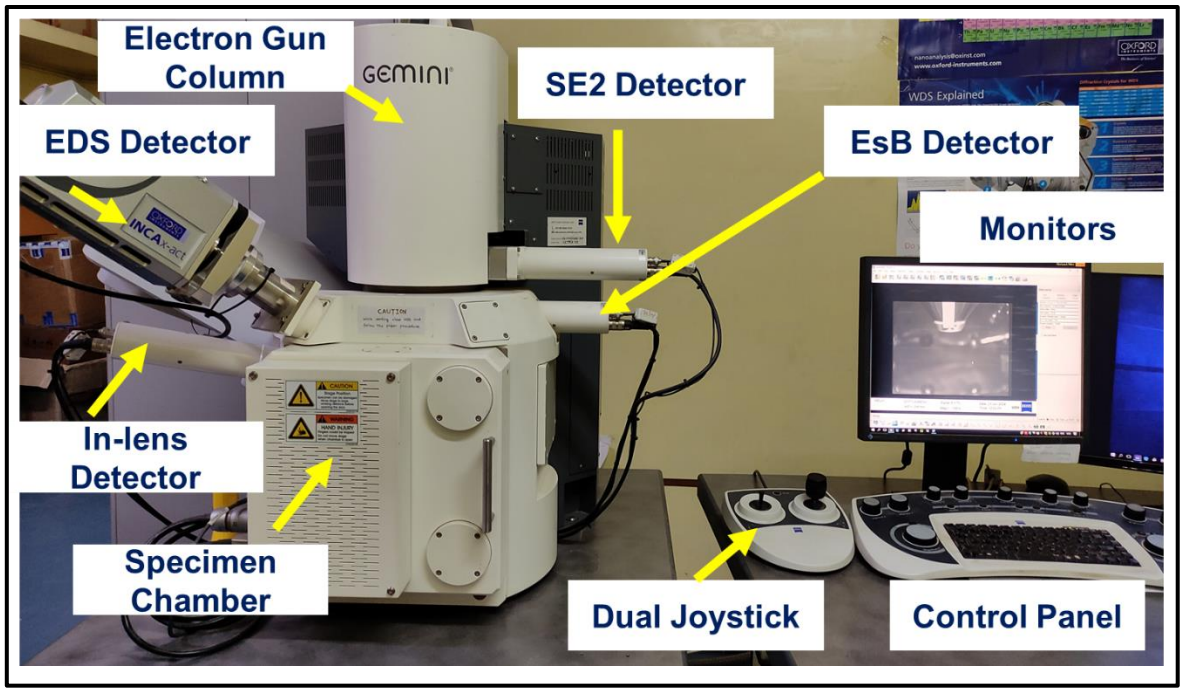

Figure 2. 13 A photograph of the FESEM is available at the School of Physics, University of Hyderabad.

The EDS detector can measure the quantity and energy of X-rays generated from the materials. Every element has a different atomic structure, which results in a distinct set of spikes on its electromagnetic radiation spectrum. This study uses an Energy Dispersive Spectrometer (EDS) connected to an Ultra 55 field emission scanning electron microscope (FESEM) from Carl ZEISS that operates at 30 kV.

2.7.5 Atomic Force Microscopy (AFM)

AFM, or atomic force microscopy, was created by Binnig et al. in 1986 [27]. It is based on precisely measuring the Vander Waals forces between the surface being studied and a delicate cantilever utilizing mechanical means. A delicate cantilever bends due to repulsive interactions between the atoms at the tip of the cantilever and the atoms on a target surface. A laser beam is used to quantify the deflection during the scanning process. The piezoelectric translator scans the sample in three directions: X, Y, and Z. The computer system, which also captures the signal of the reflected laser beam, governs the translations of XYZ. A computer algorithm will generate a topographic representation of the sample. An external piezoelectric device is used to stimulate the oscillating cantilever. A deflection sensor detects the

oscillation. The tip is close to the surface of the sample. The resonance frequency experiences a little change due to the limited contact between the sample and the tip. Using a negative feedback circuit, the controller unit induces oscillation in the cantilever at its resonance frequency and with a predetermined amplitude. Subsequently, the frequency is converted into an analog signal, used in the same way a scanning tunneling microscopy utilizes the tunneling current. A picture of the topography is produced with a constant force. Improved picture quality may be largely accomplished via contact, non-contact, and tapping modes.

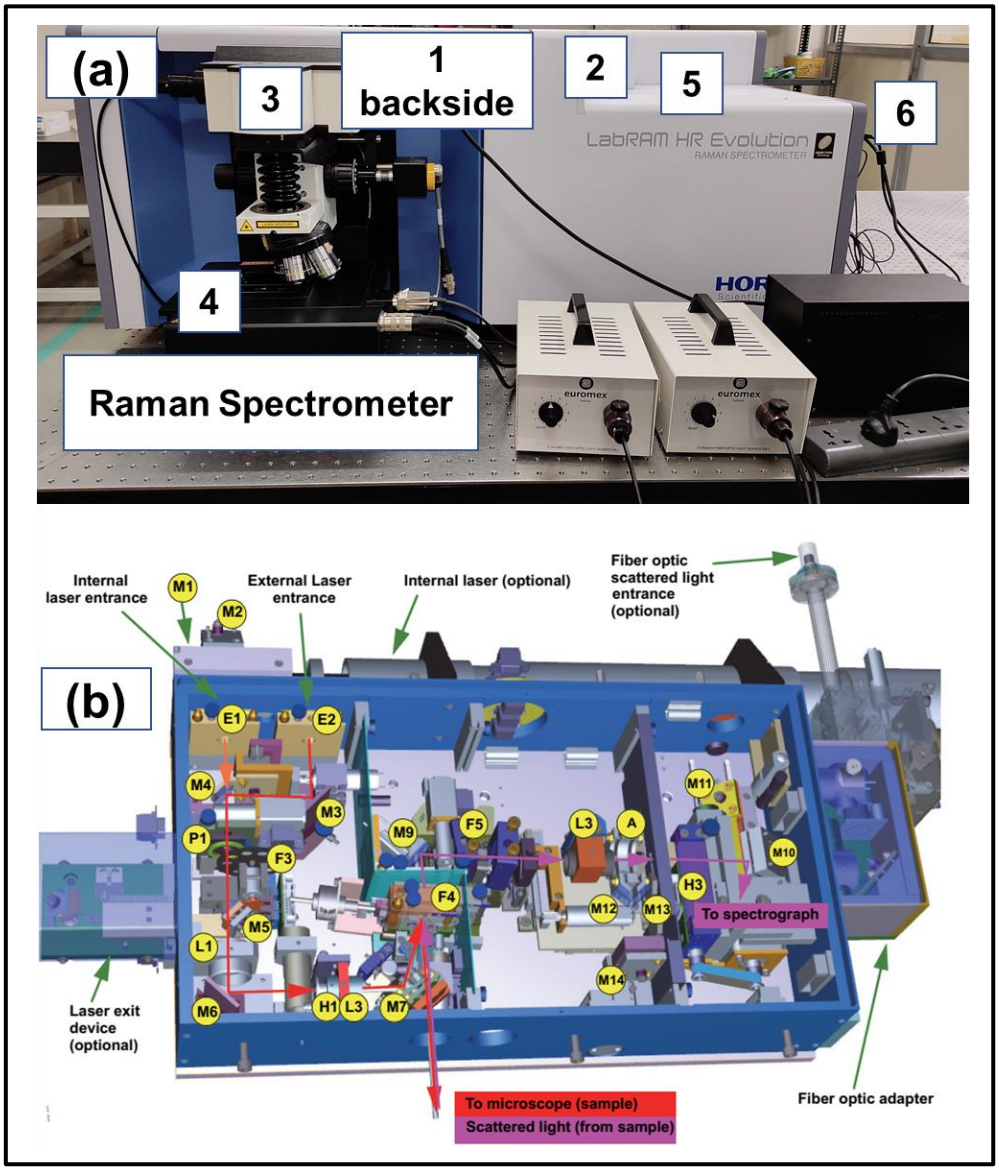

Figure 2. 14 (a) Photograph of the LabRAM HR Evolution Raman spectrometer (available at ACRHEM, University of Hyderabad) (b) Optical path inside LabRAM HR Evolution, image adapted from Horiba Scientific, LabRAM HR evolution user manual.

2.7.6 Horiba μ-Raman spectrometer

Figure 2.14 shows the schematic diagram of the Raman spectrometer's major parts. To prevent mistakes in the Raman shift, it is imperative to utilize (1) lasers with a stable frequency and, a narrow bandwidth is engaged. Subsequently, the spectrometer and low power loss system use (2) mirrors, optics, and filters to direct the laser light. (3) The target area on the object's surface is located using a microscope and a white light (reflection/transmission). Objectives are utilized to gather and direct the specimen's dispersed light onto it. The specimen's dispersed light was gathered in a backscattering pattern. (4) The sample is scanned using an X-Y stage. (5) There are two kinds of scattered light, Rayleigh and Raman scattered light. Rayleigh scattered rays are eliminated by a highly efficient filter, and the Raman scattered light is allowed. This Raman scattered light interacts with grating and disperses the ray. (6) The pixel size of CCD (26 μm × 26 μm) determines the spectral resolution of the CCD detector utilized to gather the Raman photons. Some of the Raman experiments in this article were conducted using the Yvon-Raman spectrometer, LabRAM Horiba HR Evolution Jobin. The system has four different wavelengths as excitation sources: 325 nm, 532 nm, 632 nm, and 785 nm. There are focusing options of 10X, 20X, 50X and 100X. The signal from the grating spectrometer is received by the CCD, having a (1024 × 256) pixel detector. The spectrometer has a resolution of 0.35 cm^{-1}. Before the Raman observations, the spectrometer was tested using a Si wafer (~520 cm^{-1}). In this work, a portable Raman spectrometer was employed for most SERS measurements [28–34], whereas a micro-Raman spectrometer was utilized to investigate the role of nanostructures in the SERS phenomenon.

2.7.7 Portable Raman spectrometer

The materials' Raman spectra were obtained using a portable Raman spectrometer (B&W Tek, i-Raman plus, USA, BWS465-785S), the picture of which is displayed in Figure 2.15(a). A diode laser with a maximal output power of around 300 mW and an output wavelength of 785 nm is included in this spectrometer. A BAC150 Raman probe holder that may be manually adjusted, the sample's data is gathered at different points using XYZ phases. The Raman spectra of liquid samples were obtained using the BCR100A cuvette holder, which has an overall length of 1 cm. The spectrometer had a resolution of ~ 4.5 cm^{-1}.

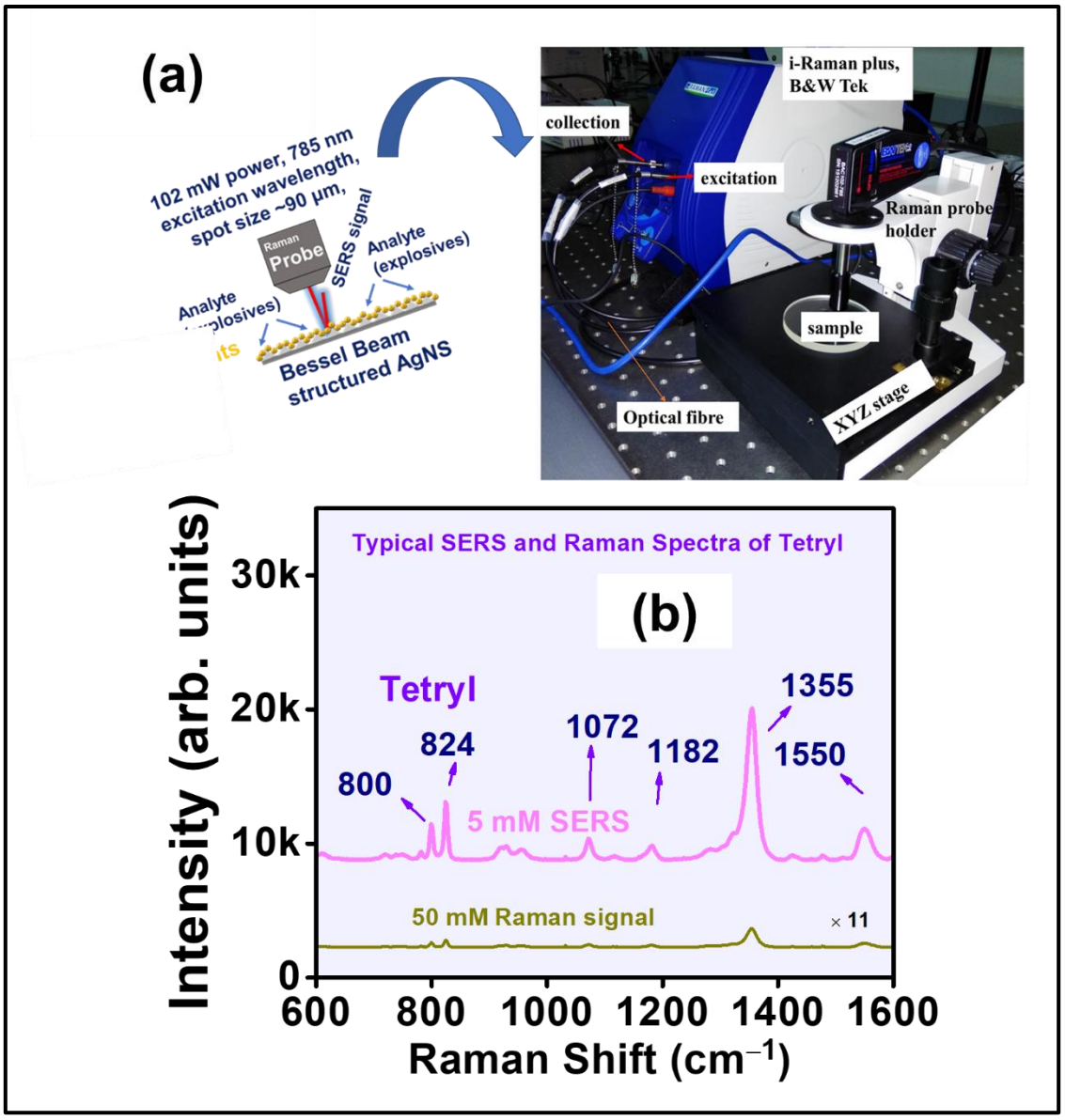

Figure 2. 15 (a) Schematic and photograph of portable Raman spectrometer (available at ACRHEM, University of Hyderabad) (b) large variation in typical SERS and Raman spectra of the Tetryl.

Drop casting is also a significant parameter in the case of SERS measurements. In our studies, we have followed a particular technique to maximize the effectiveness of the drop-casting. We heated the laser-structured NSs, keeping them on the oven plate at 50^0C, and then drop cast our analytes on them. Due to the high temperature, the solvent was observed to evaporate much faster compared to normal conditions. Hence the spreading of our analyte was restrained to a lesser area while forming the coffee ring effect. In these studies, the enhancement factor

(EF) for a molecule has been calculated using the well-established mathematical relation [28–34], i.e.,

$$E.F = \frac{I_{SERS}}{I_{Raman}} \times \frac{C_{HC}}{C_{LC}}$$

The I_{SERS} term represents the heightened intensity of the prominent Raman peak of a specific analyte derived from the structured SERS substrate. The I_{Raman} is the intensity of the same Raman peak obtained from the plain pristine substrate. C_{LC} represents the minimum detectable concentration of the analyte, while C_{HC} represents the maximum concentration of the analyte when measuring the pure Raman signal. The large variation in typical SERS and Raman spectra of the Tetryl compound has been depicted in Figure 2.15(b).

2.8 Optical Nonlinearity Measurement via Z-scan Technique

We used a Ti: sapphire amplifier (Libra, manufactured by Coherent) operating at a repetition rate of 1 kHz, producing pulses with a duration of around 50 fs at a wavelength of 800 nm. A 532 nm nanosecond Nd: YAG laser is used as a pump for the amplifier. An 80 MHz broadband oscillator with a repetition rate of 80 MHz, a pulse duration of ~35 fs at a wavelength of 800 nm, and a bandwidth of around 35 nm is placed as a seed for the amplifier. The laser system produced pulses with a duration of ~50 fs, an energy of around 4 mJ, centered at a wavelength of 800 nm, and a bandwidth (FWHM) of ~28 nm. The repetition rate of the pulses was 1 kHz. To reach the visible and near-IR regions of the electromagnetic spectrum, the use of TOPAS-C, an optical parametric amplifier (OPA), was used to produce pulses with a duration of around 70 femtoseconds. The specimens were positioned on a linear translation stage, and the transmission was captured using a photodiode (Silicon PD, Thorlabs - SM1PD2A (VIS), DET10C/M (NIR)). The photodiode's output was then connected to a lock-in amplifier (signal recovery 7265). The instruments were operated by a custom LabVIEW software. The Z-scan experimental scheme is shown in Figure 2.16. Within the nonlinear optics field, the Z-scan method [35,36] is widely accepted as a standard approach for independently measuring nonlinear absorption (NLA) and refractive index (NLR). It is also used to investigate third-order optical nonlinearity owing to its straightforward procedure and data analysis.

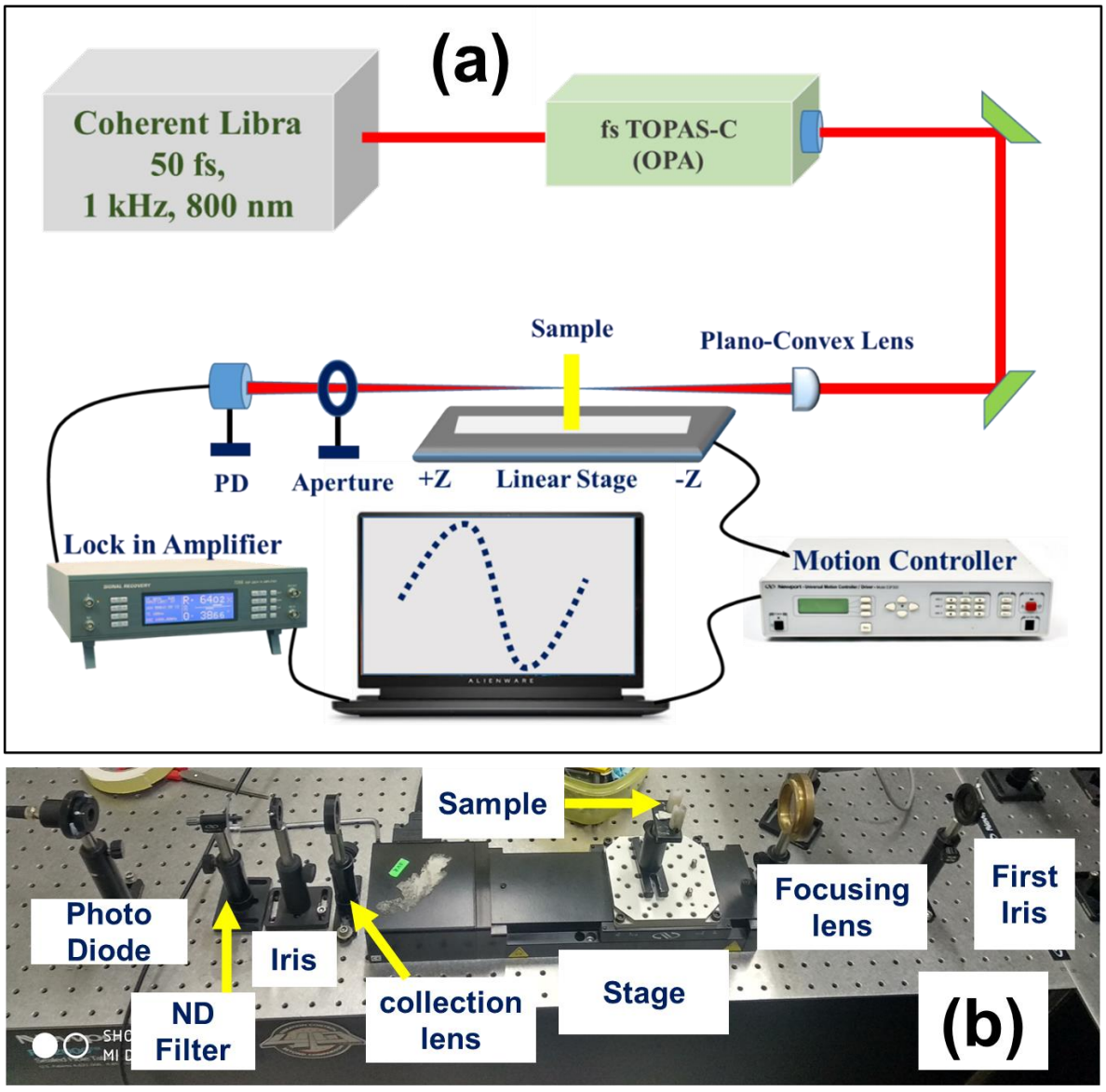

Figure 2. 16 (a) Schematic of the fs Z-scan experimental setup (b) Actual experimental setup of fs Z-scan utilized for the experiment.

2.9 Transient Absorption Spectroscopy

The development of ultrafast tunable lasers has opened up an intriguing new field of study for the molecular analysis of ultrafast occurrences. Using existing techniques, Ultrashort pulse-based spectroscopies have been used to understand previously unreachable charge transfer, structural dynamics, and ultrafast photophysical processes. Transient absorption spectroscopy (TAS) [37–43] is a potent technique for examining their dynamics by tracking the absorbed

energy of photo-excited states. Within TAS, molecules are stimulated to higher excited states by a powerful pump beam of frequency ω_p. A low-energy probe beam observes the pump-induced changes in delay time t (ω_{pr}). Broadband light with a spectral range from UV to NIR is typically used as the probe beam in TAS. It is possible to acquire [ΔA (t, λ)] by obtaining the differential absorption spectra (ΔA) of the excited state and ground state for each probe wavelengths λ and delay time t. The information on the excited state process following photoexcitation, including excited-state energy relaxation, charge transfer, and vibrational relaxation, is contained in the $\Delta A(t, \lambda)$. Investigating the development of the nonradiative process is one of the advantages of absorption spectroscopy over emission spectroscopic methods. Figure 2.17 illustrates the numerous photo-processes contributing to the ΔA (t, λ) spectrum.

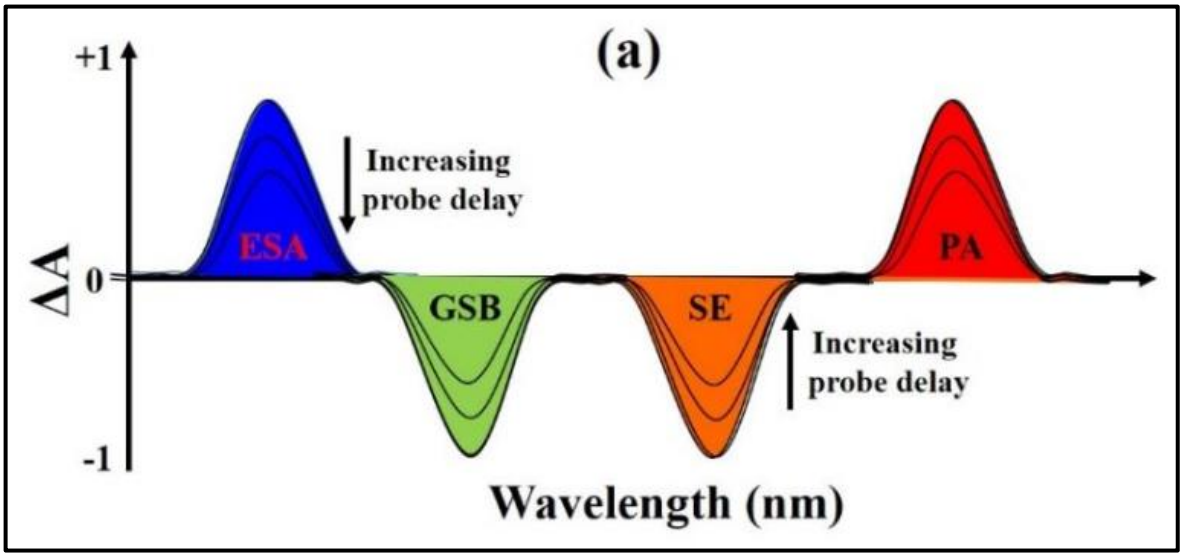

Figure 2. 17 (a) Typical transient absorption spectra (ESA; excited-state absorption, PA; product absorption, GSB; ground state bleach, SE; stimulated emission). Image adapted from Ref. [11]

- Ground state blech (GSB): A portion of the molecules are stimulated to excited states when they are energized by pump pulses. As a result, the quantity of molecules at the ground state is greatly decreased. Consequently, there will be less absorption by the ground state of the excited state sample to a non-excited sample. Consequently, the sample's ground state absorption results in a negative signal in the ΔA spectrum.

- Excited-state absorption (ESA): There is a visible positive signal in the ΔA spectrum when the transmitted probe photons are further absorbed by the excited states and achieve a higher excited state when the pump pulse illuminates.
- Stimulated emission (SE): The Einstein absorption (A_{12}) and emission (A_{21}) coefficients are the same in the case of a two-level laser system. Consequently, when the probe pulse travels across the pumping pulse excited region during pumping pulse illumination, a stimulated emission from an excited state to the ground state occurs. Therefore, In the ΔA spectrum, a negative signal is visible. Only optically permitted states with spectral characteristics similar to the sample of interest's fluorescence spectrum will exhibit SE, meaning that the SE band is displaced concerning the GSB band. This procedure converts the excited state population into the SE photon by a probe pulse. The probing pulse and the SE photon move in the same path; consequently, an enhanced probe beam arrives at the detector.
- Product absorption (PA): Various responses may occur when the sample is photoexcited, primarily in photobiological or photochemical processes. Consequently, molecular states that are either transitory or long-lived will emerge, including isomerized, triplet, and charge-separated forms. In the ΔA spectrum, the absorption outcome will be a positive signal. Furthermore, a ground-state absorption (GSB) signal is observed at the bands where the product state resides on the sample (chromophore).

Given that the third-order nonlinear susceptibility $\chi^{(3)}$ causes a light-matter contact to produce the transitory signal. Cross-phase modulation and coherent artifacts are examples of non-resonant contributions to the ΔA spectrum. By eliminating the early dynamics within the pulse period, these contributions can be eliminated in the data analysis. These inputs to the experiment may be removed from the data by recoding the solvent-only TA spectra. When working with anisotropic substances, the excited entities comply with the polarization of the pumping beam. In this scenario, the population and redirection of the excited state entities will contribute to the probe beam, which can be positioned parallel or orthogonal to the pumping beam. This impact is often eliminated by keeping the so-called "magic angle" between the polarization of the pump and the probe at 54.70^{o}. [44]

2.9.1 Principle

Time-resolved spectroscopy helps us recognize the molecules' dynamical properties by their optical characteristics like absorption and emission. The absorbance of a substance is given by Beer-Lamberts law,

$$A(\lambda) = \varepsilon(\lambda).c.d \tag{8}$$

Where d, c, $\varepsilon(\lambda)$ signifies sample length, molar concentration (in M), and molar extinction (in $M^{-1}\,cm^{-1}$), respectively. For more than one species, the equation becomes,

$$A(\lambda, t) = \sum_i \varepsilon_i(\lambda) \,.\, c_i.d \tag{9}$$

As a result, tracking variations in absorption over time provides information on the species and their dynamic. The sample's absorption differential before (with concentration c_{i0}) and after the absorption, at a certain delay time Δt, is given by,

$$\Delta A(\lambda, \Delta t) = \sum_i \varepsilon_i(\lambda) \,.\, \Delta c_i(\Delta t).d \tag{10}$$

Information about the concentration variations Δc_i provided by the $\Delta A(\lambda, \Delta\ t)$. Response constraints (ns) of traditional electronic devices prevent them from working since the dynamics we seek occur at ultrafast time scales. This condition is broken by the pump-probe technology, which pumps and probes the sample with ultrafast pulses. [38,45] The spectrometer gathers the probe's absorbance at various time intervals. The variation in the absorption spectrum may be obtained by measuring the intensity of the probe before and after pump pulses, which record the absorption change before and after the pump and this differential spectrum is given as,

$$\Delta A(\lambda, \Delta t) = \sum_i \varepsilon_i(\lambda) \,.\, (c_i(\Delta t) - c_{i0})d \tag{11}$$

It includes all the dynamics data for the species found in the sample.

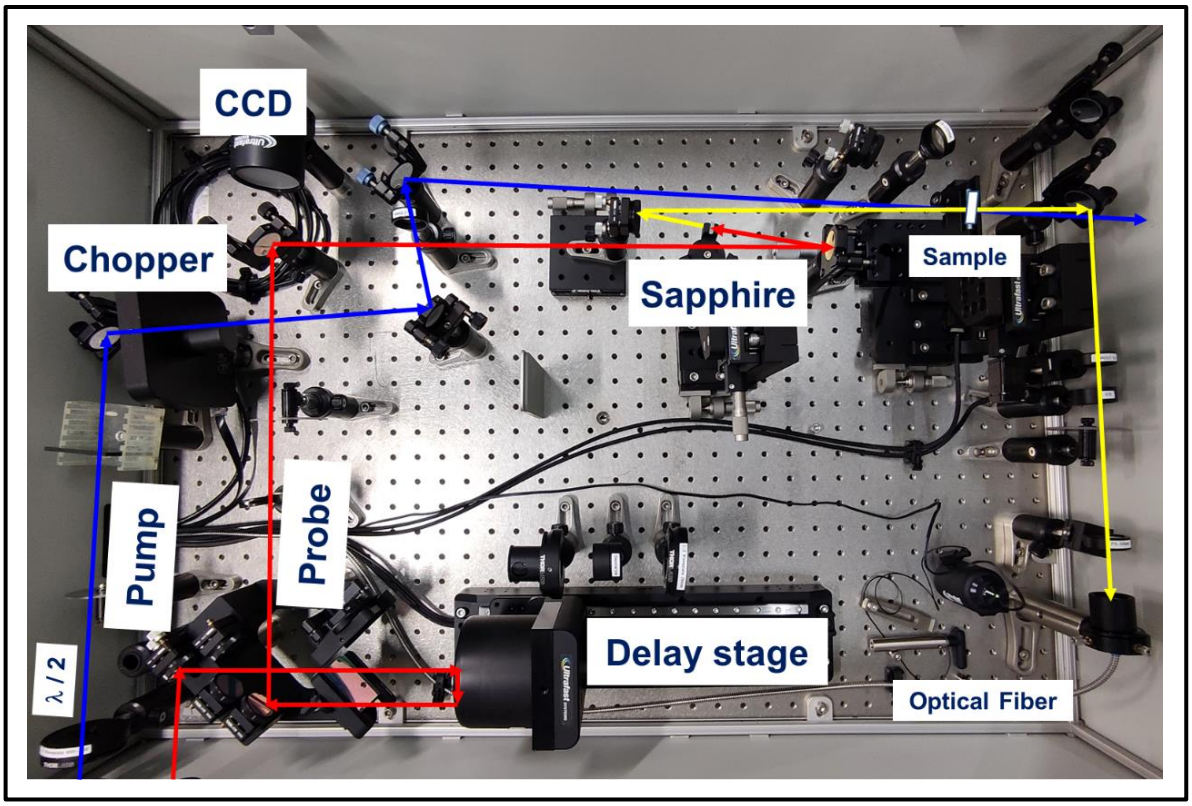

Figure 2. 18 Experimental layout of the HELIOS transient absorption spectrometer.

2.9.2 HELIOS

A broadband transient absorption spectrometer, HELIOS functions on a femtosecond amplifier (LIBRA, Coherent M/S) that provides ~50 fs pulse with a repetition rate of 1 kHz having a wavelength of 800 nm illustrated in Figure 2.18. It includes a PC with the required software and hardware and an optical unit. Two halves are present in the LIBRA amplifier system's output: one portion was used to pump OPA, and the other was used to create a WLC by concentrating on a sapphire crystal (2 mm thick). Five nanoseconds of delay were used to orient the probe beam. A system of parabolic reflectors compressed the probe laser before it reached the sample. The pump laser converged on the specimen (~100 μm diameter), and the sample prevented the pump beam from being transmitted. The pump beam was cut at 500 Hz to improve the signal-to-noise ratio. The following formula is used to gather the transitory data: $\Delta A = \log(I_0/I_{ex})$, here When the pump is incident on the sample, its intensity is represented by I_{ex}, and its probe intensity when it is blocked by the chopper is denoted by I_0. To avoid constant exposure, the specimen was maintained on an XY-motorized platform. A

fiber-coupled spectrometer was used to gather the transmission data of the probe beam. A set of ND filters was available to regulate the power supply of the two lasers before and after the sample. As seen in Figure 2.19, the Surface Xplorer software package, built on a LabView platform, was used for the whole data-gathering process.

Instrument specifications

- Spectral resolution – 1.5 nm
- Time window – 5.5 ns, Probe spectral range – 400 – 800 nm
- Intrinsic temporal resolution – 7 fs
- Laser frequency range – up to 5kHz
- VIS detector – fiber-coupled multi-channel spectrometer with CMOS sensor
- Data acquisition – Surface Xplorer software package

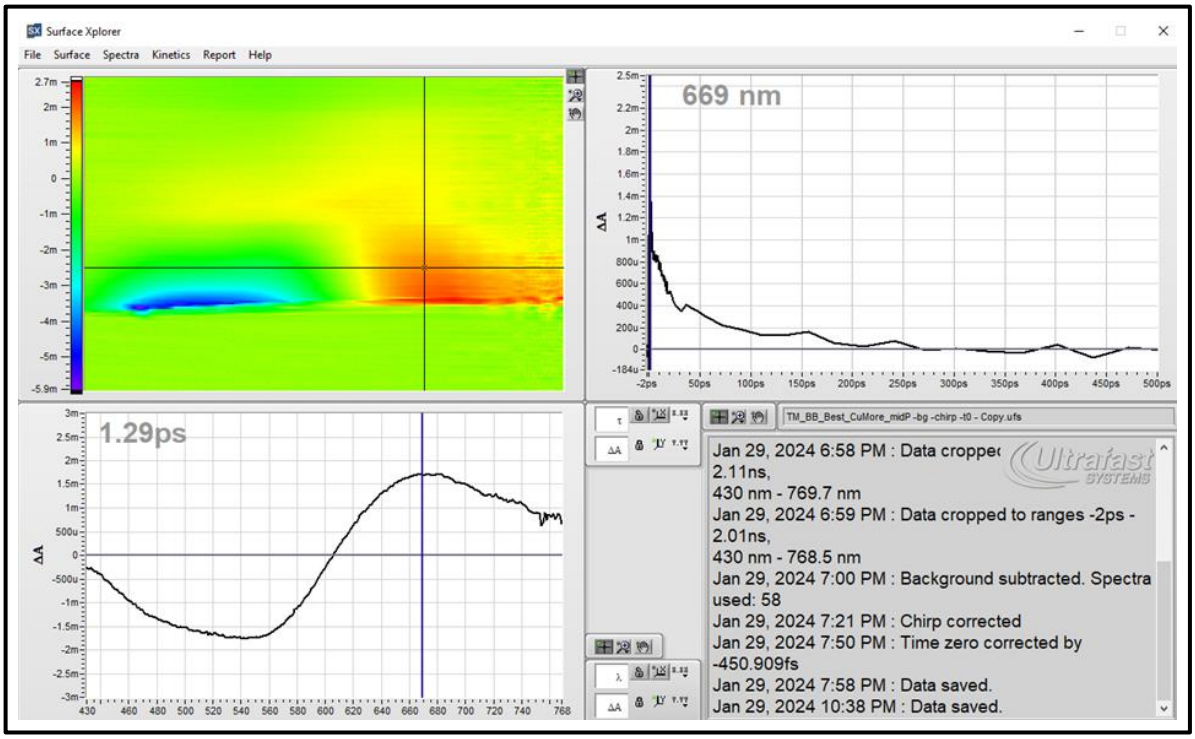

Figure 2. 19 The TAS spectra of Ag-Au-Cu trimetallic alloy NPs visible on Surface Xplorer software graphical layout. The top left panel shows the ΔA(t, λ) surface; it contains several transient spectra at closely spaced probe time delays. The below-left corner shows the transient spectra at successive probe delays. The top right corner displays the individual kinetic profile with a probe delay. The lower right corner contains experimental details during the measurement.

2.9.3 Chirp correction

The white-light continuum (WLC) is chirped throughout the probe pulse-generating process so that distinct probe spectrum components overlap at various sampling times. Consequently, inherent group velocity dispersion (GVD) is present in the WLC [38]. The GVD increases to several picoseconds when the WLC passes through many optics (lenses and cuvettes) before reaching the sample. A pair of parabolic reflectors for the collimation and sample focusing can lessen this. This may also impact the studied sample's assessment of temporary components. A quadratic polynomial function may be used to fit the data and accurately describe this dispersion trend. As seen in Figure 2.20, this may be used to adjust the data acquired numerically. This procedure may be easily carried out using the surface Xplorer program, which fits the selected spots throughout the wavelength range using the following equation $t_0 = a\sqrt{b.\lambda^2 - 1/c.\lambda^2 - 1} + d$, here 'a', 'b', 'c', and 'd' are fitting parameters, t_0 denotes time zero, λ is the wavelength. The data is modified by interpolation of the signal [i. e. $\Delta A_{cor}(\chi, \Delta t_{cor}) = \Delta A(\lambda, \Delta t + \delta t(\lambda))$] for every wavelength at another time $t_{cor} = t+\delta t$.

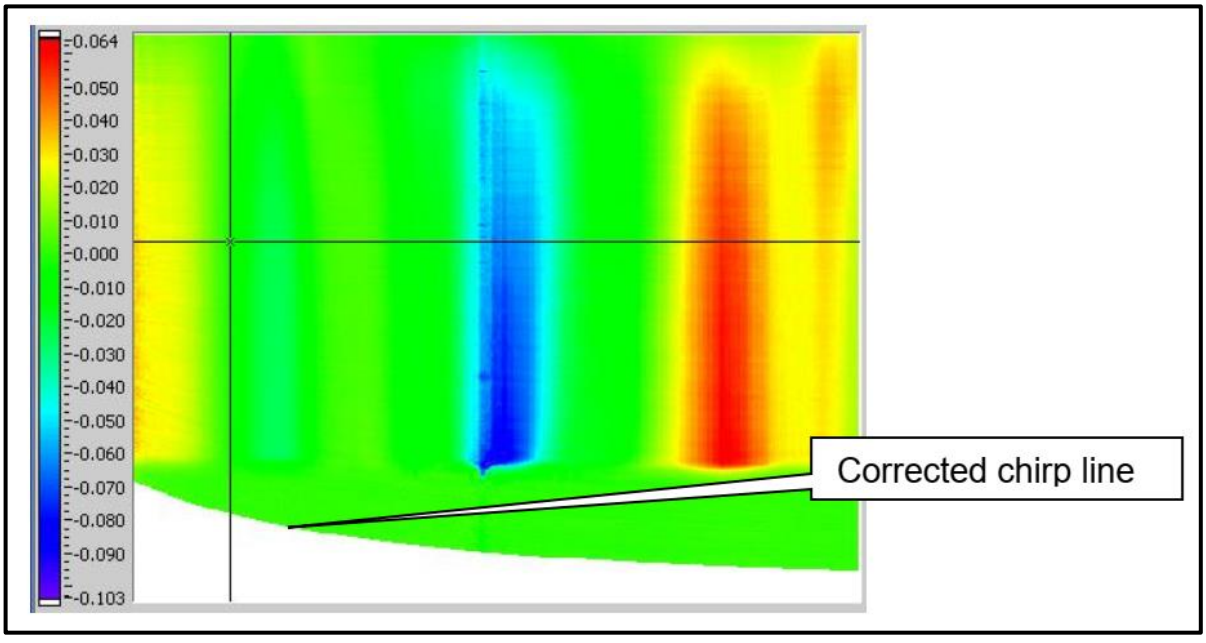

Figure 2. 20 Chirp corrected 3D surface panel data. Image adapted from Surface Xplorer operation manual, Ultrafast Systems. Here the Y-axis (***ΔA***) is a function of time as well as broadband probe wavelength.

To provide a complete presentation, we have also shown a typical fs transient absorption spectra of Ag-Au-Cu trimetallic alloy NPs in Figure 2.21. The bleach and ESA bands are displayed at different time delays.

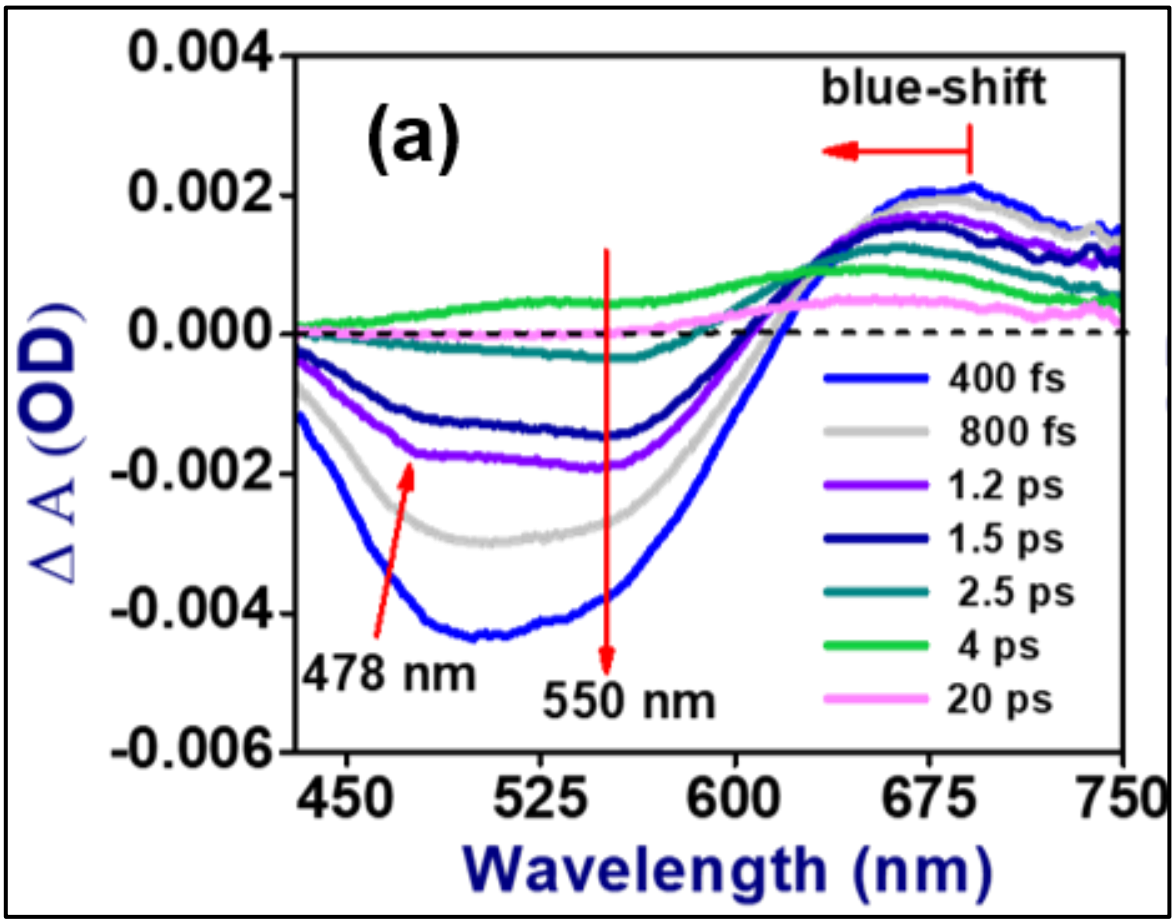

Figure 2. 21 (a) Typical fs transient absorption spectra of Ag-Au-Cu trimetallic alloy NPs at a time delay increased from 0 to 20 ps for a pump wavelength of 400 nm. Image adapted from Ref. [46]

References:

[1] A.M. Weiner, Ultrafast optics, John Wiley & Sons, 2011.

[2] T.A. Maldonado, Electro-optic modulators, Handb. Opt. 2 (1995) 11–13.

[3] T. Brabec, C. Spielmann, P.F. Curley, F. Krausz, Kerr lens mode locking, Opt. Lett. 17 (1992) 1292–1294.

[4] D. Maydan, R.B. Chesler, Q-Switching and Cavity Dumping of Nd: YAlG Lasers, J. Appl. Phys. 42 (1971) 1031–1034.

[5] G.P. Agrawal, N.A. Olsson, Self-phase modulation and spectral broadening of optical pulses in semiconductor laser amplifiers, IEEE J. Quantum Electron. 25 (1989) 2297–2306.

[6] A.M. Weiner, Ultrafast optical pulse shaping: A tutorial review, Opt. Commun. 284 (2011) 3669–3692.

[7] R. Paschotta, Field guide to laser pulse generation, SPIE press Bellingham, 2008.

[8] D.N. Schimpf, Pulse-shaping strategies in short-pulse fiber amplifiers, (2010), https://www.osti.gov/etdeweb/servlets/purl/21394977.

[9] H. Fattahi, H. Fattahi, Regenerative Amplifiers, Third-Generation Femtosecond Technol. (2016) 73–86.

[10] K. Wynne, G.D. Reid, R.M. Hochstrasser, Regenerative amplification of 30-fs pulses in Ti: sapphire at 5 kHz, Opt. Lett. 19 (1994) 895–897.

[11] K.N. Krishnakanth, Ultrafast Molecular Dynamics and Third order Nonlinear Optical Studies of Novel Organic Inorganic and Energetic Materials, Ph.D Thesis, Submitted. to Univ. Hyderabad. (2020).

[12] J.M. Liu, G. Zhou, S.J. Pyo, Parametric gain of the generation and the amplification of ultrashort optical pulses, JOSA B. 12 (1995) 2274–2287.

[13] I.N. Ross, Optical Parametric Amplification Techniques BT - Strong Field Laser Physics, in: T. Brabec (Ed.), Springer New York, New York, NY, 2009: pp. 35–59. https://doi.org/10.1007/978-0-387-34755-4_3.

[14] A.G. Ciriolo, M. Negro, M. Devetta, E. Cinquanta, D. Faccialà, A. Pusala, S. De Silvestri, S. Stagira, C. Vozzi, Optical parametric amplification techniques for the generation of high-energy few-optical-cycles IR pulses for strong field applications, Appl. Sci. 7 (2017) 265. https://doi.org/10.3390/app7030265.

[15] M. Raghuramaiah, A.K. Sharma, P.A. Naik, P.D. Gupta, R.A. Ganeev, A second-order autocorrelator for single-shot measurement of femtosecond laser pulse durations,

Sadhana. 26 (2001) 603–611.

[16] D. Rompotis, A single-shot nonlinear autocorrelation approach for time-resolved physics in the vacuum ultraviolet spectral range, Deutsches Elektronen-Synchrotron (DESY), 2016.

[17] B. Tatian, Fitting refractive-index data with the Sellmeier dispersion formula, Appl. Opt. 23 (1984) 4477–4485.

[18] A.A. Voronin, A.M. Zheltikov, The generalized Sellmeier equation for air, Sci. Rep. 7 (2017) 1–11.

[19] S. Barcikowski, Handbook of laser synthesis of colloids, (2016).

[20] M. Procházka, P. Mojzeš, J. Štěpánek, B. Vlčková, P.-Y. Turpin, Probing applications of laser-ablated Ag colloids in SERS spectroscopy: improvement of ablation procedure and SERS spectral testing, Anal. Chem. 69 (1997) 5103–5108.

[21] T. Owen, Fundamentals of UV-visible spectroscopy, (2000), https://personal.utdallas.edu/~goeckner/plasma_tech_class/AgilentSpectroPub4.pdf.

[22] D.F. Swinehart, The beer-lambert law, J. Chem. Educ. 39 (1962) 333.

[23] W. Mäntele, E. Deniz, UV–VIS absorption spectroscopy: Lambert-Beer reloaded, Spectrochim. Acta Part A Mol. Biomol. Spectrosc. 173 (2017) 965–968.

[24] M. Lee, X-Ray Diffraction for Materials Research: From Fundamentals to Applications, Apple Academic Press, 2017. https://books.google.co.in/books?id=fWxdDgAAQBAJ.

[25] D.B.W.C.B. Carter, Transmission electron microscopy A textbook for materials science, 2009.

[26] N. Brodusch, H. Demers, R. Gauvin, Field emission scanning electron microscopy: New perspectives for materials characterization, Springer, 2018.

[27] G. Binnig, C.F. Quate, C. Gerber, Atomic force microscope, Phys. Rev. Lett. 56 (1986) 930.

[28] P.G. Etchegoin, E.C.L. Ru, Basic Electromagnetic Theory of SERS, Surf. Enhanc. Raman Spectrosc. Anal. Biophys. Life Sci. Appl. (2010) 1–37. https://doi.org/10.1002/9783527632756.ch1.

[29] E.C. Le Ru, B. Auguié, Enhancement Factors: A Central Concept during 50 Years of Surface-Enhanced Raman Spectroscopy, ACS Nano. 18 (2024) 9773–9783. https://doi.org/10.1021/acsnano.4c01474.

[30] R. Pilot, R. Bozio, Validation of SERS enhancement factor measurements, J. Raman

Spectrosc. 49 (2018) 462–471.

[31] W. Xi, B.K. Shrestha, A.J. Haes, Promoting intra-and intermolecular interactions in surface-enhanced Raman scattering, Anal. Chem. 90 (2017) 127-143.

[32] H. Ma, S.Q. Pan, W.L. Wang, X. Yue, X.H. Xi, S. Yan, D.Y. Wu, X. Wang, G. Liu, B. Ren, Surface-Enhanced Raman Spectroscopy: Current Understanding, Challenges, and Opportunities, ACS Nano. (2024). https://doi.org/10.1021/acsnano.4c02670.

[33] N. Guillot, M.L. de la Chapelle, The electromagnetic effect in surface enhanced Raman scattering: Enhancement optimization using precisely controlled nanostructures, J. Quant. Spectrosc. Radiat. Transf. 113 (2012) 2321–2333. https://doi.org/10.1016/j.jqsrt.2012.04.025.

[34] J. Langer, D.J. de Aberasturi, J. Aizpurua, R.A. Alvarez-Puebla, B. Auguié, et al., Present and future of surface-enhanced Raman scattering, ACS Nano. 14 (2020) 28–117. https://doi.org/10.1021/acsnano.9b04224.

[35] M. Sheik-Bahae, A.A. Said, E.W. Van Stryland, High-sensitivity, single-beam n 2 measurements, Opt. Lett. 14 (1989) 955–957.

[36] M. SHEIK-BAHAE, A.A. SAID, T.-H. WEI, D.J. HAGAN, E.W. Van Stryland, Sensitive measurement of optical nonlinearities using a single beam, SPIE Milestone Ser. 174 (2003) 292–301.

[37] X. Zhang, C. Huang, M. Wang, P. Huang, X. He, Z. Wei, Transient localized surface plasmon induced by femtosecond interband excitation in gold nanoparticles, Sci. Rep. 8 (2018) 10499. https://doi.org/10.1038/s41598-018-28909-6.

[38] R. Berera, R. van Grondelle, J.T.M. Kennis, Ultrafast transient absorption spectroscopy: principles and application to photosynthetic systems, Photosynth. Res. 101 (2009) 105–118.

[39] A. Gaál, I. Bugár, I. Capek, L. Fialová, T. Pálszegi, V. Szöcs, A. Šatka, F. Uherek, Femtosecond multicolor transient absorption spectroscopy of colloidal silver nanoparticles, Laser Phys. 19 (2009) 961–968. https://doi.org/10.1134/s1054660x09050120.

[40] H.F. Zarick, A. Boulesbaa, E.M. Talbert, A. Puretzky, D. Geohegan, R. Bardhan, Ultrafast Excited-State Dynamics in Shape- and Composition-Controlled Gold-Silver Bimetallic Nanostructures, J. Phys. Chem. C. 121 (2017) 4540–4547. https://doi.org/10.1021/acs.jpcc.6b12669.

[41] C. Engelbrekt, K.T. Crampton, D.A. Fishman, M. Law, V.A. Apkarian, Efficient Plasmon-Mediated Energy Funneling to the Surface of Au@Pt Core-Shell Nanocrystals, ACS Nano. 14 (2020) 5061–5074.

https://doi.org/10.1021/acsnano.0c01653.

[42] A.M. Brown, R. Sundararaman, P. Narang, A.M. Schwartzberg, W.A. Goddard, H.A. Atwater, Experimental and Ab Initio Ultrafast Carrier Dynamics in Plasmonic Nanoparticles, Phys. Rev. Lett. 118 (2017) 87401. https://doi.org/10.1103/PhysRevLett.118.087401.

[43] W.H. Lin, Y. Shi, X.Z. Yang, J. Li, E. Cao, X.F. Xu, T. Pullerits, W.J. Liang, M.T. Sun, Physical mechanism on exciton-plasmon coupling revealed by femtosecond pump-probe transient absorption spectroscopy, Mater. Today Phys. 3 (2017) 33–40. https://doi.org/10.1016/j.mtphys.2017.12.001.

[44] D.R. Klug, T. Rech, D.M. Joseph, J. Barber, J.R. Durrant, G. Porter, Primary processes in isolated Photosystem II reaction centres probed by magic angle transient absorption spectroscopy, Chem. Phys. 194 (1995) 433–442.

[45] G. Lanzani, The photophysics behind photovoltaics and photonics, John Wiley & Sons, 2012.

[46] D. Banerjee, M. Akkanaboina, V.R. Soma, Plasmonic alloy nanocolloids fabricated via femtosecond Bessel beam for photonic and SERS-based sensing applications, Opt. Mater. (Amst). 154 (2024) 115668. https://doi.org/https://doi.org/10.1016/j.optmat.2024.115668.

Intentional Blank Page

Intentional Blank Page

Chapter 3

Femtosecond Gaussian Beam Laser Ablated Colloidal TiO_2, Silver-doped TiO_2 Nanoparticles as well as Solid Nanostructures Engaged in SERS-based Sensing of Hazardous Compounds

Abstract

We present our comprehensive results on femtosecond (fs) laser ablation in liquid (LAL) generated titanium dioxide (TiO_2) and silver (Ag) doped titanium dioxide (Ag-TiO_2) nanoparticles. TiO_2 and Ag-TiO_2 nanoparticles (NPs) were produced in deionized water utilizing simultaneous laser-induced chemical reduction by irradiation and fs laser ablation, respectively. We have performed surface-enhanced Raman spectroscopy (SERS) experiments using TiO_2 and Ag-doped TiO_2 NPs. However, we could not detect any signal when utilizing the TiO_2 NPs. Only with the Ag-doped TiO_2 NPs could we successfully achieve the SERS signal during the real-time detection of RDX (100 µM) and ammonium nitrate (AN, 20 µM). Remarkably, SERS experiments with the Ag-Ti solid nanostructure (NS) revealed a signal that was 16 times stronger than that of pure TiO_2 NS. A graphical abstract for this chapter is presented below.

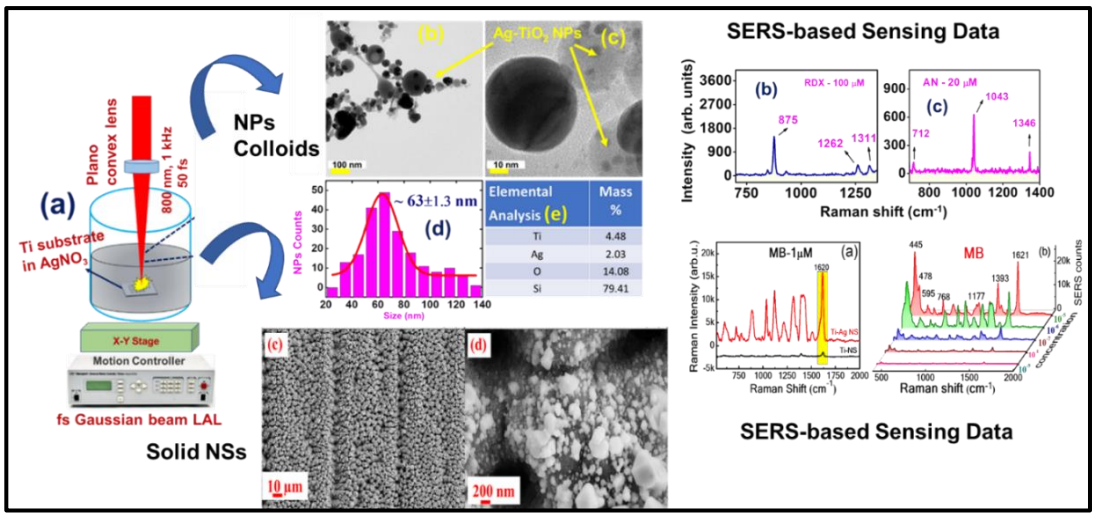

The work presented in this chapter has been published in

1. **D. Banerjee**, S.S.B. Moram, C. Byram, J. Rathod, T. Jena, G.K. Podagatlapalli, V.R. Soma, Plasmon-enhanced ultrafast and tunable thermo-optic nonlinear optical properties of femtosecond laser ablated TiO2 and Silver-doped TiO2 nanoparticles, Appl. Surf. Sci. 569 (2021) 151070. https://doi.org/10.1016/j.apsusc.2021.151070
2. **D. Banerjee**, S. S. B. Moram, and V. R. Soma, "Ag-doped TiO2 Nanoparticles Generated with Femtosecond Laser Ablation for Sensing RDX and Ammonium Nitrate," in *Frontiers in Optics + Laser Science 2023 (FiO, LS)*, Technical Digest Series (Optica Publishing Group, 2023), paper JM7A.1, https://doi.org/10.1364/FIO.2023.JM7A.1
3. M. S. S. Bharathi, **D. Banerjee**, and V. R. Soma, "Femtosecond Laser Ablation Assisted Single-step Fabrication of Metal-semiconductor Interfaced SERS-active Substrate," in *Laser Congress 2023 (ASSL, LAC)*, Technical Digest Series (Optica Publishing Group, 2023), paper JW2A.7, https://doi.org/10.1364/ASSL.2023.JW2A.7

3.1. Introduction

Researchers from various backgrounds have shown a fascinating interest in photonic studies utilizing nanoparticles (NPs) and nanocomposites due to their potential optical applications. These nano entities seem to have a promising future not only in photonics but also in photovoltaic cells, photo-catalysis, catalytic chemistry [1], and nonlinear optics [2–4] because of the significant quantum confinement effects that result from the sub-nano dimensional exotic size and shapes that exist within them. Some of the most exotic optical properties, like the tunable surface plasmon resonance (SPR) effect, the finely tunable energy band gap, the ideal electronic response for nonlinear multi-photon absorption, the higher sensitivity in ultrafast laser-matter interaction, etc., originate in the nano-regime, where a higher surface to volume ratio leads to more conduction electron density. In addition to pure nanoparticles, chemically synthesized metal-semiconductors, metal-metal nanoparticles in alloy, bi/tri-metal, or doped form, as well as those aided by laser irradiation, offer several benefits [5,6], including enhanced stability, plasmon band tunability, and the creation of excited electron-hole pairs, which make them perfect for photo-catalysis, solar energy conversion [7,8], among many other potential uses. To explore novel applications for optical limiting, optoelectronics, and optical switching devices, the third-order nonlinear optical (NLO) characteristics of metal and metal-alloy nanoparticles have been thoroughly investigated [9–13] and examined by several spectroscopic approaches [14–18]. Further, ultrafast laser ablation [19–28] in the air (LAA) as well as in liquid (LAL) techniques used for producing nanoparticles and nanostructures have been explored for numerous applications. TiO_2 semiconductor NPs, out of all the semiconductor NPs studied, have a large band gap of ~3.2 eV, which makes them valuable in many cross-disciplinary scientific domains. Optoelectronic applications are among the well-known uses of TiO_2 NPs that have drawn the attention of several researchers [29]. TiO_2 nanoparticles, particularly, are required to display remarkable nonlinear optical (NLO) capabilities due to their optically induced properties when exposed to powerful, coherent laser beams. Furthermore, novel device applications of TiO_2 NPs after doping with appropriate metal ions like silver (Ag), gold (Au), etc., were covered in the currently available literature. The extensive research that is now accessible makes it clear that, depending on the metal type or percentage doped into the TiO_2 matrix, the appropriate doping of metal ions

into TiO_2 NPs will affect their optical, chemical, and physical characteristics to the necessary degree. It is also evident that the optical limiting capabilities of the TiO_2 NPs are much improved by doping Ag ions into the TiO_2 matrix [30]. Furthermore, compared to other nanomaterials, TiO_2 NPs have been discovered to have a wide range of cross-disciplinary applications. It was discovered that TiO_2 nanoparticles were less hazardous and had an effective photocatalytic nature. Additionally, recent studies showed that the anatase phase of the nanoparticles improved the plant leaves' ability to absorb light. TiO_2 NPs also affect photophosphorylation and electron chain transit [31], affecting photosynthetic activity. Nevertheless, the TiO_2 nanoparticles' larger bandgap makes it more difficult for them to interact with visible light. The published literature shows TiO_2 NPs have a bandgap between 3 and 3.2 eV [32]. Consequently, less than 400 nm wavelength light is needed to activate TiO_2 NPs. Only 4–5% of UV radiation is available in natural sunshine, which might result in relatively little TiO2 NP activation. Visible light must activate TiO_2 NPs to improve the process of photosynthesis. To increase the likelihood of light absorption in the visible range (400–700 nm), noble metals, including silver (Ag), gold (Au), palladium (Pd), and platinum (Pt), may be added to TiO_2 NPs [33,34].

Parallelly, plasmonic metal-doped TiO_2 NPs have also found profound applications in surface-enhanced Raman spectroscopy (SERS)-based sensing studies. Zou et al. [35] have shown a permanent accumulation of the SERS activity caused by the exposure of near-infrared (NIR) light to a hybrid system consisting of 4-mercaptobenzoic acid connected with silver and silver-doped titanium dioxide (4MBA/Ag/Ag-doped TiO_2). The SERS intensity of 4MBA exhibited an irreversible exponential rise as the irradiation period increased, whereas the Raman signal of the Ag/Ag-doped TiO2 substrate showed an exponential decline. The phenomena have been explained by considering three factors: (1) photo-induced charge transfer, (2) increased crystallinity of the Ag/Ag-doped TiO2 substrate, and (3) charge-induced molecular reorientation. Yang et al. have used a hydrothermal approach and a magnetron sputtering method [36] to fabricate single-crystalline TiO_2 nanosheets (TNS) arrays on a fluorine-doped tin oxide (FTO) substrate. The TNS arrays have prominent {001} facets and are adorned with Ag nanoparticles. They examined the SERS substrates' sensitivity, reversibility, and uniformity using Rhodamine 6G (R6G) as the probe molecule.

Wang et al.[37] adopted the SERS technique that relied on a semiconducting substrate to identify various antibiotic residues in ultrapure and real water systems. The Ag-TiO_2 nanoparticle substrate, produced via simultaneous deposition and doping of Ag onto TiO_2, demonstrates remarkable sensitivity in SERS-based detection of danofloxacin, difloxacin hydrochloride, enoxacin, enrofloxacin, and ciprofloxacin- five commonly used quinolone antibiotics - in real water samples. Another recent study by Muniz-Miranda [38] used the SERS method to examine the catalytic reduction of 4-nitrophenol under UV irradiation and identify the resulting reaction products in Ag/titania colloidal nanocomposites. Hong et al. [39] have conducted a study on the SERS response of a defective TiO_2 thin film adorned with silver nanoparticles using laser ablation. Furthermore, several other research groups have extensively researched plasmonic metal-doped Ti nanoentities [40–42]. This study used the methods of simultaneous laser-induced chemical reduction by irradiation and fs laser ablation to synthesize TiO_2 and Ag-TiO_2 nanoparticles (NPs) in deionized water. XRD, TEM, FESEM, and UV-VIS-IR spectroscopy have been used to characterize the NPs carefully. We have thus performed the SERS experiments using Ag-doped TiO_2 NPs and TiO_2 NPs for explosive trace detection. In SERS experiments, the Ti-Ag solid nanostructure (NS), produced in the same LAL experiment, also showed a sixteen times stronger signal than pure TiO_2 NS.

3.1.1. Experimental Details

Experiments performed in this study involved two steps; in the first step, pure TiO_2 and Ag-doped TiO_2 NPs were prepared and utilized in SERS studies, and in the second step, the solid nanostructures were engaged in SERS sensing.

3.1.2. Fabrication of TiO_2 and Ag-TiO_2 NPs by femtosecond laser ablation

We started by cleaning the titanium (Ti) substrate, which was submerged in an ultrasonic cleaner for around 15 minutes to remove surface contaminants while being successively submerged in acetone, ethanol, and deionized water. After being cleaned of surface impurities, the fresh Ti metallic target was immersed in deionized water and exposed to concentrated laser pulses (~50 fs duration). These pulses were produced by a regenerative fs amplifier (Ti: sapphire, LIBRA, M/s Coherent, USA) and had a central maximum of about 800 nm, with a repetition rate of 1 kHz. The Ti target submerged in deionized water was the

focal point of the intense ultrafast pulses, which had an estimated energy of less than 100 µJ. Using a plano-convex lens with a focal length of about 100 mm, the input laser pulse with a Gaussian profile (TEM_{00}) and a full width at half maximum (FWHM) of approximately 8 mm was focused on the Ti target surface. Creating a plasma plume and the continuous, loud cracking sound at the spot where the focused laser beam made contact with the target surface were indicators of optimal laser beam focusing. At the focal plane (in air), the estimated beam waist was about 20 µm. The predicted beam waist on the Ti target surface, immersed in a deionized water medium, may exceed the initial value of around 60 µm. Using a defined energy ultrafast laser beam with extreme focus, a (5×5) mm^2 Ti target was raster scanned at 0.1 mm/s. On the Ti target surface, the distance between each line was about 50 µm. The synthesized TiO_2 NPs are released into the surrounding liquid medium as colloids, and the area of the Ti target surface on which ablation was performed remains with the nano-protrusions, pores, domes, or periodic surface structures acting as the nanostructures (NSs). This is the advantage of ultrafast laser ablation [43–51] of Ti targets immersed in any liquid medium. The normal yield in fs ablation is close to mg/second [52]. A new Ti substrate was later laser ablated in the same procedure while a solution of silver nitrate ($AgNO_3$, 0.5 mM) was present. For the creation of TiO_2 NPs, several other ablation parameters, such as pulse energy and raster scan speed, were left unchanged. In this case, a strong laser-matter interaction produced TiO_2 NPs, and $AgNO_3$ reduction produced Ag^+ ions. Under the effect of moderately strong fs laser pulse irradiation, these reduced Ag ions finally began to become integrated and doped on the surface of the previously created TiO_2 NPs. Ag ions cluster when the $AgNO_3$ continues to be reduced. Ag atoms are liberated into the liquid medium used for laser ablation of the Ti target. Subsequently, the metallic plume of the Ti target will be combined with Ag ions/Ag atomic clusters, stopping the nucleation process that produces the TiO_2 NPs. Consequently, Ag ion-doped TiO_2 NPs will arise due to the photo-irradiated interaction rather than TiO_2 NPs. These NPs were then distributed in distilled water after being centrifuged for 15 minutes at 3500 rpm. The previously stated advancement in the production of the Ag-doped TiO_2 NP has been conclusively verified by FESEM-EDAX pictures. Consequently, the single-step fs laser ablation was used to create the spherical TiO_2 and Ag-doped TiO_2 NPs as colloidal suspensions with an average size of 50–65 nm.

3.1.3. Results & Discussion

3.1.4. XRD Characterization

The X-ray diffraction (XRD) characterization of the TiO_2 NPs synthesized by (a) laser ablation of Ti target in deionized water and (b) reducing the $AgNO_3$ in the presence of TiO_2 colloids in deionized water by irradiation was performed using Cu K_α line (using a Discover D8 diffractometer, Bruker, Germany). The XRD data provided proof of the presence of Ag in the TiO_2 NPs and the purity of the TiO_2 phase. Figure 3.1 displays the XRD data for both TiO_2 and Ag-doped TiO_2 [(a) displays the Ag-TiO_2 NPs data, whereas (b) displays the TiO_2 NPs data]. The data shows a distinct difference between the two. The X-axis break was used to prevent the strong peak from the substrate (around 28O) from dominating the spectrum. We drop casted 20 µl of NPs onto a cleaned silicon wafer for XRD measurements. It is evident from the existence of miller planes like (1 0 1), (1 1 5), and (1 0 6) in Figure 3.1(b) (the spectrum is shown in blue color) that laser ablation was used to create the TiO_2 NPs [53,54]. Furthermore, the XRD data [red line; Figure 3.1(a)] demonstrates the presence of the miller planes (1 1 1), (2 0 0), (2 2 0), and (3 1 1), which highlights the presence of Ag [JCPDS file number Ag: 03-0921] inside the TiO_2 nanoparticles[53,55]. As a result, the observed XRD data verified the Ag content and purity of the TiO_2 NPs doped with Ag.

TiO_2 is a well-recognized semiconducting material with a wide band gap and is used in several applications, including light absorption and charge transfer. Three mineral forms of TiO_2 exist: rutile [JCPDS # 21-1276], brookite, and anatase [JCPSDS # 98-015-4610, JCPDS # 21-1272], or sometimes both. Of these, anatase is classified as an indirect band gap semiconductor and the other two as direct band gap materials. A few of the miller indices (101, 200, and 105), as shown in Figure 3.1(b), verified that most of the produced TiO_2 NPs were in the anatase phase. The Ag-doped TiO_2 NPs' XRD spectra did not reveal any unique phases of Ag. Since the ionic radius of Ag (1.15 Å) is larger than the radius of Ti (0.61 Å), Ag ions cannot replace the Ti site in TiO_2 NPs directly [34]. In conclusion, the XRD data and analysis proved that Ag and TiO_2 NPs were present. Ag is reduced during laser ablation of a titanium target submerged in $AgNO_3$, and Ag ions interact with the titanium metallic plume and pre-synthesized TiO_2 NPs due to photoinduced ablation. There are two possible outcomes: either the Ag ions penetrate the Ti plasma plume, or the Ag ions mix and graft clusters inside the TiO_2 NPs. Alternatively, the Ag ion clusters might have been nucleated to

create Ag NPs, which would have been inserted into the TiO_2 NPs. This would have resulted in a non-uniform distribution of Ag ions, Ag ion clusters, and Ag NPs. The XRD data (displayed in Figure 3.1) indicates that although some similar peaks indicate the existence of TiO_2, the XRD spectra of Ag-doped TiO_2 and TiO_2 do not seem to be the same. Since we would have gotten the same XRD patterns for the TiO_2 NPs and the Ag-doped TiO_2 NPs if they formed similarly, the likelihood of a uniform distribution of Ag NPs in the TiO_2 NPs is low. We believe there has been a non-uniform distribution of Ag NPs in the bigger TiO_2 NPs.

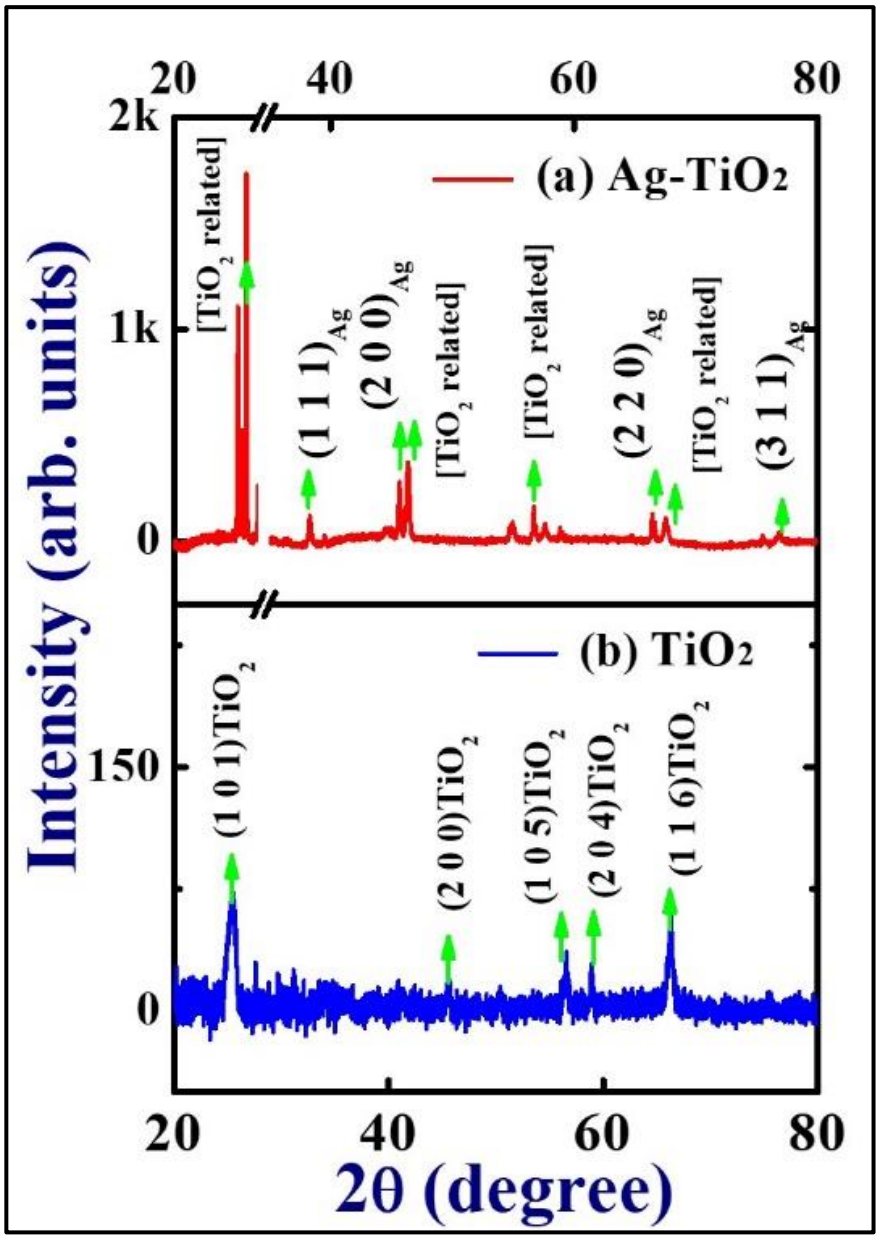

Figure 3. 1 XRD spectra of the synthesized (a) Ag-TiO_2 NPs (b) TiO_2 NPs.

Interestingly, the diffraction peaks for TiO_2 ascribed to Ag-doped TiO_2 and TiO_2 particles are at distinct diffraction angles, suggesting that the doped NPs may have a different phase than the pure NPs. Additionally, there may be trace amounts of NPs with other phases, including AgO and Ag_2O, which have no bearing on the overall research reported here. SAED patterns and related data were carefully examined to conduct more in-depth research and search for any additional crystalline phases (which seemed likely given the laser ablation synthesis technique used here). The analysis of these data is provided in the following section.

3.1.5. UV-Visible Absorption Spectroscopy

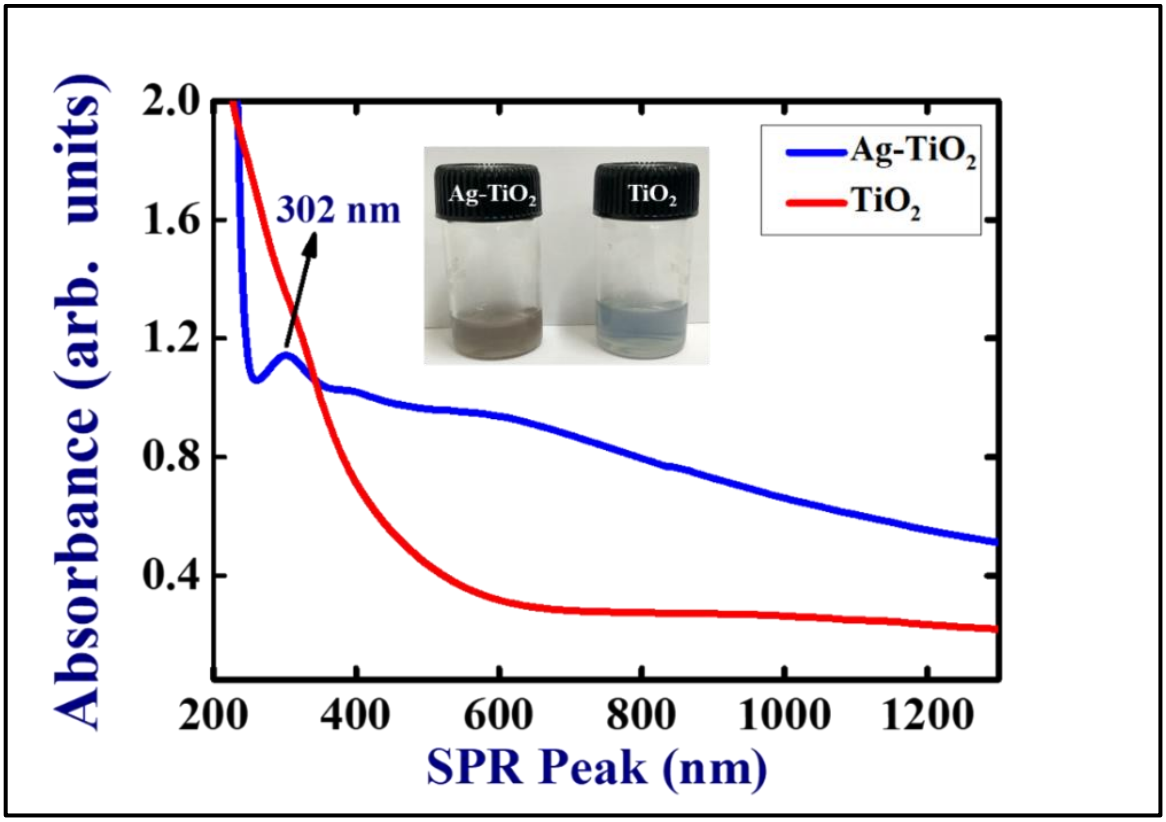

Figure 3. 2 UV-visible absorption spectra of pure TiO2 NPs prepared by fs laser ablation (red) and Ag-doped TiO_2 NPs prepared by reduction (blue). The inset shows the pictures of the prepared nanoparticles.

A UV-visible-IR spectrometer (Perkin Elmer, Lambda 750) was used to record the absorption spectra of TiO_2 nanocolloids in deionized water and Ag-TiO_2 NPs after they were prepared and settled down. The spectral range covered by the instrument was 250–1200 nm.

The acquired data is shown in Figure 3.2. Figure 3.2 data indicates that no significant surface plasmon resonance (SPR) peak was seen for TiO_2 NPs in deionized water. This appears to be consistent with previously published findings.

TiO_2 NPs have a typical bandgap of 3-3.2 eV [56]. This implies that they must absorb pure UV light with a wavelength of less than 400 nm. Furthermore, TiO_2 NPs function as semiconductors, and no SPR signature was seen in the UV absorption spectrum. Notably, the SPR peak in the Ag-doped TiO_2 at 302 nm was elevated in response to the Ag content of the TiO_2 NPs. It is likely that the doping of Ag in the TiO_2 matrix results in the creation of modified band-gaps and changed energy levels in the Ag-TiO_2 NPs [34], which have caused the absorption at 302 nm and the elongation of the SPR peak shoulder into the visible range. A wider hump in the 450–1200 nm region is also depicted in Figure 3.2, which undoubtedly contains information about the modification of the SPR peak in the presence of the TiO_2 matrix and the potential creation of a lower-level state with a minimum energy (the ideal configuration for which would support the saturable absorption nature observed at higher wavelengths in the NLO studies). Ag-TiO_2 NP production was well highlighted by the UV-visible absorption spectra in Figure 3.2, which complemented the XRD data shown in Figure 3.1.

3.1.6. Transmission Electron Microscope (TEM) studies

A TEM (FEI Tecnai, G2 S-Twin200 kV) was used to understand the morphology of the TiO_2 and Ag-doped TiO_2 NPs in deionized water. This permitted for the estimation of the average size nanoscale morphologies, distribution, and crystallographic phases [54] of the produced NPs. After sonicating colloids of TiO_2 and Ag-doped TiO_2 NPs in deionized water to create mono dispersions, the Cu grids were drop-casted onto carbon-coated copper surfaces and allowed to cure before being subjected to TEM examination. Figure 3.3 displays TEM pictures of the monodispersed TiO_2 NPs with spherical morphologies. At varying magnifications, the spherical shape of TiO_2 nanoparticles is seen in Figures 3.3(a) and 3.3(b). The histogram created by the ImageJ program to ascertain the average size of the TiO_2 NPs in deionized water by taking into account five TEM images taken at the same magnification is shown in the inset of Figure 3.3(b).

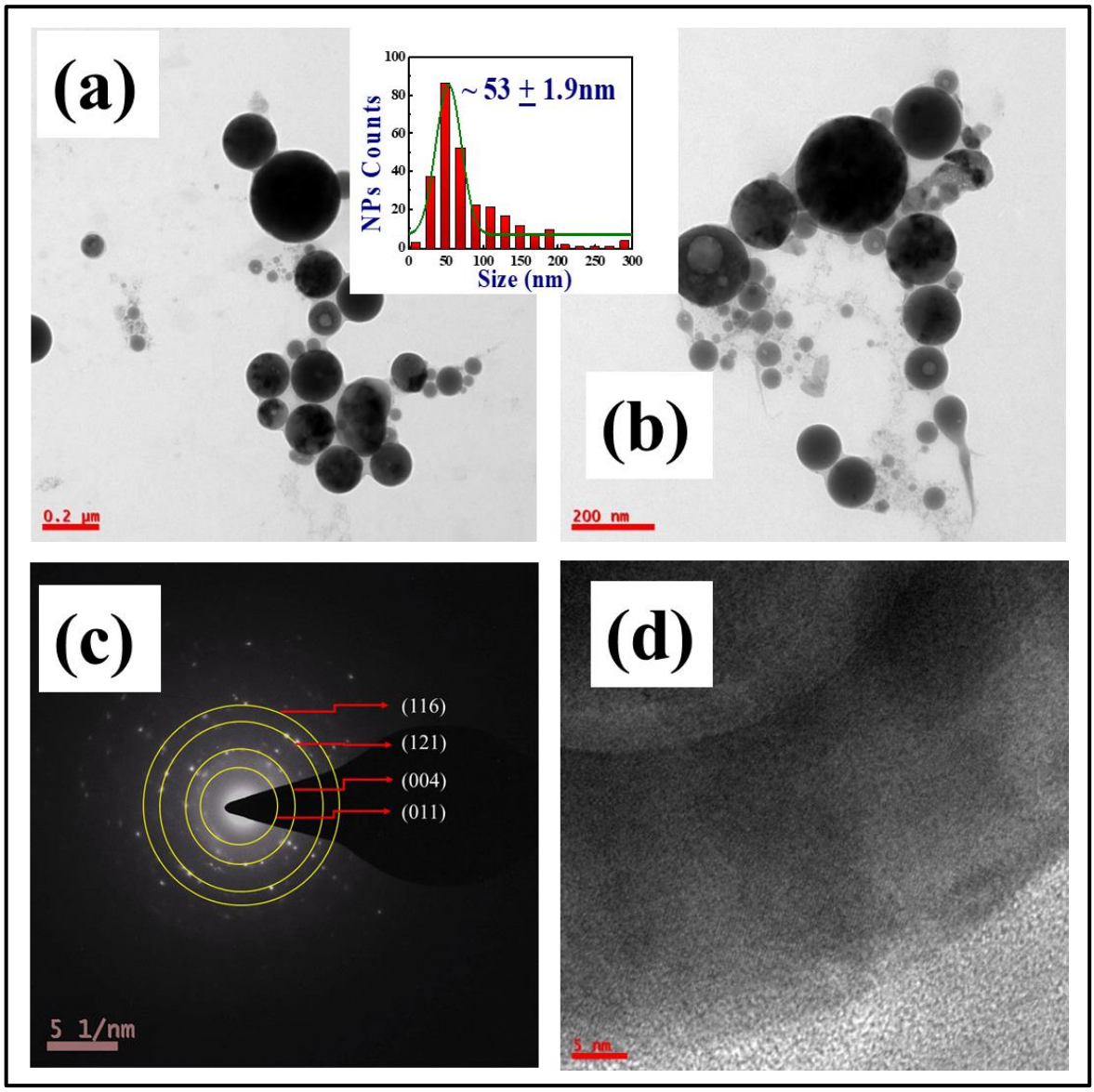

Figure 3. 3 TEM images of (a) TiO_2 NPs synthesized in deionized water and its (b) magnified view. Inset lying at the intersection of Figures (a) and (b) is the histogram constructed by the number density of TiO_2 NPs (c) SAED pattern of the TiO_2 NPs demonstrate a polycrystalline nature (d) HRTEM image of a single TiO_2 NP exhibiting a clear shell structure.

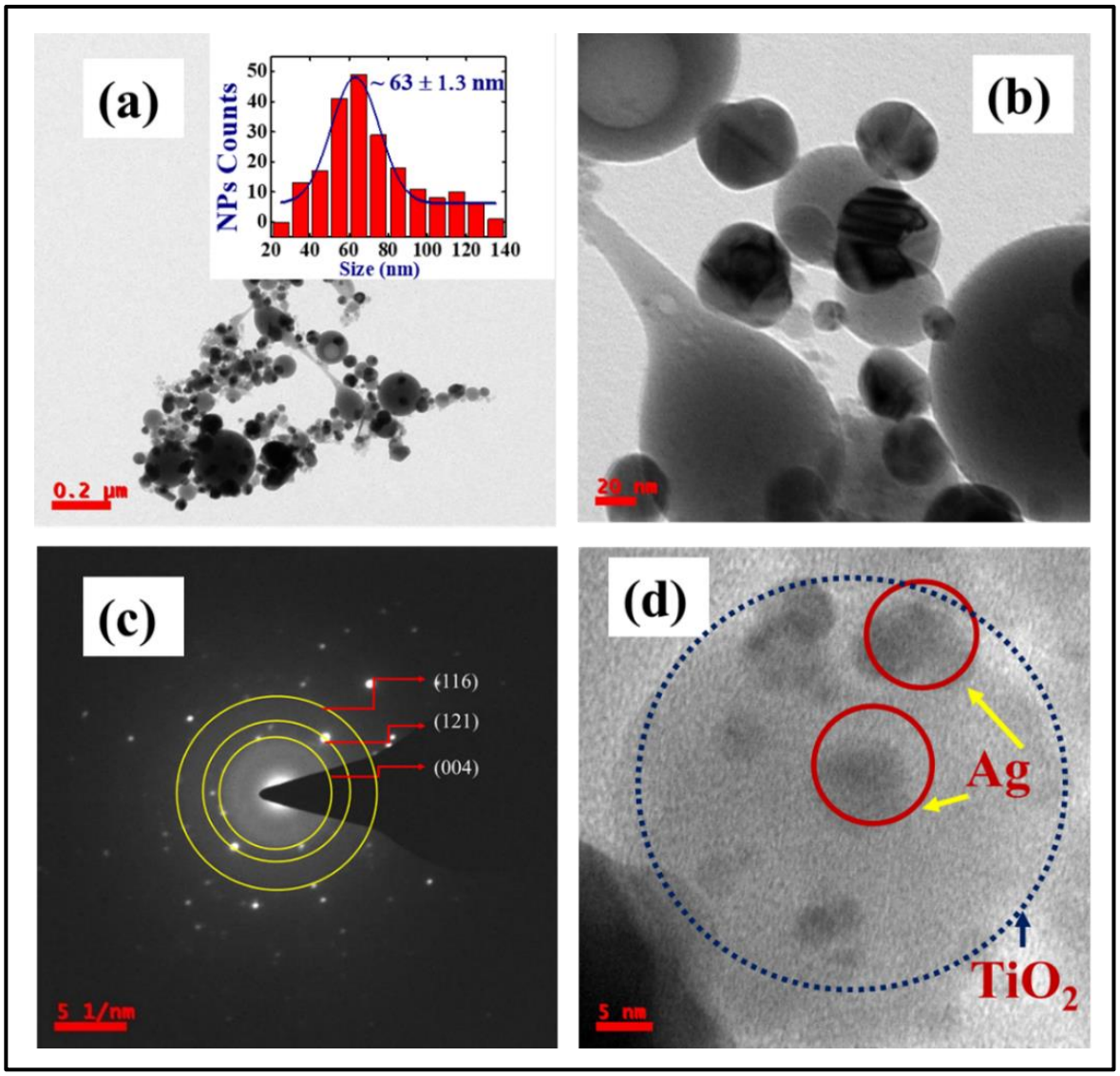

Figure 3. 4 TEM images of (a) Ag-doped TiO_2 NPs in deionized water and its (b) magnified view. Inset of Figure (a) is the histogram constructed by the number density of TiO_2 NPs (c) SAED pattern of the Ag-TiO_2 NPs demonstrating the polycrystalline nature (d) HRTEM image of a single Ag-TiO_2 nanoparticle (represented by a blue dotted circle) indicating the presence of embedded Ag nanoparticle (shown inside the red circles).

The average size of the TiO_2 NPs was found to be around 53 nm by a Gaussian fit of the NPs histogram. The recorded SAED pattern in Figure 3.3(c) verified the polycrystalline phase of the TiO_2 NPs. On Ti NPs, an oxide layer formed, as shown in Figure 3.3(d). The TEM pictures of well-monodispersed, spherically shaped Ag-doped TiO_2 NPs are shown in Figure 3.4. Figures 3.4(a) and 3.4(b) verified the spherical shape of Ag-TiO_2 NPs at varying magnifications.

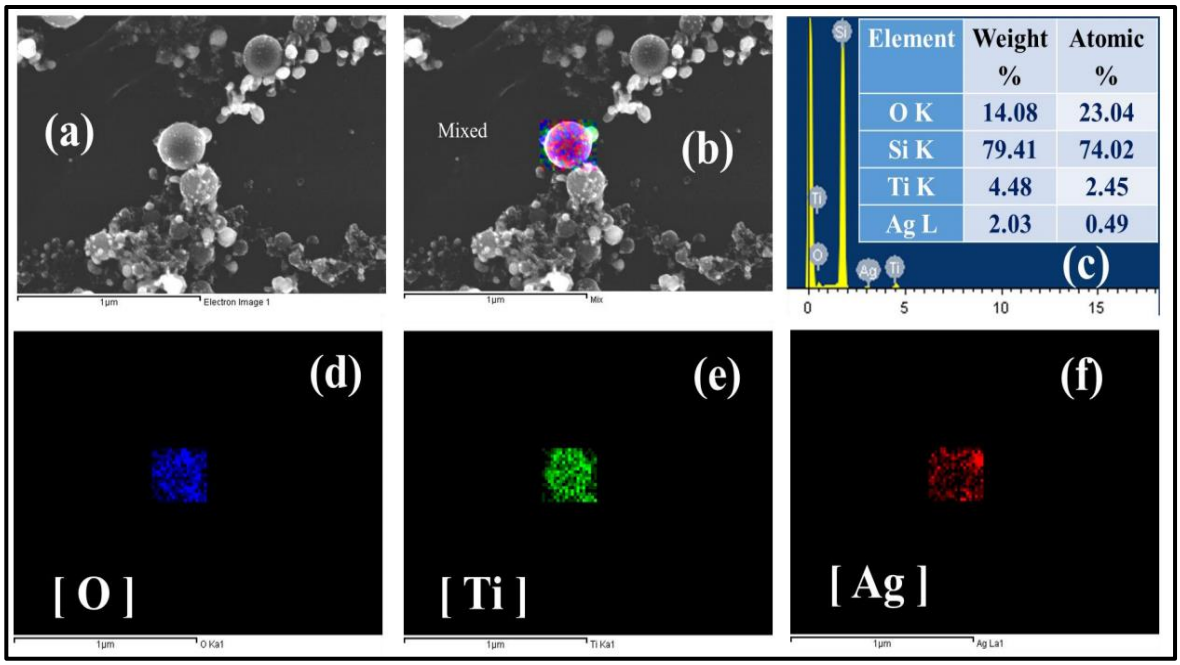

Figure 3. 5 FESEM-EDX elemental mapping images of Ag-doped TiO2 NPs (a) Electron microscopic image of Ag-TiO2 (b) Single particle colored mix-map of Ag-TiO_2 containing each constituent (c) EDS spectra inset depicting the atomic % and weight% of individual elements. (d, e, f) clarifies the presence and distribution of Oxygen (blue), Titanium (green), and Silver (red), respectively. [magnification bar of all images is 1 µm]

The histogram of Ag-TiO_2 NPs and its Gaussian fit is shown in the inset of Figure 3.4(a), showing that the average size of the TiO_2 NPs is around 63 nm. The SAED pattern shown in Figure 3.4(c) confirmed the polycrystalline phase of the TiO_2 nanoparticles. The SAED patterns of TiO_2 [Figure 3.3(c)] and Ag-TiO_2 NPs [Figure 3.4(c)] both display concentric rings that provide insight into the crystalline planes and are consistent with the XRD data. According to JCPSD 98-015-4610, the TiO_2 NPs had interplanar spacings of d = 0.24 nm and d = 0.14 nm, corresponding to the (0,0,4) and (1,1,6) planes, respectively. In contrast, the Ag-TiO_2 NPs had interplanar spacings of d = 0.25 nm and d = 0.15 nm, corresponding to the same plane order. The doping of Ag inside the TiO_2 matrix is explained by this little change in the 'd' values. Nonetheless, a few more peaks have been discovered that provide light on the presence of a crystalline rutile phase or a mix of anatase and rutile phases. Only further XRD tests will clarify this finding, and that is what we want to do moving forward. Ag is present in the TiO_2 NP matrix, as shown in Figure 3.4(d). However, the planes are not easily visible to establish the presence of Ag; hence, elemental distribution FESEM-EDX mapping was done. The sample was made by simply dropping 5 µl of NPs onto a Si wafer that had been

cleaned. The Ag-TiO_2 NPs' FESEM results are shown in Figures 3.5[(a)–(f)], and the mapping was performed on a single particle. These data determined the presence of Ag, Ti, and O. The presence of silver in Ag-doped TiO_2 NPs was amply demonstrated by the EDX spectrum with weight percentages and individual elemental mapping data.

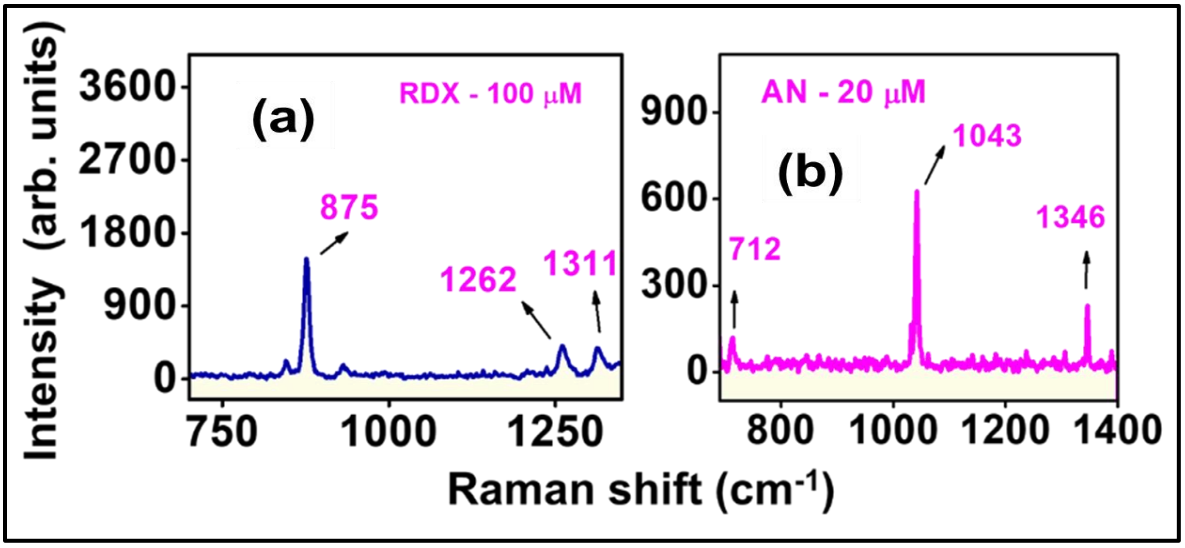

Figure 3. 6 (a) UV-Vis-IR absorption spectra of Ag-doped TiO_2 NPs (b) SERS spectrum of RDX traces (100 µM) sensed employing Ag-doped TiO_2 NPs (c) SERS spectrum of AN traces (20 µM) sensed employing Ag-doped TiO_2 NPs.

3.1.7. SERS-based sensing studies engaging the nanoparticles and nanostructures

Additionally, using a portable Raman system-based SERS [57–63] approach, the Ag-doped TiO_2 NPs were used in sensing investigations of real-time explosives such as AN and RDX. The data collection settings were 785 nm excitation, 5 ms acquisition duration, and three spectral averaging. It was discovered that the lowest detectable quantities were 100 µM (RDX) and 20 µM (AN). The relevant spectra are shown in Figures 3.6(a) and 3.6(b). The maxima of the RDX signature [in Figure 3.6(b)] were seen at 876 cm^{-1} (caused by C–N stretching) and 1261 cm^{-1} (caused by N–N stretching). Similarly, hallmark Raman peaks of AN [57–63] were seen at 1043 cm^{-1} [matching the symmetric stretch mode of NO_3] in the SERS spectra shown in Figure 3.6(c). The computed enhancement factors are 2.9×10^3 and 4.9×10^3, respectively.

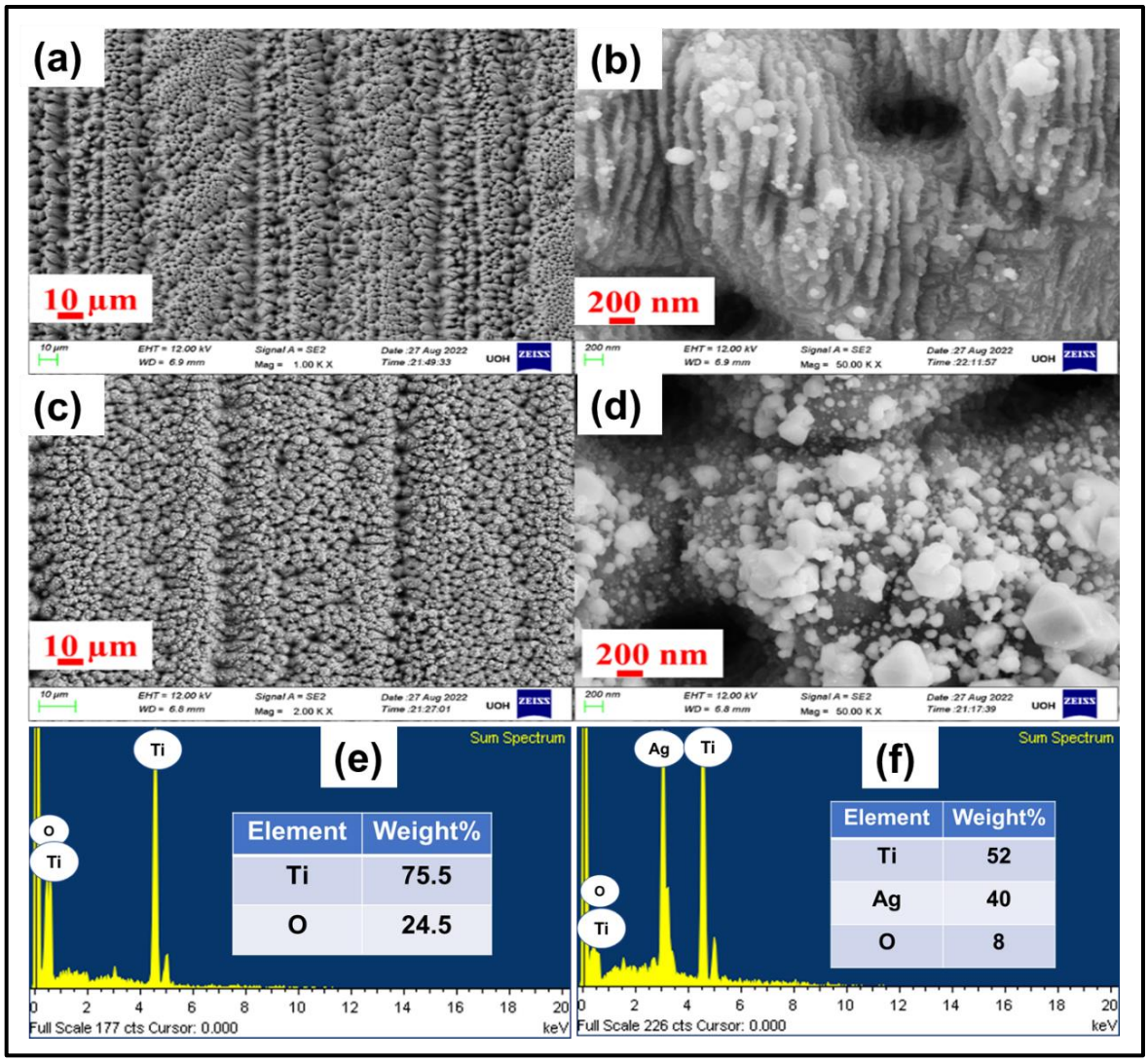

Figure 3. 7 Lower and higher magnification FESEM images of (a and b) Ti NSs (c and d) Ti-Ag NSs. FESEM EDX spectra of Ti (e) and Ti-Ag NS (f), with elemental composition table inside.

Subsequently, we wanted to investigate the solid NSs produced by the same experiment's SERS performance. The shape and chemical makeup of the laser-ablated Ti in DW and $AgNO_3$ are characterized by the FESEM. The elemental distribution of the laser-ablated Ti NSs and Ti-Ag NSs was shown by the FESEM-EDS mapping. Figure 3.7 displays the lower and higher magnification FESEM pictures of the laser-processed Ti surface, having it submerged in DW [Figure 3.7(a-b)] and $AgNO_3$ [Figure 3.7(c-d)]. The surface topography was discovered to consist of periodic nanostructures, micrometric troughs, and alternating micrometric peaks with cone-like protrusions. The laser beam's interaction with the dispersed

waves from the material might result in the formation of these microstructures via intensity modulation. Ag NPs are mainly found on top of the periodic patterns and peaks that have been formed. The combination of Ag and Ti with a ~1:3 ratio for the Ti substrate was shown by the EDX spectrum data [Figure 3.7(e-f)]. Additionally, a clear oxidation impact was seen. Through photo-reduction of $AgNO_3$, the very intense laser contact results in the in-situ creation of Ag nanoparticles, and the surface structuring of Ti creates self-organized protrusions microstructure. Creating distinct topography Ag-Ti NSs in a single step is possible by combining NP synthesis by multi-photon photo reduction and surface structuring via laser ablation.

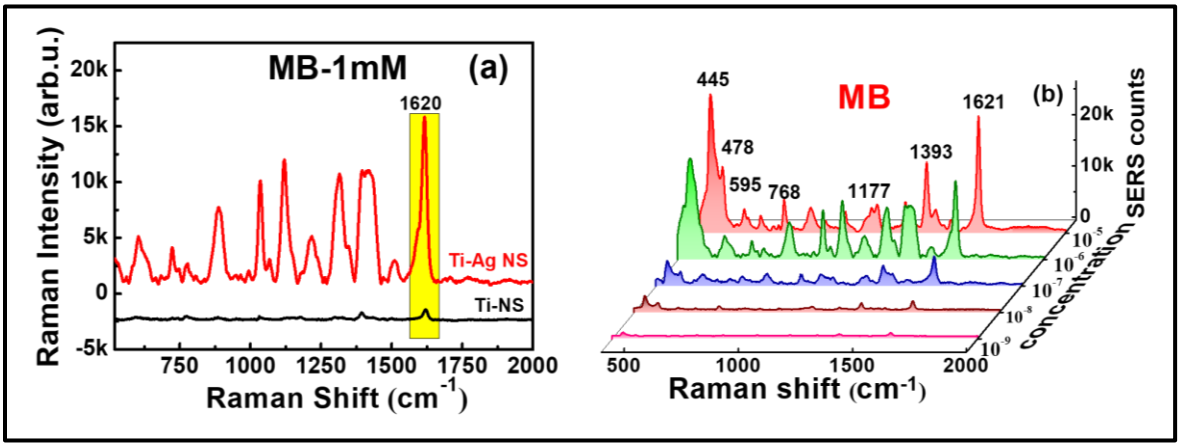

Figure 3. 8 (a) SERS of MB 1 µM using Ti and Ti-Ag NSs (b) Concentration SERS spectra of MB from 10^{-5} to 10^{-9} M using Ti-Ag NS.

Using methylene blue (MB) at a concentration of 1µM, the SERS performance of laser-textured Ti and Ti-Ag substrates was investigated; the corresponding spectra are shown in Figure 3.8(a). The major Raman bands were located at 445 and 1621 cm^{-1}; our previous investigations [61–64] revealed the matching assignments. The strongest signal is seen at 1621 cm^{-1}, which is thought to be a distinctive identifier for MB. A greater signal was seen in the case of Ti-Ag compared to the Ti NS, with counts in the most prominent peak (1620 cm^{-1}) almost 16 times higher. The TiO_2/Ag bilayer SERS substrate was reported by Wang et al.[65] using the chemical colloidal and sputtering approach. They also highlighted that the combination of charge-transfer (CT) and electromagnetic mechanism (EM) allowed them to generate a better signal from the metal-semiconductor system. The SERS spectra of MB at different concentrations (ranging from 10^{-5} M to 10^{-9} M) are shown in Figure 3.8(b). At 10^{-9}

M concentration, the signal strength (1622 cm^{-1} mode) is weakly noticed, as it declined with the concentration.

3.1.8. Conclusions

We present our research findings on femtosecond laser ablation in liquid, which includes the production of titanium dioxide (TiO_2) and titanium dioxide nanoparticles doped with silver (Ag-TiO_2). Titanium dioxide (TiO_2) and silver-titanium dioxide (Ag-TiO_2) nanoparticles were produced in deionized water utilizing the methods of fs laser ablation and simultaneous laser-induced chemical reduction by irradiation, respectively. In addition, we have conducted SERS experiments using both TiO_2 and Ag-doped TiO_2 nanoparticles (NPs). Nevertheless, we effectively detected the presence of RDX (100 µM) and ammonium nitrate (AN, 20 µM) in real-time utilizing Ag-doped TiO_2 NPs. However, we did not see any signal when employing TiO_2 NPs alone. We created a nanostructured Ti surface adorned with Ag using fs laser ablation and irradiation during this one-step procedure. The topographical ornamentation of Ag nanoparticles (NPs) and the nanoscale characteristics of the Ti nanospheres (NS) and the Ag-decorated Ti NSs have been discovered to be extraordinary, resulting in a substantial increase in the SERS signal. The Ag-Ti solid nanostructure (NS) used in SERS investigations exhibited a remarkably higher signal, 16 times stronger than Ti NS.

References:

[1] M.S. Chen, D.W. Goodman, The structure of catalytically active gold on titania, Science (80). 306 (2004) 252–255.

[2] H.B. Liao, R.F. Xiao, H. Wang, K.S. Wong, G.K.L. Wong, Large third-order optical nonlinearity in Au: TiO 2 composite films measured on a femtosecond time scale, Appl. Phys. Lett. 72 (1998) 1817–1819.

[3] Z. Chunfeng, L. Ye, Y. Guanjun, L. Bo, S. Jianlin, Q. Shixiong, Ultrafast nonlinear optical response of Au: TiO_2 composite nanoparticle films, Physica. B. Condens. Matter. 357 (2005) 334-339.

[4] G. Ma, J. He, S.-H. Tang, Femtosecond nonlinear birefringence and nonlinear dichroism in Au: TiO2 composite films, Phys. Lett. A. 306 (2003) 348–352.

[5] E.J. Heilweil, R.M. Hochstrasser, Nonlinear spectroscopy and picosecond transient grating study of colloidal gold, J. Chem. Phys. 82 (1985) 4762–4770.

[6] M.J. Bloemer, J.W. Haus, P.R. Ashley, Degenerate four-wave mixing in colloidal gold as a function of particle size, JOSA B. 7 (1990) 790–795.

[7] A. Rana, N. Gupta, A. Lochan, G.D. Sharma, S. Chand, M. Kumar, R.K. Singh, Charge carrier dynamics and surface plasmon interaction in gold nanorod-blended organic solar cell, J. Appl. Phys. 120 (2016) 063102.

[8] G. V Hartland, Optical Studies of Dynamics in Noble Metal Nanostructures, Chem. Rev. 111 (2011) 3858–3887. https://doi.org/10.1021/cr1002547.

[9] R. Allu, D. Banerjee, R. Avasarala, S. Hamad, S.V. Rao, G.K. Podagatlapalli, Broadband femtosecond nonlinear optical properties of silver nanowire films, Opt. Mater. (Amst). 96 (2019) 109305. https://doi.org/10.1016/j.optmat.2019.109305.

[10] S. Hamad, G. Krishna Podagatlapalli, R. Mounika, S.V.S. Nageswara Rao, A.P. Pathak, S. Venugopal Rao, Studies on linear, nonlinear optical and excited state dynamics of silicon nanoparticles prepared by picosecond laser ablation, AIP Adv. 5 (2015) 127127.

[11] K.N. Krishnakanth, B. Chandu, M.S.S. Bharathi, S.S.K. Raavi, S. V Rao, Ultrafast excited state dynamics and femtosecond nonlinear optical properties of laser fabricated Au and AgAu nanoparticles, Opt. Mater. (Amst). 95 (2019). https://doi.org/ARTN 10923910.1016/j.optmat.2019.109239.

[12] S.V. Rao, N. Venkatram, L. Giribabu, D.N. Rao, Ultrafast nonlinear optical properties of alkyl-phthalocyanine nanoparticles investigated using Z-scan technique, J. Appl. Phys. 105 (2009) 3109. https://doi.org/10.1063/1.3079801.

[13] A. Seetharaman, D. Sivasubramanian, V. Gandhiraj, V.R. Soma, Tunable nanosecond and femtosecond nonlinear optical properties of C–N–S-doped TiO2 nanoparticles, J. Phys. Chem. C. 121 (2017) 24192–24205.

[14] Y. Zhang, Y. Wang, Nonlinear optical properties of metal nanoparticles: a review, RSC Adv. 7 (2017) 45129–45144.

[15] M. Ren, B. Jia, J.-Y. Ou, E. Plum, J. Zhang, K.F. MacDonald, A.E. Nikolaenko, J. Xu,

M. Gu, N.I. Zheludev, Nanostructured plasmonic medium for terahertz bandwidth all-optical switching, Adv. Mater. 23 (2011) 5540–5544.

[16] Y. Lin, X. Zhang, Ultrafast multipolar plasmon for unidirectional optical switching in a hemisphere-nanoshell array, Adv. Opt. Mater. 5 (2017) 1601088.

[17] Y. Takeda, O.A. Plaksin, J. Lu, N. Kishimoto, Optical switching performance of metal nanoparticles fabricated by negative ion implantation, Nucl. Instruments Methods Phys. Res. Sect. B Beam Interact. with Mater. Atoms. 242 (2006) 194–197.

[18] M.S.S. Bharati, B. Chandu, S.B. Muvva, S.V. Rao, Third-Order Nonlinear Optical Studies of Ti and Hybrid Ti-Au Nanoparticles Generated by Laser Ablation in Liquids, in: ICOL-2019 Proc. Int. Conf. Opt. Electro-Optics, Dehradun, India, Springer, 2021: pp. 491–494.

[19] S.I. Kudryashov, P.A. Danilov, A.P. Porfirev, I.N. Saraeva, T.H.T. Nguyen, A.A. Rudenko, R.A. Khmelnitskii, D.A. Zayarny, A.A. Ionin, A.A. Kuchmizhak, S.N. Khonina, O.B. Vitrik, High-throughput micropatterning of plasmonic surfaces by multiplexed femtosecond laser pulses for advanced IR-sensing applications, Appl. Surf. Sci. 484 (2019) 948–956. https://doi.org/10.1016/j.apsusc.2019.04.048.

[20] D.A. Zayarny, A.A. Ionin, S.I. Kudryashov, S. V. Makarov, A.A. Rudenko, S.G. Bezhanov, S.A. Uryupin, A.P. Kanavin, V.I. Emel'yanov, S. V. Alferov, S.N. Khonina, S. V. Karpeev, A.A. Kuchmizhak, O.B. Vitrik, Y.N. Kulchin, Nanoscale boiling during single-shot femtosecond laser ablation of thin gold films, JETP Lett. 101 (2015) 394–397. https://doi.org/10.1134/S0021364015060132.

[21] A.A. Nastulyavichus, S.I. Kudryashov, A.M. Emelyanenko, L.B. Boinovich, Laser Generation of Colloidal Nanoparticles in Liquids: Key Processes of Laser Dispersion and Main Characteristics of Nanoparticles, Colloid J. 85 (2023) 233–250. https://doi.org/10.1134/s1061933x23600136.

[22] S.I. Kudryashov, G. Mourou, A. Joglekar, J.F. Herbstman, A.J. Hunt, Nanochannels fabricated by high-intensity femtosecond laser pulses on dielectric surfaces, Appl. Phys. Lett. 91 (2007) 1111.

[23] A.A. Ionin, S.I. Kudryashov, S.V. Makarov, A.A. Rudenko, P.N. Saltuganov, L.V. Seleznev, D.V. Sinitsyn, E.S. Sunchugasheva, Femtosecond laser fabrication of sub-diffraction nanoripples on wet Al surface in multi-filamentation regime: High optical harmonics effects?, Appl. Surf. Sci. 292 (2014) 678–681. https://doi.org/10.1016/j.apsusc.2013.12.032.

[24] S.I. Kudryashov, P.A. Danilov, S.G. Bezhanov, A.A. Rudenko, A.A. Ionin, S.A. Uryupin, S.F. Umanskaya, N.A. Smirnov, Plasmon-Enhanced Two-Photon Absorption of Infrared Femtosecond Laser Pulses in Thin Gold Films, JETP Lett. 109 (2019) 382–386. https://doi.org/10.1134/S0021364019060110.

[25] S.I. Kudryashov, I.N. Saraeva, V.N. Lednev, S.M. Pershin, A.A. Rudenko, A.A. Ionin, Single-shot femtosecond laser ablation of gold surface in air and isopropyl alcohol, Appl. Phys. Lett. 112 (2018) 3101. https://doi.org/10.1063/1.5026591.

[26] A.A. Ionin, S.I. Kudryashov, S. V Makarov, L. V Seleznev, D. V Sinitsyn, E. V Golosov, O.A. Golosova, Y.R. Kolobov, A.E. Ligachev, Femtosecond laser color marking of metal and semiconductor surfaces, Appl. Phys. A. 107 (2012) 301–305. https://doi.org/10.1007/s00339-012-6849-y.

[27] A.A. Nastulyavichus, S.I. Kudryashov, N.A. Smirnov, A.A. Rudenko, A.Y. Kharin, N.I. Busleev, D.A. Zayarny, A.A. Ionin, D.A. Kirilenko, P.N. Brunkov, Novel approach of controllable stoichiometric fabrication of alloyed Au/Ag nanoparticles by nanosecond laser ablation of thin bi-layered films in water, Laser Phys. Lett. 16 (2019) 096002. https://doi.org/10.1088/1612-202X/ab35cf.

[28] S.I. Kudryashov, A.A. Samokhvalov, S.N. Shelygina, N.I. Busleev, A.K. Ivanova, N.A. Smirnov, S.G. Bezhanov, S.A. Uryupin, A.A. Ionin, V.P. Veiko, Ultrafast Broadband Diagnostics of the Filling of the s Band at the Two-Photon Femtosecond Laser Excitation of a Gold Film, JETP Lett. 110 (2019) 250–253. https://doi.org/10.1134/s0021364019160069.

[29] U. Kreibig, M. Vollmer, Optical Properties of Metal Clusters, Springer Berlin Heidelberg, Berlin, Heidelberg, 1995. https://doi.org/10.1007/978-3-662-09109-8.

[30] K.M. Rahulan, N. Padmanathan, L.D. Stephen, C.C. Kanakam, Structural features and existence of three photon absorption in Ag doped TiO2 nanoparticles, synthesized by sol–gel technique, J. Alloys Compd. 554 (2013) 432–437.

[31] M. Qi, Y. Liu, T. Li, Nano-TiO_2 Improve the Photosynthesis of Tomato Leaves under Mild Heat Stress, Biol. Trace Elem. Res. 156 (2013) 323–328. https://doi.org/10.1007/s12011-013-9833-2.

[32] D. Banerjee, S.S.B. Moram, C. Byram, J. Rathod, T. Jena, G.K. Podagatlapalli, V.R. Soma, Plasmon-enhanced ultrafast and tunable thermo-optic nonlinear optical properties of femtosecond laser ablated TiO2 and Silver-doped TiO2 nanoparticles, Appl. Surf. Sci. 569 (2021) 151070. https://doi.org/10.1016/j.apsusc.2021.151070.

[33] R.P. Barkul, V.B. Koli, V.B. Shewale, M.K. Patil, S.D. Delekar, Visible active nanocrystalline N-doped anatase TiO2 particles for photocatalytic mineralization studies, Mater. Chem. Phys. 173 (2016) 42–51.

[34] J. Gomes, J. Lincho, E. Domingues, R.M. Quinta-Ferreira, R.C. Martins, N–TiO2 photocatalysts: A review of their characteristics and capacity for emerging contaminants removal, Water. 11 (2019) 373.

[35] L. Zhou, J. Zhou, W. Lai, X. Yang, J. Meng, L. Su, C. Gu, T. Jiang, E.Y.B. Pun, L. Shao, L. Petti, X.W. Sun, Z. Jia, Q. Li, J. Han, P. Mormile, Irreversible accumulated SERS behavior of the molecule-linked silver and silver-doped titanium dioxide hybrid system, Nat. Commun. 11 (2020) 1–10. https://doi.org/10.1038/s41467-020-15484-6.

[36] L. Yang, W. Wang, H. Jiang, Q. Zhang, H. Shan, M. Zhang, K. Zhu, J. Lv, G. He, Z. Sun, Improved SERS performance of single-crystalline TiO2 nanosheet arrays with coexposed {001} and {101} facets decorated with Ag nanoparticles, Sensors Actuators, B Chem. 242 (2017) 932–939. https://doi.org/10.1016/j.snb.2016.09.162.

[37] W. Wang, Q. Sang, M. Yang, J. Du, L. Yang, X. Jiang, X. Han, B. Zhao, Detection of several quinolone antibiotic residues in water based on Ag-TiO2 SERS strategy, Sci. Total Environ. 702 (2020) 134956. https://doi.org/10.1016/j.scitotenv.2019.134956.

[38] M. Muniz-Miranda, SERS monitoring of the catalytic reduction of 4-nitrophenol on Ag-doped titania nanoparticles, Appl. Catal. B Environ. 146 (2014) 147–150. https://doi.org/10.1016/j.apcatb.2013.03.008.

[39] R. Hong, J. Shi, Z. Li, J. Liao, C. Tao, Q. Wang, H. Lin, D. Zhang, Surface enhanced Raman scattering of defective TiO2 thin film decorated with silver nanoparticles by laser ablation, Opt. Mater. (Amst). 109 (2020) 110338. https://doi.org/10.1016/j.optmat.2020.110338.

[40] Z. Chen, Y. Sun, X. Zhang, Y. Shen, S.A.M. Khalifa, X. Huang, J. Shi, Z. Li, X. Zou, Green and sustainable self-cleaning flexible SERS base: Utilized for cyclic-detection of residues on apple surface, Food Chem. 441 (2024) 138345. https://doi.org/10.1016/j.foodchem.2023.138345.

[41] Y. Cao, R. Wu, W. Zhang, J. Luo, Y. Li, L. Ning, R. Shen, D. Wang, W. Ye, Killing two birds with one stone: Silver nanoparticles loaded on ultrathin N-doped carbon-coated TiO_2 porous spheres with narrow bandgap for efficient SERS sensing and photoinduced antibacterial applications, Appl. Surf. Sci. 583 (2022) 152512. https://doi.org/10.1016/j.apsusc.2022.152512.

[42] Y. Xie, Y. Meng, M. Wu, Visible-light-driven self-cleaning SERS substrate of silver nanoparticles and graphene oxide decorated nitrogen-doped titania nanotube array, Surf. Interface Anal. 48 (2016) 334–340. https://doi.org/10.1002/sia.5964.

[43] S. Xu, Y. Chen, H. Liu, X. Miao, X. Yuan, X. Jiang, Femtosecond laser ablation of Ti alloy and Al alloy, Optik (Stuttg). 212 (2020) 164628. https://doi.org/10.1016/j.ijleo.2020.164628.

[44] M. Akkanaboina, D. Banerjee, K. Ravi Kumar, R. Sai Prasad Goud, V.R. Soma, S.V.S. Nageswara Rao, Sub-70 nm surface structures on femtosecond laser irradiated GaAs in distilled water and sensing application, Opt. Lett. 48 (2023) 5539. https://doi.org/10.1364/OL.502527.

[45] S. Barcikowski, A. Hahn, A. V. Kabashin, B.N. Chichkov, Properties of nanoparticles generated during femtosecond laser machining in air and water, Appl. Phys. A Mater. Sci. Process. 87 (2007) 47–55. https://doi.org/10.1007/s00339-006-3852-1.

[46] S. V. Starinskiy, Y.G. Shukhov, A. V. Bulgakov, Laser-induced damage thresholds of gold, silver and their alloys in air and water, Appl. Surf. Sci. 396 (2017) 1765–1774. https://doi.org/10.1016/j.apsusc.2016.11.221.

[47] A.Y. Vorobyev, C. Guo, Femtosecond laser nanostructuring of metals, Opt. Express. 14 (2006) 2164. https://doi.org/10.1364/OE.14.002164.

[48] A. Plech, V. Kotaidis, M. Lorenc, J. Boneberg, Femtosecond laser near-field ablation from gold nanoparticles, Nat. Phys. 2 (2005) 44–47. https://doi.org/10.1038/nphys191.

[49] B. Rethfeld, D.S. Ivanov, M.E. Garcia, S.I. Anisimov, Modelling ultrafast laser

ablation, J. Phys. D. Appl. Phys. 50 (2017). https://doi.org/10.1088/1361-6463/50/19/193001.

[50] M. Senegačnik, P. Gregorčič, Diffraction-driven laser surface nanostructuring: Towards patterning with curved periodic surface structures, Appl. Surf. Sci. 610 (2023) 155486. https://doi.org/10.1016/j.apsusc.2022.155486.

[51] K.H. Leong, T.Y. Plew, R.L. Maynard, A.A. Said, L.A. Walker, Ablation of metals with femtosecond laser pulses, 4423 (2018) 1538–1546. https://doi.org/10.2351/1.5059824.

[52] I.N. Saraeva, S.I. Kudryashov, A.A. Rudenko, M.I. Zhilnikova, D.S. Ivanov, D.A. Zayarny, A. V Simakin, A.A. Ionin, M.E. Garcia, Effect of fs/ps laser pulsewidth on ablation of metals and silicon in air and liquids, and on their nanoparticle yields, Appl. Surf. Sci. 470 (2019) 1018–1034. https://doi.org/10.1016/j.apsusc.2018.11.199.

[53] P. Jafarkhani, S. Dadras, M.J. Torkamany, J. Sabbaghzadeh, Synthesis of nanocrystalline titania in pure water by pulsed Nd: YAG Laser, Appl. Surf. Sci. 256 (2010) 3817–3821.

[54] P. Russo, R. Liang, R.X. He, Y.N. Zhou, Phase transformation of TiO 2 nanoparticles by femtosecond laser ablation in aqueous solutions and deposition on conductive substrates, Nanoscale. 9 (2017) 6167–6177.

[55] M.S.S. Bharati, C. Byram, V.R. Soma, M. Sree Satya Bharati, C. Byram, V.R. Soma, Femtosecond Laser Fabricated Ag@Au and Cu@Au Alloy Nanoparticles for Surface Enhanced Raman Spectroscopy Based Trace Explosives Detection, Front. Phys. 6 (2018) 1–13. https://doi.org/10.3389/fphy.2018.00028.

[56] F. Moslehirad, M.H.M. Ara, M.J. Torkamany, M. Afsary, M. Ghorannevis, J. Sabbaghzadeh, Thermal nonlinear optical properties of TiO2 nanocrystals prepared through pulsed laser ablation, Laser Phys. 23 (2013) 55402.

[57] M.S. Satya Bharati, B. Chandu, S. V Rao, Explosives sensing using Ag-Cu alloy nanoparticles synthesized by femtosecond laser ablation and irradiation, RSC Adv. 9 (2019) 1517–1525. https://doi.org/10.1039/c8ra08462a.

[58] C. Byram, S.S.B. Moram, D. Banerjee, R. Beeram, J. Rathod, V.R. Soma, Review of ultrafast laser ablation for sensing and photonic applications, J. Opt. 25 (2023) 043001. https://doi.org/10.1088/2040-8986/acbc31.

[59] S.S.B. Moram, C. Byram, S.N. Shibu, B.M. Chilukamarri, V.R. Soma, Ag/Au Nanoparticle-Loaded Paper-Based Versatile Surface-Enhanced Raman Spectroscopy Substrates for Multiple Explosives Detection, ACS Omega. 3 (2018) 8190–8201. https://doi.org/10.1021/acsomega.8b01318.

[60] J. Rathod, C. Byram, R.K. Kanaka, M. Sree Satya Bharati, D. Banerjee, M. Akkanaboina, V.R. Soma, Hybrid Surface-Enhanced Raman Scattering Substrates for the Trace Detection of Ammonium Nitrate, Thiram, and Nile Blue, ACS Omega. 7 (2022) 15969–15981. https://doi.org/10.1021/acsomega.2c01095.

[61] V.S. Vendamani, S. Rao, A.P. Pathak, V.R. Soma, Robust and cost-effective silver

dendritic nanostructures for SERS-based trace detection of RDX and ammonium nitrate, RSC Adv. 10 (2020) 44747–44755. https://doi.org/10.1039/d0ra08834j.

[62] M.S.S. Bharati, V.R. Soma, Flexible sers substrates for hazardous materials detection: Recent advances, Opto-Electronic Adv. 4 (2021) 1–26. https://doi.org/10.29026/oea.2021.210048.

[63] H. Syed, G.K. Podagatlapalli, M.A. Mohiddon, V.R. Soma, SERS studies of explosive molecules with diverse copper nanostructures fabricated using ultrafast laser ablation, Adv. Mater. Lett. 6 (2015) 1073–1080. https://doi.org/10.5185/amlett.2015.6007.

[64] S. Hamad, G.K. Podagatlapalli, M.A. Mohiddon, V.R. Soma, Cost effective nanostructured copper substrates prepared with ultrafast laser pulses for explosives detection using surface enhanced Raman scattering, Appl. Phys. Lett. 104 (2014) 263104. https://doi.org/10.1063/1.4885763.

[65] Y. Wang, M. Li, D. Wang, C. Han, J. Li, C. Wu, K. Xu, Fabrication of highly uniform Ag nanoparticle-TiO2 nanosheets array hybrid as reusable SERS substrates, Colloid Interface Sci. Commun. 39 (2020) 100324.

Intentional Blank Page

Chapter 4

4A. Femtosecond Bessel Beam Induced Ladder-like LIPSS on Trimetallic, Bimetallic Surface for SERS-based Sensing of Tetryl and PETN

4B. Nanotubular Arrayed LIPSS Achieved with Femtosecond Bessel Beam on Silver and Uniform LIPSS on Copper Surface for SERS-based Multiple Explosives Sensing

4A.

Femtosecond Bessel Beam Induced Ladder-like LIPSS on Trimetallic, Bimetallic Surface for SERS-based Sensing of Tetryl and PETN

Abstract

Laser-induced periodic surface structures (LIPSS) have recently become a promising area of nanophotonics, with wide-ranging applications in several research domains, including on-chip microelectronics, hydrogen evolution, solar-energy conversion, photodetectors, photocatalysis, and sensing. This work presents the creation of a new kind of nanostructure called a trimetallic, ladder-like LIPSS using an axicon-generated femtosecond Bessel beam. This is the first time such a structure has been made using a combination of silver, gold, and copper alloys. The process behind the generation of LIPSS, which involves the adjustment of the ablation fluence profile and the interference of photon-induced surface plasmon polariton with the incoming beam, has been systematically explained. The use of overlapping Bessel beam profiles has been acknowledged to enhance the coupling of electromagnetic modes with pre-patterned surfaces. The period (Λ) of the created low spatial frequency LIPSS was determined to be 540±12 nm. In addition, a comparison analysis has been conducted to examine the unique topographical characteristics of nanostructures produced by a Gaussian beam with the same intensity. Moreover, these trimetallic plasmonic nanostructures have shown exceptional performance as active surface-enhanced Raman scattering substrates for sensing applications. Real-time explosives such as Tetryl and pentaerythritol tetranitrate (PETN) have been identified at a concentration of ~200 nM. The detection process has achieved enhancement factors in the region of 10^5, which makes it suitable for practical applications. In a follow-up work, we conducted laser ablation of a bimetallic alloy consisting of 50% gold and 50% silver in the presence of a fs Bessel beam that was produced. The interaction between high-intensity Bessel beams and matter created unique bimetallic nanostructures. The ladder-like nanoscale topographical structures were studied using extensive field emission scanning electron microscope and atomic force microscopy characterizations. These plasmonic nanostructures were then used as platforms for surface-enhanced Raman spectroscopy (SERS) to detect real-time residues of explosives, namely ammonium nitrate (AN) and Tetryl (TL). AN's SERS spectra showed a distinct Raman peak at 1043 cm^{-1}, whereas TL had a characteristic peak at about 1353 cm^{-1}. The minimum detectable concentrations were 10 µM for AN and 5 µM for TL. A graphical abstract for this chapter is shown below.

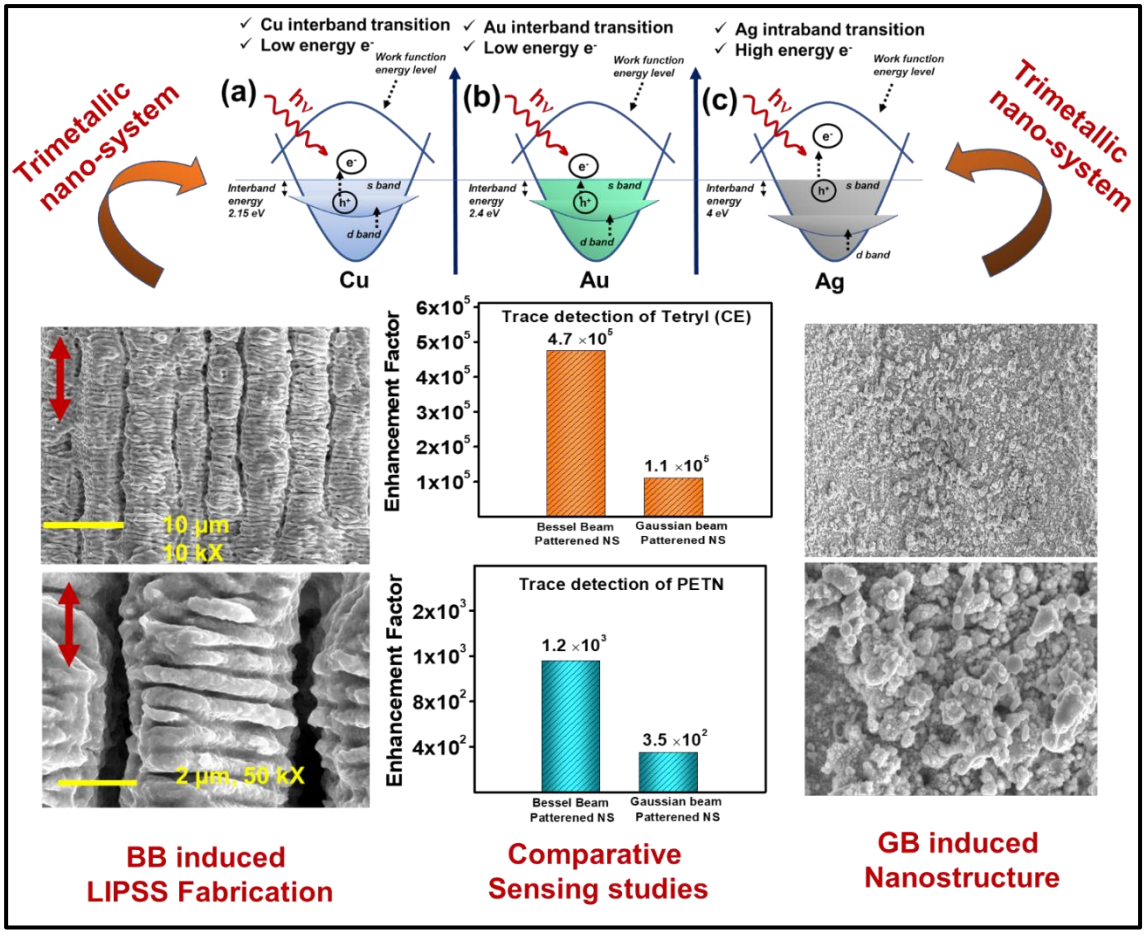

The work presented in this chapter has been published in,

1. **D. Banerjee**, M. Akkanaboina, R. Kumar Kanaka, V. Rao Soma, Femtosecond Bessel beam induced ladder-like LIPSS on the trimetallic surface for SERS-based sensing of Tetryl and PETN, Appl. Surf. Sci. 616 (2023) 156561. https://doi.org/10.1016/j.apsusc.2023.156561.

2. **D. Banerjee**, M. Akkanaboina, R.K. Kanaka, V.R. Soma, Ag-Au bimetallic ladder-like nanostructures achieved with femtosecond Bessel beam for real-time sensing of tetryl and ammonium nitrate, Laser-Based Micro- Nanoprocessing XVII. (2023) Proc. of SPIE Vol. 12409, https://doi.org/10.1117/12.2649704.

4A.1. Introduction

Nanotechnology and nanophotonics have grown significantly over the last fifty years [1-5], thanks to advancements in ultrafast laser-matter interaction. In the field of laser-matter interaction, laser-induced periodic surface structure (LIPSS) has emerged as a fascinating area of research. It has revealed exciting applications in photochemical water splitting, hydrogen evolution, surface chemistry, biomedical science, solar-thermal conversion, data storage, photodetectors, and industrial applications. Nanopatterning is crucial in the current semiconductor industry, photocatalysis, and microelectronics [6]. In addition to laser-based approaches, many additional procedures have also emerged for surface changes. Surface chemistry, catalysis-assisted surface modification, ion beam irradiation, electron beam irradiation, co-catalysis, and ion beam milling [7-11] are established methods for surface alteration. However, laser ablation has emerged as one of the most efficient techniques for producing periodic surface micro/nanostructures. Periodic, hierarchical topographies provide exceptional biomimetic and mechano-bactericidal properties [12], especially in biosensing applications. Many pioneering investigations [13,14] have methodically elucidated the intricate physics underlying the creation of different LIPSS topographies. Recently, the production of LIPSS by the interaction of ultrafast lasers has been recognized as a highly effective and practical approach. Bonse et al. [4,14,16] have conducted comprehensive investigations to comprehend the intricate process behind the genesis of LIPSS throughout the last decade. Senegacnik et al. have recently introduced a diffraction-assisted laser structuring technology [17] that utilizes cavitation bubbles created during the ablation process. This approach utilizes thermo-optical tweezers powered by thermocapillary pressures to create arc-shaped concentric microgroove channels determined by the beam guiding pattern. Chang et al. [18] recently demonstrated femtosecond laser-induced periodicity on a copper surface. The high repetition rate ablation experiment was simulated using a two-temperature model (TTM), which strongly correlated with the experimental results. Taher et al. [19] conducted thorough experiments on forming wavelength-dependent LIPSS on stainless steel, using a range of excitation wavelengths from 400 to 2200 nm. The achievement of regulated periodicity has been reported for both low spatial frequency LIPSS (LSFL) and high spatial frequency LIPSS (HSFL). Liu et al. studied metal film-assisted femtosecond laser structuring on a ZnO surface [20]. They could create ripples with a depth of around 100 nm that were smaller than the wavelength of light. A significant decrease in the damage

threshold was discovered, revealing a novel method for generating Laser-induced LIPSS in wide-bandgap materials. It also exhibited a fascinating anisotropic wetting behavior by conducting contact-angle measurements. Elshorbagy et al. [21] presented an intriguing study on the conversion of polarization state in infrared radiation, followed by the reflective interaction on LIPSS. The research examines the birefringence of the LIPSS to investigate how the incoming light's polarization state is modified. The subwavelength grating structure functions as a retarder, converting linearly polarized light into circularly polarized light. Lately, the advancement of structured light has provided opportunities to use many unique light patterns, including Bessel beams (BB), vector vortex beams, Mathew beams, and other non-diffracting beams. The beams have several notable advantages, including a self-healing optical profile [22,23], possession of orbital angular momentum [24], higher depth of focus (DOF), and invariance of intensity profile along propagation length [25]. These characteristics make them suitable for laser-matter interaction investigations [26,27], surface lithography studies [28], optical trapping, and optical coherence tomography [23]. The Axicon-produced BB [23] is a device that produces a distance-invariant, self-healing intensity profile. It is worth noting that this device has a superior depth of field. Remarkably, there is a lack of research studies on the interaction between fs BB and metals.

In this study, we used an axicon-generated femtosecond broadband (fs BB) light to perform surface structuring on an alloy substrate, taking advantage of the benefits of non-diffracting light. Alloy nanoentities, mixtures of several materials, provide better advantages and have more functions than typical plasmonic pure nanoparticles and nanostructures. The area of alloy nano-systems has been seeing significant growth, resulting in remarkable breakthroughs in optical, chemical, and photocatalytic capabilities. Amendola et al. [29], a group that has made considerable contributions to laser ablation, have provided a comprehensive overview of current progress in several areas of alloy nanostructures. Extensive research has been conducted on nano-systems consisting of metal-metal and metal-semiconductor alloys. These systems exhibit unique magneto-optical properties, generate hot carriers, enhance catalytic reactions through plasmon effects, have potential applications in medicine at the nanoscale, can tune localized surface plasmons (LSP), and exhibit properties that enhance Raman scattering on surfaces. The research conducted by Jiang et al. has uncovered a noteworthy finding about the detection of hydrogen using bimetallic Au/Pd nanostructures. [30] The

adjustable changes in plasmon resonance frequencies on the Au/Pd nanoparticles contributed to developing effective hydrogen sensors. Sytwu et al. [31] investigated using an antenna-reactor arrangement in a bimetallic nanoparticle system to analyze light-controlled reactions. Additionally, they have examined the adjustability of the photocatalytic reaction of the alloy nanostructures. Dahiya et al. [32] examined the plasmonic properties of gold-copper alloy nanoparticles. They thoroughly investigated the applications, including suitable simulations. Researchers have synthesized trimetallic nanoparticles using sol-gel, solvothermal, hydrothermal, and seed growth techniques. Gebre et al. [33] have comprehensively summarized the significant uses of trimetallic nanoparticles with regulated compositions in many areas, such as biosensing, dye-degradation, arsenic removal, improved catalysis, and H_2O_2 detection. There have been no reports on producing clean, chemical-free, ultrafast laser ablation technique-treated nanostructures made from a trimetallic (TM) alloy of Ag, Au, and Cu. There is still much to discover about the intriguing plasmonic reactions of various transition metal nanospheres (TM NSs) in the context of surface-enhanced Raman spectroscopy (SERS) sensing research.

This chapter describes our successful fabrication of unique ladder-like low spatial frequency LIPSS on a newly developed Ag-Au-Cu transition metal alloy nanostructure. We achieved this by using a femtosecond (fs) laser beam, specifically a Bessel beam (BB), created optically using an axicon. Later, in a comparative investigation, we uncovered the significant structural distinctions between Gaussian beam (GB) and BB-manufactured NSs, which, to our knowledge, is the first observation of its kind. The innovative nanoscale structures (NSs) have shown captivating uses as substrates active in SERS for detecting explosives in real-time, namely Tetryl and PETN. The experimental results have been corroborated by detailed discussions on the development process of LIPSS and the nanophotonic behavior of the Ag-Au-Cu transition metal (TM) system.

4A.2. Experimental details

The process of femtosecond laser ablation in the air (LAA) was performed with a Bessel beam profile. The Bessel beam with a wavelength of 800 nm, a repetition rate of 1 kHz, and a pulse duration of 50 fs was produced using an Axicon (10^0, model AX1210-B, AR coated, suitable for the infrared range) from Thorlabs, UK. The axicon was used to shape

a Gaussian profiled beam obtained from a chirped-pulse amplified Ti: Sapphire laser system (model LIBRA, manufactured by Coherent). The trimetallic substrates used to create TM NSs were formed by melting and alloying Au, Ag, and Cu, all of which had a purity level above 99.9%. After the targets were cleaned in an ultrasonic bath, they were subjected to a BB interaction ablation procedure. Ablation was performed using a time-limited single spot method, lasting 2 seconds and consisting of 2000 pulses. This was followed by a full laser raster scan ablation, which took around 26 minutes. The ablation process used two X-Y stages and a LabVIEW interfaced motion controller (ESP 300, Newport, USA). A laser was irradiated at a rate of around 3300 pulses per millimeter. The scan speed was 0.3 millimeters per second, and the distance between each line was 55 micrometers during the raster scan. Therefore, a significant TM NS region (5 mm x 5 mm) was created by BB ablation. To examine the characteristics of the nanoscale structures and identify their components, we used a field emission scanning electron microscope (FESEM, ZEISS ULTRA 55, Graz, Austria) to detect the topographical features. This was followed by conducting energy dispersive X-ray spectroscopy (EDX). The NSs were analyzed using the atomic force microscopy (AFM) method using Japan's HI-TACHI AFM 5000-SPA400 apparatus to get accurate measurements of the ablation-depth profiles. The SERS measurements were conducted using a portable Raman system (102 mW, 785 nm excitation, about 90 μm spot size, accumulation duration of 5 seconds, spectral averaging of 3) known as the i-Raman plus (manufactured by B&W Tek, USA). The SERS Mapping tests were conducted using a Micro Raman spectrometer, namely the LabRAM HR Evolution manufactured by M/s Horiba France SAS, France. The acquisition settings for mapping were configured as follows: wavelength of 532 nm, an input power of 135 mW, a 10X objective, a spot size of about 3 μm, and an acquisition period of 5 seconds.

4A.3. Results & Discussion

4A.3.1 Nanoscale topographies designed under Bessel beam contact

Initially investigated by Durnin et al. [34], non-diffracting Bessel beams have potential applications in optical trapping and ultrafast material processing [22,23]. This is due to their notable optical properties, including an intensity profile that remains unchanged over long distances, self-healing capabilities, and an extended depth of focus. The Bessel beam has notable characteristics that provide benefits over the Gaussian beam, making it a

preferable option for surface structuring research. The fs, zeroth order BB, involved in this study have a center maximum intensity on the axis, with surrounding circular ring nodes [23]. The surface modification procedure included using the unique and unusual beam profile and the benefits outlined earlier to carry out ablation. To get a comprehensive understanding of fs BB ablation, which involves the creation of various NSs, we conducted LAA experiments using multiple configurations, including single spot ablation and raster scanned ablation.

4A.3.1.1. Ablation on a single spot

An evident beam profile imprint was seen on the ablation site of the TM substrate surface [Figure 4A.1(a)], after the interaction of about 2000 pulses (equivalent to 2 seconds of ablation duration). An area with a radius of about 15.1 µm (CR1) that had been ablated was seen in the FESEM picture of the region irradiated by a single spot. This ablated area was encircled by concentric, periodic rings. In Figure 4A.1(b), the concentric rings were seen to have a spatial periodicity of around 5 µm. These rings stretched across a distance of more than 50 µm around the central lobe part. Subsequently, creating a captivating geographical characteristic in a specific location, resulting from fs BB profiled ablation, inspired the desire to produce a vast NS across a wide region. The intensity profile of the generalized Bessel beam, as shown in Figure 4A.1(c), was simulated using MATLAB's zeroth-order Bessel function (J_0) profile. This simulation is consistent with the experimental evidence of the Bessel beam imprint on a single location. The profile of Figure 4A.1(c) reveals a greater intensity in the central lobe area and a notable presence of concentric rings on both sides.

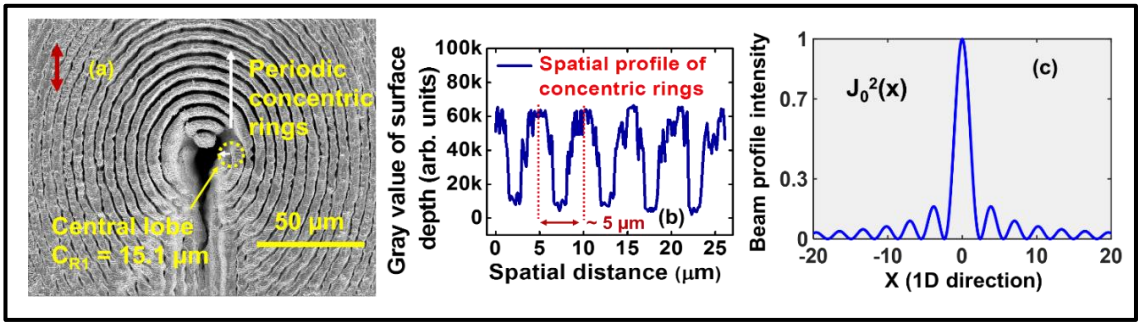

Figure 4A. 1 (a) FESEM image of single spot fs BB ablation producing BB profiled ablation imprint on TM substrate surface, red arrow depicts the laser polarization direction, (b) Spatial periodic profile analysis of the concentric rings surrounding the central lobe portion. (c) MATLAB simulated intensity beam profile of generalized zeroth order BB from Bessel function $J_0(x)$ term.

4A.3.1.2. Large area Bessel beam overlapping

The surface of the TM substrate was subjected to a raster scan using fs BB ablation to create an extensive area of NS. A significant overlap was detected in the large area of the ablated zones, namely in the region shown in [Figure 4A.2(a)], during the nanoscale topography characterization using FESEM. The higher magnification photos in Figure 4A.2(b) and 4A.2(c) (at 700X and 1500X) provide a zoomed-in view of a specific part of Figure 4A.2(a).

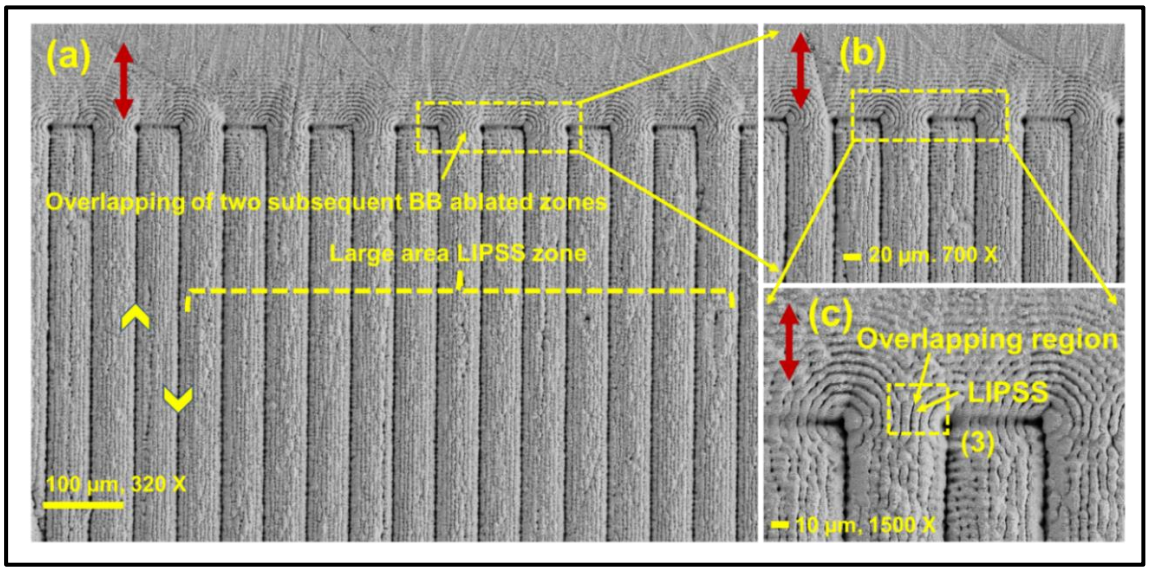

Figure 4A. 2 (a) Large area overlapping of BB ablated zones, leading to the formation of the complete raster scanned NS, (b) 700X magnified portion from Figure 4A.2(a), (c) overlapping between two consecutive BB profiled laser ablated region, with 1500X magnification. The square-marked (3) region displays the region of overlap. The red arrow depicts the laser polarization direction.

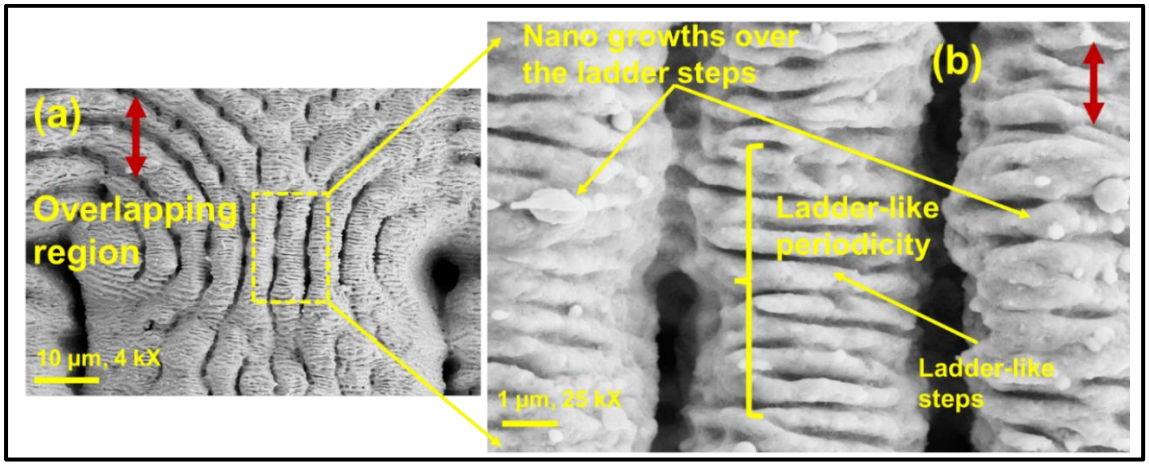

Figure 4A. 3 (a) Region of overlap, 4 kX magnified (b) magnified region from Figure 4A.3(a), revealing ladder-like periodic NSs, having nano growths on the ladder steps. The red arrow depicts the laser polarization direction.

These images demonstrate the overlapping of a BB ablated zone with its following ablated region. Figure 4A.2(c) illustrates the complete overlap of two consecutive BB-profiled ablation zones at the beginning of both corresponding ablation lines. Additional photographs at greater magnification, namely from the area shown with a square in Figure 4A.2(c), provide a detailed comprehension of the overlapping occurrences. The production of ladder-like periodic nanoscale structures (NSs), mainly resulting from the overlap of ablation zones, was also verified in Figure 4A.3(a) and 4A.3(b). Nanostructures of interest were also seen on the ladder's steps, plainly visible in the same photograph.

4A.3.1.3. Trimetallic nanostructures possessing having ladder-like features

Extensive field-emission scanning electron microscopy (FESEM) experiments were conducted to characterize different parts of the laser-ablated area following the raster scan and demonstrate the production of trimetallic periodic nanostructures throughout. After extensive adjustment, it has been shown that a central threshold fluence of 10 J/cm^2 is the most effective for generating mature, ladder-like LIPSS on the Ag-Au-Cu trimetallic substrate. When using a BB fluence below the optimal amount, we observed the production of underdeveloped, randomly dispersed periodic patterns that differed from the desired ladder-like LIPSS. Therefore, we have used a fluence of 10 J/cm^2 for surface structuring. Figure 4A.4(a) displays a high-resolution picture (5 µm × 5 µm) of the laser-induced periodic surface patterns. Figure 4A.4(b) shows an enlarged portion. Figures 4A.4(c) and 4A.4(d) demonstrate the presence of ladder-like periodic nanostructures when seen at magnifications of 10 kX and 50 kX, respectively. In addition, the highlighted regions in Figure 4A.4(c) and 4A.4(d) have been shown in more detail in Figures 4A.4(e) and 4A.4(f) correspondingly. The periodic ladder-step-like nanostructures (NSs) are visible in Figure 4A.4(f), which shows an image magnified at 100kX. The NSs have a periodicity (Λ) of 540±12 nm. The periodicity (Λ) of the generated trimetallic NS has been determined to be low spatial frequency laser-induced periodic structures (LSFL), with $\Lambda > \lambda/2$. Specifically, Λ equals 0.7 times the excitation wavelength (λ). Furthermore, the LIPSS were seen to be formed at a right angle to the excitation laser polarization, which aligns well with the findings in the literature [4, 37, 38].

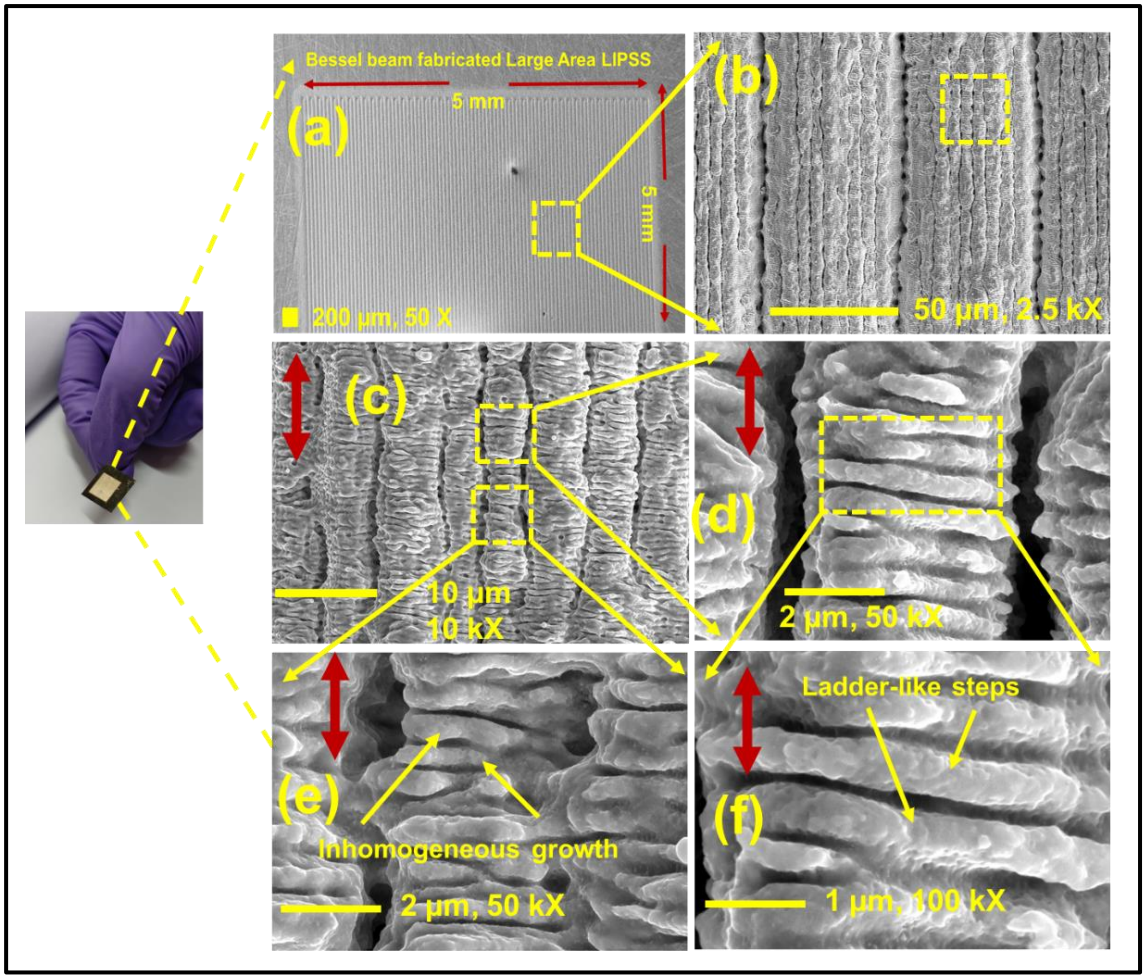

Figure 4A. 4 The image on the left-most side portrays the physical outlook of the BB ablated TM NS substrate (a) FESEM image (50 kX magnification) of the large area NS (b) FESEM image of BB ablated TM NS, under 2.5 kX magnification (c) lower magnification image corresponding to the yellow square-dashed position in Figure 4A.4(b), 4A.4(d), (e) 50 X magnified images from separate, correspondingly identified positions of the image (c), (f) exhibits the ladder-like NS, with 100 kX magnification. Yellow dashed boxes with arrow lines indicate the region that has been magnified in the subsequent image. The red arrow depicts the laser polarization direction.

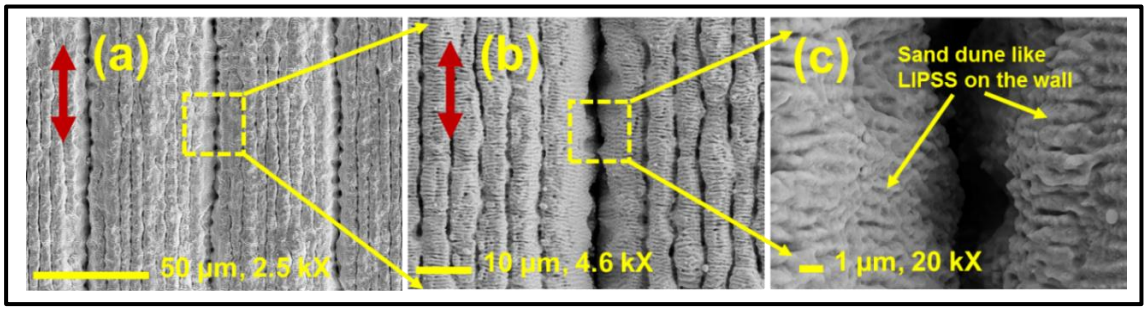

Figure 4A. 5 (a) FESEM image of BB central lobe ablated lines in 2.5 kX magnification, (b) and (c) central lobe ablated line regions in higher magnifications, 4.6 kX, 20 kX, respectively. Yellow dashed boxes with arrow lines indicate the region that has been magnified in the subsequent image. Sand dune-like periodicity is observed around the walls of the central lobe ablated line. The red arrow depicts the laser polarization direction.

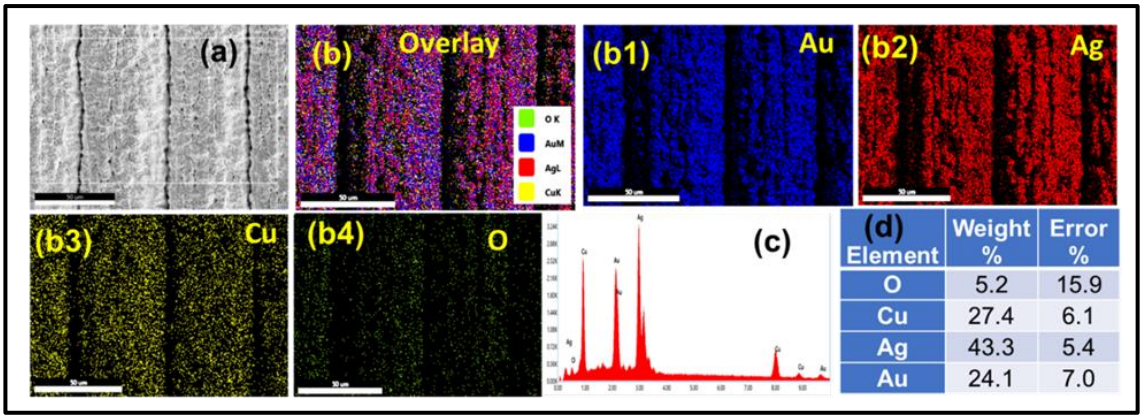

Figure 4A. 6 EDX mapping data of BB patterned TM NS. (a) the region under EDX mapping, (b) overlay mapping data exhibiting the existence of all the elements. Individual exhibition of EDX mapping data for all the elements found (b1) Au, (b2) Ag, (b3) Cu, (b4) O, (c) and (d) show elemental peaks and weight percentages of each element found respectively.

Apart from the ladder-like, periodic, nanostructured area [shown in Figure 4A.4(b)], the characteristics of the center lobe ablation line region [Figure 4A.5(a)] were also revealed. Figures 4A.5(b) and 4A.5(c) clearly show the small-scale characteristics formed in the stated area at magnifications of 4.6 kX and 20 kX, respectively. Figure 4A.5(c) clearly shows the formation of a deep ablation line surrounded by nanogrowths resembling 'sand dunes'. The sand dune-like growths, seen on the central-line wall (refer to Figure 4A.5(c)), exhibit a structural resemblance to ladder-like NS (refer to Figure 4A.4(d)). EDX mapping measurements were conducted to determine the elemental compositions of the NSs generated during BB ablation. The produced NSs exhibited the presence of three metals, namely Cu, Ag, and Au, coupled with Oxygen (O) in specific weight percentages: Cu - 27%, Ag - 43%, Au - 24%, and O - 5%. This observation was widespread throughout a considerable region. The full EDX overlay mapping image and data have been shown in Figures 4A.6(a-b). The corresponding EDX spectrum and elemental quantification table have been shown in Figures 4A.6(c) and 4A.6(d). Moreover, AFM measurements have been conducted on different areas of the same NS to provide data on its average depth profile [Figure 4A.7(a)]. The greatest distance between two ladder-like structures was approximately calculated to be 900 nanometers. In contrast, the average distance among the periodic ladder step-like nanostructures was determined to be about 95 nanometers. Figure 4A.7(b) displays the comprehensive AFM data regarding the depth profile.

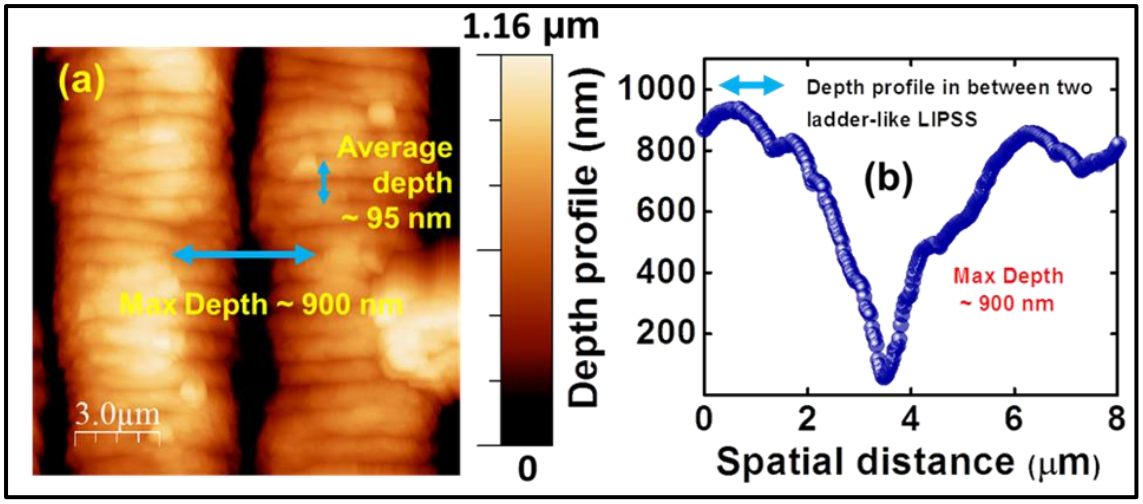

Figure 4A. 7 (a) AFM data corresponding to the BB ablated ladder-like periodic NS, the average depth within the periodic ladder step-like NSs is estimated to be ~95 nm. (b) the maximum depth between two ladder-like structures was ~900 nm, extracted from the AFM image and shown on the right.

4A.3.2. Bessel beam interacted LIPSS formation mechanism

LIPSS has become a perennial and cutting-edge scientific discipline, branching into other relevant areas. The extensive research conducted on LIPSS formations on metals and semiconductors [39–45] has focused on explaining the underlying phenomena using electromagnetic theories related to the excitation of different surface electromagnetic waves (SEWs) [14], particularly surface plasmon polaritons (SPP) [46]. When ultrashort pulses excite the conduction band (CB) electrons, delocalized coherent electron oscillations known as surface plasmon polaritons (SPPs) are generated. These SPPs travel over metal-dielectric interfaces, as seen in Figure 4A.8(a). The interaction between the dispersed field of the surface plasmon polariton (SPP) and the incoming beam causes a modulation in the intensity pattern (fluence) of the local ablation at the metal surface. It also leads to changes in the distribution of temperature [13,49,50]. The modulation of the intensity profile in the interaction field is a significant factor in the periodic alteration of the surface topography, as shown in Figure 4A.8(b). Consequently, spatially modulated melting may occur due to the interaction between electrons and phonons within a picosecond timeframe. The LIPSS period is directly correlated with the dielectric permittivity in the following manner,

$$\Lambda = \lambda_{SPP} = \lambda * Re\sqrt{\frac{(\varepsilon_d+\varepsilon_m)}{(\varepsilon_d*\varepsilon_m)}} \quad \text{..... (1)}$$

The symbols ε_d and ε_m represent the dielectric constants of the air and metal systems, respectively, with ε_d approximately equal to 1. For metallic systems, it has been shown that Re(ϵ_m) is less than -1[14]. Therefore, the λ_{SPP} may be expected to fall between the range of $\lambda/2$ to λ. The theoretical estimate of periodicity is in excellent agreement with the experimentally measured LIPSS period (Λ) for the trimetallic system ($\Lambda=0.7\lambda$, as determined in the preceding section).

For the generation of multi-pulse (kHz) LIPSS in the case of fs, the expansion of the initial seed, created by intra-pulse, inter-pulse feedback [4], is crucial in the ablative regime. Photons in free space have less momentum than surface plasmon polaritons (SPPs). As a result, the repeating irradiation method, which involves unique surface roughness modulations caused by the initial pulses, helps enhance the coupling between SPPs and photons by matching their momenta [14]. This phenomenon has also been denoted as grating-assisted surface plasmon polariton (SPP) coupling [51]. Therefore, under the scenario of 1 kHz, fs ablation, the changes in surface topography caused by the main pulses might promote the creation of LIPSS. Gurevich et al. [52,53] have provided detailed explanations for creating single-pulse LIPSS to corroborate the earlier hypothesis. Maragkaki et al. have successfully demonstrated an improved efficiency in coupling electromagnetic modes using pre-patterned surfaces [54]. The work highlights the importance of seed development triggered, pre-patterned LIPSS generation in facilitating the analogical comprehension of BB beam-induced LIPSS. In the case of BB ablation, the beam profile with concentric rings may provide the benefits of pre-patterning, as described in section 3.1.2, and stimulate the excitation of SPPs in numerous areas. It is reasonable to assume that interactions between these surface plasmon polaritons (SPPs) might have an additional impact on the interference between the dispersed light field that has been altered and the incoming beam. One possible explanation for this phenomenon is the ladder-like TM LIPSS generated during BB ablation. In contrast, no such LIPSS creation was seen in the case of GB contact [see Figure 4A.9]. Recent advancements in the comprehension of LIPSS creation indicate that when a high intensity (~1 J/cm^2) fs laser pulse is applied, a pair of counterpropagating SPPs [with opposing directional propagation vectors K_{S1}, K_{S2}, as shown in Figure 4A.8(a)] are produced [55]. The interference field induces periodic changes in the permittivity, amplifying the magnitudes of surface plasmon polaritons (SPPs), leading to the formation of LIPSS.

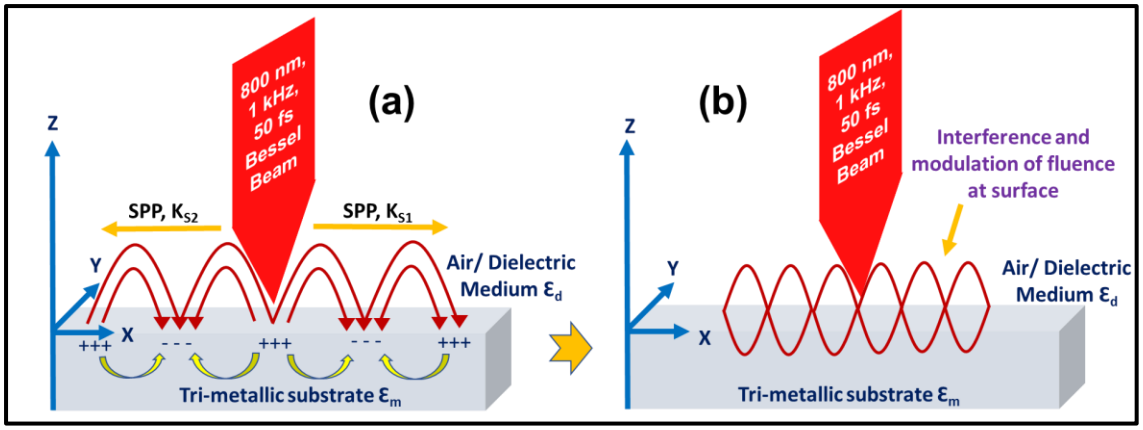

Figure 4A. 8 (a) Bessel beam induced SPP generation and propagation towards counter-direction along TM surface-air interface. (b) A periodic modulated intensity profile was developed following the interference of a scattered field with the incident beam.

The creation of LIPSS is greatly influenced by the decay length (mean free path) of the SPPs, which refers to the decrease in coherence qualities of the SEWs. According to the findings presented by Gnilitskyi et al. [49], plasmonic metals such as Ag, Au, and Cu, which have substantial optical damping, show a very short decay duration of surface plasmon polaritons (SPP). This may have also served as an advantage for the TM LIPSS formations. Additionally, to fully understand the ablation process of a trimetallic system, it is crucial to examine the ablation threshold as a critical factor. When exposed to fs pulses, plasmonic metals, including Au, Ag, and Cu, show significant differences in ablation thresholds [56]. These differences may be due to variations in thermal conductivity, heat capacity, and absorption coefficients. Au has a higher ablation threshold than Cu and Ag [56,57]. Moreover, alloys have a reduced ablation threshold compared to pure metals, mostly because of their diminished heat conductivity [58]. The notable differences in the solid-state physical characteristics of these three plasmonic metals are likely to influence the ablation process. The emergence of inhomogeneous LIPSS formations, which are observable in some parts [as shown in Figure 4A.4(e)] of the NS, may be comprehended based on that. This section provides a comprehensive analysis of several factors that contribute to the creation of TM LIPSS and reveals, for the first time, the basic relationship between BB ablation and TM LIPSS.

4A.3.3. Differences in structural formation between Gaussian beam ablation

Ablation using a Gaussian beam, created using a plano-convex lens with a diameter of 10 cm, was also conducted on the surface of the TM substrate. The fluence used was kept

constant, matching that produced by the centre lobe of the BB. We were motivated to study the specific structural changes that resulted from changing the beam profile. The highest intensity, generated in the centre region of the Bessel beam [59], may be mathematically represented as,

$$F = \frac{2Q\beta}{w\sqrt{e}} \quad \text{…….. (2)}$$

$\beta = \frac{2\pi(n-1)\alpha}{\lambda}$; n being the refractive index of the axicon lens materials, α is the apex angle of the same. After calculating the BB fluence, it was determined to be constant [estimated at around 10 J/cm^2, using equation (2)] in the case of the GB-interacted LAA scenario. The fs Gaussian beam produced noticeably different nanostructures while maintaining the same values for other ablation parameters, such as raster scan speed and interline spacing [Figure 4A.9]. Figures 4A.9(a) and 4A.9(b) show the lower magnification pictures of the TM NS created using GB. The photos were taken at magnifications of 300X and 500X. The TM NS segments seen in Figure 4A.9(b), highlighted by light and dark blue dashed line boxes, are shown in greater magnification (10 X) pictures in Figures 4A.9(c) and 4A.9(d). Figures 4A.9(e) and 4A.9(f) depict two distinct areas from Figure 4A.9(d), which are marked by dashed boxes in dark red and purple. These areas are seen with a magnification scale of 50 kX. The manufactured TM NS exhibited a distinct nanoscale surface topography, which differed significantly from the TM NS created by BB. This work demonstrates the significant disparities in the nanostructures generated using fs Bessel and Gaussian beams while keeping the laser fluence constant. Figures 4A.4 and 4A.9 vividly show the topographical disparity. Exotic LIPSS NSs emerge while using BB. In contrast, the Gaussian beam produces spherical and aspherical nanogrowths throughout the laser-patterned surface. In addition, we want to do a comprehensive investigation in the future that will use both beams and vary the fluence. Subsequently, the EDX mapping was conducted on the NS created by the GB to examine the primary constituents in the area that had been removed. The data is shown in Figure 4A.10. The compositional properties of the GB ablated NS, consisting of 23% Cu, 48% Ag, 26% Au, and 2.5% O, are similar to those of the BB-produced TM NS, as shown by the EDX results. Figure 4A.11 displays the FESEM picture of the pure TM substrate before any ablation, providing a clear explanation.

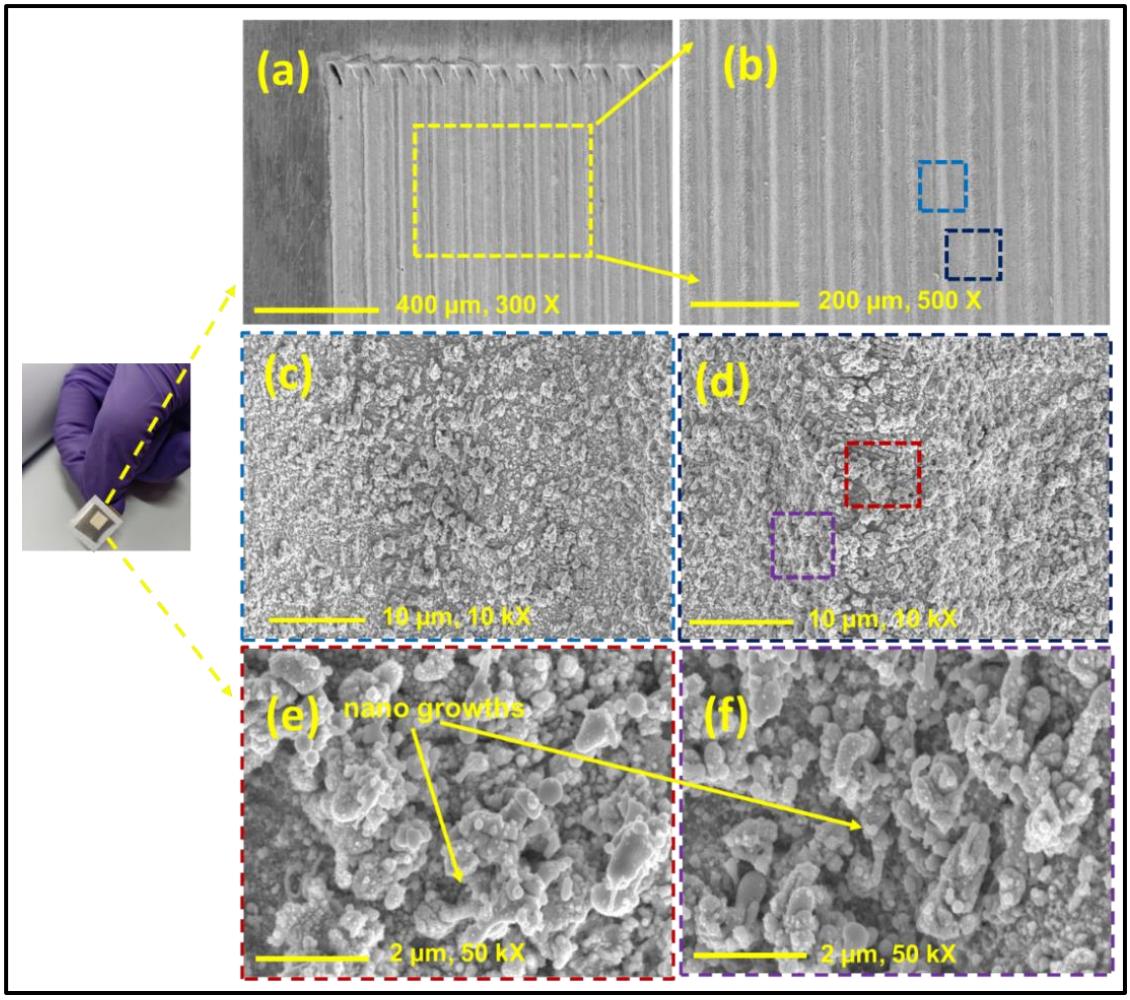

Figure 4A. 9 The image on the left-most side portrays the physical outlook of the GB ablated TM NS substrate (a), (b) depict lower magnification (300 X, 500 X correspondingly) images of fs GB fabricated TM NS, (c) and (d) exhibit 10 kX magnification images of corresponding sections marked in light, dark blue dashed boxes in Figure 4A.9(b). Similarly, (e) and (f) present 50 kX magnified regions identified with dark red- and purple-colored dashed boxes, respectively, in Figure 4A.9(d).

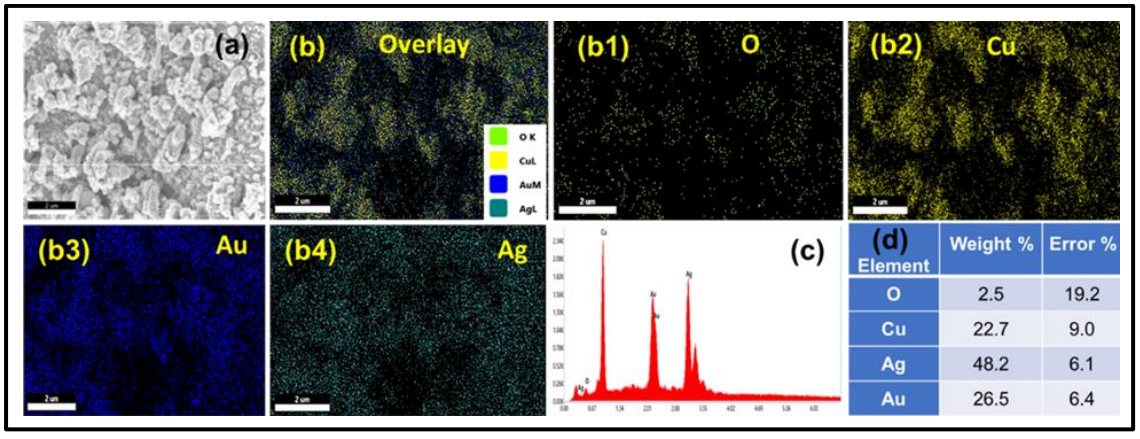

Figure 4A. 10 EDX mapping data of Gaussian beam patterned TM NS. (a) the region under EDX mapping, (b) overlay mapping data exhibiting the existence of all the elements. Individual exhibition of EDX mapping data for all the elements found- (b1) O, (b2) Cu, (b3) Ag, (b4) Au, (c) and (d) depict elemental peaks and weight percentages of each element found respectively.

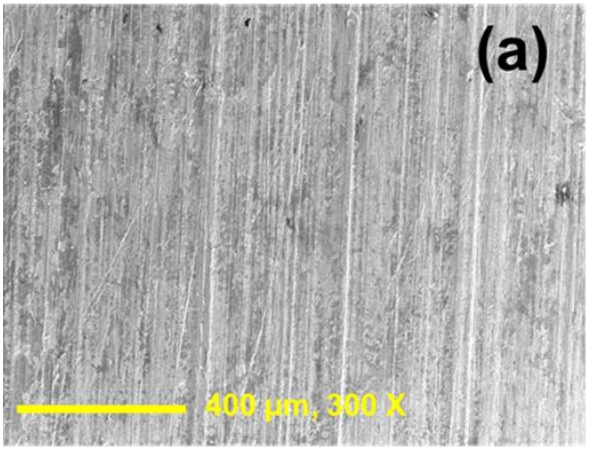

(b)

Element	Weight %	Error %
O	15.5	12.0
Cu	27.8	6.3
Ag	39.4	5.2
Au	17.3	8.2

Figure 4A. 11 (a) FESEM image of unablated, pristine TM substrate surface. (b) EDX data was collected from the unablated, pristine TM substrate surface, confirming the presence of three metals, Ag, Au, and Cu.

4A.3.4. Sensing studies based on SERS

The finding of surface-enhanced Raman scattering has established a significant milestone and facilitated a substantial advancement in spectroscopy, analytical photonics, and sensing [60]. In addition to SERS, the rapidly developing area of plasmonics has provided a vast platform for a wide range of photonics applications, including biosensors, photodetectors, photochemical water splitting, hydrogen evolution, waveguiding, and biomedicines. Extensive studies have been conducted on the plasmon-enhanced SERS approach in sensing [25,61–68]. Our objective has been to analyze the effectiveness of the trimetallic NS generated by BB as on-chip SERS substrates. Therefore, their main focus was on using the SERS approach to detect explosives in real-time, namely Tetryl (CE-2,4,6-trinitrophenylmethylnitramine) and PETN (pentaerythritol tetranitrate). The ladder-shaped periodic nanostructure effectively functioned as a highly plasmonic, reusable substrate for SERS in detecting small amounts of the aforementioned dangerous substances. Figure 4A.12(a) illustrates the concentration-dependent SERS signal data for CE. The minimum detectable concentration is 200 nM. The molecule's hallmark Raman peaks were discovered at 826 cm^{-1}, 1183 cm^{-1}, and 1357 cm^{-1} at 200 nM, 500 nM, 5 µM, 50 µM, 100 µM, 0.5 mM, and 5 mM. No peaks were seen at concentrations lower than 200 nM. The primary characteristic peaks of CE are ascribed to the symmetric and asymmetric stretching of NO_2 at 1357 cm^{-1} and the vibrations of nitro-aromatic compounds at 826 cm^{-1} [69]. To assess the uniformity of the SERS signal produced by the TM NS, about 25 SERS spectra were obtained from various random locations. The

relative standard deviation (RSD) of the SERS signals corresponding to the 1357 cm^{-1} peak of the compound of interest (CE) at a concentration of 100 μM was determined to be around 12% [refer to Figure 4A.12(b)]. This indicates that the substrate is very effective for real-time sensing applications. Subsequently, the TM NS was immersed in a methanol-filled ultrasonic bath for 2 hours to eliminate any residual contaminants. The same substrate was used to detect PETN molecules in small quantities.

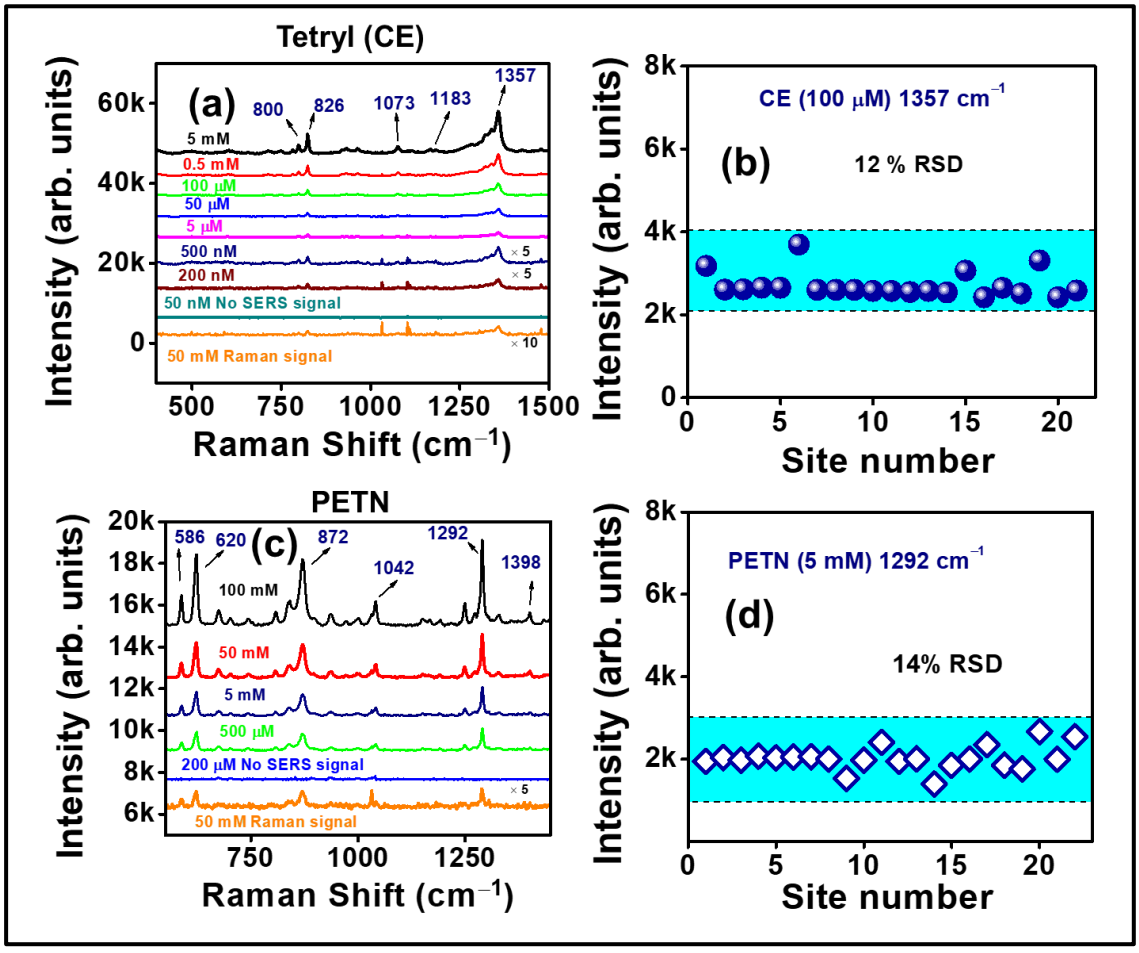

Figure 4A. 12 (a) Concentration-dependent SERS spectra of CE using BB ablated TM NS, along with pure Raman spectrum (in orange color) of CE (50 mM) collected from unablated TM pristine, (b) Reproducibility spectra (with ~12% RSD) of CE (100 μM), (c) Concentration-dependent SERS spectra of PETN using recycled BB ablated TM NS, along with pure Raman spectrum (in orange color) of PETN (50 mM) collected from unablated TM pristine, (d) Reproducibility spectra (with ~14% RSD) of PETN (5 mM). The portable Raman acquired the complete SERS data in this Figure, with the same acquisition parameters mentioned in the experimental details.

The Raman peaks corresponding to various doses of PETN were detected at 620 cm^{-1}, 872 cm^{-1}, 1042 cm^{-1}, and 1292 cm^{-1}, respectively. The minimum detectable concentration was 500 micromolar (μM) [data presented in Figure 4A.12(c)]. The Raman modes associated

with the conspicuous peaks of PETN were seen at 620 cm^{-1} [corresponding to the rocking transition of the O− NO_2 bond], 872 cm^{-1} [corresponding to the stretching of the O− N bond], and 1292 cm^{-1} [corresponding to the symmetric stretching of the NO_2 bond] [reference 70]. In addition, the uniformity of the plasmonic enhancement in terms of SERS signals was evaluated for this molecule, resulting in a disclosed relative standard deviation (RSD) of around 14% [data presented in Figure 4A.12(d)]. The recyclability of these substrates has a considerable influence on practical applications.

The consistency of the SERS signal for PETN (5 mM) was confirmed for the 1292 cm^{-1} peak. The size and form of the NSs are key factors that significantly influence the evanescent field due to the enhanced Raman signal resulting from localized surface plasmons. To examine if there was any change in signal amplification caused by significant structural variations, the SERS analysis was conducted again using GB-ablated TM NSs under comparable circumstances. Upon examination, we have seen a substantial disparity in the CE molecule's minimum detectable amount (500 nM). Additionally, there was a noticeable shift in the repeatability data, with somewhat elevated RSD values for both Tetryl and PETN. Concerning the chemical PETN, the minimum detectable concentration remained the same. However, the SERS signal counts exhibited a significant drop. Figure 4A.13(a-d) shows the SERS data obtained using GB-ablated TM NS. To get a clear picture, we assessed the enhancement factors (EFs) corresponding to both NSs, using the well-established mathematical relation, i.e.,

$$E.F = \frac{I_{SERS}}{I_{Raman}} \times \frac{C_{HC}}{C_{LC}} \qquad \text{…….. (3)}$$

The I_{SERS} term represents the heightened intensity of the prominent Raman peak of a specific analyte derived from TM NS. The I_{Raman} is the intensity of the same Raman peak obtained from plain TM pristine. C_{LC} represents the minimum detectable concentration of the analyte, while C_{HC} represents the maximum concentration of the analyte when measuring the pure Raman signal.

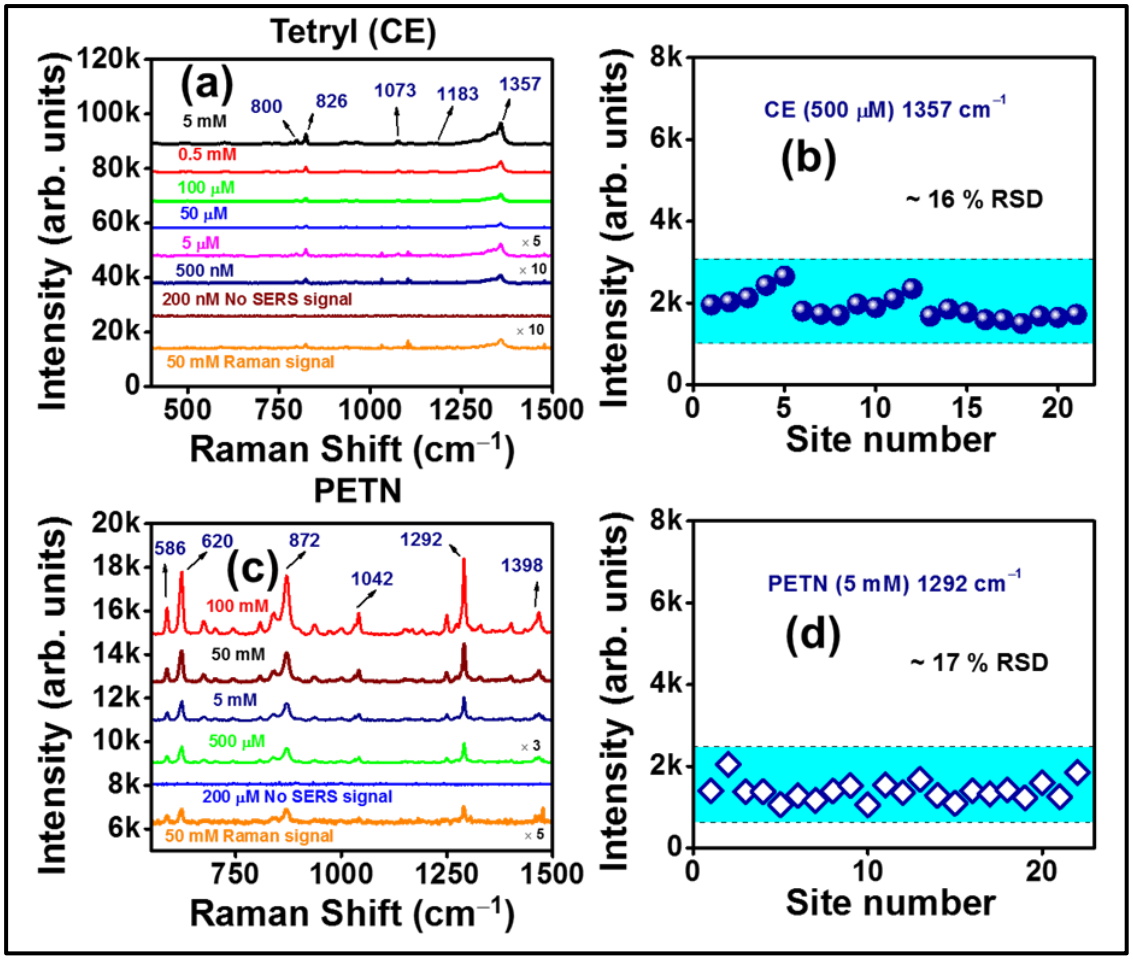

Figure 4A. 13 (a) Concentration-dependent SERS spectra of CE collected by GB ablated TM NS, along with pure Raman spectrum (in orange colour) of CE (50 mM) collected from unablated TM pristine, (b) Reproducibility spectra (with ~16% RSD) of CE (500 μM), (c) Concentration-dependent SERS spectra of PETN using recycled GB ablated TM NS, along with pure Raman spectrum (in orange colour) of PETN (50 mM) collected from unablated TM pristine, (d) Reproducibility spectra (with ~17% RSD) of PETN (5 mM). The portable Raman acquired the complete SERS data in this Figure, with the same acquisition parameters mentioned in the experimental details section.

Therefore, we provide a concise and informative visual representation of the EFs in Figure 4A.14. The BB patterned TM NS demonstrated an EF that was more than four times bigger than the GB ablated TM NS in the context of Tetryl sensing, as shown in Figure 4A.14(a). In BB patterning TM NS, the EF for PETN was consistently predicted to be about 3.4 times better, as shown in Figure 4A.14(b). The improved efficiency, in terms of a superior plasmonic response, is thought to be closely linked to the underlying structural distinctions between the two types of TM NSs. The occurrence of LIPSS is thought to result in the production of an enhanced SERS signal. Milligan et al. conducted detection tests of Tetryl using SERS with the assistance of Janowsky complex chemical treatment.

They observed a detection limit of 17.2 ng/mL, corresponding to millimolar (mM) concentrations. Kalasung et al. [70] have recently obtained the lowest detection limit of 10^{-7} g/ml using SERS sensors based on geometrically enhanced Au/ZnO film.

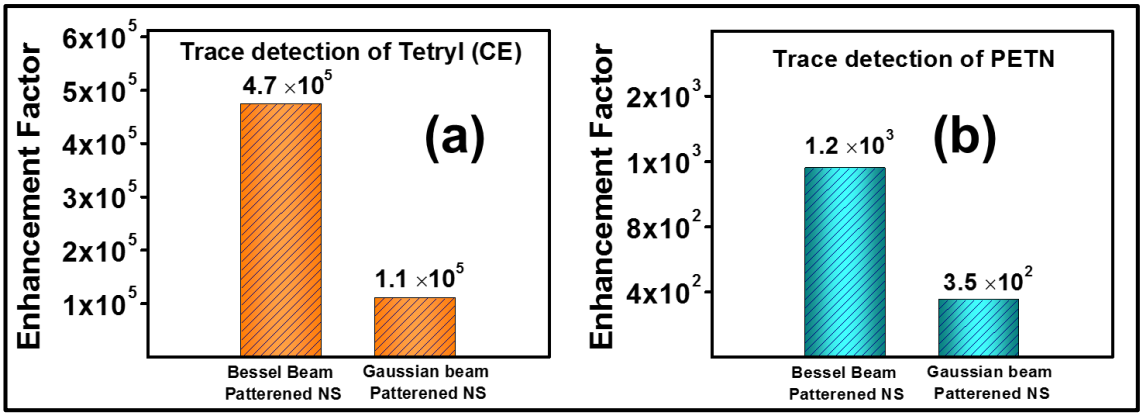

Figure 4A. 14 (a) Comparison of EFs between BB patterned TM NS and GB patterned TM NS, for the detection of Tetryl (CE), (b) similar comparative data of EFs between BB patterned TM NS and GB patterned TM NS, for the detection of PETN.

Liyanage et al. [71] have created a self-assembled, flexible nanosensor with an extremely sensitive SERS response. The sensor also exhibits a high level of repeatability. They were able to effectively showcase the detection of highly reactive explosives such as RDX, PETN, and TNT. Botti et al. [72] used principal component analysis to identify PETN even at very low levels of picograms. Panariello et al. [73] researched sensing utilizing gold nanoparticles and found that the SERS approach can detect Tetryl with a detection limit of around 1.7 mM. Shabtai et al. [74] recently revealed a sensing approach based on the SERS that used gold nanoparticles to detect PETN. They have demonstrated the lowest detectable limit of 1.5 µM for PETN. Zapata et al. [75] have comprehensively summarized important detection experiments using SERS for PETN, Tetryl, and other explosive compounds. Upon comparing our current research with previous studies, it is clear that our substrates, particularly for detecting Tetryl, have the potential to outperform many of the previously published ones. Furthermore, we are confident that there is room for future enhancements. For SERS mapping experiments, the effective TM NS manufactured using BB was then chosen to investigate the amplification in the Raman signal emanating from a sub-micron scale. Figure 4A.15(a) illustrates the SERS mapping conducted using a 532 nm excitation Micro Raman spectrometer, namely the LabRAM HR Evolution, for detecting CE at a concentration of 0.5 mM. The signal acquisition settings are specified in the section dedicated to experimental specifics.

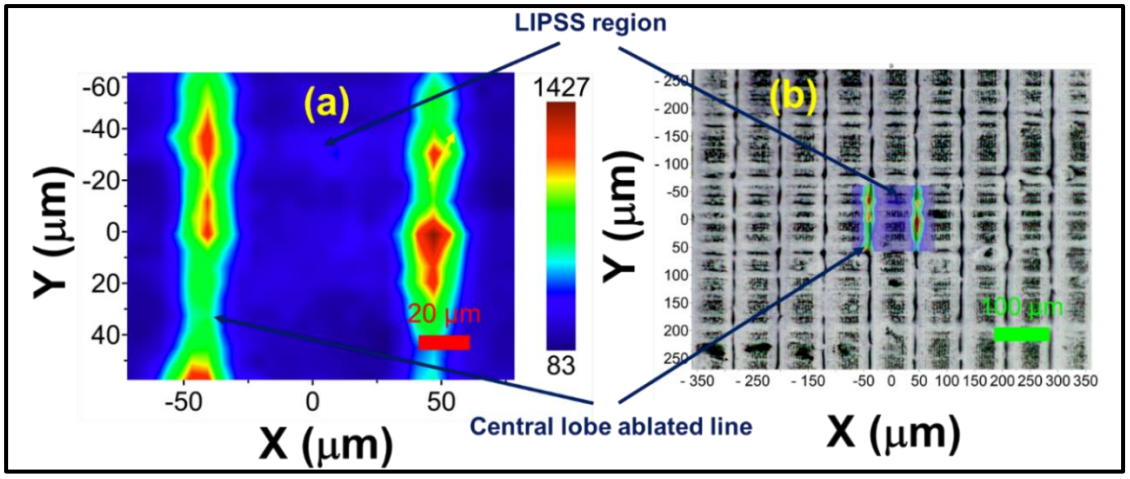

Figure 4A. 15 (a) SERS mapping data of CE (0.5 mM), corresponding to 1357 cm^{-1} peak. (b) overlay the SERS mapping data representation with TM NS under the 10X objective.

Figure 4A.15(b) exhibits the superimposed picture of the mapping data, presenting a distinct depiction of the strength of the SERS signal (1357 cm-1 peak), which aligns with its respective position. When using a micro-Raman system with a spot size of about 3 µm, it is clear from the color patterns in the mapping data [Figure 4A.15] that the SERS signal amplification is more significant in the central lobe ablated line than other areas. The observed result is thought to be caused by the strong evanescent field generated by the localized surface plasmons (LSP) formed at the sand dune-like nanostructures (NSs) [refer to Figure 4A.5(c)]. ii) The drop-cast analyte molecules tend to accumulate more along the ablation line, with an average depth of around 700 nm and a maximum depth of around 900 nm. The molecules that have been adsorbed gather in the central lobe ablation line, creating an area with a high concentration of the analyte. This results in an increased SERS signal. Homogeneous signals were reported to be generated across a broader area in the LIPSS region. However, the SERS signal obtained using a portable Raman device with a larger spot size of around 90 µm is thought to result from the combined enhancement effects from the ablated line in the central lobe and the LIPSS area. Therefore, combining SERS mapping and portable Raman SERS measurements provides a comprehensive understanding of the increases. Figure 4A.16 displays the SERS mapping data of the PETN analyte, using the recycled TM NS (BB patterned) as a substrate.

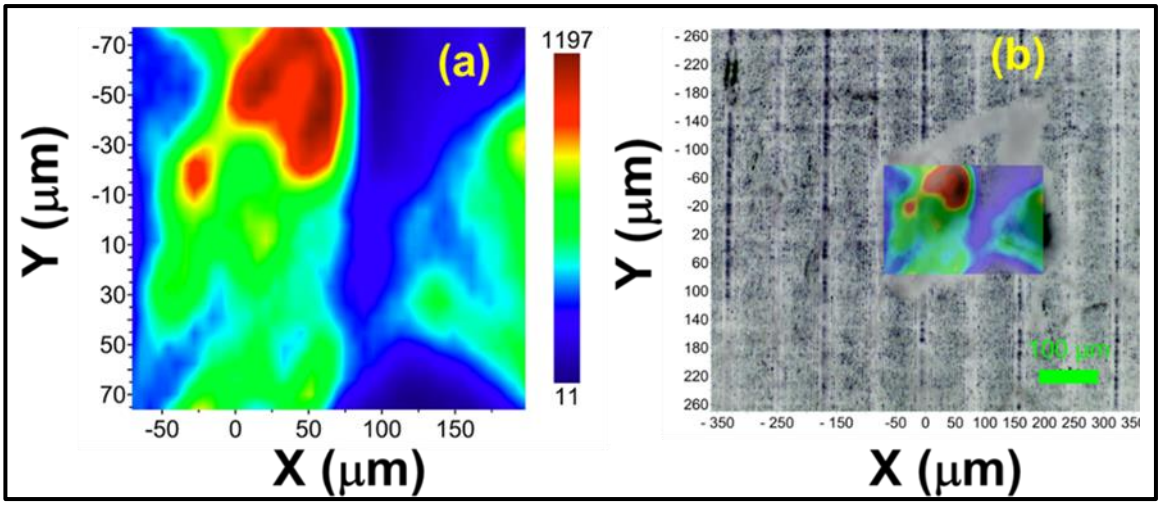

Figure 4A. 16 (a) SERS mapping data of PETN (5 mM), corresponding to 1292 cm^{-1} peak. (b) overlay representation of the aforementioned SERS mapping data with TM NS under the 10X objective.

4A.3.5. In-depth understanding of the trimetallic nano-system

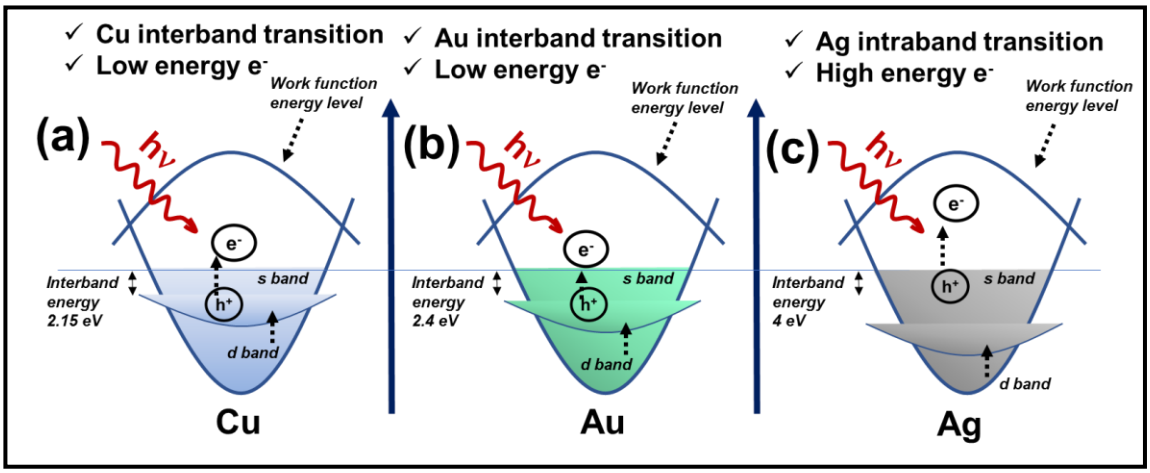

Figure 4A. 17 A complete picture of charge transition in TM nano-system. (a) incident photon-assisted interband transition in Cu NS, (b) photon-excited interband transition in Au NS (c) photon-induced intraband charge excitation in Ag NS.

Localized surface plasmons (LSP) create strong electric fields around nanostructures or nanoparticles. This results in a significant increase in the Raman signal of molecules intimately attached to these structures. LSPs are generally considered the basis for SERS [2, 60, 65]. The localized plasmon modes strongly depend on the surface's geometry [76], forming specific areas known as 'hotspots' [77]. This dependence is primarily influenced by size, shape, and nano-structural topography. Under these circumstances, the high-energy electrons (conduction band electrons) play a vital role in amplifying the small Raman scattering signal by plasmonic amplification. To fully illustrate the plasmonic

response generated by the trimetallic micro-entities, it is crucial to comprehend the process of hot electron creation in these systems. Metallic nanoparticles are being studied for their ability to exhibit collective oscillation of surface plasmons and free conduction band electrons when subjected to the quantum confinement effect generated by light. For plasmonic metals such as Ag, Au, and Cu, the excitation of hot electrons in the nano regime happens in two ways: i) inside the conduction band, from the occupied s-band to the unfilled s-band (intra-band excitation), and ii) from the d-band to the empty s-band (inter-band transition) [78]. The energy needed for inter-band jumps is 4 eV for Ag, 2.4 eV for Au, and 2.15 eV for Cu [1,78]. Ag is more likely to provide hot electrons by intra-band excitations because of its more significant energy gap, unlike Au and Cu, which can undergo inter-band population transfers with lower energy pumping. Based on recent theoretical discoveries [1,79], plasmon-induced hot electron pools are believed to be very responsive to the alloy composition of the NSs. This composition determines the population and dynamics of the hot charges. Additional research indicates that the excitation of visible light causes a transition within the same band, producing high-energy hot electrons and holes. Conversely, when visible light is used, inter-band jumps produce low-energy electrons and highly excited holes [1,80]. The photo-excitation processes naturally control the density of charge carriers, directly affecting the intensities of the localized surface plasmons (LSPs) in the system and the amplification of SERS. Therefore, Ag is hypothesized to be a supplier of high-energy electrons in the trimetallic system being studied. At the same time, Au and Cu generate high charge density via inter-band excitations, as shown in Figure 4A.17. Furthermore, by combining Ag with Au and Cu, the absorption resonance of Ag, located in the violet area, may be shifted towards longer wavelengths, resulting in a red shift of the resonance frequency [1]. This report also suggests that using excitation wavelengths of 532 nm/785 nm is advantageous in SERS experiments. Valenti et al. [1] have demonstrated that Ag/Au alloy nanoparticles exhibited greater charge injection efficiency than pure Ag and Au nanoparticles. In summary, the elements that cause excitation in the TM system, including the described hot carriers and other related plasmonic characteristics, are important for understanding the SERS response of the specific TM system.

4A.3.6. LIPSS formation on Ag-Au bimetallic surface and its SERS response

Subsequently, we have produced a non-diffracting Bessel beam of zeroth order using an axicon in the infrared range. The beam has a wavelength of 800 nm, a repetition rate of 1

kHz, and a pulse duration of 50 fs. As mentioned before, the axicon is coated with an anti-reflective material and operates in the femtosecond range. Using a femtosecond Bessel beam, we conducted laser ablation of a bimetallic alloy of 50% gold and 50% silver in ambient air. We endeavored to create LIPSS NSs (Laser-Induced Periodic Surface Structures Nanostructures) on the surface of an Ag-Au bimetallic (BM) alloy. This was done by exposing the surface to a femtosecond (fs) Bessel beam (BB). This research illustrates the production of ladder-like, bimetallic LIPSS by BB contact. The intricate interplay of consecutive BB profile impressions has been thoroughly investigated.

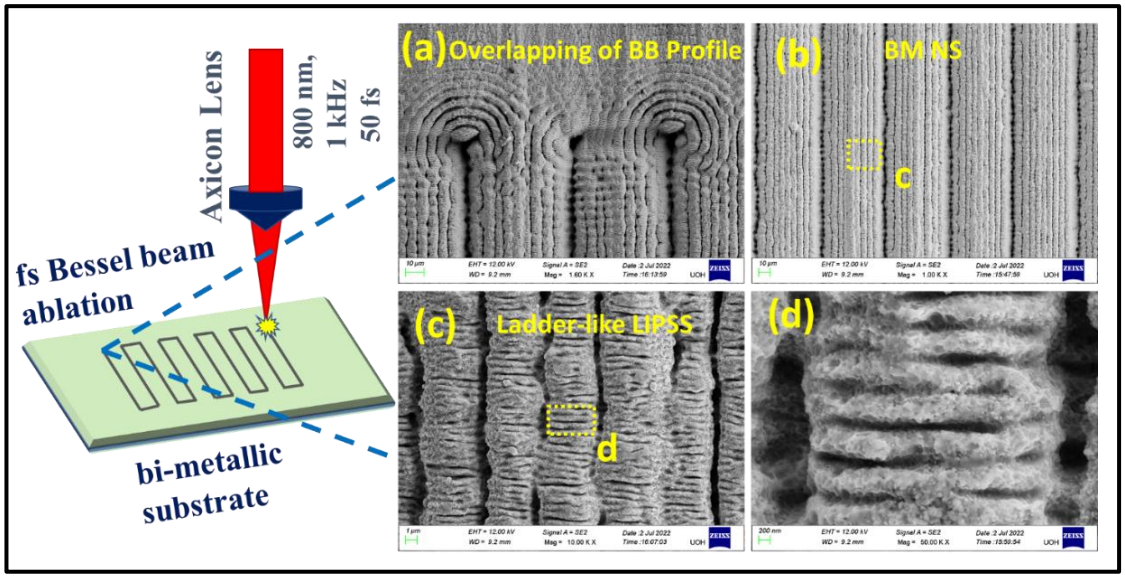

Figure 4A. 18 Schematic of BB induced laser ablation in air, engaging 50 fs, 800 nm BB generated using an axicon (a) FESEM image of the overlap of two consecutive BB profile ablation imprints on BM alloy surface (b) lower magnification image of the BB patterned surface (c) ladder-like LIPSS formed in nanoscale topography due to BB interaction (d) higher magnification image of BM NS revealing ladder-like steps with various nano growths all over.

The BB was used to systematically scan the BM surface using two X-Y directed stages, creating a full (3 mm x 3 mm) laser-patterned surface. The BM NSs were used as active substrates in SERS measurements and extensively characterized in their topography. Analytical investigations using AN and TL molecules have been successfully conducted using the B&W Tek i-Raman Plus, a hand-held portable Raman spectrometer suitable for field use. The spectrometer operates at an excitation wavelength of 785 nm and has a spot size of about 90 µm. The experimental details have been previously described in the section dedicated to experimental details. The study also examined the intersection of two consecutive ablation zones imprinted with BB profiles. The ablation imprints are evident in Figure 4A.18(a). The topological characteristics of the ablation zones illustrate the

ablation mechanism during the ablation process. This demonstrates the natural formation process of ladder-like LIPSS over the NS (nanostructured surface) during the raster scan. This occurs due to the concentric rings overlapping around the central lobe area. Figure 4A.18(b) demonstrates the presence of the vast area of LIPSS, while the ladder-like structure can be seen in Figure 4A.18(c). The high-magnification FESEM picture [Figure 4A.18(d)] displays the distinct intrinsic nano-growths formed on each ladder level. The core lobe section and the concentric rings are evident in the ablation zones, indicating the distinct beam profile impression generated on the BM surface. The overlapping of the ablated zones owing to the raster scan is shown by the interacting areas of the BB imprints. This overlap may be a pivotal factor in forming periodic surface structures. The periodic area is generated by concentric rings of the BB profile around the ablated region in the center. The central line is formed by the central lobe of the BB. The LIPSS sections exhibited a periodicity of around 550 nm, classifying the NS as low spatial frequency LIPSS. The LSFL-I NSs discussed before comprised several ladder-like structures, with many nanogrowths on these ladder steps. The disparities in ablation thresholds of the two metals, gold (Au) and silver (Ag), are thought to impact these nanogrowths substantially. The EDX examination [data presented in Figure 4A.19] also revealed the elemental compositions, confirming the existence of both Au and Ag. The presence of oxidation has also been verified as a result of high-temperature production during the ablation process.

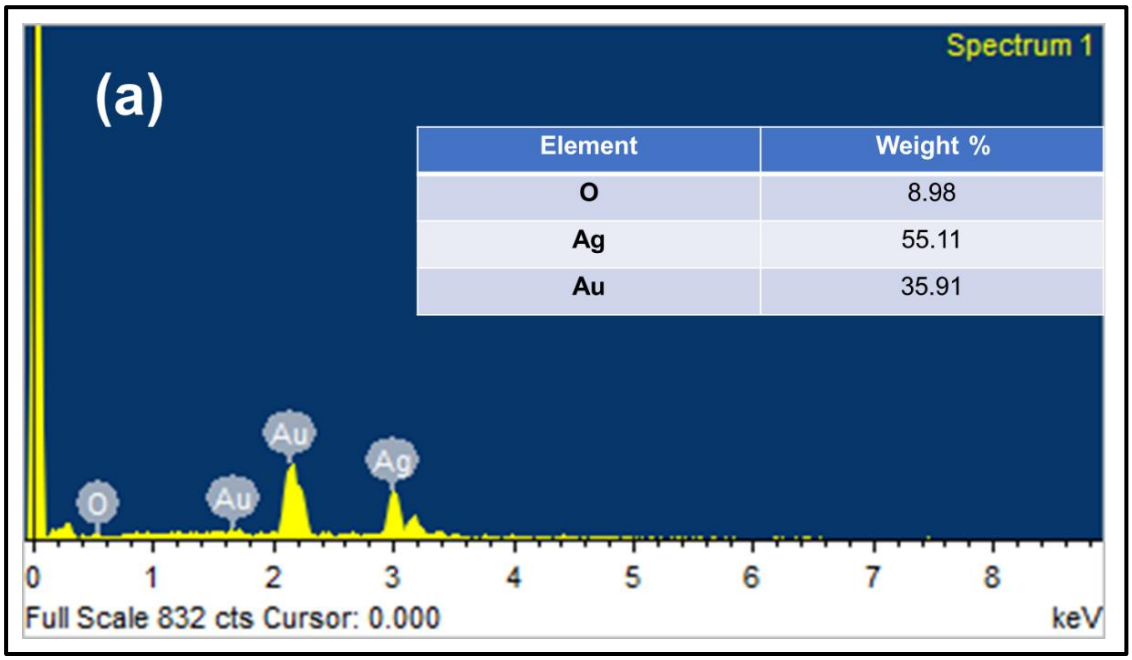

Figure 4A. 19 (a) EDX spectrum of fs BB ablated Ag-Au BM LIPSS NS. The elemental weight percentage table has been provided as an inset.

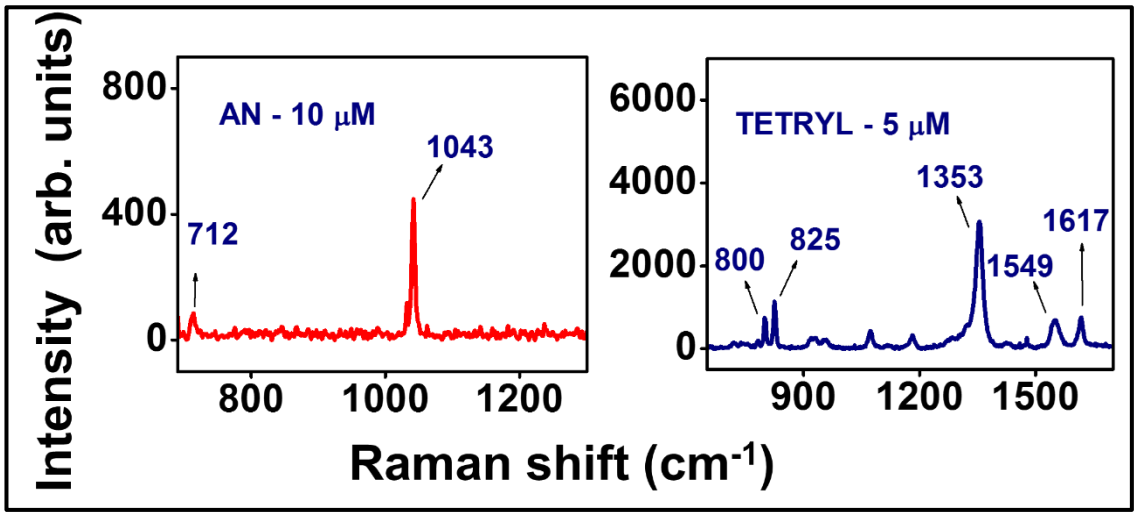

Figure 4A. 20 (a) SERS data of trace concentration of AN (10 μM), with its signature peak at 1043 cm^{-1} (b) SERS spectrum of TETRYL (5 μM), displaying its signature peak at 1353 cm^{-1}.

The plasmonic BM NS was used as a SERS sensor. Figure 4A.20 displays the comprehensive SERS-sensing investigation. The Bessel beam patterned BM NS effectively identified small amounts of two explosives: ammonium nitrate (AN) and Tetryl (TL). The minimum detectable concentrations were determined to be 10 μM and 5 μM using the SERS method. The EF has been estimated to be about in the range of 10^3 to 10^4. TL had distinct Raman peaks at 1353 cm^{-1}, which may be attributed to the symmetric and asymmetric stretching of NO_2. On the other hand, AN showed a peak at 1043 cm^{-1}, corresponding to the symmetric stretching mode of NO_3.

4A.4. Conclusions

This study showcases the creation of unique ladder-shaped trimetallic (Ag-Au-Cu alloyed) LIPSS using a femtosecond Bessel beam. The BB profile imprint on the surface was thoroughly investigated using single spot ablation and wide-ranging overlapping raster scan during the big area ablation procedure. An unusual ladder-like pattern was discovered to emerge throughout the nanostructured system. The intrinsic nanoscale topographical characteristics of the NSs were thoroughly examined using FESEM and AFM. The interaction between the BB-induced SPP and the incoming beam causes periodic changes in the ablation fluence on the surface. This is the main factor responsible for the formation of LSFL I category LIPSS, which have a period (Λ) of around (540±12) nm. Following that, the investigation comparing a fs Gaussian beam with the same fluence

showed a notable difference in structure between the two NSs created using changed beam profiles. In addition, the BB-induced TM LIPSS NS showed excellent effectiveness when used as a plasmonic, SERS-active substrate for detecting explosives. The research revealed that the detection of 200 nM Tetryl, at the lowest level, had an enhancement factor of around 10^5, making it one of the most reliable findings available. SERS mapping was conducted over a substantial area of the TM NS to extract the plasmonic reactions arising from several sub-micron segments. We also endeavored to examine the routes by which charges are excited in the TM nano-system, which determine the intensity of localized surface plasmon (LSP) and its strong correlation with improved Raman signal. To scale up the whole process, it is crucial to acknowledge that the throughput of the BB may be somewhat lower than that of the GB scenario. Nevertheless, the benefits the BB structures provide in processing [81-83] and the exceptional sensing capability shown in this study continue to make it appealing for a wide range of applications. Duocastella et al. [82] noted that creating uniform features on non-planar/uneven surfaces is feasible without altering the sample position and focus, which is not achievable with shorter depth of field beams (Gaussian). Further investigation is needed to compare the surface structure of both BB and GB under various fluence levels. This will help us better understand the potential for LIPSS creation on the unique TM surface under different beam profiles and fluence situations. We have also fabricated Ag-Au BM LIPSS NSs with fs BB and engaged them in SERS studies, successfully detecting traces of AN (10 µM) and Tetryl (5 µM). In this chapter, we have successfully proven the fabrication of a new kind of trimetallic LIPSS in multiple metal alloyed surfaces, which, to the best of our knowledge, has not been done before. This discovery opens possibilities for prospective applications in several research areas, such as solar-thermal conversion, bio-medical applications, nanophotonics, and hydrogen evolution.

References

[1] M. Valenti, A. Venugopal, D. Tordera, M.P. Jonsson, G. Biskos, A. Schmidt-Ott, W.A. Smith, Hot Carrier Generation and Extraction of Plasmonic Alloy Nanoparticles, ACS Photonics. 4 (2017) 1146–1152. https://doi.org/10.1021/acsphotonics.6b01048.

[2] N.J. Halas, S. Lal, W.S. Chang, S. Link, P. Nordlander, Plasmons in strongly coupled metallic nanostructures, Chem. Rev. 111 (2011) 3913–3961. https://doi.org/10.1021/cr200061k.

[3] S.A. Jalil, B. Lai, M. ElKabbash, J. Zhang, E.M. Garcell, S. Singh, C. Guo, Spectral absorption control of femtosecond laser-treated metals and application in solar-thermal devices, Light Sci. Appl. 9 (2020) 14. https://doi.org/10.1038/s41377-020-0242-y.

[4] J. Bonse, S. V. Kirner, J. Krüger, Laser-Induced Periodic Surface Structures (LIPSS), in: Handb. Laser Micro- Nano-Engineering, Springer International Publishing, Cham, 2021: pp. 1–59. https://doi.org/10.1007/978-3-319-69537-2_17-2.

[5] J. Zhang, Y. Wang, D. Li, Y. Sun, L. Jiang, Engineering Surface Plasmons in Metal/Nonmetal Structures for Highly Desirable Plasmonic Photodetectors, ACS Mater. Lett. 4 (2022) 343–355. https://doi.org/10.1021/acsmaterialslett.1c00768.

[6] J. Geng, L. Shi, X. Sun, W. Yan, M. Qiu, Artificial Seeds-Regulated Femtosecond Laser Plasmonic Nanopatterning, Laser Photon. Rev. 16 (2022) 2200232. https://doi.org/10.1002/lpor.202200232.

[7] S.Y. Chae, N. Yoon, E.D. Park, O.S. Joo, Surface modification of CuInS2 photocathodes with ruthenium co-catalysts for efficient solar water splitting, Appl. Surf. Sci. 612 (2023) 155856. https://doi.org/10.1016/j.apsusc.2022.155856.

[8] L. Huang, Q. Wang, H. Liu, Y. Wu, Y. Yang, G. Ma, Z. Lei, S. Ren, N+ irradiation regulates surface defects and doping towards efficient hydrogen evolution reaction on Sb2Te3, Appl. Surf. Sci. 609 (2023) 155347. https://doi.org/10.1016/j.apsusc.2022.155347.

[9] D.S. Chezganov, E.O. Vlasov, L.V. Gimadeeva, M.M. Neradovskiy, A.R. Akhmatkhanov, M.A. Chuvakova, D.O. Alikin, H. Tronche, F. Doutre, P. Baldi, V.Y. Shur, Short-period domain patterning by ion beam irradiation in lithium niobate waveguides produced by soft proton exchange, Opt. Laser Technol. 158 (2023) 108813. https://doi.org/10.1016/j.optlastec.2022.108813.

[10] X. Ge, Y. Hu, H. Shen, W. Liang, Z. Sun, X. Zhang, G. Ospankulova, M. Muratkhan, K.Z. Kh, W. Li, Electron beam irradiation application for improving the multiscale structure and enhancing physicochemical and digestive properties of acetylated naked barley, Food Chem. 404 (2023) 134674. https://doi.org/10.1016/j.foodchem.2022.134674.

[11] M. Jaworski, A. Chudzyńska, P. Mrowiński, G. Sęk, Efficient Emission in the Telecom Range from Quantum Dots Embedded in Photonic Structures Fabricated by Focused Ion Beam Milling, Acta Phys. Pol. A. 142 (2022) 662–667. https://doi.org/10.12693/APhysPolA.142.662.

[12] A. Nakhoul, A. Rudenko, C. Maurice, S. Reynaud, F. Garrelie, F. Pigeon, J.P. Colombier, Boosted Spontaneous Formation of High-Aspect Ratio Nanopeaks on Ultrafast Laser-Irradiated Ni Surface, Adv. Sci. 9 (2022) 2200761. https://doi.org/10.1002/advs.202200761.

[13] F. Nyenhuis, P.N. Terekhin, T. Menold, B. Rethfeld, A. Michalowski, J.A. L'huillier, Fundamentals of Scanning Surface Structuring by Ultrashort Laser Pulses: From Electron Diffusion to Final Morphology, Adv. Photonics Res. 3 (2022) 2200045. https://doi.org/10.1002/adpr.202200045.

[14] J. Bonse, S. Gräf, Maxwell Meets Marangoni—A Review of Theories on Laser-Induced Periodic Surface Structures, Laser Photon. Rev. 14 (2020) 1–25. https://doi.org/10.1002/lpor.202000215.

[15] Y. Zhang, Q. Jiang, M. Long, R. Han, K. Cao, S. Zhang, D. Feng, T. Jia, Z. Sun, J. Qiu, H. Xu, Femtosecond laser-induced periodic structures: mechanisms, techniques, and applications, Opto-Electronic Sci. 1 (2022) 220005–220005. https://doi.org/10.29026/oes.2022.220005.

[16] J. Bonse, Quo Vadis LIPSS?—Recent and Future Trends on Laser-Induced Periodic Surface Structures, Nanomaterials. 10 (2020) 1950. https://doi.org/10.3390/nano10101950.

[17] M. Senegačnik, P. Gregorčič, Diffraction-driven laser surface nanostructuring: Towards patterning with curved periodic surface structures, Appl. Surf. Sci. 610 (2023) 155486. https://doi.org/10.1016/j.apsusc.2022.155486.

[18] C.-L. Chang, C.-W. Cheng, J.-K. Chen, Femtosecond laser-induced periodic surface structures of copper: Experimental and modelling comparison, Appl. Surf. Sci. 469 (2019) 904–910. https://doi.org/10.1016/j.apsusc.2018.11.059.

[19] M.A. Taher, N. Chaudhary, K. Thirunaukkarasu, V.K. Rajput, S.R.G. Naraharisetty, Controlled periodicities of ladder-like structures via femtosecond laser of wavelength from 400 nm to 2200 nm, Surfaces and Interfaces. 28 (2022) 101622. https://doi.org/10.1016/j.surfin.2021.101622.

[20] Y. Liu, Y. Wang, M. Yang, Q. Wu, Z. Li, C. Zhang, J. Zhang, J. Yao, J. Xu, Deep-subwavelength ripples on the ZnO surface obtained via metal-film-assisted femtosecond laser processing, Appl. Surf. Sci. 573 (2022) 151576. https://doi.org/10.1016/j.apsusc.2021.151576.

[21] M.H. Elshorbagy, L.M. Sánchez-Brea, J. Buencuerpo, J. del Hoyo, Á. Soria-García, V. Pastor-Villarrubia, A. San-Blas, A. Rodríguez, S.M. Olaizola, J. Alda, Polarization conversion using customized subwavelength laser-induced periodic surface structures on stainless steel, Photonics Res. 10 (2022) 2024. https://doi.org/10.1364/PRJ.454451.

[22] Y. Shen, S. Pidishety, I. Nape, A. Dudley, Self-healing of structured light: a review, J. Opt. 24 (2022) 103001. https://doi.org/10.1088/2040-8986/ac8888.

[23] S.N. Khonina, N.L. Kazanskiy, S.V. Karpeev, M.A. Butt, Bessel beam: Significance and applications —A progressive review, Micromachines. 11 (2020) 1–27. https://doi.org/10.3390/mi11110997.

[24] G. Kontenis, D. Gailevičius, N. Jiménez, K. Staliunas, Optical Drills by Dynamic High-Order Bessel Beam Mixing, Phys. Rev. Appl. 17 (2022) 034059.

https://doi.org/10.1103/PhysRevApplied.17.034059.

[25] G.K. Podagatlapalli, S. Hamad, M.A. Mohiddon, S.V. Rao, Fabrication of nanoparticles and nanostructures using ultrafast laser ablation of silver with Bessel beams, Laser Phys. Lett. 12 (2015) 036003. https://doi.org/10.1088/1612-2011/12/3/036003.

[26] R. Stoian, M.K. Bhuyan, A. Rudenko, J.-P. Colombier, G. Cheng, High-resolution material structuring using ultrafast laser non-diffractive beams, Adv. Phys. X. 4 (2019) 1659180. https://doi.org/10.1080/23746149.2019.1659180.

[27] T. Chen, G. Zhang, H. Zhang, J. Lv, Y. Wang, P. Qu, R. Stoian, G. Cheng, Nano-spheroid formation on YAG surfaces induced by single ultrafast Bessel laser pulses, Appl. Surf. Sci. 604 (2022) 154360. https://doi.org/10.1016/j.apsusc.2022.154360.

[28] F. Courvoisier, J. Zhang, M.K. Bhuyan, M. Jacquot, J.M. Dudley, Applications of femtosecond Bessel beams to laser ablation, Appl. Phys. A. 112 (2013) 29–34. https://doi.org/10.1007/s00339-012-7201-2.

[29] V. Coviello, D. Forrer, V. Amendola, Recent Developments in Plasmonic Alloy Nanoparticles: Synthesis, Modelling, Properties and Applications, ChemPhysChem. 23 (2022) e202200136. https://doi.org/10.1002/cphc.202200136.

[30] R. Jiang, F. Qin, Q. Ruan, J. Wang, C. Jin, Ultrasensitive plasmonic response of bimetallic Au/Pd nanostructures to hydrogen, Adv. Funct. Mater. 24 (2014) 7328–7337. https://doi.org/10.1002/adfm.201402091.

[31] K. Sytwu, M. Vadai, J.A. Dionne, Bimetallic nanostructures: combining plasmonic and catalytic metals for photocatalysis, Adv. Phys. X. 4 (2019) 1619480. https://doi.org/10.1080/23746149.2019.1619480.

[32] A. Dahiya, M. Verma, P.S. Kumar, Plasmonic Applications of Gold-Copper Bimetallic Alloy Nanoparticles, Plasmonics. 17 (2022) 2173–2186. https://doi.org/10.1007/s11468-022-01704-w.

[33] S.H. Gebre, Synthesis and potential applications of trimetallic nanostructures, New J. Chem. 46 (2022) 5438–5459. https://doi.org/10.1039/d1nj06074k.

[34] J. Durnin, Exact solutions for nondiffracting beams. I. The scalar theory, J. Opt. Soc. Am. A. 4 (1987) 651–654. https://doi.org/10.1364/JOSAA.4.000651.

[35] G.S. Sokolovskii, V. V. Dudelev, S.N. Losev, K.K. Soboleva, A.G. Deryagin, K.A. Fedorova, V.I. Kuchinskii, W. Sibbett, E.U. Rafailov, Bessel beams from semiconductor light sources, Prog. Quantum Electron. 38 (2014) 157–188. https://doi.org/10.1016/j.pquantelec.2014.07.001.

[36] B. Yalizay, T. Ersoy, B. Soylu, S. Akturk, Fabrication of nanometer-size structures in metal thin films using femtosecond laser Bessel beams, Appl. Phys. Lett. 100 (2012) 1–4. https://doi.org/10.1063/1.3678030.

[37] A.Y. Vorobyev, V.S. Makin, C. Guo, Periodic ordering of random surface nanostructures induced by femtosecond laser pulses on metals, J. Appl. Phys. 101 (2007). https://doi.org/10.1063/1.2432288.

[38] J. Bonse, J. Krüger, S. Höhm, A. Rosenfeld, Femtosecond laser-induced periodic surface structures, J. Laser Appl. 24 (2012) 572–579. https://doi.org/10.2351/1.4712658.

[39] M. Navickas, Low spatial frequency laser-induced periodic surface structures in

fused silica inscribed by widely tunable femtosecond laser pulses structures in fused silica inscribed by widely tunable, Sci. Rep. 12 (2022) 20231. https://doi.org/10.1038/s41598-022-24771-9.

[40] A. Abou Saleh, A. Rudenko, S. Reynaud, F. Pigeon, F. Garrelie, J.P. Colombier, Sub-100 nm 2D nanopatterning on a large scale by ultrafast laser energy regulation, Nanoscale. 12 (2020) 6609–6616. https://doi.org/10.1039/c9nr09625f.

[41] A. Rudenko, A. Abou-Saleh, F. Pigeon, C. Mauclair, F. Garrelie, R. Stoian, J.P. Colombier, High-frequency periodic patterns driven by non-radiative fields coupled with Marangoni convection instabilities on laser-excited metal surfaces, Acta Mater. 194 (2020) 93–105. https://doi.org/10.1016/j.actamat.2020.04.058.

[42] X. Sedao, A. Abou Saleh, A. Rudenko, T. Douillard, C. Esnouf, S. Reynaud, C. Maurice, F. Pigeon, F. Garrelie, J.P. Colombier, Self-Arranged Periodic Nanovoids by Ultrafast Laser-Induced Near-Field Enhancement, ACS Photonics. 5 (2018) 1418–1426. https://doi.org/10.1021/acsphotonics.7b01438.

[43] A. Rudenko, J.P. Colombier, S. Höhm, A. Rosenfeld, J. Krüger, J. Bonse, T.E. Itina, Spontaneous periodic ordering on the surface and in the bulk of dielectrics irradiated by ultrafast laser: A shared electromagnetic origin, Sci. Rep. 7 (2017) 12306. https://doi.org/10.1038/s41598-017-12502-4.

[44] A. Rudenko, C. Mauclair, F. Garrelie, R. Stoian, J.P. Colombier, Amplification and regulation of periodic nanostructures in multipulse ultrashort laser-induced surface evolution by electromagnetic-hydrodynamic simulations, Phys. Rev. B. 99 (2019) 1–11. https://doi.org/10.1103/PhysRevB.99.235412.

[45] D. Zhang, R. Liu, Z. Li, Irregular LIPSS produced on metals by single linearly polarized femtosecond laser, Int. J. Extrem. Manuf. 4 (2021) 015102. https://doi.org/10.1088/2631-7990/ac376c.

[46] P.N. Terekhin, O. Benhayoun, S.T. Weber, D.S. Ivanov, M.E. Garcia, B. Rethfeld, Influence of surface plasmon polaritons on laser energy absorption and structuring of surfaces, Appl. Surf. Sci. 512 (2020) 144420. https://doi.org/10.1016/j.apsusc.2019.144420.

[47] J. Bonse, S. Gräf, Ten Open Questions about Laser-Induced Periodic Surface Structures, Nanomaterials. 11 (2021) 3326. https://doi.org/10.3390/nano11123326.

[48] A.Y. Vorobyev, C. Guo, Direct femtosecond laser surface nano/microstructuring and its applications, Laser Photon. Rev. 7 (2012) 385–407. https://doi.org/10.1002/lpor.201200017.

[49] I. Gnilitskyi, T.J.Y. Derrien, Y. Levy, N.M. Bulgakova, T. Mocek, L. Orazi, High-speed manufacturing of highly regular femtosecond laser-induced periodic surface structures: Physical origin of regularity, Sci. Rep. 7 (2017) 8485. https://doi.org/10.1038/s41598-017-08788-z.

[50] M. Huang, F. Zhao, Y. Cheng, N. Xu, Z. Xu, Origin of laser-induced near-subwavelength ripples: interference between surface plasmons and incident laser, ACS Nano. 3 (2009) 4062–4070. https://doi.org/10.1021/nn900654v.

[51] J. Bonse, J. Krüger, Pulse number dependence of laser-induced periodic surface structures for femtosecond laser irradiation of silicon, J. Appl. Phys. 108 (2010) 034903. https://doi.org/10.1063/1.3456501.

[52] E.L. Gurevich, Y. Levy, S. V. Gurevich, N.M. Bulgakova, Role of the temperature dynamics in formation of nanopatterns upon single femtosecond laser pulses on gold, Phys. Rev. B. 95 (2017) 054305. https://doi.org/10.1103/PhysRevB.95.054305.

[53] E.L. Gurevich, Y. Levy, N.M. Bulgakova, Three-step description of single-pulse formation of laser-induced periodic surface structures on metals, Nanomaterials. 10 (2020) 1–15. https://doi.org/10.3390/nano10091836.

[54] S. Maragkaki, P.C. Lingos, G.D. Tsibidis, G. Deligeorgis, Impact of pre-patterned structures on features of Laser Induced Periodic Surface structures Impact of pre-patterned structures on features of Laser Induced Periodic Surface structures, 26 (2021) 7330.

[55] I. Oladyshkin, Self-induced decay of intense laser pulse into a pair of surface plasmons, Phys. Rev. B. 106 (2022) 1–6. https://doi.org/10.1103/PhysRevB.106.L081408.

[56] K. Furusawa, K. Takahashi, H. Kumagai, K. Midorikawa, M. Obara, Ablation characteristics of Au, Ag, and Cu metals using a femtosecond Ti: sapphire laser, Appl. Phys. A. 69 (1999) S359–S366. https://doi.org/10.1007/s003390051417.

[57] J. Byskov-Nielsen, J.M. Savolainen, M.S. Christensen, P. Balling, Ultra-short pulse laser ablation of metals: Threshold fluence, incubation coefficient and ablation rates, Appl. Phys. A Mater. Sci. Process. 101 (2010) 97–101. https://doi.org/10.1007/s00339-010-5766-1.

[58] S. V. Starinskiy, Y.G. Shukhov, A. V. Bulgakov, Laser-induced damage thresholds of gold, silver and their alloys in air and water, Appl. Surf. Sci. 396 (2017) 1765–1774. https://doi.org/10.1016/j.apsusc.2016.11.221.

[59] P. Wu, W. Huang, Theoretical analysis of quasi-bessel beam for laser micromachining, Zhongguo Jiguang/Chinese J. Lasers. 41 (2014) 82–86. https://doi.org/10.3788/CJL201441.s102002.

[60] J. Langer, D.J. de Aberasturi, J. Aizpurua, R.A. Alvarez-Puebla, B. Auguié, J.J. Baumberg, et al., Present and future of surface-enhanced Raman scattering, ACS Nano. 14 (2020) 28–117. https://doi.org/10.1021/acsnano.9b04224.

[61] A. Mangababu, R. Sai Prasad Goud, C. Byram, J. Rathod, D. Banerjee, V. Rao Soma, S.V.S.V.S. Nageswara Rao, Multi-functional gallium arsenide nanoparticles and nanostructures fabricated using picosecond laser ablation, Appl. Surf. Sci. 589 (2022) 152802. https://doi.org/10.1016/j.apsusc.2022.152802.

[62] M. Haribabu, B. Dipanjan, M.S.S. Bharati, J. Chelsea, A. Chandrasekhar, P. Kanaka raju, S. Venugopal Rao, S. Hamad, G. Krishna Podagatlapalli, Exciton-mediated surface-enhanced Raman studies of Aluminum doped platinum nano colloids, Opt. Mater. (Amst). 133 (2022) 113013. https://doi.org/10.1016/j.optmat.2022.113013.

[63] D. Banerjee, S.S.B. Moram, C. Byram, J. Rathod, T. Jena, G.K. Podagatlapalli, V.R. Soma, Plasmon-enhanced ultrafast and tunable thermo-optic nonlinear optical properties of femtosecond laser ablated TiO2 and Silver-doped TiO2 nanoparticles, Appl. Surf. Sci. 569 (2021) 151070. https://doi.org/10.1016/j.apsusc.2021.151070.

[64] M.S.S. Bharati, C. Byram, V.R. Soma, M. Sree Satya Bharati, C. Byram, V.R. Soma, Femtosecond Laser Fabricated Ag@Au and Cu@Au Alloy Nanoparticles for

Surface Enhanced Raman Spectroscopy Based Trace Explosives Detection, Front. Phys. 6 (2018) 28. https://doi.org/10.3389/fphy.2018.00028.

[65] G.K. Podagatlapalli, S. Hamad, S.V. Rao, Trace-Level Detection of Secondary Explosives Using Hybrid Silver-Gold Nanoparticles and Nanostructures Achieved with Femtosecond Laser Ablation, J. Phys. Chem. C. 119 (2015) 16972–16983. https://doi.org/10.1021/acs.jpcc.5b03958.

[66] M.S.S. Bharati, V.R. Soma, Flexible sers substrates for hazardous materials detection: Recent advances, Opto-Electronic Adv. 4 (2021) 210048. https://doi.org/10.29026/oea.2021.210048.

[67] D. Banerjee, M. Akkanaboina, S. Ghosh, V.R. Soma, Picosecond Bessel Beam Fabricated Pure, Gold-Coated Silver Nanostructures for Trace-Level Sensing of Multiple Explosives and Hazardous Molecules, Materials (Basel). 15 (2022) 4155. https://doi.org/10.3390/ma15124155.

[68] M. Akkanaboina, D. Banerjee, K.R. Kumar, R.S.P. Goud, V.R. Soma, S.V.S.N. Rao, Gold nanoparticles coated LIPSS on GaAs for trace detection of RDX and Tetryl, Surfaces and Interfaces. 36 (2023) 102563. https://doi.org/10.1016/j.surfin.2022.102563.

[69] K. Milligan, N.C. Shand, D. Graham, K. Faulds, Detection of Multiple Nitroaromatic Explosives via Formation of a Janowsky Complex and SERS, Anal. Chem. 92 (2020) 3253–3261. https://doi.org/10.1021/acs.analchem.9b05062.

[70] S. Kalasung, K. Aiempanakit, I. Chatnuntawech, N. Limsuwan, K. Lertborworn, V. Patthanasettakul, M. Horprathum, N. Nuntawong, P. Eiamchai, et al. Patthanasettakul, V. Patthanasettakul, M. Horprathum, N. Nuntawong, P. Eiamchai, Trace-level detection and classifications of pentaerythritol tetranitrate via geometrically optimized film-based Au/ZnO SERS sensors, Sensors Actuators B Chem. 366 (2022) 131986. https://doi.org/10.1016/j.snb.2022.131986.

[71] T. Liyanage, A. Rael, S. Shaffer, S. Zaidi, J. V. Goodpaster, R. Sardar, Fabrication of a self-assembled and flexible SERS nanosensor for explosive detection at parts-per-quadrillion levels from fingerprints, Analyst. 143 (2018) 2012–2022. https://doi.org/10.1039/c8an00008e.

[72] S. Botti, S. Almaviva, L. Cantarini, A. Palucci, A. Puiu, A. Rufoloni, Trace level detection and identification of nitro-based explosives by surface-enhanced Raman spectroscopy, J. Raman Spectrosc. 44 (2013) 463–468. https://doi.org/10.1002/jrs.4203.

[73] L. Panariello, K. Chuen To, Z. Khan, G. Wu, G. Gkogkos, E. Al., Kinetics-based design of a flow platform for highly reproducible on demand synthesis of gold nanoparticles with controlled size between 50 and 150 nm and their application in SERS and PIERS sensing, Chem. Eng. J. 423 (2021) 129069. https://doi.org/10.1016/j.cej.2021.129069.

[74] V. Heleg-Shabtai, A. Zaltsman, M. Sharon, H. Sharabi, I. Nir, D. Marder, G. Cohen, I. Ron, A. Pevzner, E. Al., Explosive vapour/particles detection using SERS substrates and a hand-held Raman detector, RSC Adv. 11 (2021) 26029–26036. https://doi.org/10.1039/d1ra04637c.

[75] F. Zapata, M. López-López, C. García-Ruiz, Detection and identification of

explosives by surface enhanced Raman scattering, Appl. Spectrosc. Rev. 51 (2016) 227–262. https://doi.org/10.1080/05704928.2015.1118637.

[76] T.A. Kelf, Y. Sugawara, J.J. Baumberg, M. Abdelsalam, P.N. Bartlett, Plasmonic band Gaps and trapped plasmons on nanostructured metal surfaces, Phys. Rev. Lett. 95 (2005) 116802. https://doi.org/10.1103/PhysRevLett.95.116802.

[77] H. Wei, H. Xu, Hot spots in different metal nanostructures for plasmon-enhanced Raman spectroscopy, Nanoscale. 5 (2013) 10794–10805. https://doi.org/10.1039/c3nr02924g.

[78] C. Lee, Y. Park, J.Y. Park, Hot electrons generated by intraband and interband transition detected using a plasmonic Cu/TiO2 nanodiode, RSC Adv. 9 (2019) 18371–18376. https://doi.org/10.1039/c9ra02601k.

[79] R. Sundararaman, P. Narang, A.S. Jermyn, W.A. Goddard III, H.A. Atwater, Theoretical predictions for hot-carrier generation from surface plasmon decay, Nat. Commun. 5 (2014) 5788. https://doi.org/10.1038/ncomms6788.

[80] P.K. Jain, M.A. El-Sayed, Plasmonic coupling in noble metal nanostructures, Chem. Phys. Lett. 487 (2010) 153–164. https://doi.org/10.1016/j.cplett.2010.01.062.

[81] S.N. Khonina, N.L. Kazanskiy, S.V. Karpeev, M.A. Butt, Bessel Beam: Significance and Applications—A Progressive Review. Micromachines 11 (2020) 997. https://doi.org/10.3390/mi11110997

[82] M. Duocastella and C.B. Arnold, Bessel and annular beams for materials processing, Laser Photonics Rev. 6(5) (2012) 607–621. DOI 10.1002/lpor.201100031

[83] N. Stsepuro, P. Nosov, M. Galkin, G. Krasin, M. Kovalev, S. Kudryashov, Generating Bessel-Gaussian Beams with Controlled Axial Intensity Distribution, Applied Sciences 10 (2020) 7911. https://doi.org/10.3390/app10217911

Intentional Blank Page

4B.

Nanotubular Arrayed LIPSS Achieved with Femtosecond Bessel Beam on Silver and Uniform LIPSS on Copper Surface for SERS-based Multiple Explosives Sensing

Abstract

Ultrashort laser-matter interactions led to the development of laser-induced periodic surface structures (LIPSS), which have shown great promise in many areas, including nanophotonics, solar energy conversion, photodetectors, photocatalysis, and sensors. This study shows how a novel nanotubular Silver (Ag) LIPSS was fabricated using a femtosecond Bessel beam produced by an axicon. We have carefully studied how the Bessel beam causes LIPSS to form, and we now know that the modulation of the ablation fluence profile, along with the interaction of photon-induced surface plasmon polariton (SPP) and the incoming beam, is a key factor. The uniqueness of the Bessel beam shape and the SPP decay length have been crucial in making these unique nanostructures (NSs). It is estimated that the period of the low spatial frequency LIPSS has been 575±10 nm. We have also shown the different surface features of Ag nanostructures made with a Gaussian beam at the same laser fluence. In addition, these plasmonic NSs have demonstrated great effectiveness as SERS-active platforms. Small traces of real-time explosives like TNT, Tetryl, RDX, and HMX have been detected, with amounts ranging from 50 nM to 500 nM. The enhancement factors that were reached were around 10^6. Moreover, our investigation of the BB ablation process unveiled its promising applications in creating anti-reflection surfaces. Overall, this study adds a lot to what is known about the unexplored area of Bessel beam-metal interaction, leading to the creation of novel nanotubular LIPSS demonstrating versatile SERS-based sensing applications.

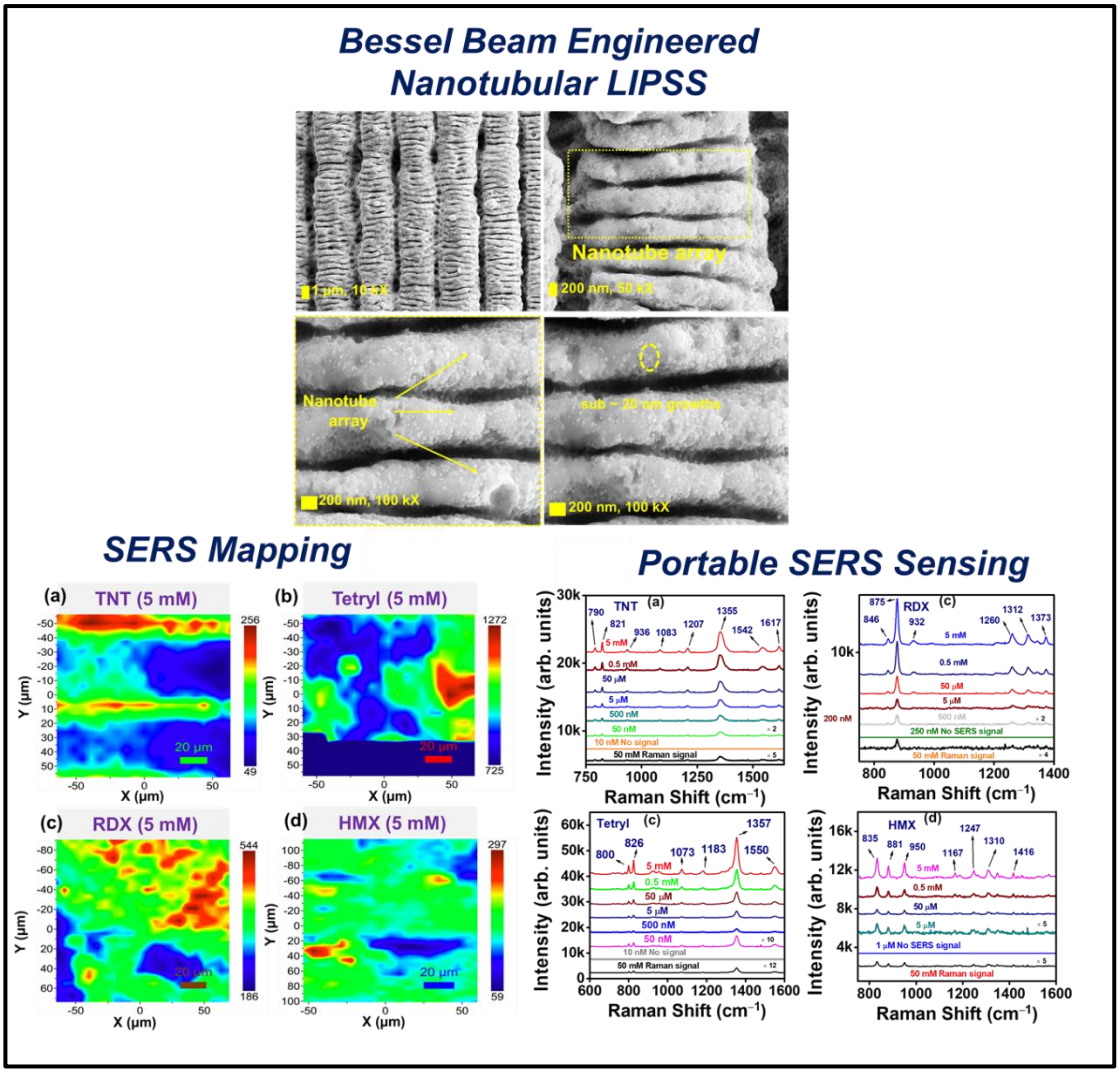

The work presented in this chapter has been published in

1. **D. Banerjee**, M. Akkanaboina, R.K. Kanaka, B. Ghose, V.R. Soma, Nanotubular Arrayed LIPSS Achieved with Femtosecond Bessel Beam on Silver Surface for SERS-Based Multiple Explosive Sensing, J. Phys. Chem. C. 128 (2024) 4655–4665. https://doi.org/10.1021/acs.jpcc.4c00160.

2. **D. Banerjee**, M. Akkanaboina, S. Pradhan, V. Rao Soma, Uniform LIPSS on copper created using zeroth-order femtosecond Bessel beam for SERS-based applications, Int. Conf. Opt. Photonic Eng. (IcOPEN 2023). (2024) 3. https://doi.org/10.1117/12.3021658.

4B.1. Introduction

The field of nanostructured surfaces, resurrected by ultrashort laser-matter irradiation, has gained significant attention due to its potential uses in scientific, biological, and industrial fields [1]. There are several methods for producing nanostructured surfaces, including sputtering, chemical and plasma etching, chemical vapor deposition, self-assembly, nanoimprint, optical, electron beam, and physical lithography. Ultrashort laser irradiation has been a reliable and effective method for creating various nano-textured surfaces, namely laser-induced periodic surface structures (LIPSS) [7-11]. LIPSS encompasses a fascinating field of study with potential applications in several areas, such as hydrogen evolution, photochemical water splitting, solar-thermal conversion, data storage, surface chemistry, photodetectors, and biological applications. The emerging area of nanopatterning plays a fundamental role in several industries, including semiconductors, microelectronics, and photocatalysis [12-18]. Moreover, there has been notable progress in nano-systems, namely in optical, chemical, and photocatalytic characteristics. Amendola et al. [19] and other pioneering groups have summarized recent advancements in various nano entities, emphasizing their unique magneto-optical properties, ability to generate hot carriers, catalytic enhancements through plasmonics, applications in nano-medicine, the adjustability of localized surface plasmons (LSP), and their effectiveness in surface-enhanced Raman spectroscopy (SERS). Several pioneering investigations have methodically shown the complex physics that underlie the formation of different LIPSS topographies.

The production of LIPSS (laser-induced periodic surface structures) via ultrafast laser interaction is a very efficient technology that has gained significant attention recently. Bonse et al.[20] have undertaken a thorough study in the last 10 years, investigating the intricate processes behind the creation of LIPSS. Senegacnik et al. [21] have developed a diffraction-assisted laser shaping technique that used cavitation bubbles created during the ablation process. This method employs thermo-optical tweezers driven by thermocapillary forces to effectively create arc-shaped concentric microgroove channels, which are physically dictated by the pattern of the guiding beam. Chang and his colleagues [22] have achieved femtosecond (fs) laser-induced periodicity on a copper surface, a notable feat. Their experiment on ablation, which included a high repetition rate, was simulated using a two-temperature model (TTM). The simulation showed a strong correlation with the actual experimental findings. Structured light has recently allowed for the use of several

distinct light profiles, including Bessel beams (BB). These beams have particular advantages, including their ability to heal themselves optically [23, 24], carry orbital angular momentum [25], have an extended depth of focus (DOF) [26-28], maintain consistent intensity profiles as they propagate [26], and thus show promise for investigating new laser-matter interactions [29], surface lithography [30], and optical trapping. Out of these options, the Axicon-generated BB [25] is particularly notable for its distance-invariant and self-repairing intensity profile, which improves the depth of field. Remarkably, studies are lacking in investigating the interactions between fs Bessel beams and metals.

In our earlier study [31], we successfully created a new kind of trimetallic NS (nanoscale structure) that showed a highly stimulating ladder-like LIPSS topography. This unique structure has considerable potential for sensing applications. We could accurately identify minute amounts (200 nM) of live explosives, namely Tetryl and pentaerythritol tetranitrate (PETN), with a significant increase in their detectability by around 105 times. Although the current values are positive, more enhancements are necessary for the sensitivity and feasible detection limit of a hand-held or portable Raman spectrometer. The detection of other commonly found explosive chemicals should also be considered. The appealing outcomes and benefits of fs BB-interaction have inspired us to conduct more studies to get better improvements and showcase extra adaptability. By using the advantages of non-diffracting light, we used an fs Bessel beam created by an axicon to modify the surface of Silver (Ag) substrates with strong plasmonic properties. This chapter section outlines our significant achievement in creating distinctive nanotubular arrays LIPSS using silver nanostructures (NS). We examined the basic elements and benefits of the interaction between the Bessel beam and metal surfaces, specifically investigating the formation of LIPSS in this setting. This research is very new and builds upon our present knowledge. These nanostructures have shown great versatility as substrates for SERS, particularly in the real-time detection of multiple explosives such as Tetryl (2,4,6-Trinitrophenylmethylnitramine, $C_7H_5N_5O_8$), TNT (2,4,6-Trinitrotoluene, $C_7H_5N_3O_6$), HMX (1,3,5,7-Tetranitro-1,3,5,7-tetrazocane, $C_4H_8N_8O_8$), and RDX (1,3,5-Trinitroperhydro-1,3,5-triazine, $C_3H_6N_6O_6$). Furthermore, our investigation into the BB ablation technique has shown its potential for generating anti-reflection surfaces. To support our experimental results, we comprehensively explain how nanotubular LIPSS is formed and the observed nanophotonic response in the SERS-active substrate.

4B.2. Experimental and characterization details:

Utilizing a Bessel beam profile, fs laser ablation in the air (LAA) was carried out on a silver target. The specifications of the fs Bessel beam are as follows: 800 nm, a pulse duration of ~50 fs, and a repetition rate of 1 kHz. The BB was produced by passing a laser beam from a chirped-pulse amplified Ti: Sapphire laser system via an axicon (100, M/s Thorlabs, UK, AX1210-B, IR range, AR coated). Silver substrates of > 99.9% purity were used to create NSs. Following a meticulous cleaning in an ultrasonic bath, these substrates underwent an ablation procedure aided by the Bessel beam. The ablation process involved analyzing the intersection of two successive BB ablation lines and performing a thorough laser raster scan ablation that lasted about 30 minutes. The operation was executed using two X-Y stages controlled by a LabVIEW interfaced motion controller (ESP 300, Newport, USA). The laser irradiation rate was roughly 3320 pulses per millimeter, with a scan speed of 0.3 mm/sec and an inter-line spacing of 55 μm during the raster μscan. As a result, an entire region of Ag nanostructures was effectively formed using Bessel beam ablation with a center peak intensity of 13 J/cm^2. We conducted field emission scanning electron microscopy (FESEM) using a ZEISS ULTRA 55 instrument from Graz, Austria, and energy dispersive X-ray spectroscopy (EDX) to examine the nanostructures' surface characteristics and chemical composition. Accurate measurements of the depth profiles of ablation were performed using atomic force microscopy (AFM) using the HI-TACHI AFM 5000-SPA400 device from Japan. The SERS measurements were conducted using a portable Raman system (i-Raman plus, M/s B&W Tek, USA). The parameters used were an input power of ~100 mW, an excitation wavelength of 785 nm, and a spot size of about 90 μm at the focus. The exposure period/accumulation time was set to 5 seconds, with a spectral averaging of three (3) spectra. Furthermore, the sampling method was diligently maintained before conducting the SERS measurements. The first stage of the sampling procedure is subjecting the substrate to gentle heating, typically at a temperature of around 500 degrees Celsius, using a temperature-controlled heater. Subsequently, we deposited about 20 μL of the analyte onto the substrate, allowing it to evaporate. Ultimately, the SERS tests were conducted on the substrate mentioned above. The SERS Mapping studies were performed using a micro-Raman spectrometer, specifically the LabRAM HR Evolution model manufactured by Horiba in France. The spectrometer had a 10X objective and a spot size of ~3.1 μm. The acquisition time for each measurement was set

to 5 seconds, and spectral averaging was performed thrice. The excitation wavelength was 532 nm, with an input power of approximately 135 mW.

4B.3. Results & Discussion

4B.3.1. Enhanced efficiency in structuring surfaces by the interplay of Bessel beams

The self-healing Bessel beam, which has lately gained recognition as a superior option for surface engineering research [23, 24], was first investigated by Durnin et al. [32]. The non-diffracting beam, characterized by its consistent intensity profile, inherent self-restoration, and extended focal depth, provides clear advantages over the Gaussian beam. As a result, it is the preferred choice for studying laser-induced surface modifications. Therefore, with the given characteristics, an fs zeroth-order BB (Bessel beam) profile was used to change the surface using the laser ablation in the air (LAA) method. Figure 4B.1(a) illustrates a schematic that explains the laser ablation technique used to generate the NS substrate and the following SERS-based detection procedure.

4B.3.1.1. Comparative analysis of BB and GB line ablation

The single-line profile resulting from BB-induced ablation was thoroughly investigated to get a comprehensive comprehension. Just like our previous report, we have observed a distinct similarity between the theoretically simulated plot [shown in Figure 4B.1(b)] of the zeroth order Bessel intensity profile on MATLAB, using the zeroth order Bessel function (J_0) [33, 34], and the ablation imprint [shown in the FESEM image presented in figure 4B.1(c)], which is located at the beginning of the ablation line. This also enhances our comprehension of the fs BB-metal surface interaction, which has been little investigated in previous research. The topography of the BB imprint on the surface was systematically examined by analyzing a line profile across it, as shown by the navy-blue line in Figure 4B.1(c). The line profile plot, shown in Figure 4B.1(d), clearly demonstrated that the development of the ablation imprint closely mimics the intensity curve of the zeroth order Bessel function, as shown in Figure 4B.1b. The center intensity peak of the BB profile has caused the bigger ablated region in the central lobe area, as shown in Figure 4B.1(d). Additionally, concentric ring ablation imprints were seen in the surrounding area of the central lobe. An average spatial period of about 5.5 µm was reported for the concentric rings. In addition, a detailed comparison of the FESEM images in Figures 4B.1(c) and 4B.1(e) has been provided to analyze the differences in line-ablation achieved utilizing both BB and GB techniques. The NS area created by the BB is substantially

bigger, at least 1.8 times, than the identical area generated by the GB. The length of the NS region is around 70 µm, while the size of the GB-generated area was around 38 µm.

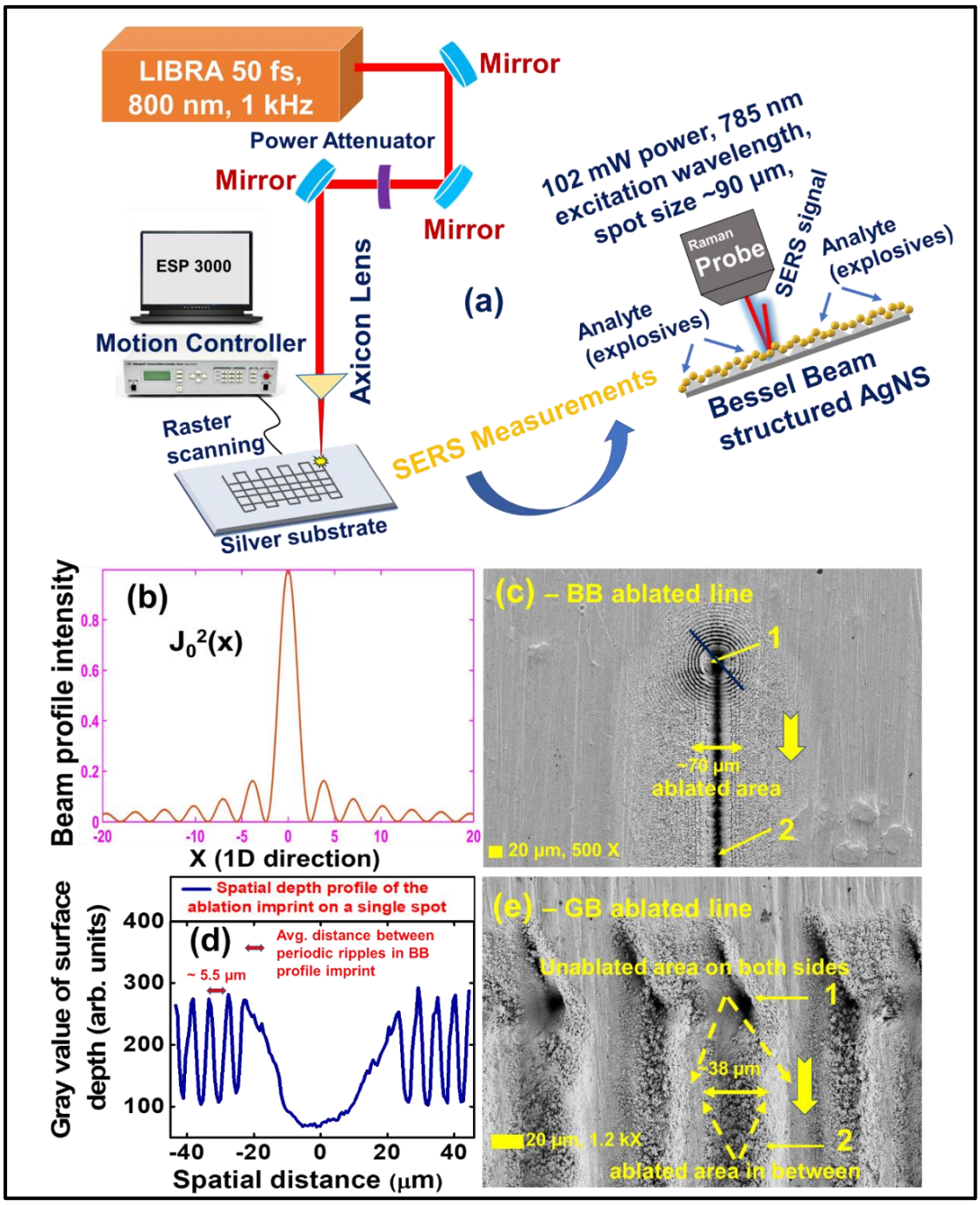

Figure 4B. 1 (a) Schematic diagram explaining the laser ablation process to prepare the NS substrate and the subsequent SERS-based detection process. (b) Simulated intensity beam profile on MATLAB for the zeroth order BB from Bessel function J_0 (x) term (c) FESEM image of BB ablated single line forming NSs both sides (d) Line profile plot corresponding to the navy-blue line over the BB imprint on the starting point in figure 4B.1(c). The plot reveals the central lobe ablated portion surrounded by periodic concentric rings. (e) FESEM image of GB ablated single line forming NSs within the line.

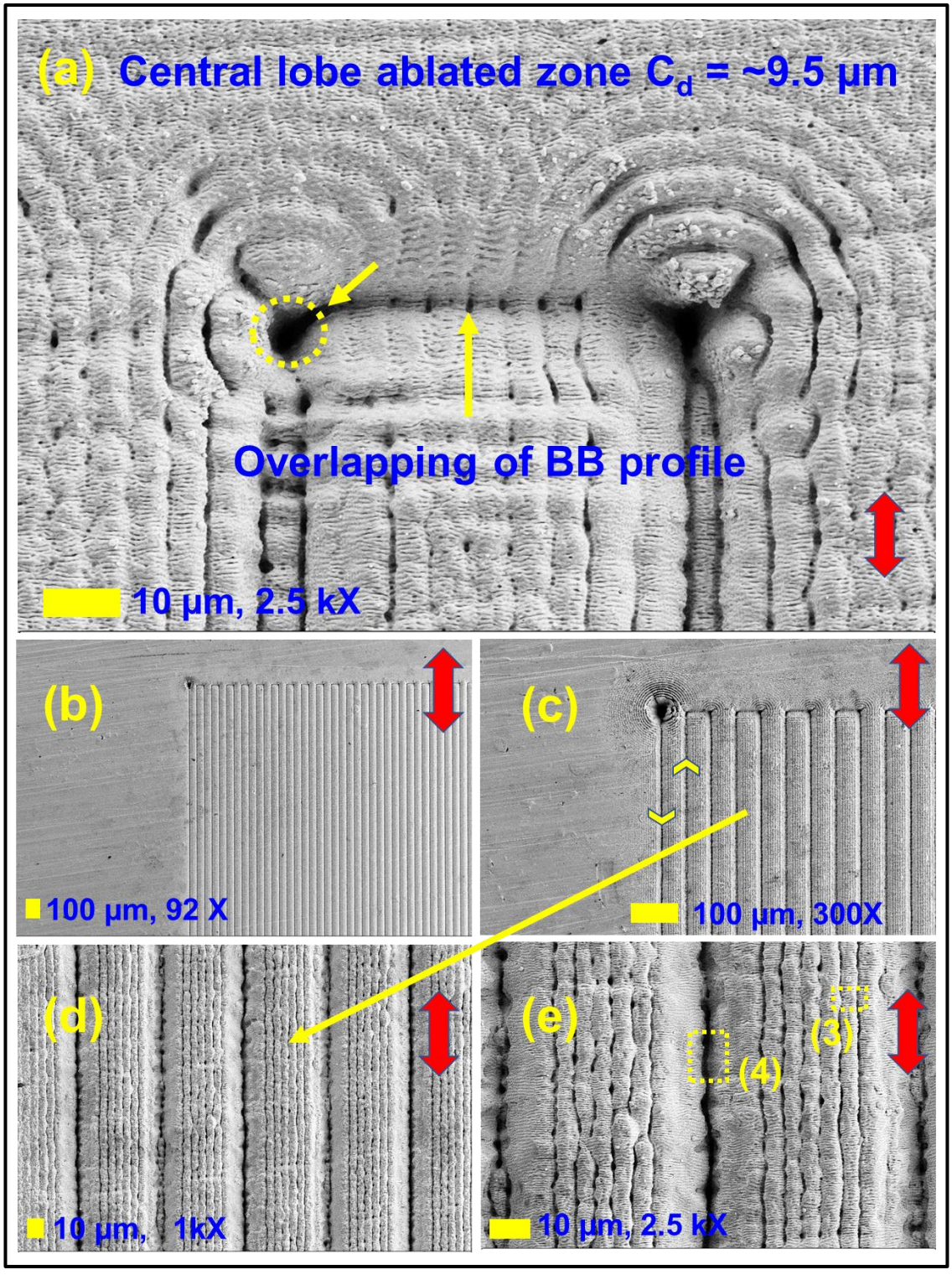

Figure 4B. 2 (a) FESEM image of overlapping two Bessel beam profiled ablation zones causing periodic structures. FESEM images of the fabricated complete NS with different magnifications, (b) 92X (c) 300X (d) 1kX (e) 2.5 kX. The red arrow depicts the direction of laser polarization. The ablation parameters are 0.3 mm/sec scan speed, an inter-line spacing of 55 µm, and 13 J/cm^2 central peak fluence.

These measurements were taken under the same ablation circumstances, including a peak intensity of approximately 13 J/cm^2, a 10 mm incident beam diameter before the lens, and

a scanning speed of 0.3 mm/sec. In all situations, the direction of ablation is indicated by an arrow symbol. Furthermore, it has been shown that the nucleoside triphosphates (NSs) generated by the guanine bases (GB) are located near the area where tissue ablation occurs. Meanwhile, NSs are present on both sides of the core ablation line in BB line ablation. Therefore, the BB ablation method enhanced the effectiveness of surface structuring and engineering. Because of the unique beam shape and high effectiveness in removing material, we decided to focus on creating larger nanoscale structures by scanning the beam throughout the whole area.

4B.3.2. Bessel beam structured nanostructures

The Ag substrate was subjected to a precise raster scanning procedure using fs BB ablation to generate the whole NS. While investigating nanoscale structures using FESEM, a clear overlapping pattern was detected between two consecutive BB ablation imprints (also known as ablated zones), as shown in Figure 4B.2(a). The diameter of the ablated zone in the central lobe has been calculated to be around 9.5 µm. Notably, periodic surface patterns were also created where the surfaces overlap. Figure 4B.2(a) significantly verified the smooth overlap of two successive BB-characterized ablation zones at the beginning segment of their respective ablation lines. The NS has been shown in Figures 4B.2(b) and 4B.2(c) at magnifications of 92X and 300X, respectively, providing a comprehensive representation. In addition, more detailed images of the NS are shown in Figures 4B.2(d) and 4B.2(e), corresponding to magnifications of 1kX and 2.5 kX, respectively. The red arrows in all the photographs represent the direction of polarization of the input laser pulse.

4B.3.3. Nanotubular arrayed LIPSS nanostructures

A unique nanoscale surface texture was created due to the innovative BB interaction. To optimize the formation of fine LIPSS structures, we conducted several BB-ablations using various incident fluences ranging from 7 to 13 J/cm^2. Comprehensive field-emission scanning electron microscopy (FESEM) analyses were conducted after the surface structuring. After careful examination, a precise central threshold fluence level of 13 J/cm^2 was established for the Ag substrate to generate distinct nanotubular LIPSS.

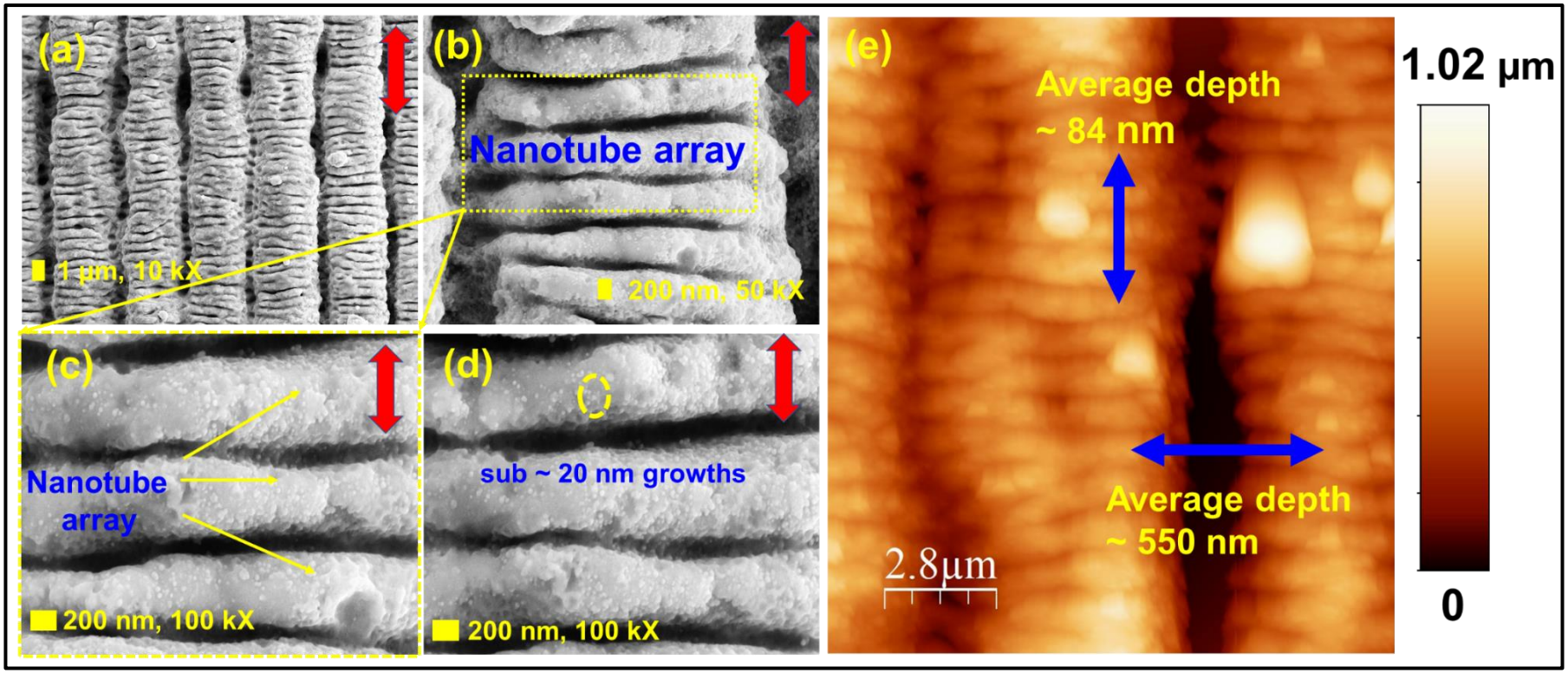

Figure 4B. 3 (a) FESEM image of column-wise periodic NSs on Ag surface, with 10 kX magnification (b) FESEM image of nanotubular LIPSS, with 50 kX magnification (c), (d) Higher (100 kX) magnification image of the same nanotubular LIPSS in a different region (e) AFM image of the column-wise LIPSS. The ablation parameters were 0.3 mm/sec scan speed and 13 J/cm^2 peak fluence.

When BB ablation was performed with an incidence fluence below the threshold, it led to the formation of LIPSS with a lower level of structural fineness. Based on the given fluences, it was determined that a scan speed of 0.3 mm/s and an inter-line spacing of 55 mm were the most effective for establishing consistent LIPSS. Because of the distinct features of the BB intensity profile, which includes a well-defined distribution of the total energy (refer to Figures 4B.1b and 4B.2a), the threshold fluence needed for ablation is relatively high. It has been shown that decreasing the amount of energy applied to the surface leads to a decline in the quality of the NS. Therefore, the specified ablation fluence was established to get a well-developed and distinct nanoscale structural quality in a nanotubular-arranged LIPSS. The validation process for forming laser-induced periodic nanostructures in the laser-treated region (after raster scanning) required thorough characterization using FESEM across several segments.

To provide a clear understanding, we have analyzed a specific section [dashed yellow line marked as 3] from Figure 4B.2(e), and Figure 4B.3 displays magnified photographs of this section. Figures 4B.3(a) and 4B.3(b) accurately depict the natural surface features of the NSs that were created. At a magnification of 10 kX, columnar formations were revealed in Figure 4B.3(a). Moreover, at a magnification of 50 kX, nanotubular structures were visible. To examine the unique LIPSS structure, highly magnified FESEM images [4B.3(c), 4B.3(d)] were obtained at a magnification of 100 kX, which corresponds to the region indicated by the yellow dashed line box in Figure 4B.3(b). Significant nanotubular arrays were seen over the extensive surface of the manufactured NS, exhibiting periodicity in a columnar fashion. The mean width of these nano-tubular structures was determined to be around 535 nm. Additionally, we observed the presence of sub-20 nm spherical and aspherical nano-growths covering the whole surface of the tubes. In addition, the period of the LIPSS was determined to be (Λ) of 575±10 nm. In this study, the BB-interacted Ag NS LIPSS was determined to have low spatial frequency LIPSS (LSFL), specifically with a period (Λ) calculated to be 0.73 times the excitation wavelength (λ) of 800 nm. In addition, to thoroughly investigate these very promising nanosheets (NSs), atomic force microscopy (AFM) was used to analyze the laser-treated NSs. Figure 4B.3(e) illustrates the same sample's Atomic Force Microscopy (AFM) results. An in-depth atomic force microscopy (AFM) investigation revealed that the average vertical distance between the array of nanotubular low-intensity LIPSS was ~84 nm.

The approximate average horizontal depth between consecutive LIPSS columns was calculated to be about 550 nanometers. The alignment of LIPSS has been determined to be perpendicular to the laser polarization (shown by red arrows) and is consistent with the findings in the literature [9, 35, 36]. The fineness and quality of LIPSS in the BB-treated NSs are much better than those obtained in our earlier investigation employing a trimetallic (Au-Cu-Ag) LIPSS. Therefore, this work is expected to enhance the understanding, and the literature is currently limited to the interaction between fs laser pulses and metal surfaces, producing LIPSS. Afterwards, the center ablated line segment, shown as (4) in Figure 4B.2(e), was also investigated. The inclined NSs shown on the adjacent walls of the deep center line were similar to the tubular structure of nanotubes. Figures 4B.4(a) and 4B.4(b) illustrate the same. EDX measurements were conducted before and during the ablation procedure to ascertain the elemental composition. The oxidation caused by ablation was verified by a change in the weight proportion of Silver and oxygen [Ag- 92.5 %, O – 7.5%] after ablation. The EDX results for the original substrate and the substrate with BB-structured following ablation are shown in Figure 4B.5 [(a) to (c)] and Figure 4B.6 [(a) to (c)], respectively.

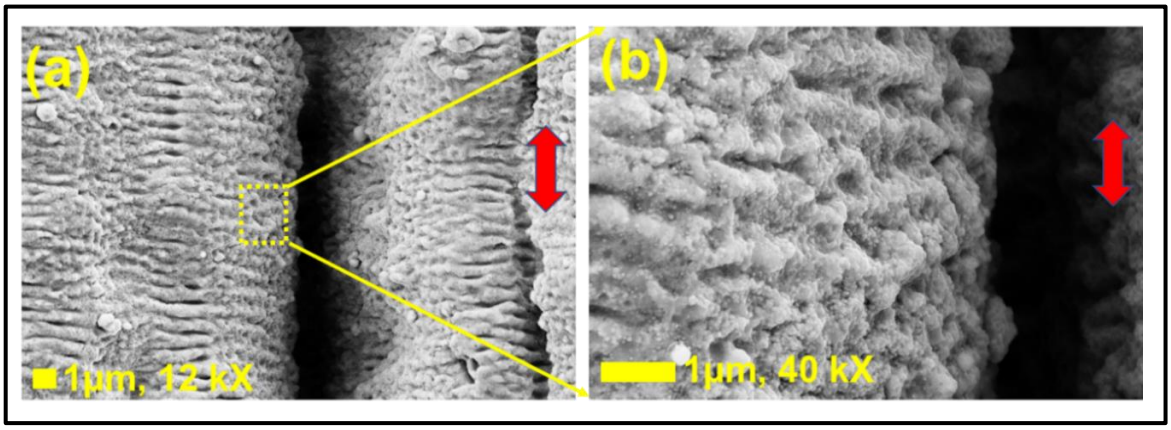

Figure 4B. 4 FESEM images of central ablation line for (a) 12 kX and (b) 40 kX magnification. The ablation parameters are 0.3 mm/sec scan speed and 13 J/cm^2 central peak fluence.

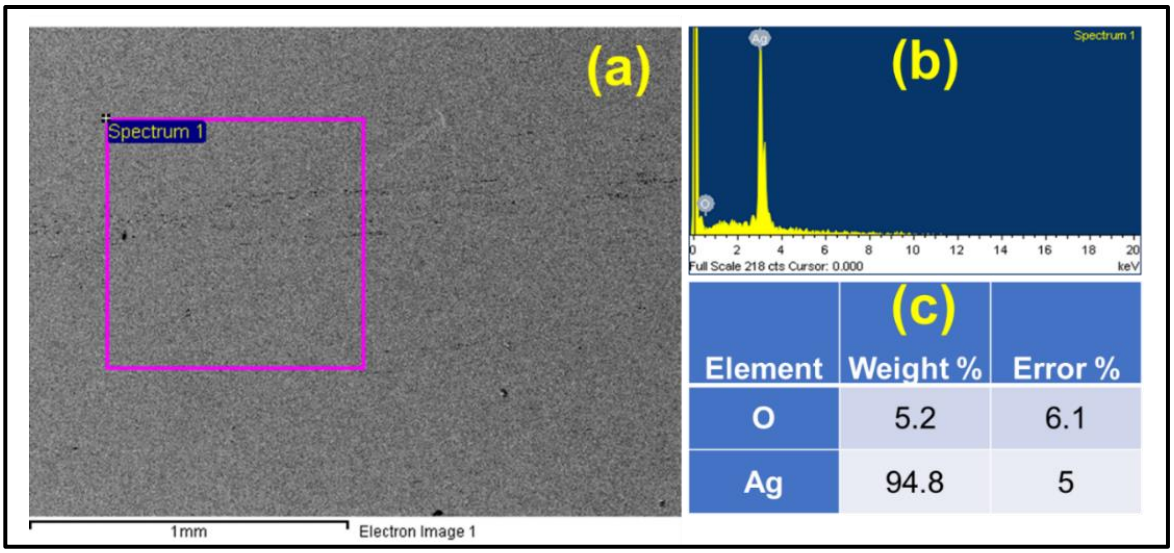

Figure 4B. 5 (a) FESEM image of pristine, unablated Ag surface and (b), (c) its corresponding EDX data revealing Ag and O elemental weight percentage.

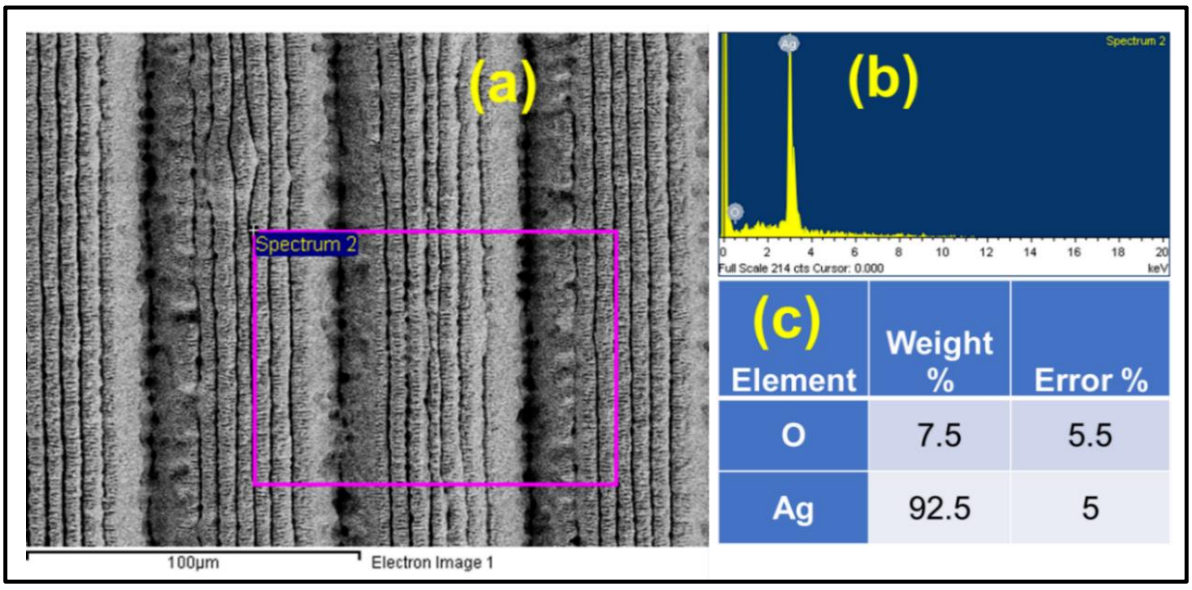

Figure 4B. 6 (a) FESEM image of BB-ablated Ag nanostructure and (b), (c) its corresponding EDX data revealing Ag and O elemental weight percentage.

4B.3.4. Principle mechanisms of nanotubular LIPSS generation using Bessel beam

Based on the established concept of LIPSS formation [37-43], the laser-excited surface plasmon polariton (SPP) [44] interacts with the scattered electromagnetic field along metal-air interfaces [45]. This interaction causes a change in the local ablation fluence profile on the metal surface, affecting the temperature distribution [46] on the same surface. The

interplay between the two elements results in a controlled variation in the intensity profile, which is crucial in the periodic modification of the surface's topography. In the instance of BB ablation, we achieve many benefits in terms of LIPSS formation, which are expected to play a significant role in the potential production of nanotubular arrays of LIPSS. Maragkaki et al. [47] have shown that using pre-patterned surfaces leads to a more effective coupling of electromagnetic modes. The creation of pre-patterned surfaces caused by BB may be crucial in similarly understanding the benefits of pre-patterning, as shown in the research described earlier. Regarding BB ablation, the beam profile with concentric rings and their overlapping has two advantages: it allows for pre-patterning during raster scanning. It stimulates the excitation of SPPs in numerous locations. Furthermore, in the case of a high repetition rate (1 kHz), repeated exposure to laser radiation leads to noticeable changes in surface roughness. These changes, caused by the initial pulses, are crucial in promoting the interaction between surface plasmon polaritons and photons by ensuring that their momenta are in sync. This effect has also been called grating-assisted surface plasmon polariton (SPP) coupling [35]. Thus, in this case of 1 kHz BB ablation, the alterations in surface topography caused by the initial BB pulses and their interaction across different regions (owing to concentric rings of the BB profile) are thought to have significantly contributed to the formation of these unique LIPSS in this study. Gurevich et al. [48, 49] have recently further developed a similar idea by studying the genesis of single-pulse LIPSS. Furthermore, the development of LIPSS is heavily dependent on the decay length, also known as the mean free path [1], of surface plasmon polaritons (SPPs). This pertains to reducing the coherence properties of surface excitation waves (SEWs) under various circumstances. The features of SPP are characterized by the SPP wave number β.

$$\beta = \pm\frac{\omega}{c}\sqrt{\frac{\varepsilon_{metal}\varepsilon_{air}}{\varepsilon_{metal}+\varepsilon_{air}}} \quad \ldots\ldots (1)$$

where ω, c, and ε represent the laser frequency, the speed of light, and the dielectric permittivity of the material, respectively. Additionally, the mean free path of the surface plasmon polaritons (SPPs) ($L_{spp)}$) and the spatial period of the modulated electromagnetic (EM) field (Δ_{SPP}) Calculating The complex components of β may be determined using the following equations.

$$L_{SPP} = \frac{1}{Im(\beta)} \quad \ldots\ldots (2)$$

$$\Delta_{SPP} = \frac{1}{Re(\beta)} \quad \ldots\ldots (3)$$

Gnilitskyi et al. [1] recently reported that plasmonic metals like Ag, Au, and Cu have moderate SPP decay lengths and exhibit LIPSS with low spatial regularity. In contrast, metals like molybdenum and titanium demonstrate superior and highly regular LIPSS. In our particular situation, we have investigated the interaction between BB-metal based on the critical and analogical comparison described earlier. The mid-range magnitude of the SPP decay length in the case of silver and the unique intensity profile of the BB, which has concentric rings, are critical factors in creating nanotubular LIPSS during ablation. Please refer to Figures 4B.3(b) and 4B.3(c) for visual representation. The construction of the unique nanoscale topography, characterized by a less consistent spatial pattern and a structure composed of nanotubular columns, is primarily influenced by the two characteristics stated above. This section explores many elements of the interaction between BB-metal, which remains unexplored until now, providing a complete understanding of the topic. Additionally, it reveals, for the first time, BB ablation's intrinsic and fundamental benefits in generating LIPSS.

4B.3.5. Contrast with fluence using Gaussian beam ablation

Fluence is a significant parameter in laser ablation when comparing surface structuring methods. GB ablation research was conducted to examine the effect of beam profile variation while keeping the fluence setting the same. The estimated fluence of the center peak of BB was about 13 J/cm^2, based on the mathematical connection previously published in references [26, 31]. While keeping other ablation parameters like raster scan speed and interline spacing constant, a fs Gaussian beam resulted in noticeably distinct nanostructures (see Figure 4B.7). Figures 4B.7(a) and 4B.7(b) show the lower magnification pictures of the Ag NS produced with GB at 79 kX and 1 kX magnifications. Additional portions of the Ag NS seen in Figure 4B.7(b), marked by yellow dashed line boxes, are shown at a greater level of magnification (4 kX) in Figure 4B.7(c). Similarly, Figure 4B.7(d) illustrates a specific area (at a magnification scale of 50 kX) from Figure 4B.7(c), which is marked by a dashed box colored

blue. The GB-fabricated Ag NS displayed a multitude of spherical and aspherical nanogrowths on its surface, which were noticeably dissimilar from the Ag NS formed by BB, as shown in Figure 4B.3. This study emphasizes significant disparities in nanostructures generated by fs Bessel and Gaussian beams at a constant laser fluence. Figures 4B.3 and 4B.7 provide a good depiction of the topographical differences resulting from the action of two beams. Exotic LIPSS are produced using broadband laser sources. However, when a Gaussian beam is used, it forms both spherical and non-spherical nanogrowths over the surface shaped by the laser. In addition, EDX mapping was conducted on the NS manufactured by GB to examine the elemental composition in the region that was ablated [Figure 4B.8(a)]. The compositional characteristics [weight percentages, Ag- 93.1 %, O- 6.9 %] of the GB ablated NS closely resemble those of the BB-fabricated NS, as shown by the EDX data as mentioned earlier [Figures 4B.8(b), 4B.8(c)]. To get a deeper understanding, there are plans to conduct an extensive inquiry on ablation, specifically focusing on varying fluence. This investigation will include BB (Black Body) and GB (Gray Body).

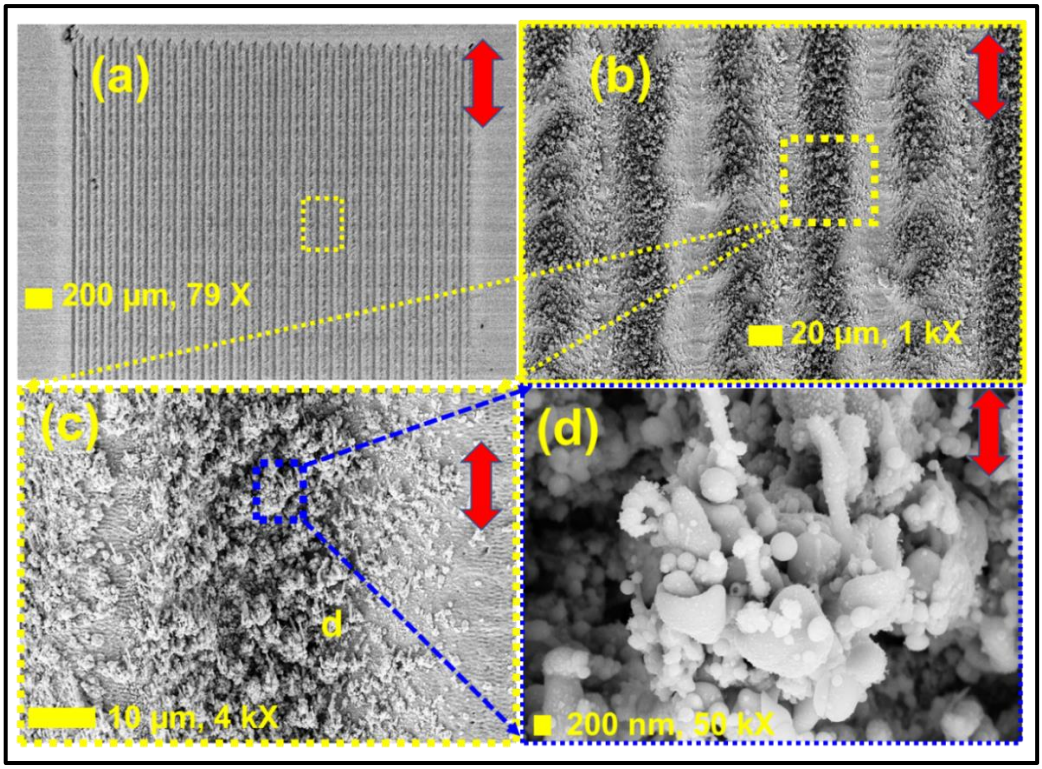

Figure 4B. 7 FESEM images of Gaussian beam ablated NSs for (a) 79 kX, (b) 1 kX, (c) 4 kX, and (d) 50 kX magnifications, respectively. The red arrow depicts the direction of laser polarization. The ablation parameters, such as BB ablation, were kept unchanged, as mentioned in Figure 4B.3.

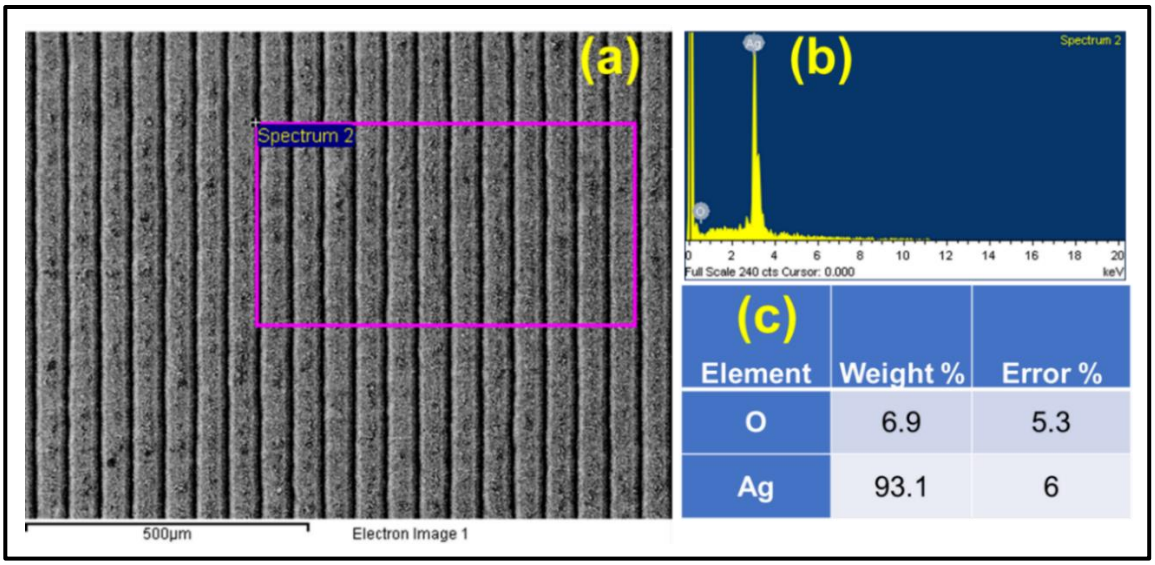

Figure 4B. 8 (a) FESEM image of GB-ablated Ag nanostructure and (b), (c) its corresponding EDX data revealing Ag and O elemental weight percentage.

4B.3.6. SERS-based detection of multiple explosives

Explosive compounds of military quality, such as TNT, Tetryl, RDX, HMX, and others, provide substantial worldwide concerns over both the danger of terrorism and their effect on the environment. Currently, the prevailing methods for detecting large amounts of explosives depend on colorimetric testing, which provides rapid and portable detection. Nevertheless, these procedures often provide inaccurate positive results and lack the required sensitivity and selectivity. Other approaches for detecting substances include ion mobility mass spectrometry, gas chromatography-mass spectrometry (GC-MS), and liquid chromatography-mass spectrometry (LC-MS) [50-53]. Although these procedures provide more reliable outcomes, they usually require significant investment in expensive equipment and the expertise of trained staff to operate these devices. This video showcases the efficacy of the SERS technology as a fast, highly sensitive, and selective method for detecting trace amounts of substances. The introduction of the SERS technology has significantly contributed to the progress of spectroscopy, analytical chemistry, photonics, and sensing. Significant research efforts have been concentrated on using plasmon-enhanced SERS approaches in sensing [31, 54-60]. We investigated the effectiveness of nanotubular LIPSS Ag NS generated using BB in real-time explosive sensing. The objective is to evaluate their potential as on-chip SERS substrates. Our main focus was on using the SERS technique to detect explosives such as

Tetryl (2,4,6-Trinitrophenylmethylnitramine, $C_7H_5N_5O_8$), TNT (2,4,6-Trinitrotoluene, $C_7H_5N_3O_6$), HMX (1,3,5,7-Tetranitro-1,3,5,7-tetrazocane, $C_4H_8N_8O_8$), and RDX (1,3,5-Trinitroperhydro-1,3,5-triazine, $C_3H_6N_6O_6$). The nanotubular periodic nanostructures displayed remarkable plasmonic characteristics, serving as extremely effective, reusable substrates for SERS to detect minuscule amounts of these dangerous substances. The graph in Figure 4B.9(a) displays the SERS signal data for TNT, which may be detected at concentrations as low as 50 nM. The Raman peaks corresponding to this molecule were consistently seen at 790 cm^{-1}, 821 cm^{-1}, 1355 cm^{-1}, 1542 cm^{-1}, and 1617 cm^{-1} throughout a range of doses from 50 nM to 5 mM. No peaks were identified below the threshold concentration of 50 nM. The peaks observed at 790 cm^{-1}, 821 cm^{-1}, 1355 cm^{-1}, 1524 cm^{-1}, and 1617 cm^{-1} are attributed to specific modes: CH out-of-plane vibrations, scissoring NO_2 mode, symmetric NO_2 stretching, asymmetric NO_2 stretching, and aromatic NO_2 conjugation, respectively. These modes match the literature reports [50, 61, 62]. An analysis of around 40 SERS spectra obtained from various locations on the nanostructures revealed a relative standard deviation (RSD) of approximately 15% for the 1355 cm^{-1} peak of TNT at a concentration of 5 mM. This highlights the effectiveness of the substrate in real-time sensing applications, as shown in Figure 4B.9(b). Afterward, the Ag NS substrate underwent two ultrasonic baths in acetone and methanol for 2 hours each to obliterate any remaining residues. The substrate was then used to detect remnants of Tetryl molecules.

Figure 4B.9(c) depicts the SERS signal data for Tetryl, which shows a correlation between concentration and signal strength. The data demonstrates that Tetryl may be detected at concentrations as low as 50 nM. The Raman peaks associated with the molecule were detected at 826 cm^{-1} and 1357 cm^{-1} throughout a range of doses spanning from 50 nM to 5 mM. No discernible peaks were seen for values below 50 nM. The observed peaks correspond to the symmetric and asymmetric stretching of NO_2 groups and the nitro-aromatic vibrations in Tetryl [31, 50, 63]. A total of over 40 SERS spectra were obtained from randomly selected locations. The results revealed a relative standard deviation (RSD) of around 17% for the 1357 cm^{-1} peak of Tetryl at a concentration of 5 µM. This further demonstrates the effectiveness of the substrate for real-time sensing applications, as shown in Figure 4B.9(d). In addition, a BB-structured Ag NS made in the same way was used to detect two more commonly found explosive compounds, RDX and HMX. In the concentration-dependent

analysis, the Raman peaks corresponding to different concentrations of RDX were identified at certain wavenumbers: 875 cm^{-1}, 932 cm^{-1}, 1260 cm^{-1}, 1312 cm^{-1}, and 1373 cm^{-1}. The smallest detectable amount was measured at 500 nM. The whole of the data is illustrated in Figure 4B.10(a). The Raman bands of RDX were clearly distinguished: the band at 875 cm^{-1} corresponds to the symmetric ring-breathing mode, whereas the band at 932 cm^{-1} combines ring stretching with N–O deformation. The 1260 cm^{-1} band is caused by the scissoring of CH_2 and the stretching vibration of N–N, whereas the 1312 cm^{-1} band is associated with the wagging of CH_2.

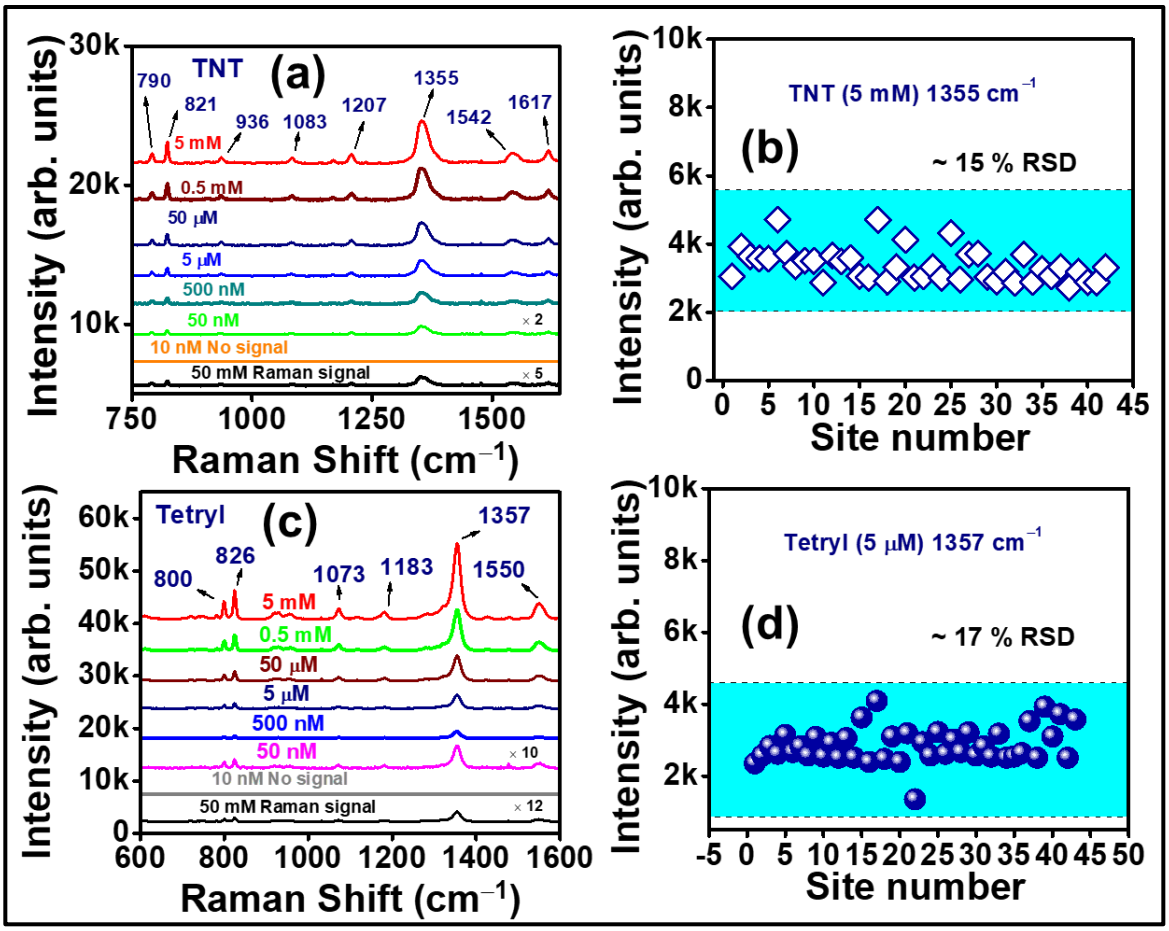

Figure 4B. 9 (a) Concentration-dependent SERS spectra of TNT using BB ablated Ag NS, along with pure Raman spectrum (in black color) of TNT (50 mM) collected from unablated Ag pristine, (b) Reproducibility spectra (with ~15% RSD) of TNT (5 mM), (c) Concentration-dependent SERS spectra of Tetryl using recycled BB ablated Ag NS, along with pure Raman spectrum (in black color) of Tetryl (50 mM) collected from unablated Ag pristine, (d) Reproducibility spectra (with ~17% RSD) of Tetryl (5 μM). The portable Raman acquired the complete SERS data in this figure, with the same acquisition parameters mentioned in the experimental details.

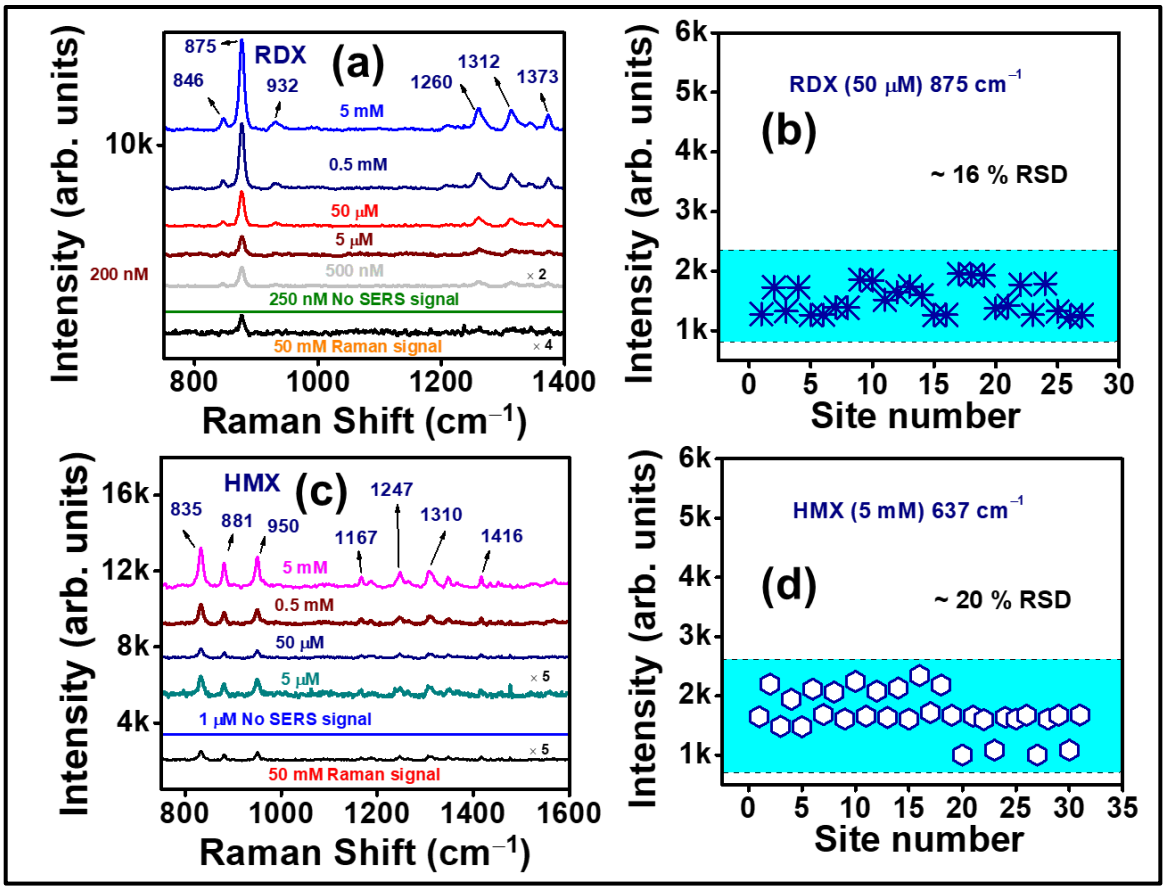

Figure 4B. 10 (a) Concentration-dependent SERS spectra of RDX using BB ablated Ag NS, along with pure Raman spectrum (in black color) of RDX (50 mM) collected from unablated Ag pristine, (b) Reproducibility spectra (with ~16% RSD) of RDX (50 μM), (c) Concentration-dependent SERS spectra of HMX using recycled BB ablated Ag NS, along with pure Raman spectrum (in black color) of HMX (50 mM) collected from unablated Ag pristine, (d) Reproducibility spectra (with ~20% RSD) of HMX (5 mM). The complete SERS data in this figure has been acquired by the portable Raman, with the same acquisition parameters mentioned in experimental details.

The 1373 cm^{-1} band corresponds to the υNO_2 symmetric stretching vibration and βCH_2 scissoring, which together indicate the many vibrational modes of RDX [64, 65]. The uniformity of the SERS signal was also assessed using numerous SERS spectra (> 30), which yielded an approximate relative standard deviation (RSD) value of 16% for 50 μM RDX, as shown in Figure 4B.10(b). Following thorough solvent cleaning with the help of an ultrasonic bath, the Ag NS substrate was used to detect HMX. Figure 4B.10(c) shows the SERS spectra of HMX at various concentrations, with the lowest concentration being 5 μM. Figure 4B.10(d) presents the plot of relative standard deviation (RSD), indicating an RSD value of around 20%. The discovered peaks correspond to HMX's vibrational/Raman modes [66, 68]. The peak at 835 cm^{-1} is associated with NO_2 deformation, while the peak at 950 cm^{-1} is

related to C-C ring stretching. The modes at 1167 cm^{-1} and 1247 cm^{-1} indicate C-N-C stretching. The peak seen at 1310 cm^{-1} corresponds to the vibrations of NO_2. To acquire a comprehensive understanding, the enhancement factors (EFs) for all the trace detections conducted by BB structured Ag NS have been calculated using established methods from earlier reports [26, 31, 54, 57, 59].

The EF values were computed as 2.2×10^6, 2.4×10^6, 2.1×10^5, and 1.78×10^4 for TNT (50 nM), Tetryl (50 nM), RDX (500 nM), and HMX (5 µM), respectively. We conducted SERS investigations on GB ablated NSs to investigate the potential variations in sensing capability resulting from the contrasting structural characteristics of BB ablated NSs. It has been shown that the BB NSs functioned much better, with EFs that were at least one order of magnitude greater than the GB-ablated NSs. The measured relative standard deviation (RSD) values for BB-structured substrates have shown much lower than GB-structured substrates, indicating their potential as highly effective, real-time surfaces for SERS. The minimum detectable concentrations for TNT and Tetryl were 200 nM and 500 nM, respectively. Figures 4B.11(a) and 4B.11(c) give SERS data for different concentrations, whereas Figures 4B.11(b) and 4B.11(d) display the RSD plots. The observed drop in RSD values is due to the nanotubular array's periodic topographical aspect, specifically LIPSS. The overall superiority of the BB-engineered NS over the GB-structured NS in terms of EFs and signal consistency (RSD) has been visually shown in Figure 4B.12 of the Supplementary Information file. Furthermore, the Ag NS effectively produced by BB contact was used in SERS mapping investigations to understand the enhanced Raman signal at a sub-micron scale. Figure 4B.13 displays the comprehensive SERS mapping data obtained from a Micro-Raman spectrometer, LabRAM HR Evolution, using a 532 nm excitation. The experimental section provides specific details on the signal acquisition settings. The mapping Figures offer statistics on large-area SERS signal variation. Four compounds were analyzed in the following Figures: 4B.13(a)- TNT (peak at 821 cm^{-1}, concentration of 5 mM), 4B.13(b)- Tetryl (peak at 1357 cm^{-1}, concentration of 5 mM), 4B.13(c)- RDX (peak at 875 cm^{-1}, dosage of 5 mM), and 4B.13(d)-HMX (peak at 881 cm^{-1}, concentration of 5 mM). The analysis covered an area of more than 2500 μm^2 for each picture. The variation in the SERS response is seen in distinct regions of each of the mapping pictures. During drop-casting of the analyte, the differences in the adsorption of various explosive molecules are very influential in the SERS mapping data.

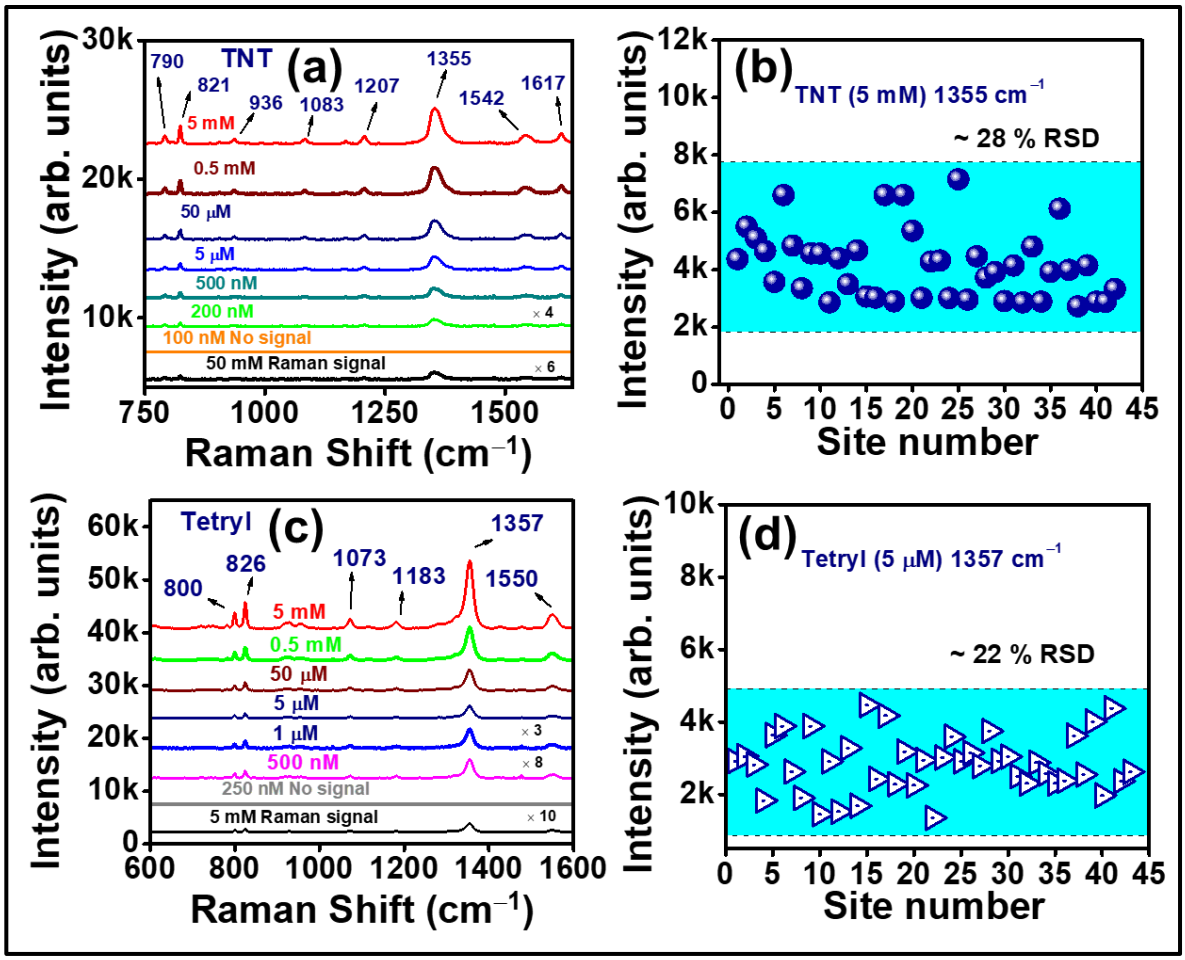

Figure 4B. 11 (a) Concentration-dependent SERS spectra of TNT using GB ablated Ag NS, along with pure Raman spectrum (in black colour) of TNT (50 mM) collected from unablated Ag pristine, (b) Reproducibility spectra (with ~28% RSD) of TNT (5 mM), (c) Concentration-dependent SERS spectra of Tetryl using recycled GB ablated Ag NS, along with pure Raman spectrum (in black colour) of Tetryl (50 mM) collected from unablated Ag pristine, (d) Reproducibility spectra (with ~22% RSD) of Tetryl (5 μM). The portable Raman acquired the complete SERS data in this figure, with the same acquisition parameters mentioned in the experimental details.

This element is considered one of the primary variables responsible for the difference in strength of the SERS signal throughout various parts of the NS. Combining SERS mapping data with portable Raman SERS measurements provides a comprehensive assessment of the BB-interacted NS, serving as an on-chip sensor. Milligan et al. [50] detected several nitroaromatic explosives using SERS, accomplished with remarkable sensitivities. For instance, the sensitivity achieved for TNT is 6.81 ng/mL, while for Tetryl it is 17.2 ng/mL. This high sensitivity is achieved by forming a Janowsky complex. Dasary et al. [68] used gold nanoparticle-based label-free SERS probes to showcase their very sensitive detection

abilities, reaching a detection limit of 2 picomolar (pM) specifically for TNT. Marrapu et al. [61] generated silver nanoribbons by picosecond ablation utilizing cylindrical focusing and used them to detect trace amounts of TNT using SERS. They estimated an enhancement factor of roughly ~10^7 for the 1362 cm^{-1} SERS peak, corresponding to the symmetric stretching mode of the NO_2 group in TNT. Almaviva et al. [64] documented a very sensitive method for detecting RDX using commercially available SERS substrates. They achieved detection limits in the region of a few tens of picograms. Hatab et al. [65] used gold nanoparticles with around 90-100 nm diameter as SERS substrates. They detected RDX in polluted groundwater at concentrations as low as 0.15 mg/l, achieving an enhancement factor of roughly 6×10^4. Liyanage et al. [69] have successfully shown a self-assembled, adaptable nanosensor exhibiting sensitive SERS reactions and exceptional consistency. This nanosensor efficiently detects explosive substances such as RDX and TNT.

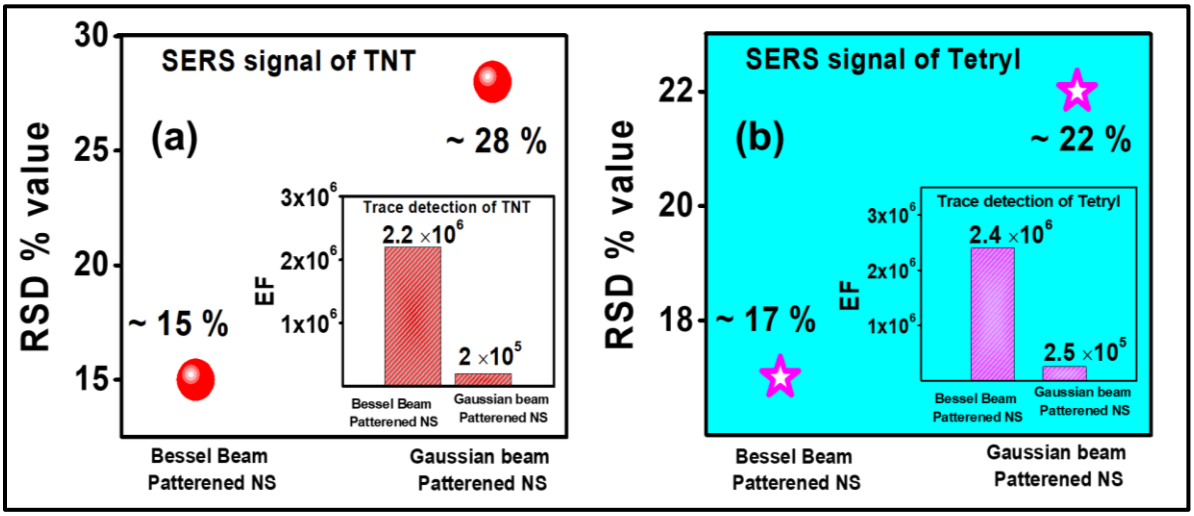

Figure 4B. 12 SERS performance comparison plot of the BB-engineered Ag NS, with GB-structured Ag NS, regarding EFs and signal consistency (RSD). (a) Comparison of RSDs between BB patterned Ag NS and GB patterned Ag NS for the detection of TNT. The inset bar plot shows the comparison of the EFs. (b) Comparison of the RSDs between BB patterned Ag NS and GB patterned Ag NS for the detection of Tetryl. The inset bar plot shows the comparison of the EFs.

Zapata et al. [70] provided a comprehensive overview of essential detection experiments using SERS for Tetryl and other explosive compounds. Compared to current research, the nanotubular LIPSS Ag substrates investigated in this work demonstrate superior or equivalent capabilities in detecting different explosives, including TNT, Tetryl, RDX, and HMX. These

substrates display flexibility and sensitivity. There is still a possibility for additional improvements in these substrates as active materials in the SERS studies.

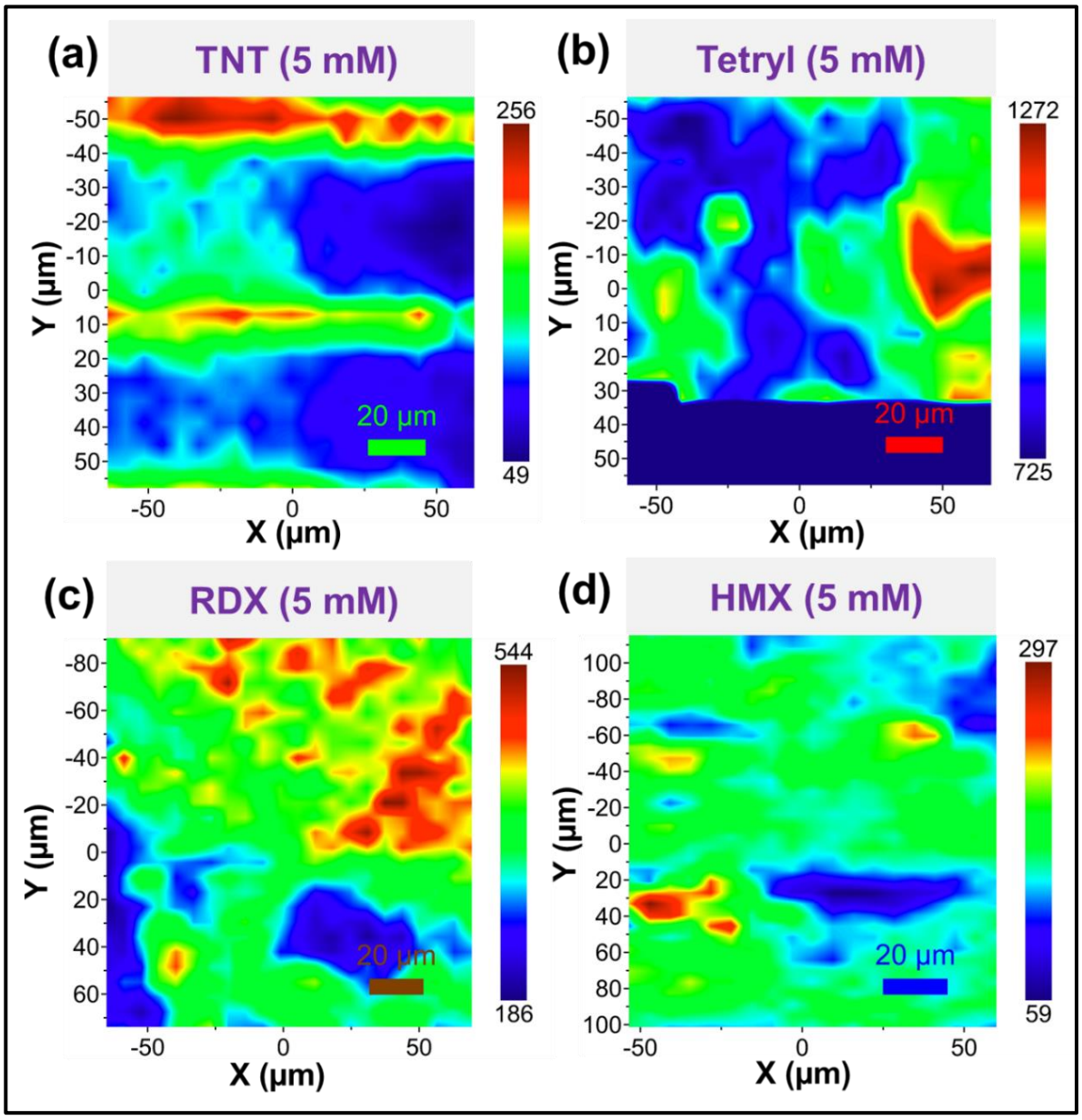

Figure 4B. 13 Large area mapping image data, 8(a)- TNT (corresponding peak 821 cm^{-1}, 5 mM concentration), 8(b)- Tetryl (corresponding peak 1357 cm^{-1}, 5 mM concentration), 8(c)- RDX (corresponding peak 875 cm^{-1}, 5 mM concentration), and 8(d)-HMX (corresponding peak 881 cm^{-1}, 5 mM concentration), covering more than 2500 μm^2 area for each image.

Furthermore, we have conducted reflectivity measurements, including all the nanosheets (BB Ag NS, GB Ag NS, Ag pure) manufactured in this study. Reflectivity measurements were performed at an incidence angle of 45^0 degrees, covering a range of wavelengths from 300 to

800 nm. Regardless of the situation, the Ag NSs consistently exhibited a rise in reflectance when the incident wavelength approached 800 nm. The Ag NS that underwent GB ablation had a maximum reflectance of 40-50%, but the pristine Ag demonstrated the greatest reflectance, reaching 56-66%. On the other hand, the NS with a BB structure showed a much-reduced reflectance of 30-35%, as seen in the results shown in Figure 4B.14(a). The unique and innovative structures of LIPSS, which have a hierarchical roughness, are expected to enhance their ability to trap light [71] greatly. This results in a considerable reduction in reflectance. In their study on amorphous silicon films, Dostovalov et al. [72] provided a comparable explanation for the hierarchical anti-reflective structures created using LIPSS, designed explicitly for sensing purposes. LIPSS, characterized by their large aspect ratios, improve the anti-reflective qualities in the visible and near-infrared range. The research shows a significant decrease in the amount of light reflected by the nanotubular LIPSS surface in the 450 to 800 nm range. This result is due to the strong trapping of light inside the surface's periodic and rough texture. This behavior aligns with findings obtained from FESEM and AFM data (refer to the pictures of nanotubular LIPSS shown in Figure 4B.3). The incident light is restricted between the periodic gaps and the spaces between columnar NS, which have diameters larger than the wavelength of light. Moreover, the process of effective light dissipation is facilitated by repeated absorptions [73, 74] that occur during subsequent reflections inside the described LIPSS breaks. As a result, there is a significant decrease in reflectance [73-75]. The enhanced optical absorption of the BB-structured Ag nanostructures in the visible spectrum suggests that fs BB surface engineering is a potential technique for creating anti-reflective surfaces. This approach has the potential to be used in several applications, including the production of black surfaces [72], the creation of anti-reflection surfaces for high-powered or ultra-broadband coherent light sources [71], aerospace technology, solar cells, and optical design [76]. These nanotubular LIPSS may also have potential use in the newly studied thermal-induced reflectance oscillation study [76]. In addition, we performed a comprehensive investigation to evaluate the practical feasibility of using this BB-structured Ag NS substrate for real-time detection. The study included monitoring its plasmonic characteristics over an extended period. Using a portable Raman spectrometer, we continuously acquired several SERS spectra of TNT (at a concentration of 5 mM) for 90 days, with weekly measurements while keeping the experimental conditions

constant. Before each measurement, the substrate was subjected to washing. Subsequently, an equivalent quantity of the analyte (~20 µL, 5 µM) was deposited, and signal buildup ensued. Figure 4B.14(b) depicts the progressive decrease in the Raman signal counts of TNT (specifically the peak at 1335 cm^{-1}) over 90 days. The Figure's inset displays the appropriate spectrum. The decrease in SERS counts may be caused by the deterioration of nanoscale hotspots in the plasmonic Ag NS owing to repeated substrate cleaning.

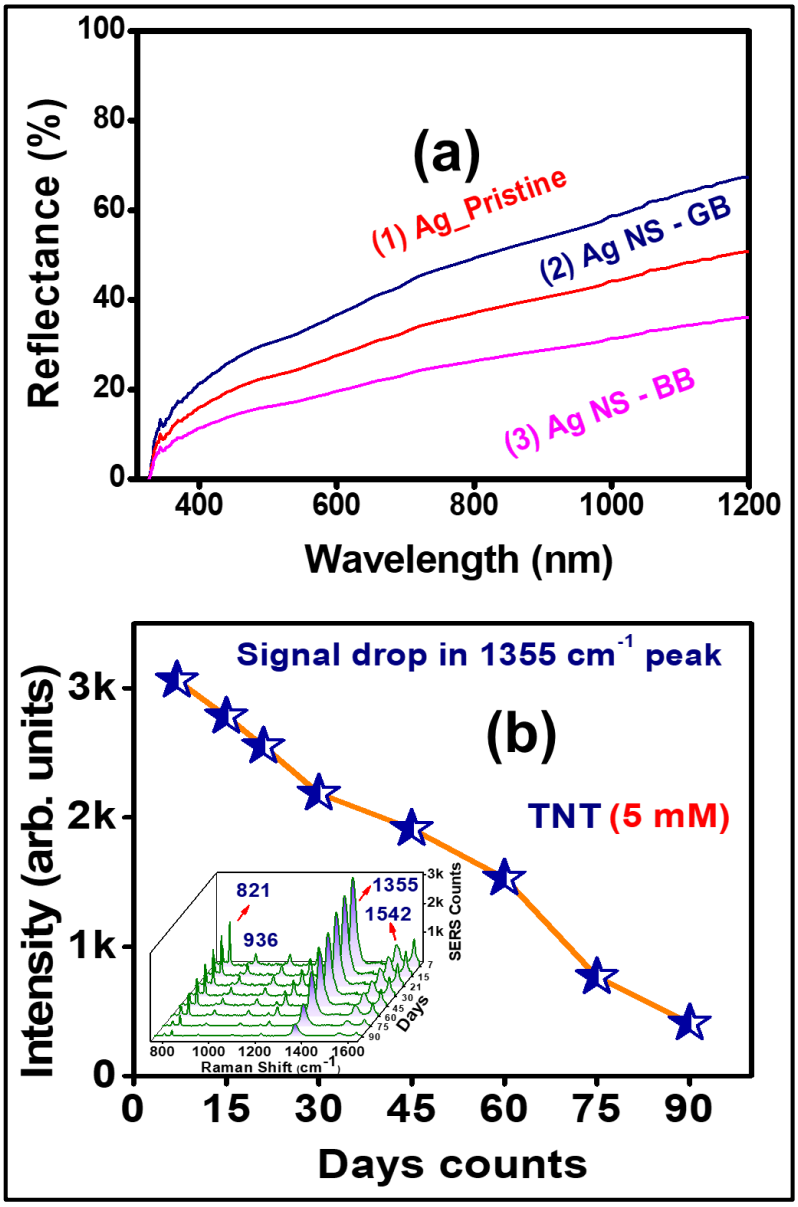

Figure 4B. 14 (a) Reflectivity spectra for BB structured LIPSS Ag NS, GB structured Ag NS, and pristine Ag surface at 45^0 angle of incidence (b) Signal strength stability data for the sensing of TNT (5 mM) molecule, unveiling the presence of 1355 cm^{-1} peak signature. The SERS data was collected for up to 90 days.

Significantly, we have seen that even after 90 days, identifying the TNT distinctive Raman peak at 1335 cm-1 remained apparent, albeit the signal decreased to less than 20% of its original strength (on day one). This emphasizes the efficiency and usefulness of the BB-ablated, SERS-active substrate in real-time applications for detecting hazardous chemicals. Nevertheless, we are currently investigating methods to enhance the sensitivity and stability of our system over a 20–24-week period. This involves optimizing the structures by adjusting laser parameters such as focusing conditions and pulse repetition rate. Additionally, we are considering storing the samples in air-free or vacuum-packed containers and applying a thin layer of gold (<20 nm thick) to enhance plasmonic effects further. This approach has been successfully demonstrated in our previous research, resulting in a (10-100) times increase in sensitivity and long-term stability lasting several months.

4B.3.7. Uniform LIPSS on Copper Created Using Zeroth-Order Femtosecond Bessel Beam for SERS-based Applications

In a subsequent study, we provide findings on the creation of LIPSS when fs amplifier pulses (1 kHz, 800 nm) interact with a copper target in the shape of a non-diffracting, propagation invariant, zeroth-order Bessel beam. Afterward, the laser-engineered plasmonic surface was used as a substrate for SERS to detect small amounts of secondary explosives such as Tetryl (TL) - 2,4,6-Trinitrophenylmethylnitramine and pentaerythritol tetranitrate (PETN) in real-time. The SERS spectra of TL and PETN revealed distinct Raman modes/peaks at 1357 cm^{-1} and 1292 cm^{-1}, respectively. The minimum detectable concentrations for TL and PETN were 5 µM and 1 mM, respectively. This work shows that the inexpensive Cu NSs may serve as durable, adaptable, and useful SERS platforms. A pristine copper target was used to perform laser ablation in the air (LAA) medium using a Bessel beam [800 nm, 1 kHz, 50 fs] created by an axicon. The distribution of elements and the topographical properties of the NSs were analyzed using energy dispersive spectroscopy (EDS) and field emission scanning electron microscopy (FESEM) after ablation. A surface design measuring 3 mm x 3 mm was created on copper using the BB to do a raster scan in two X-Y guided steps. The Cu NSs were used as SERS-active platforms following a thorough topography analysis. The B&W Tek i-Raman plus, a small and hand-held Raman spectrometer with an excitation wavelength of 785 nm and a spot size of around 90 µm, has been used to identify studies using PETN

and TL molecules. The details of the experiment have already been addressed. The use of non-diffracting BB resulted in the generation of large periodic regions and ladder-like structures during a comprehensive raster scan on the copper (Cu) surface. An investigation was conducted to see whether two subsequent ablation zones imprinted with BB profiles had spatial overlap. The ablation imprints are visible in Figure 4B.15(a). The topographical properties of the ablation zones illustrate the process during ablation. This demonstrates the inherent process of BB ablation, whereby the concentric rings encircling the central lobe region overlap distinctly.

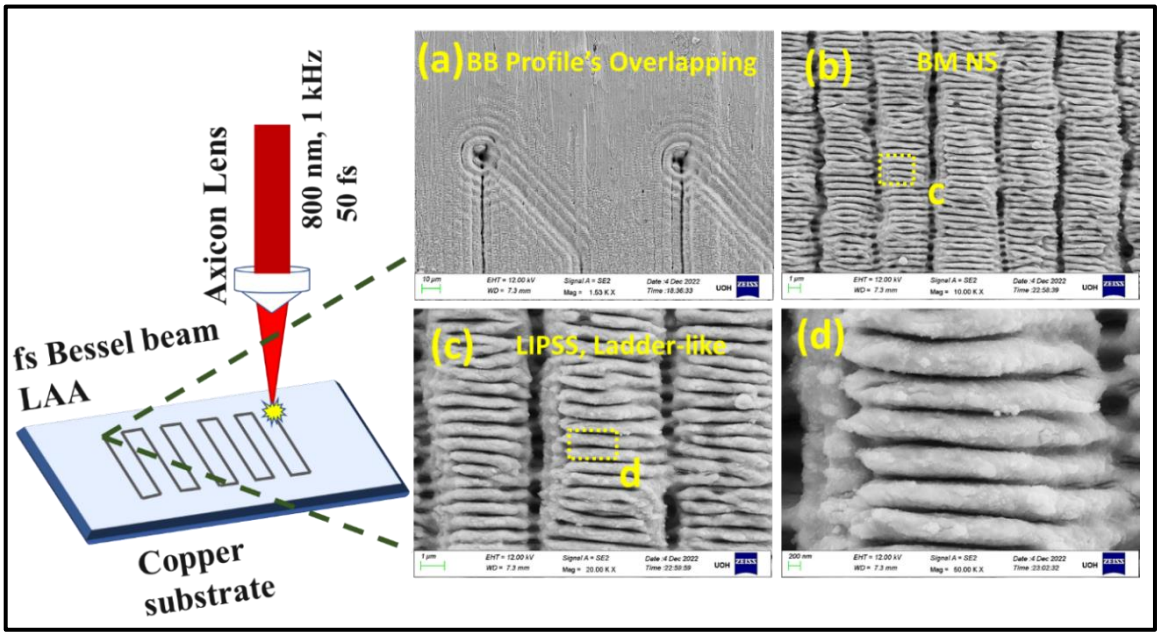

Figure 4B. 15 Schematic of BB generated laser ablation in air, with a 50 fs, 800 nm BB generated using an axicon (a) FESEM image of the spatial overlap of two consecutive BB profile ablation imprints on Cu surface (b) lower magnification image of the BB patterned Cu surface (c) ladder-like LIPSS formed in nanoscale topography due to BB interaction (d) higher magnification image of Cu NS revealing ladder-like steps with numerous nano growths on them.

Figure 4B.15(b) depicts the extensive expanse of LIPSS, whereas Figure 4B.15(c) exhibits the ladder-like arrangement. Figure 4B.15(d) shows a high-resolution FESEM image illustrating the organic nanostructures developed at each process step. The ablated zones exhibit distinct core lobe sections and circular rings, providing evidence of the beam's form imprint on the Cu surface. Furthermore, the locations where the BB imprints interacted provide evidence of the overlapping ablated zones caused by the raster scan. An essential

factor contributing to the production of periodic surface patterns is the phenomenon of overlap. The center line is formed by the core lobe of the BB, whereas the periodic section is created by the concentric rings of the BB profile around the ablated region of the central lobe. The development of nanostructures across a large region is attributed chiefly to the ablation generated by BB. The primary area of research has been on the periodic neutron stars, which resemble ladders, due to the interaction of the concentric circles in the BB. This is in addition to the core lobe line. Due to the periodicity of the LIPSS sections being less than 550 nm, the NS was categorized as a low spatial frequency LIPSS. It was found that the LSFL-I NSs, which were previously described, exhibit several ladder-like steps with observable nano growths. Figure 4B.16[(a) to (f)] displays the whole EDX data. The EDX analysis revealed that the elemental components present in the sample were mostly copper, accounting for about 79% of the weight. Additionally, the study confirmed the presence of oxidation, which accounted for approximately 21% of the weight. This oxidation is believed to have occurred due to the high temperatures involved in the ablation process.

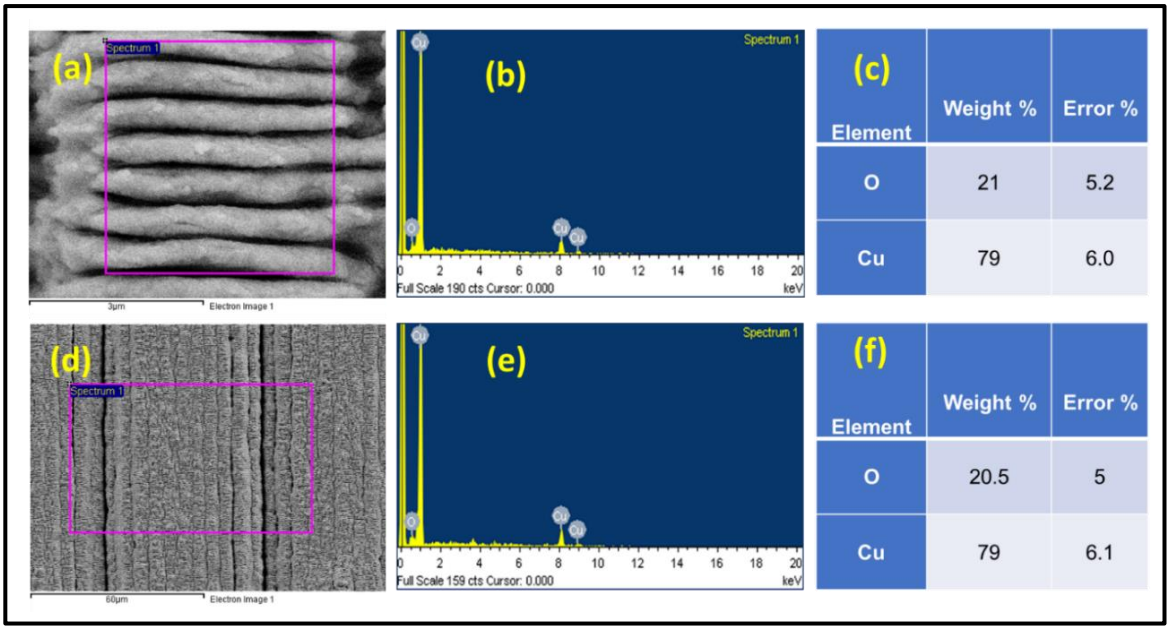

Figure 4B. 16 (a)-(c) FESEM EDX elemental analysis data for the ladder-like LIPSS region depict the amount of O and Cu in the same area. (d)-(f) FESEM EDX elemental analysis data for the larger NS region, depicting the amount of O and Cu present.

The measured period of LIPSS was around 580 nm for the Copper Nanostructures (Cu NSs) species, with a value of (Λ =0.73λ) for the LSFL parameter. Historically, plasmonic

nanoelements with single metal/semiconductor/alloy interfaces have been used for research focused on sensing and have significant applications in nanophotonics. Several analytical approaches have been used to identify different chemicals in recent years. However, the SERS technique is very effective and nondestructive in detecting the most dangerous substances. Due to this rationale, the plasmonic Cu nanostructure was used as a SERS sensor. Figure 4B.17 depicts the SERS-sensing study. The Bessel beam detected Cu nanostructures using Tetryl (TL) and PETN as the explosive materials. Using the SERS technique, the minimum detectable concentrations achieved were 5 µM and 1 mM, respectively. We calculated both nanostructures' enhancement factors (EFs) using a well-recognized mathematical approach to get a clear picture. The EF was around 10^3, as determined by calculation. The SERS substrates exhibit exceptional repeatability of the SERS signal, with a relative standard deviation (RSD) of <20%. This makes them suitable for real-time sensing applications that include explosive and hazardous compounds. Unlike Tetryl, which was found to have a characteristic Raman peak near 1357 cm^{-1} resulting from the symmetric stretching of NO_2, PETN had a distinct Raman peak at 1292 $cm^{-1,}$ also owing to NO_2 symmetric stretching. Table 4B.1 summarizes the additional Raman modes found for these two compounds. In Table 4B.2, we have included a comparison of the performance of the Cu NSs with the trimetallic NSs (Ag-Au-Cu) previously published [31]. The tests were conducted under comparable circumstances.

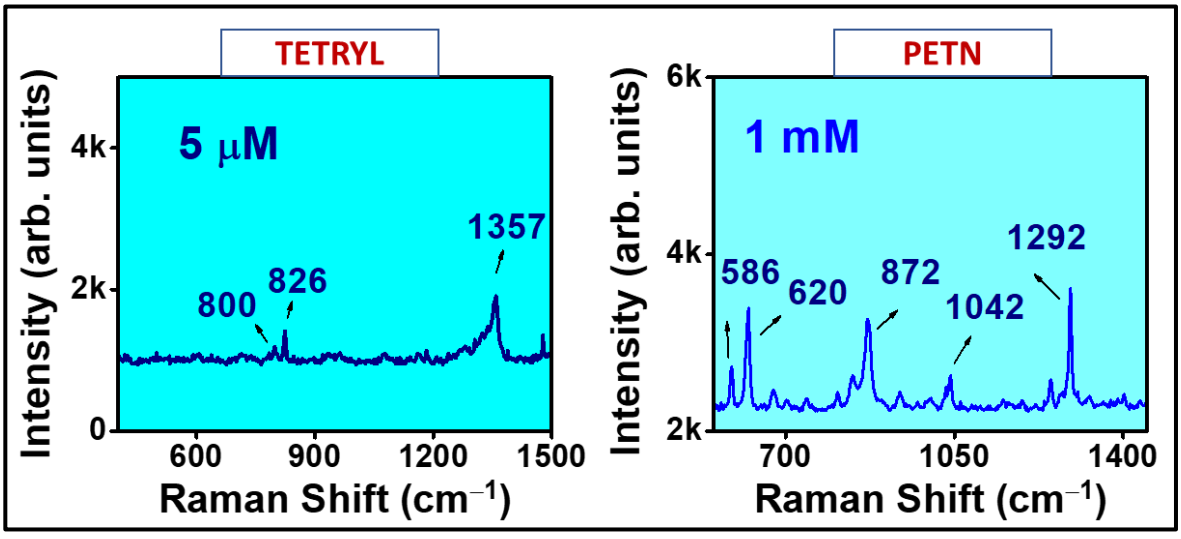

Figure 4B. 17 (a) SERS data of trace concentration of Tetryl (5 µM), with its signature peak at 1357 cm^{-1} (b) SERS spectrum of PETN (1 mM), displaying its signature peak at 1292 cm^{-1}.

Table 4B.1 Raman modes corresponding to significant Raman peaks

Analytes	Raman Peaks (cm^{-1})	Corresponding Modes
Tetryl		
	760	Out-of-plane deformation of the nitro group
	1357	NO_2 symmetric stretching
	1541	NO_2 asymmetric stretching
PETN	620	O− NO_2 rocking transition
	872	O− N stretching
	1042	CH_2 torsion, CC bending
	1292	NO_2 symmetric stretching

Table 4B.2: Lowest trace and EFs comparison of BB fabricated LIPSS NSs

SERS Substrates	Detected Analytes	Lowest Detected Concentration	Enhancement Factor
SERS studies were performed by a 785 nm excitation portable Raman spectrometer, with ~100 µm spot size			
fs BB structured Trimetallic Ag-Au-Cu NS	Tetryl, PETN	200 nM, 500 µM	4.7×10^5, 1.2×10^3
fs BB structured Cu NS	Tetryl, PETN	5 µM, 1mM	~10^3

Although the SERS performance of the Cu NSs could have been better than that of the previously mentioned substrates, the benefit of fabricating Cu NSs lies in its cost-effectiveness. Therefore, our research shows that the inexpensive Cu NSs are durable, adaptable, and useful SERS platforms. Furthermore, one may maximize the advantages of both copper (Cu) and silver/gold (Ag/Au) hybrid substrates, resulting in cost-effectiveness from Cu and significant improvements from Ag/Au.

4B.4. Conclusions

To summarize, this work demonstrates the development of novel nanotubular arrays LIPSS using a fs Bessel beam. We systematically investigated the overlapping impression of the Bessel beam profile on the silver surface and conducted a raster scan. This method created complex nanotubular patterned LIPSS over the nanoscale surface (NS). We used advanced techniques like FESEM and AFM to conduct a detailed examination and discover the nanoscale topographical characteristics of these NSs. The interaction between the Bessel beam-induced surface plasmon polaritons (SPPs) and the incoming beam may have resulted in periodic modulation of the input fluence on the surface. The formation of LSFL category I LIPSS is primarily driven by this process, which results in a period (Λ) of around 575±10 nm. Comparative ablation investigations conducted using a fs Gaussian beam with the same intensity (and similar ablation settings) showed interesting variations in the structure of the generated nanostructures. In the case of the Gaussian beam, no LIPSS were seen at these intensities. In the future, we will thoroughly evaluate the impact of fluence on surface structuring using both Bessel and Gaussian beams. This study will provide a significant understanding of the creation of LIPSS. The use of Bessel beam-induced Ag LIPSS NSs as a plasmonic, SERS-active substrate has shown great effectiveness in detecting various real-time explosives, including TNT (50 nM), Tetryl (50 nM), RDX (500 nM), and HMX (5 µM). Significant RSD values and enhancement factors (~10^6) were obtained with BB-structured LIPSS. The SERS-active substrates exhibited EFs at least one order of magnitude greater than those of the previously reported trimetallic NS. In addition, we investigated potential uses for developing anti-reflection surfaces. In this chapter, we have successfully created substantial nano-structures on a Copper (Cu) surface utilizing the fs BB LAA method, resulting in the spectacular formation of LIPSS. The LIPSS has been classified as a member of the low spatial frequency LIPSS (LSFL) category and exhibits distinct characteristics of unique nanostructures resembling ladders on step structures. Moreover, the Cu nanostructure has shown its efficacy and sensitivity as a SERS-active medium for rapid and practical detection of dangerous explosives. This chapter presented the data from the exploration study of Bessel beam-metal interaction, creating unique nanotubular arrays LIPSS with varied sensing applications based on SERS.

References

[1] I. Gnilitskyi, T.J. Derrien, Y. Levy, N.M. Bulgakova, T. Mocek, L. Orazi, High-speed manufacturing of highly regular femtosecond laser-induced periodic surface structures: physical origin of regularity, Sci Rep, 7 (2017) 8485.

[2] N.J. Halas, S. Lal, W.S. Chang, S. Link, P. Nordlander, Plasmons in strongly coupled metallic nanostructures, Chem Rev, 111 (2011) 3913-3961.

[3] S.Y. Chae, N. Yoon, E.D. Park, O.S. Joo, Surface modification of CuInS2 photocathodes with ruthenium co-catalysts for efficient solar water splitting, Applied Surface Science, 612 (2023) 155856.

[4] X. Ge, Y. Hu, H. Shen, W. Liang, Z. Sun, X. Zhang, G. Ospankulova, M. Muratkhan, K.Z. Kh, W. Li, Electron beam irradiation application for improving the multiscale structure and enhancing physicochemical and digestive properties of acetylated naked barley, Food Chem, 404 (2023) 134674.

[5] M. Jaworski, A. Chudzyńska, P. Mrowiński, G. Sęk, Efficient Emission in the Telecom Range from Quantum Dots Embedded in Photonic Structures Fabricated by Focused Ion Beam Milling, Acta Physica Polonica A, 142 (2022) 662-667.

[6] M.M. Hossain, M. Gu, Fabrication methods of 3D periodic metallic nano/microstructures for photonics applications, Laser & Photonics Reviews, 8 (2014) 233-249.

[7] J. Bonse, Quo Vadis LIPSS?-Recent and Future Trends on Laser-Induced Periodic Surface Structures, Nanomaterials (Basel), 10 (2020) 1950.

[8] J. Bonse, S. Gräf, Maxwell Meets Marangoni—A Review of Theories on Laser-Induced Periodic Surface Structures, Laser & Photonics Reviews, 14 (2020), 2000215.

[9] J. Bonse, S.V. Kirner, J. Krüger, Laser-Induced Periodic Surface Structures (LIPSS), in: Handbook of Laser Micro- and Nano-Engineering, 2021, pp. 1-59.

[10] F. Nyenhuis, P.N. Terekhin, T. Menold, B. Rethfeld, A. Michalowski, J.A. L'Huillier, Fundamentals of Scanning Surface Structuring by Ultrashort Laser Pulses: From Electron Diffusion to Final Morphology, Advanced Photonics Research, 3 (2022).

[11] Y. Zhang, Q. Jiang, M. Long, R. Han, K. Cao, S. Zhang, D. Feng, T. Jia, Z. Sun, J. Qiu, H. Xu, Femtosecond laser-induced periodic structures: mechanisms, techniques, and applications, Opto-Electronic Science, 1 (2022) 220005-220005.

[12] S.A. Jalil, B. Lai, M. ElKabbash, J. Zhang, E.M. Garcell, S. Singh, C. Guo, Spectral absorption control of femtosecond laser-treated metals and application in solar-thermal devices, Light Sci Appl, 9 (2020) 14.

[13] M. Valenti, A. Venugopal, D. Tordera, M.P. Jonsson, G. Biskos, A. Schmidt-Ott, W.A. Smith, Hot Carrier Generation and Extraction of Plasmonic Alloy Nanoparticles, ACS Photonics, 4 (2017) 1146-1152.

[14] J. Zhang, Y. Wang, D. Li, Y. Sun, L. Jiang, Engineering Surface Plasmons in Metal/Nonmetal Structures for Highly Desirable Plasmonic Photodetectors, ACS

Materials Letters, 4 (2022) 343-355.
[15] J. Geng, L. Shi, X. Sun, W. Yan, M. Qiu, Artificial Seeds-Regulated Femtosecond Laser Plasmonic Nanopatterning, Laser & Photonics Reviews, 16 (2022).
[16] S. Mitra, M. Basak, Diverse bio-sensing and therapeutic applications of plasmon enhanced nanostructures, Materials Today, 57 (2022) 225-261.
[17] K. Schwibbert, A.M. Richter, J. Krüger, J. Bonse, Laser-Textured Surfaces: A Way to Control Biofilm Formation, Laser & Photonics Reviews, (2023) 2300753.
[18] E. Stratakis, J. Bonse, J. Heitz, J. Siegel, G.D. Tsibidis, E. Skoulas, A. Papadopoulos, A. Mimidis, A.C. Joel, P. Comanns, J. Krüger, C. Florian, Y. Fuentes-Edfuf, J. Solis, W. Baumgartner, Laser engineering of biomimetic surfaces, Materials Science and Engineering: R: Reports, 141 (2020) 100562.
[19] V. Coviello, D. Forrer, V. Amendola, Recent Developments in Plasmonic Alloy Nanoparticles: Synthesis, Modelling, Properties and Applications, Chemphyschem, 23 (2022) e202200136.
[20] J. Bonse, S. Graf, Ten Open Questions about Laser-Induced Periodic Surface Structures, Nanomaterials (Basel), 11 (2021) 3326.
[21] M. Senegačnik, P. Gregorčič, Diffraction-driven laser surface nanostructuring: Towards patterning with curved periodic surface structures, Applied Surface Science, 610 (2023) 155486.
[22] C.-L. Chang, C.-W. Cheng, J.-K. Chen, Femtosecond laser-induced periodic surface structures of copper: Experimental and modeling comparison, Applied Surface Science, 469 (2019) 904-910.
[23] S.N. Khonina, N.L. Kazanskiy, S.V. Karpeev, M.A. Butt, Bessel Beam: Significance and Applications-A Progressive Review, Micromachines (Basel), 11 (2020) 997.
[24] Y. Shen, S. Pidishety, I. Nape, A. Dudley, Self-healing of structured light: a review, Journal of Optics, 24 (2022) 103001.
[25] G. Kontenis, D. Gailevičius, N. Jiménez, K. Staliunas, Optical Drills by Dynamic High-Order Bessel Beam Mixing, Physical Review Applied, 17 (2022) 034059.
[26] G.K. Podagatlapalli, S. Hamad, M.A. Mohiddon, S.V. Rao, Fabrication of nanoparticles and nanostructures using ultrafast laser ablation of silver with Bessel beams, Laser Physics Letters, 12 (2015) 036003.
[27] R. Stoian, M.K. Bhuyan, A. Rudenko, J.-P. Colombier, G. Cheng, High-resolution material structuring using ultrafast laser non-diffractive beams, Advances in Physics: X, 4 (2019) 1659180.
[28] R. Stoian, M.K. Bhuyan, G. Zhang, G. Cheng, R. Meyer, F. Courvoisier, Ultrafast Bessel beams: advanced tools for laser materials processing, Advanced Optical Technologies, 7 (2018) 165-174.
[29] T. Chen, G. Zhang, H. Zhang, J. Lv, Y. Wang, P. Qu, R. Stoian, G. Cheng, Nano-spheroid formation on YAG surfaces induced by single ultrafast Bessel laser pulses, Applied Surface Science, 604 (2022) 154360.

[30] F. Courvoisier, J. Zhang, M.K. Bhuyan, M. Jacquot, J.M. Dudley, Applications of femtosecond Bessel beams to laser ablation, Applied Physics A, 112 (2012) 29-34.
[31] D. Banerjee, M. Akkanaboina, R. Kumar Kanaka, V. Rao Soma, Femtosecond Bessel beam induced ladder-like LIPSS on trimetallic surface for SERS-based sensing of Tetryl and PETN, Applied Surface Science, 616 (2023) 156561.
[32] J. Durnin, Exact solutions for nondiffracting beams. I. The scalar theory, J. Opt. Soc. Am. A, 4 (1987) 651-654.
[33] G.S. Sokolovskii, V.V. Dudelev, S.N. Losev, K.K. Soboleva, A.G. Deryagin, K.A. Fedorova, V.I. Kuchinskii, W. Sibbett, E.U. Rafailov, Bessel beams from semiconductor light sources, Progress in Quantum Electronics, 38 (2014) 157-188.
[34] B. Yalizay, T. Ersoy, B. Soylu, S. Akturk, Fabrication of nanometer-size structures in metal thin films using femtosecond laser Bessel beams, Applied Physics Letters, 100 (2012) 031104.
[35] J . Bonse, J. Krüger, S. Höhm, A. Rosenfeld, Femtosecond laser-induced periodic surface structures, Journal of Laser Applications, 24 (2012) 042006.
[36] A. Vorobyev, V. Makin, C. Guo, Periodic ordering of random surface nanostructures induced by femtosecond laser pulses on metals, J Appl Phys, 101 (2007) 034903.
[37] A. Abou Saleh, A. Rudenko, S. Reynaud, F. Pigeon, F. Garrelie, J.P. Colombier, Sub-100 nm 2D nanopatterning on a large scale by ultrafast laser energy regulation, Nanoscale, 12 (2020) 6609-6616.
[38] M. Navickas, R. Grigutis, V. Jukna, G. Tamosauskas, A. Dubietis, Low spatial frequency laser-induced periodic surface structures in fused silica inscribed by widely tunable femtosecond laser pulses, Sci Rep, 12 (2022) 20231.
[39] A. Rudenko, A. Abou-Saleh, F. Pigeon, C. Mauclair, F. Garrelie, R. Stoian, J.P. Colombier, High-frequency periodic patterns driven by non-radiative fields coupled with Marangoni convection instabilities on laser-excited metal surfaces, Acta Materialia, 194 (2020) 93-105.
[40] A. Rudenko, J.P. Colombier, S. Hohm, A. Rosenfeld, J. Kruger, J. Bonse, T.E. Itina, Spontaneous periodic ordering on the surface and in the bulk of dielectrics irradiated by ultrafast laser: a shared electromagnetic origin, Sci Rep, 7 (2017) 12306.
[41] A. Rudenko, C. Mauclair, F. Garrelie, R. Stoian, J.-P. Colombier, Amplification and regulation of periodic nanostructures in multipulse ultrashort laser-induced surface evolution by electromagnetic-hydrodynamic simulations, Physical Review B, 99 (2019).
[42] X. Sedao, A. Abou Saleh, A. Rudenko, T. Douillard, C. Esnouf, S. Reynaud, C. Maurice, F. Pigeon, F. Garrelie, J.-P. Colombier, Self-Arranged Periodic Nanovoids by Ultrafast Laser-Induced Near-Field Enhancement, ACS Photonics, 5 (2018) 1418-1426.
[43] D. Zhang, R. Liu, Z. Li, Irregular LIPSS produced on metals by single linearly polarized femtosecond laser, International Journal of Extreme Manufacturing, 4 (2021) 015102.

[44] P.N. Terekhin, O. Benhayoun, S.T. Weber, D.S. Ivanov, M.E. Garcia, B. Rethfeld, Influence of surface plasmon polaritons on laser energy absorption and structuring of surfaces, Applied Surface Science, 512 (2020) 144420.
[45] A.Y. Vorobyev, C. Guo, Direct femtosecond laser surface nano/microstructuring and its applications, Laser & Photonics Reviews, 7 (2012) 385-407.
[46] M. Huang, F. Zhao, Y. Cheng, N. Xu, Z. Xu, Origin of laser-induced near-subwavelength ripples: interference between surface plasmons and incident laser, ACS nano, 3 (2009) 4062-4070.
[47] S. Maragkaki, P.C. Lingos, G.D. Tsibidis, G. Deligeorgis, E. Stratakis, Impact of Pre-Patterned Structures on Features of Laser-Induced Periodic Surface Structures, Molecules, 26 (2021) 7330.
[48] E.L. Gurevich, Y. Levy, N.M. Bulgakova, Three-Step Description of Single-Pulse Formation of Laser-Induced Periodic Surface Structures on Metals, Nanomaterials (Basel), 10 (2020), 1836.
[49] E.L. Gurevich, Y. Levy, S.V. Gurevich, N.M. Bulgakova, Role of the temperature dynamics in formation of nanopatterns upon single femtosecond laser pulses on gold, Physical Review B, 95 (2017) 054305.
[50] K. Milligan, N.C. Shand, D. Graham, K. Faulds, Detection of Multiple Nitroaromatic Explosives via Formation of a Janowsky Complex and SERS, Anal Chem, 92 (2020) 3253-3261.
[51] W. Fan, S. Yang, Y. Zhang, B. Huang, Z. Gong, D. Wang, M. Fan, Multifunctional Flexible SERS Sensor on a Fixate Gel Pad: Capturing, Derivation, and Selective Picogram Indirect Detection of Explosive 2,2',4,4',6,6'-Hexanitrostilbene, ACS Sens, 5 (2020) 3599-3606.
[52] S. Kalasung, K. Aiempanakit, I. Chatnuntawech, N. Limsuwan, K. Lertborworn, V. Patthanasettakul, M. Horprathum, N. Nuntawong, P. Eiamchai, Trace-level detection and classifications of pentaerythritol tetranitrate geometrically optimized film-based Au/ZnO SERS sensors, Sensor Actuat B-Chem, 366 (2022) 131986.
[53] V.S. Vendamani, S. Rao, A.P. Pathak, V.R. Soma, Robust and cost-effective silver dendritic nanostructures for SERS-based trace detection of RDX and ammonium nitrate, RSC Adv, 10 (2020) 44747-44755.
[54] M. Akkanaboina, D. Banerjee, K.R. Kumar, R.S.P. Goud, V.R. Soma, S.V.S.N. Rao, Gold nanoparticles coated LIPSS on GaAs for trace detection of RDX and Tetryl, Surfaces and Interfaces, 36 (2023) 102563.
[55] D. Banerjee, M. Akkanaboina, S. Ghosh, V.R. Soma, Picosecond Bessel Beam Fabricated Pure, Gold-Coated Silver Nanostructures for Trace-Level Sensing of Multiple Explosives and Hazardous Molecules, Materials, 15 (2022) 4155.
[56] D. Banerjee, S.S.B. Moram, C. Byram, J. Rathod, T. Jena, G.K. Podagatlapalli, V.R. Soma, Plasmon-enhanced ultrafast and tunable thermo-optic nonlinear optical properties of femtosecond laser ablated TiO2 and Silver-doped TiO2 nanoparticles,

Applied Surface Science, 569 (2021) 151070.
[57] M.S.S. Bharati, V.R. Soma, Flexible SERS substrates for hazardous materials detection: recent advances, Opto-Electronic Advances, 4 (2021) 210048-210048.
[58] M. Haribabu, B. Dipanjan, M.S.S. Bharati, J. Chelsea, A. Chandrasekhar, P. Kanaka raju, S. Venugopal Rao, S. Hamad, G. Krishna Podagatlapalli, Exciton-mediated surface-enhanced Raman studies of Aluminum doped platinum nano colloids, Optical Materials, 133 (2022) 113013.
[59] A. Mangababu, R. Sai Prasad Goud, C. Byram, J. Rathod, D. Banerjee, V. Rao Soma, S.V.S. Nageswara Rao, Multi-functional gallium arsenide nanoparticles and nanostructures fabricated using picosecond laser ablation, Applied Surface Science, 589 (2022) 152802.
[60] G.K. Podagatlapalli, S. Hamad, S.V. Rao, Trace-Level Detection of Secondary Explosives Using Hybrid Silver-Gold Nanoparticles and Nanostructures Achieved with Femtosecond Laser Ablation, J Phys Chem C, 119 (2015) 16972-16983.
[61] H. Marrapu, R. Avasarala, V.R. Soma, S.K. Balivada, G.K. Podagatlapalli, Silver nanoribbons achieved by picosecond ablation using cylindrical focusing and SERS-based trace detection of TNT, RSC Adv, 10 (2020) 41217-41228.
[62] C. Zhang, K. Wang, D. Han, Q. Pang, Surface enhanced Raman scattering (SERS) spectra of trinitrotoluene in silver colloids prepared by microwave heating method, Spectrochim Acta A Mol Biomol Spectrosc, 122 (2014) 387-391.
[63] L. Panariello, K.C. To, Z. Khan, G.W. Wu, G. Gkogkos, S. Damilos, I.P. Parkin, A. Gavriilidis, Kinetics-based design of a flow platform for highly reproducible on demand synthesis of gold nanoparticles with controlled size between 50 and 150 nm and their application in SERS and PIERS sensing, Chemical Engineering Journal, 423 (2021) 129069.
[64] S. Almaviva, S. Botti, L. Cantarini, R. Fantoni, S. Lecci, A. Palucci, A. Puiu, A. Rufoloni, Ultrasensitive RDX detection with commercial SERS substrates, Journal of Raman Spectroscopy, 45 (2013) 41-46.
[65] N.A. Hatab, G. Eres, P.B. Hatzinger, B.H. Gu, Detection and analysis of cyclotrimethylenetrinitramine (RDX) in environmental samples by surface-enhanced Raman spectroscopy, Journal of Raman Spectroscopy, 41 (2010) 1131-1136.
[66] E.D. Emmons, J.A. Guicheteau, A.W. Fountain, 3rd, S.D. Christesen, Comparison of visible and near-infrared Raman cross-sections of explosives in solution and in the solid state, Appl Spectrosc, 66 (2012) 636-643.
[67] M. Ghosh, L.L. Wang, S.A. Asher, Deep-Ultraviolet Resonance Raman Excitation Profiles of NHNO, PETN, TNT, HMX, and RDX, Applied Spectroscopy, 66 (2012) 1013-1021.
[68] S.S. Dasary, A.K. Singh, D. Senapati, H. Yu, P.C. Ray, Gold nanoparticle based label-free SERS probe for ultrasensitive and selective detection of trinitrotoluene, Journal of the American Chemical Society, 131 (2009) 13806-13812.

[69] T. Liyanage, A. Rael, S. Shaffer, S. Zaidi, J.V. Goodpaster, R. Sardar, Fabrication of a self-assembled and flexible SERS nanosensor for explosive detection at parts-per-quadrillion levels from fingerprints, Analyst, 143 (2018) 2012-2022.

[70] F. Zapata, M. López-López, C. García-Ruiz, Detection and identification of explosives by surface enhanced Raman scattering, Applied Spectroscopy Reviews, 51 (2015) 227-262.

[71] A.A. Bushunov, M.K. Tarabrin, V.A. Lazarev, Review of Surface Modification Technologies for Mid-Infrared Antireflection Microstructures Fabrication, Laser & Photonics Reviews, 15 (2021) 2000202.

[72] A. Dostovalov, K. Bronnikov, V. Korolkov, S. Babin, E. Mitsai, et al., Hierarchical anti-reflective laser-induced periodic surface structures (LIPSSs) on amorphous Si films for sensing applications, Nanoscale, 12 (2020) 13431-13441.

[73] V. Parmar, Y.C. Shin, Wideband anti-reflective silicon surface structures fabricated by femtosecond laser texturing, Applied Surface Science, 459 (2018) 86-91.

[74] S. Sarbada, Z. Huang, Y.C. Shin, X. Ruan, Low-reflectance laser-induced surface nanostructures created with a picosecond laser, Applied Physics A, 122 (2016) 453.

[75] H.P. Wang, Y.C. Guan, H.Y. Zheng, M.H. Hong, Controllable fabrication of metallic micro/nano hybrid structuring surface for antireflection by picosecond laser direct writing, Applied Surface Science, 471 (2019) 347-354.

[76] R. Liu, D. Zhang, S. Ji, Y. Cai, C. Liang, Z. Li, Femtosecond Laser Generated Hierarchical Macropore/LIPSS Metasurfaces and Their Ultrabroadband Absorbance, Photothermal Properties, and Thermal-Induced Reflectance Oscillation, ACS Applied Electronic Materials, 4 (2022) 990-1001.

Intentional Blank Page

Chapter 5

5A. Plasmonic Alloy Nanocolloids Fabricated via Femtosecond Bessel Beam for Photonic and SERS-based Sensing Applications

5B. Preliminary Studies Involving Femtosecond Vortex beam-metal Interaction and Its Initial Application in SERS-based Sensing

5A

Plasmonic Alloy Nanocolloids Fabricated via Femtosecond Bessel Beam for Photonic and SERS-based Sensing Applications

Abstract

In this chapter, we present results from our studies wherein we have created a new kind of plasmonic multi-metal nanoalloy colloids using the femtosecond (fs) Bessel beam ablation approach, which has yet to be widely investigated and is very adaptable. The samples were subjected to a comprehensive analysis of their morphology and elemental composition using transmission electron microscopy (TEM), high-resolution TEM, and energy-dispersive X-ray spectroscopy (EDX). The nanoalloys were used in surface-enhanced Raman spectroscopy (SERS)-based sensing experiments, effectively detecting minute amounts of RDX (5 µM) and PA (500 nM), two volatile/hazardous chemicals. The calculated enhancement factor (EF) values for the analytes of RDX and PA were 1.7×10^{4} and 2.4×10^{5}, respectively. The nanoalloy particles (NAPs) were examined using femtosecond (fs) pulses for their nonlinear absorption, which depicted a three-photon absorption (3PA) phenomenon in the standard open aperture Z-scan measurements. The coefficient value for the third-order nonlinearity, three-photon absorption (γ), was determined to be 1.8×10^{-22} cm^3/W^2, whereas the coefficient value for the nonlinear refraction (NLR) (n_2) was 1.1×10^{-15} cm^2/W. Additionally, the cross-section for three-photon absorption (σ_3) was calculated to be 1.9×10^{-75} cm^6/s^2. Furthermore, we have demonstrated the optical limiting prowess of these nanoalloys. In addition, we conducted fs transient absorption spectroscopy (fs TAS) to observe the time-dependent behavior of the photoexcited electrons in this nanoalloy system. The TAS data was used to extract and fit the photoexcited processes of electron-electron/thermalization ($\tau_{e\text{-}e}$ = 0.7±0.1 ps), electron-phonon ($\tau_{e\text{-}ph}$ = 1.2±0.1 ps), and phonon-phonon scattering ($\tau_{ph\text{-}ph}$ = 47.5±8 ps). The TAS measurements provided a systematic understanding of many other characteristics of the nanoalloy system, including interband-excitation-induced plasmon (EIP), delayed ESA band lifetime, and bleach splitting. The findings of this work support the benefits of using the fs BB-induced ablation approach to create a new kind of plasmonic nanoalloys with multiple metals. This work also demonstrates the possible uses of these nanoalloys in many sectors, such as sensors, photonics, and optical limiting. Below, we have included a visual representation of the chapter as a graphical abstract.

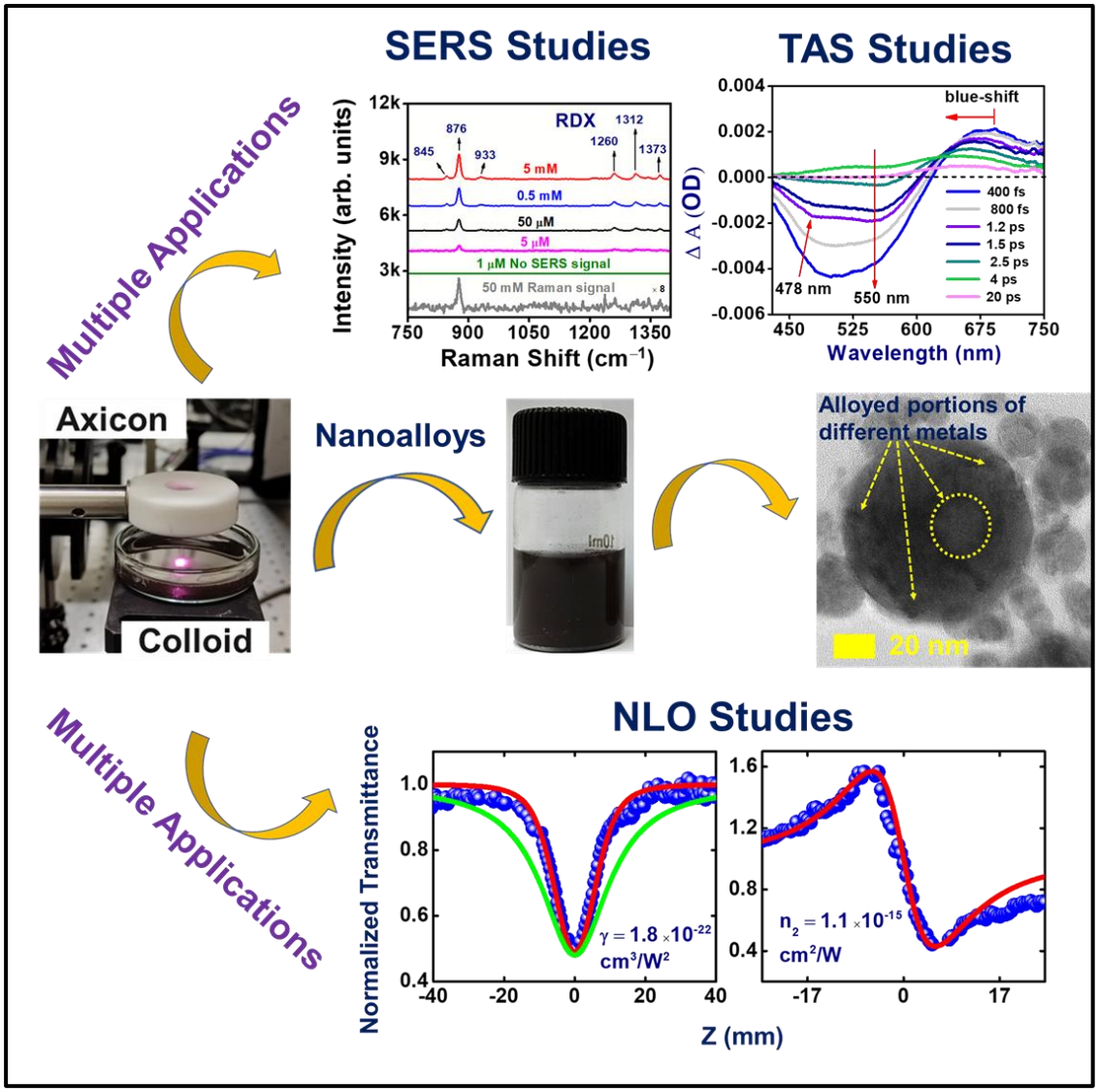

The work presented in this chapter has been published in,

1. **D. Banerjee**, A. Mangababu, Ravi Kumar Kanaka, Venugopal Rao Soma, Plasmonic Alloy Nanocolloids Fabricated via Femtosecond Bessel Beam for Photonic and SERS-based Sensing Applications, Optical Materials, 154 (2024) 115668. https://doi.org/10.1016/j.optmat.2024.115668.

5A.1. Introduction

Plasmonic metal nanoentities interact strongly with incoming electromagnetic radiation by activating localized surface plasmon resonance (LSPR) [1, 2]. Plasmon excitations have been utilized in various technological applications and research studies in the past few decades, particularly in biotechnology [3], sensing, thermo-plasmonic effects [4], light-enhanced catalysis [5], and fundamental studies on the enhancement of local electric fields in optical processes. The need for multi-metallic nanoentities, also known as nanoalloys, has increased due to the necessity of producing materials with well-defined and controlled characteristics and structures at the nanoscale level. Additionally, intermetallic materials provide a high degree of flexibility. Intermetallic nanoalloys may be synthesized by mixing different components to achieve diverse features in metallic nano-systems. Alloying often leads to an enhancement of certain characteristics due to the synergistic effects. The wide variety of compositions, topologies, and characteristics of metallic nanoalloys has resulted in a broad spectrum of uses in the fields of engineering [7], electronics [8], and catalysis [9]. Despite the restricted availability of typical plasmonic nanoparticles (NPs), several methods exist to merge them with other elements from the periodic table to form nanoalloys. This is especially useful for elements renowned for their optical, magnetic, or catalytic properties [1, 8, 10, 11]. Therefore, it is not unexpected that nanoalloys, which are now a prominent area of research, are being examined for their ability to provide new opportunities in nano-alloy-plasmonics. Several studies discuss the diverse applications of nanoalloys in photonics, hydrogen evolution [12], photocatalysis [9, 13], sensing, and magneto-optics. These applications include the combination of plasmons with other physical and chemical processes, as supported by evidence [1, 7, 11, 14]. Fagan et al. [15] conducted comprehensive research that found that size-tunable Au−Pt hybrid nanoparticles may display emergent magnetic, optoelectronic, and photonic synergistic capabilities that vary from their components. These hybrid plasmonic nanoparticles connect many unique plasmonic materials via solid-state interfaces. Ferrando et al. [6] have expansively surveyed several nanoalloys, demonstrating their versatile applications across various sectors. Widespread research studies have shown that the ability to customize alloy nanoparticles' chemical and physical properties by modifying their size, composition, and atomic arrangement is a key factor in their appeal for many applications. The work presented in this chapter also asserts that nanoalloys have the potential for increased chemical reactivity, distinctive stability, and

notably robust catalytic activity. Nanoalloys are of significant interest due to their ability to display forms and features that vary from those of the individual elemental nano-components. Due to quantum confinement phenomena, these alloys may also display distinct features that differentiate them from similar bulk alloys. The group led by Prof. Amendola, a pioneer in nanophotonics research, extensively investigated the synthesis, modeling, features, and many applications of newly produced plasmonic alloy NPs [7, 16, 17]. Alloying is a method used to incorporate the diverse properties of several components into nanostructures, resulting in a significant plasmonic response. This also provides an opportunity to alter the electronic structure of the metal to improve and maximize the efficiency of a particular plasmonic phenomenon. The work also indicates that, under some circumstances, the alloying process may be associated with innovative yet unknown physical or chemical methods. Furthermore, it may modify specific characteristics of plasmonic material, such as the final device's long-term viability, expense, and chemical vulnerability.

Cortie et al. [1] and Hartland et al. [11] have comprehensively discussed the many applications of hybrid nanoentities. Ahlawat and co-workers [18] conducted a fundamental analysis of plasmonic catalysis, focusing on recent advancements in hot hole extraction and catalysis via investigating several nano-heterointerfaces. In their detailed study, Yao et al. [8] examined high-entropy nanoparticles containing more than four equally mixed elements. They discovered several applications for these nanoparticles in energy, sustainability, and catalysis. Engelbrekt et al. [2] have reported the synthesis of Au-Pt core-shell nanocrystals, which can potentially become highly efficient plasmon-driven photocatalysts. Haldar et al. [19] have created copper-silver-gold trimetallic nanobowls for efficient catalysis. Bhunia et al. [20] successfully produced Pt-Au-Ni alloy nanoparticles as a highly efficient electrocatalyst in methanol electrooxidation. Similarly, Kushwah and colleagues have created nanoparticles made of gold, silver, and copper (Au/Ag/Cu NPs) to improve their catalytic performance. While other works used a chemical synthesis procedure, the laser ablation approach is an environmentally friendly synthesis technique in this context. The reputation of laser ablation in liquid (LAL) [7, 16, 17] has significantly enhanced in recent years due to its ability to produce nanoparticles of various materials such as metals, semiconductors, ceramics, glasses, and alloys. This method has facilitated the creation of several novel functional nanomaterials. One of the main benefits of LAL is its ability to synthesize colloidal nanoparticles and solid

nanostructures on the target surface simultaneously. The concurrent production of nanoentities reveals new possibilities for various nanophotonic and optoelectronic research fields. The pulsed LAL technology is recognized as a green chemistry method for producing ligand-free nanoparticles of different sizes and shapes. Moreover, the yields in LAL have now reached a few grams per hour [14,16], making it appealing for practical applications. Therefore, this approach of rapidly interacting lasers with matter has been widely used over the last twenty years to create various nanostructures. The use of a Bessel beam [24-28] in combination with a self-healing optical profile [22], improved depth of focus (DOF) [23], and invariance of intensity profile along propagation length [23] offer a dominant solution for the efficient creation of plasmonic nanocolloids. Interestingly, minimal investigations [29] conducted on LAL studies examined the interactions between fs BB and metals.

We attempted to use axicon-generated BB since we expect an advantage in focusing at the time of ablation because of the above-mentioned characteristics. Hence, we used an axicon-generated femtosecond broadband laser to perform LAL and produce multi-metal nanoalloy particles. This approach takes advantage of the non-diffracting nature of light and the diverse capabilities of alloyed NPs. This work effectively synthesized colloidal dispersions of multi-metal (Ag-Au-Cu) NAPs. The TEM measurements have been used for comprehensive topographical and elemental characterizations. The synthesized nanoalloys were used in surface-enhanced Raman spectroscopy (SERS) sensing experiments, effectively detecting minute amounts of RDX [1,3,5-Trinitroperhydro-1,3,5-triazine, Formula: $C_3H_6N_6O_6$] and PA (2,4,6-trinitrophenol, Formula: $C_6H_3N_3O_7$), which are explosive compounds. In addition, the NAPs were investigated using fs, a nonlinear optical domain, which resulted in the observation of three-photon absorption. In addition, we conducted fs transient absorption spectroscopy (TAS) to provide a comprehensive understanding of the BB-ablated new nanoalloys. This technique allowed us to observe the time-resolved behavior of the photoexcited electrons in the nanoalloy system. This work has shown a comprehensive grasp of the benefits of using the BB-induced LAL method in creating new, multimetallic plasmonic nanoalloys. The chapter delves into the innovative nanomaterials' nonlinear optical (NLO) and time-resolved dynamic characteristics and their use in SERS-based sensing.

5A.2. Experimental Details

The experiment included the implementation of femtosecond (fs) LAL using a Bessel beam profile in deionized water (DW). The precise characteristics of the femtosecond (fs) Bessel beam were determined by a wavelength of 800 nm, a pulse duration of about 50 fs, and a repetition rate of 1 kHz. The ultimate beam was produced utilizing an axicon (AR coated, 100, M/s Thorlabs, UK, Model #AX1210-B,) with a chirped-pulse amplified Ti: Sapphire laser system (LIBRA, M/s Coherent, USA) as the origin. The multi-metal (MM) substrates were fabricated by melting and blending silver (Ag), gold (Au), and copper (Cu) to generate colloidal multi-metal nanoalloy particles (MM NAPs). The substrates were carefully prepared to achieve a purity level of over 99.9%. The compositional proportions of the manufactured MM target strip were determined using EDX characterization to be 39% Ag, 18% Au, and 28% Cu by weight. Figure 5A.1 displays the EDX spectra and FESEM picture of the surface of the original MM substrate. Following a thorough cleansing of the target in an ultrasonic bath, it underwent the ablation procedure, which included its encounter with the Bessel beam (BB). The ablation process consisted of directing the laser beam (BB) onto the MM substrate that appeared in DW water within a petri dish. This was followed by a thorough laser raster scan ablation that lasted for ~60 minutes. The raster scan ablation procedure was conducted using two X-Y stages controlled by a LabVIEW interfaced motion controller (ESP 300, Newport, USA). To increase the production of laser-ablated nanoparticles, it is recommended to use a laser illumination rate of about 20000 pulses per millimeter, a scan speed of 0.05 mm/sec, and an inter-line spacing of 0.1 mm when performing the raster scan. As a result, a mixture of MM NAPs totaling 10 ml was successfully generated using the Bessel beam interaction LAL technique. The mixture was kept in a 15 ml borosilicate glass container, reaching a central peak intensity of ~23 J/cm^2. The examination of nanoparticles' shape, topographical characteristics, and elemental composition was performed using transmission electron microscopy (TEM) measurements. The measurements were performed using a JEM-F200 multi-purpose electron microscope manufactured by JEOL, operating at an accelerating voltage of 200 kV. The imaging samples were made by depositing a tiny quantity (~10 µL) of the colloidal solution of the NAPs onto a copper grid covered with carbon and leaving it to dry for ~12 hours. The HRTEM study was conducted using the Gatan Microscopy Suite software. The UV-visible-IR absorption spectra of the nano colloids were obtained using a UV-Visible-IR spectrometer (Perkin

Elmer, Lambda 750, Massachusetts, US) following their fabrication. The spectra were collected within the wavelength range of 250-800 nm. In addition, the researchers studied the nanostructures formed on the surface of the MM alloy substrate to gain insight into its surface topography. Field emission scanning electron microscopy (FESEM) and energy-dispersive X-ray spectroscopy (EDX) were conducted using the ZEISS ULTRA 55 instrument. The Cu K_α line was used to analyze the X-ray diffraction (XRD) characterization using a diffractometer (Discover D8 from Bruker, Germany). SERS measurements were performed using a portable Raman system (i-Raman plus, B&W Tek, USA) with particular settings, including an excitation wavelength of 785 nm, a spot size of about 90 μm, an input laser power of ~102 mW, and predetermined values for the accumulation number and spectral averaging periods. The NLO measurements were conducted using a plano-convex lens with a focal length of 15 cm. The experiments utilized the same fs amplifier (1 kHz, 800 nm, ~50 fs). These measurements were performed using Z-scan experimental research, resulting in a peak intensity of ~100 GW/cm^2 at the focal plane. We used a silicon photodiode (PD-THORLABS) to measure the transmittance of the beam. The beam output was directed toward a lock-in amplifier (Signal Recovery, Model #7265). The motorized stage was operated using a motion controller (Newport, ESP 300, USA), and both the motion controller and lock-in amplifier were connected to a bespoke LabVIEW application. The fs TAS measurements were performed using the HELIOS Ultrafast System, a typical pump-probe spectrometer. A beam splitter separated the source pulses, with one portion directed towards a sapphire window to establish a white light continuum for the probing beam. The 400 nm pump beam was produced using a BBO crystal to double the frequency of the other pulse. A LabVIEW-based system was used to build an optical delay (pump-probe delay) inside the HELIOS system, which has an adjustable range of up to 5 ns. HELIOS used an optical chopper to reduce the pump frequency by half, resulting in a frequency of 500 Hz. The pump and probe beams are polarized at an angle of roughly 54.70 degrees, creating a mystical effect. To conduct TAS measurements, the colloidal solution of the MM NAPs was carefully positioned within a quartz cuvette with a thickness of 1 mm. The measurements were made under controlled experimental settings. The experiment included capturing transient signals using high-speed multichannel fiber-coupled detectors, which had a scan rate of kilohertz. The gathered data was then processed and analyzed using the *Surface Xplorer* program.

5A.3. Results & Discussion

5A.3.1. Synthesis of multi-metal nanoalloys by femtosecond Bessel beam ablation

A comprehensive cleaning procedure was performed before treating the MM (Ag-Au-Cu) substrate. The substrate was then submerged in acetone, followed by ethanol and deionized water, in an ultrasonic cleaner for roughly 15 minutes to remove any surface contaminants. Afterward, the clean target, now free from impurities, was immersed in deionized water and irradiated by ~50 fs broadband pulses (centered at 800 nm), which were concentrated using an axicon. The powerful ultrashort pulses (~1.7 mJ energy) were focused on the MM target submerged in deionized water. The laser beam focus was optimized by monitoring the creation of the brightest plasma plume spot and the continuous powerful sound at the point of contact between the focused beam and the target surface. Using a highly concentrated ultrafast laser beam with precise energy, the MM target was subjected to a raster scanning technique, as described in the experimental details section. After subjecting the MM target to ultrafast BB-associated laser ablation in DW, the formation and dispersion of nanoparticles in the surrounding liquid were observed. The yield of the BB-interacted LAL process demonstrated a substantial increase compared to the standard Gaussian beam ablation method that was investigated in our previous findings. The greater yield of nanoparticle creation may be ascribed to the unique beam profile, which consists of numerous concentric rings around a central peak. BB offers many additional benefits for ablation, such as increased depth of focus and a self-healing beam profile. During laser ablation and laser-induced breakdown spectroscopy, the first stage consists of the surface electrons of the material absorbing laser energy by inverse-Bremsstrahlung [30]. These electrons acquire tremendous kinetic energy, resulting in a much higher temperature than the surrounding lattice. As described by a two-temperature model [7, 16, 31], the temperature difference between the hot electrons and the lattice finally forms a plasma plume. The plasma generated at the interface of the target and liquid under high-temperature and high-pressure conditions consists of a variety of ablated species, including atoms, molecules, ions, and clusters. A fraction of the thermal energy is assimilated by the adjacent liquid layer of the metallic melt, increasing temperature [32]. The liquid undergoes expansion by evaporation due to its inability to retain its phase at this particular temperature. During this expansion process, optical cavitation formation occurs at the front of the plasma and travels towards the liquid. This is caused by the quick change in the pressure gradient of the shock wave and the transfer

of energy from the plasma to the liquid. It has been shown that the temperature of the nanoentities inside the cavitation bubble [33] is higher than that of the surrounding liquid environment. The nucleation and development phases of NPs inside the cavitation bubble are believed to be initiated by the thermodynamic interaction with the liquid medium [32-34]. The cavitation bubble undergoes contraction due to variations in pressure and temperature compared to the surrounding liquid medium, leading to its eventual collapse. The temperature of the nanoentities inside the cavitation bubble is higher than that of the surrounding liquid environment. The nucleation and development phases of NPs inside the cavitation bubble are thought to start due to the thermodynamic interaction with the liquid medium [30, 35, 36]. The cavitation bubble undergoes contraction due to differences in pressure and temperature compared to the surrounding liquid, leading to its eventual collapse. The NPs are formed as the plasma cools down after the collapse of the cavitation bubble. These NPs then spread into the surrounding liquid to generate a colloidal solution. The bubble releases substantial energy into the surrounding liquid, dramatically decreasing pressure and temperature. This leads to the plasma losing its energy and results in the expulsion of ablated components into the liquid, ultimately forming the desired nanoparticles [14,30]. Subsequently, the colloidal dispersion of the MM NAPs was collected for crucial characterizations. The characteristics of the colloids of MM NAPs in deionized water were analyzed using the TEM. This facilitated the computation of the generated NPs' mean size distribution and morphology.

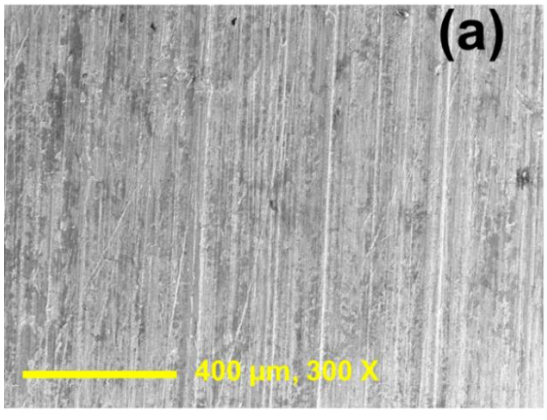

(b)

Element	Weight %	Error %
O	15.5	12.0
Cu	27.8	6.3
Ag	39.4	5.2
Au	17.3	8.2

Figure 5A. 1 (a) FESEM image of the surface of the pristine, unablated MM (Ag-Au-Cu) substrate (b) EDX spectra of the surface of the pristine, unablated MM (Ag-Au-Cu) substrate.

Figure 5A.2 displays transmission electron microscopy (TEM) pictures of the MM NAPs, which show spherical shapes. Figures 5A.2 [(a), (b), and (c)] depict the spherical shape of the alloy nanoparticles at several levels of magnification. The ImageJ application was used

to build a histogram that analyzes the size distribution of the NAPs based on the TEM images shown. The NP's histogram [shown as inset in Figure 5A.2(c)] was analyzed using a Gaussian fit, which determined that the average size of the MM NAPs was 27±3 nm. A thorough examination of the size distribution plot revealed several particles far larger than the average size. The precise beam intensity profile of the BB, characterized by a central peak and concentric rings, significantly impacts the ablation process, resulting in the observed wide size variation in the NPs. This factor is thought to impact the synthesized MM NAPs' optical absorption considerably. Figure 5A.2(d) displays the absorption spectra in the UV-visible-IR region between 300 and 900 nm. The presence of mixed surface plasmon resonance (SPR) effect is thought to be responsible for observing a single, wide absorption peak at 550 nm, followed by a prolonged zone of lower intensity up to 700 nm. These findings concur with the results from previous works [19, 21] on chemically produced Ag-Au-Cu alloy nanoparticles. The wide absorption peak may be ascribed to the greater size dispersion of the MM NAPs, which is seen from the inset plot of Figure 5A.2(c). To get a more detailed understanding of the topography, we obtained higher magnification transmission electron microscopy (TEM) images, which are shown in Figures 5A.2(e) and 5A.2(f). Figure 5A.2(f) clearly shows the topographical unevenness of the surface of the NP, indicating the creation of an alloy owing to the nucleation of various metals (Ag-Au-Cu) during BB ablation. TEM-EDX mapping was conducted to verify the successful alloying of the three metals in the produced NPs. Figures 5A.2[(g)-(j)] show the EDX mapping data of the MM NAPs, illustrating the existence of Cu [Figure 5A.2(h)], Ag [Figure 5A.2(i)], and Au [Figure 5A.2(j)] in the spherical-shaped particles. Figure 5A.2(g) shows the superimposed picture that represents the presence of all the metals. Figure 5A.2(k) displays the elemental composition obtained from the TEM-EDX data, with mass percentages of 13.4% for copper (Cu), 78.6% for silver (Ag), and 7.1% for gold (Au). The EDX spectrum is shown in Figure 5A.3. During the process of ablation, important factors such as the ablation threshold and heat of evaporation [32, 33, 38] have a considerable influence on both the alloying process and the stoichiometry of the NAPs. Engaging in a discussion about these factors leads to a deep comprehension of the specific elemental distribution of various plasmonic metals, as detected by EDX tests. Au, Ag, and Cu, three plasmonic coinage metals, exhibit significant variations in their ablation thresholds when subjected to fs pulses due to their distinct thermal conductivity, heat capacity, and absorption coefficient. Earlier studies [39-41] have demonstrated that Au has a higher ablation threshold than Cu and Ag.

Therefore, we have noticed that the presence of Au was ~7% [as shown in Figure 5A.2(k)], which is lower than the magnitude of Cu, which was ~13%. The Ag element has the highest mass among all three elements, consistent with its lowest ablation threshold value. Jakobi et al. [38] have also observed similar results in their investigation, namely that elements with lower ablation thresholds get ablated more. According to their findings, if there is a large difference in the heat of evaporation between the components, the stoichiometry of the nano entity changes to increase the presence of material with lower heat of evaporation in the resulting nanoalloy.

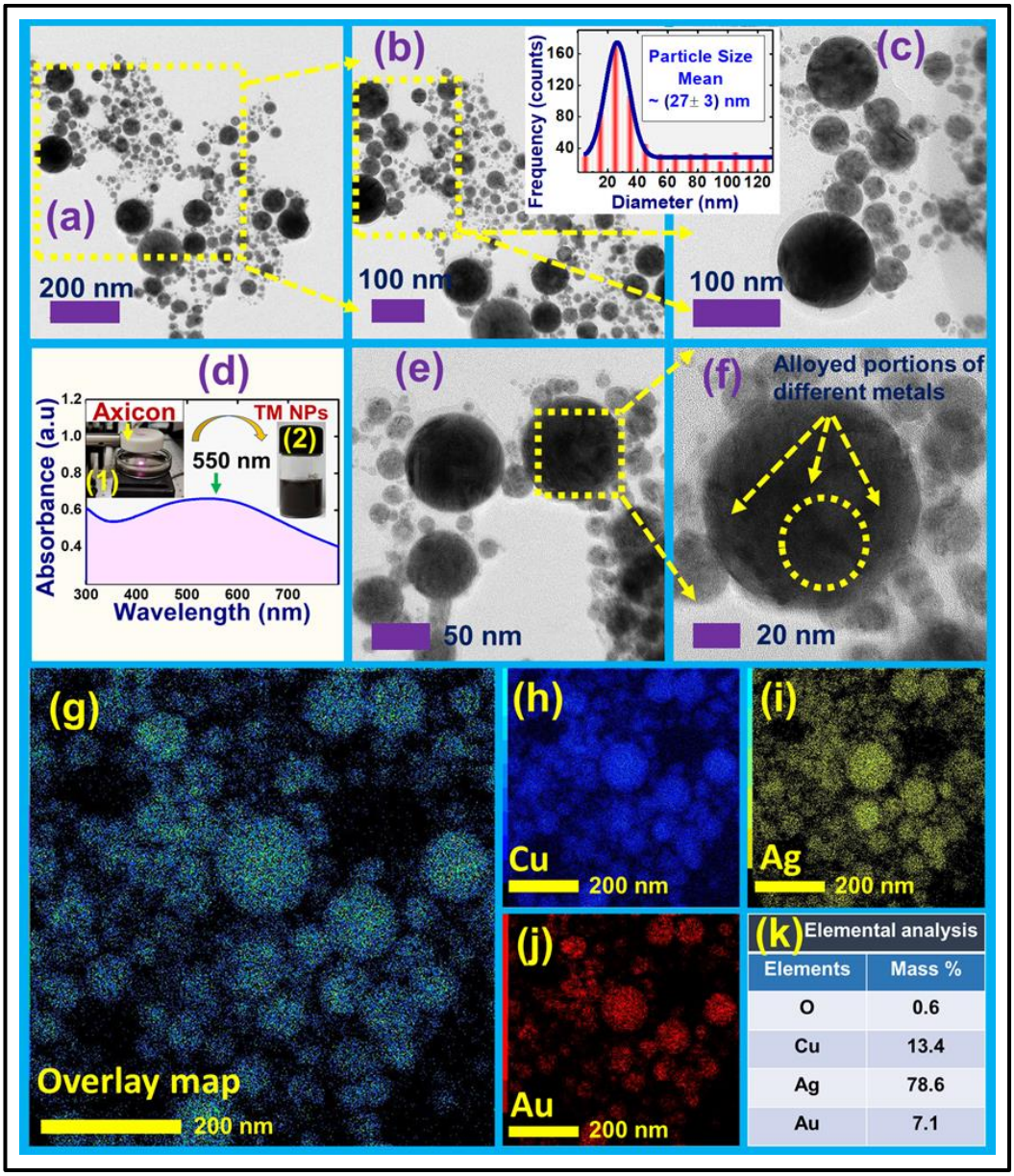

Figure 5A. 2 (a)-(c) TEM images of the MM NAPs from lower to higher magnification, (d) UV-Visible-IR absorption data of the MM NAPs. Inset (1) in Figure 5A.2(d) depicts the axicon lens and (2) shows stored colloidal NPs. (e)-(f) Higher magnification TEM images for the MM NAPs. (g) Overlay image of the EDX mapping. (h)-(j) TEM EDX mapping data of the same. (k) Elemental composition of the MM alloy NPs.

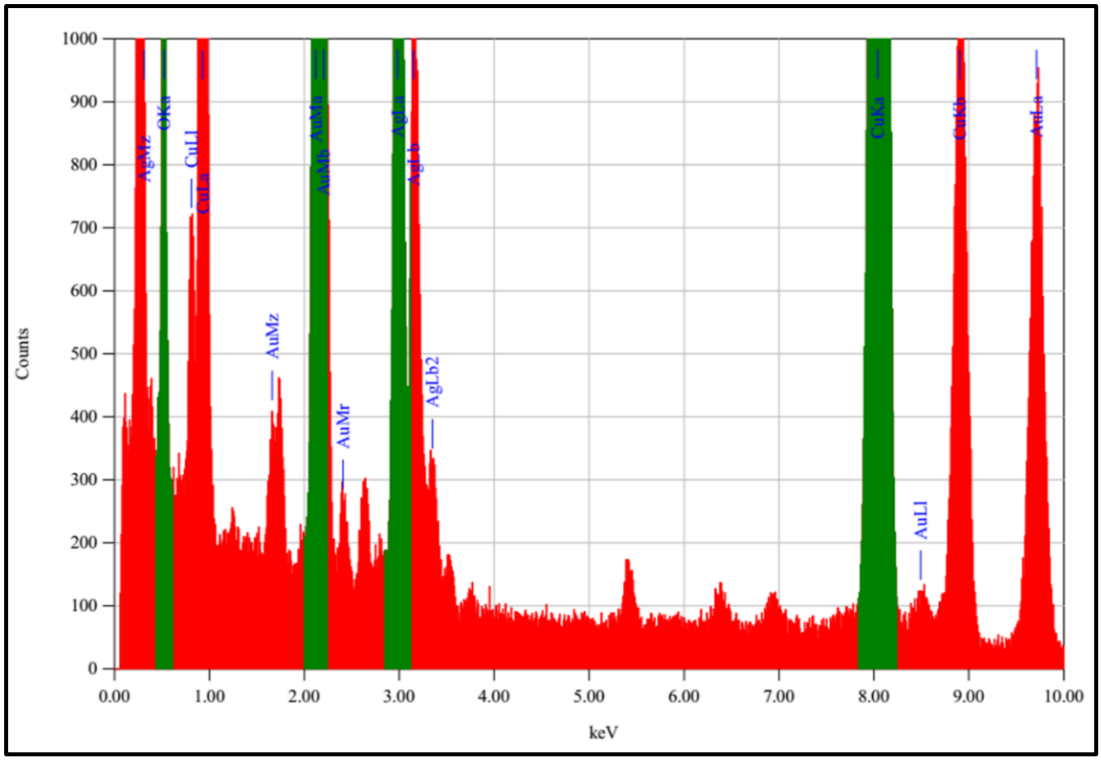

Figure 5A. 3 (a) EDX spectra of the multimetal (MM) nanoalloy particles.

Despite the high concentration of Ag within the alloy structure, the peak corresponding to surface plasmon resonance (SPR) fell between the SPR peaks of Cu and Au metals. Multiple variables contribute to this result, as outlined below. The surface plasmon resonance (SPR) peak of nanoparticles (in colloidal form) is determined by the nanoparticles' size, content, and shape. This study presents comprehensive TEM and EDX mapping investigations that provide detailed surface topography and composition information. Figures 5A.2(e) and 5A.2(f) illustrate the alloy nanoparticles' irregular and coarse surface morphology. Distinct alloyed regions are seen in many NP surface areas [Figure 5A.2 (f)]. The surface displays the existence of several nanocomponents that are implanted at various places as a result of alloying caused by the LAL. The surface morphology of the MM NPs has led to the formation of a non-spherical shape, which may cause a shift in the SPR peak. Additionally, a more detailed examination of the overlay TEM EDX picture in Figure 5A.2(g) reveals many important underlying characteristics. The distribution of Cu and Au nanocomponents is seen mostly on the outer surface area of the nanoparticles, whereas Ag is primarily situated inside the interior region of the nanoentities. The statistics cited above provide compelling evidence that the surface of the MM alloy nanoparticles contains Cu and Au nanocomponents in different locations, resulting in a non-spherical surface shape.

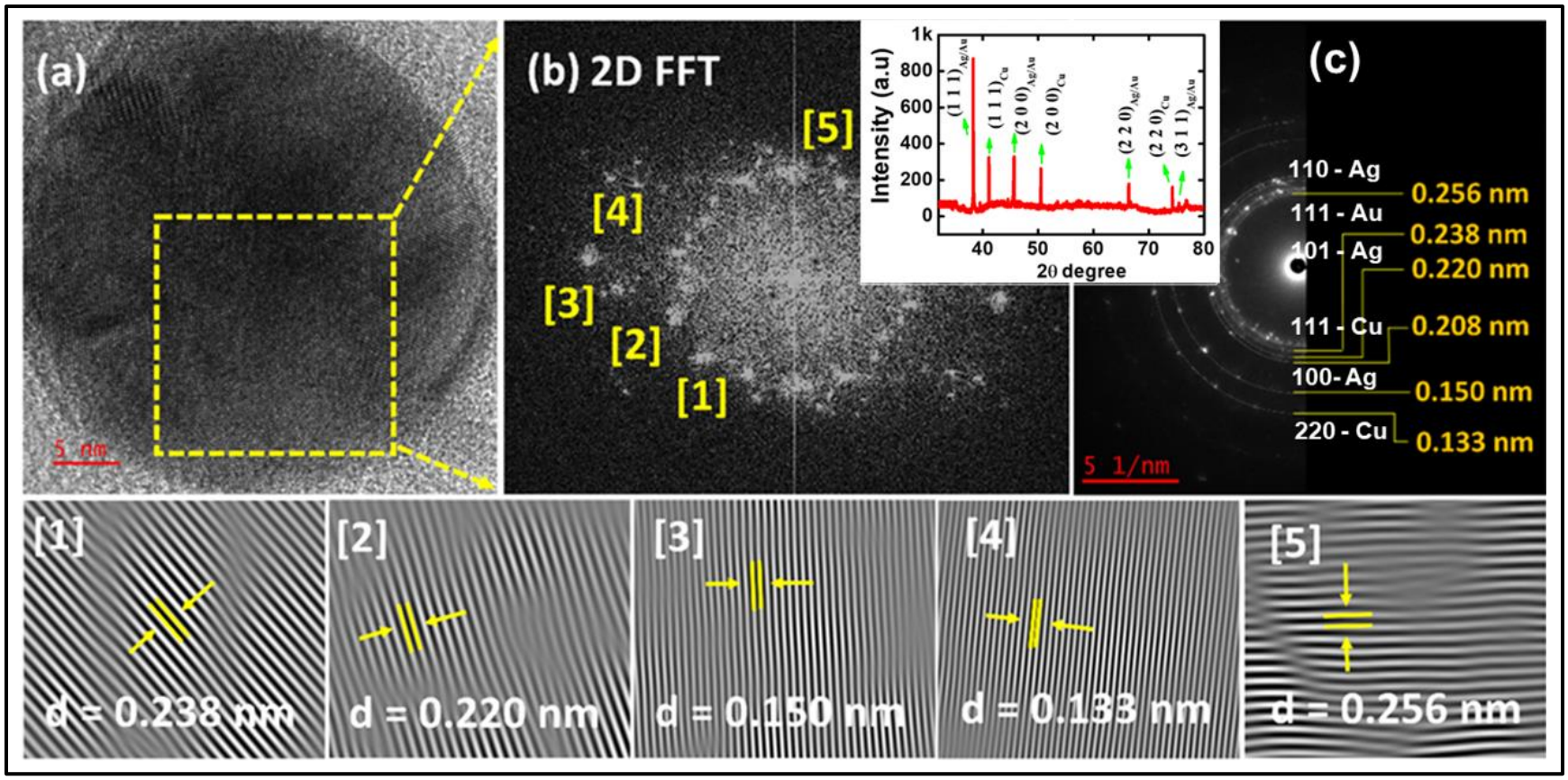

Figure 5A. 4 (a) HRTEM image of MM NAPs, (b) 2DFFT performed at an area indicated with a rectangular box. The Inset of Figure 5A.4(b) presents the XRD spectrum. In the bottom panel, images [1]-[5] represent IFFT at locations [1]-[5], as shown in (b)] and (c) SAED patterns recorded from the MM NAPs.

On the other hand, Ag is mostly concentrated in the interior area (core) of the nanoparticle. As a result of the influence of form, surface geometry, and composition, the SPR peak shifted towards longer wavelengths, namely at 550 nm. This shift occurred between the SPR peaks of copper (around 600 nm) and gold (around 520 nm). Further investigation is required to explore this topic, which calls for conducting investigations using X-ray photoelectron spectroscopy (XPS) in conjunction with theoretical calculations. In addition, the alloy nanoparticles undergo HRTEM and SAED studies [refer to Figure 5A.4] to validate their crystallographic properties. The HRTEM picture, shown in Figure 5A.4(a), revealed the existence of crystal planes oriented in various directions. Therefore, to fully understand the specifics, a 2D fast Fourier transform (2D FFT) is conducted on the particle inside the yellow rectangle box shown in Figure 5A.4(a). The resulting 2D FFT pattern is seen in Figure 5A.4(b). In Figure 5A.4(b), the bright dots at places labeled with numbers [1] to [5] illustrate the existence of distinct ‘d’ spacings. The inverse 2D Fast Fourier Transform (IFFT) was computed and shown in the lower section of Figure 5A.4 at positions [1] to [5]. The observed ‘d’ spacings were 0.238 nm, 0.220 nm, 0.15 nm, 0.133 nm, and 0.256 nm. In addition, the examination of selected area electron diffraction (SAED) shown in Figure 5A.4(c) provides further evidence of the existence of planes with specific distances of 0.256 nm, 0.238 nm, 0.220 nm, 0.208 nm, 0.150 nm, and 0.133 nm, respectively. The lattice spacings mentioned above correspond to specific crystal planes in different materials. The spacings of 0.256 nm, 0.220 nm, and 0.150 nm correspond to the Ag (110), (101), and (100) planes, respectively. These correspondences are based on the JCPDS codes 01-071-5025 and 00-003-0921. The spacing of 0.238 nm corresponds to the Au (111) plane, based on the JCPDS code 00-004-0784. Lastly, the spacings 0.208 nm and 0.133 nm correspond to the Cu (111) and (220) planes, respectively, based on the analysis of JCPDS code 01-071-3761. These correspondences are supported by the data presented in references 42 and 43. Therefore, three distinct crystal planes associated with the elements Ag, Au, and Cu confirm the creation of alloy particles during the laser ablation procedure.

To provide further verification, X-ray diffraction (XRD) data has been shown in the inset of Figure 5A.4. The close resemblance in lattice constants between Ag and Au (Au: 0.40786 nm, Ag: 0.40862 nm) leads to the overlapping of peaks in the XRD data of Ag and Au nanoparticles, making it challenging to differentiate between them. Hence, the peaks observed at 38.40, 44.60, 64.80, and 77.70 indicate the presence of silver (Ag) or gold (Au) based on the JCPDS reference

codes 00-003-0921 and 00-004-0784. The crystal planes (1 1 1), (2 0 0), (2 2 0), and (3 1 1) are associated with the peaks seen in both Ag and Au. The additional peaks located at 41.10, 50.50, and 74.30 corresponded to the crystal planes (1 1 1), (2 0 0), and (2 2 0) of Cu [JCPDS: 01-071-3761]. Therefore, the SAED and HRTEM 2D IFFT 'd' spacings data are consistent with the XRD information. We also examined if there was an undesired occurrence of distinct Ag/Au/Ag-Cu/Ag-Au nanoparticles. Nevertheless, in this context, there are certain elements that we may methodically analyze. The TEM EDX mapping data in Figure 5A.2(g) definitively verifies the existence of all three metal constituents inside every alloy nanoparticle, namely Ag, Au, and Cu. We gathered TEM/EDX data from several areas, and the same findings were expressed. Furthermore, the XRD data corroborates the presence of Ag-Au-Cu alloy nanoparticles. These meticulous observations rule out the possibility of creating distinct, undesired nanoparticles. Although X-ray examinations and alloying may not always be completely consistent, we can confidently state that even if there is a small amount of these individual components, they will not significantly affect the optical qualities.

Further, we compared two laser-assisted lithography techniques: broadband (BB) lasers and standard Gaussian beam lasers. This study aimed to provide a novel LAL method that utilizes laser parameters of 800 nm, 50 fs, 1 kHz, and the same incident fluence. When the BB method is used instead of the Gaussian beam LAL technique, we have seen that the concentration of MM NPs generated by BB is at least three times higher. To determine the concentration of the produced nanocolloids, we measured the weight of the target strip before and during the ablation technique. Furthermore, the increased depth of focus provided by the BB is a notable benefit during LAL, in contrast to the usual Gaussian beam. We are doing more research to manufacture pure and alloy nanoparticles utilizing both BB and Gaussian beams. These investigations are part of our future goal. A thorough investigation is required to confirm and solidify our initial notion that the BB-involved LAL process may result in enhanced synthesis of nanoparticles. Prior research [44-46] has shown that the concentration of NPs generated by LAL is greater when ablated in air than when ablated in water. This difference in ablation rate may be attributed to the shielding effect of the NPs in the liquid environment. BB LAL might be considered a more efficient choice in this context.

5A.3.2. Detection of explosives using the SERS technique

Trace-level detection of explosive chemicals is becoming more critical in the field of homeland security to prevent the proliferation of terrorism and mitigate its global threats. Consequently, there has been a significant increase in the need for rapid detection of potentially explosive compounds during the last several decades. Aside from the identification of improvised explosive devices (IEDs) in significant quantities, the police force and forensic scientists' inquiries need the development of effective methodologies for pinpointing and classifying the sources of minute amounts of explosive substances. In recent years, techniques such as electrochemical detection, mass spectrometry, liquid chromatography, ion mobility spectrometry, infrared spectroscopy, and terahertz spectroscopy have been developed to detect small amounts of high explosives. However, to get accurate results, each method has distinct limitations, including the need for complex sample preparations, highly regulated conditions, and extensive data analysis durations. These paths result in problems detecting on-field tests and implementing them in actual situations. The main emphasis is developing the SERS techniques [39, 42, 48, 49] that can accurately identify various chemical species by analyzing their vibrational "fingerprints." In addition, SERS allows for rapid measurements with exceptional selectivity, the capacity to analyze many samples simultaneously, and very high sensitivity. Therefore, we used the BB-fabricated plasmonic MM nanoalloys to conduct SERS-based sensing experiments. The nanoparticles were deposited onto a clean silver surface without any surface modification, and the analyte solutions (typically about 20 µL in volume) were also deposited on top of them. Subsequently, SERS measurements were conducted using a portable Raman spectrometer (as described in the experimental details section). The presence of the explosive chemicals RDX and PA was discovered utilizing the MM NAPs. The concentration-dependent research allowed for the differentiation of Raman peaks [see Figure 5A.5(a)] associated with different concentrations of the analyte (RDX) at 876 cm^{-1}, 933 cm^{-1}, 1260 cm^{-1}, 1312 cm^{-1}, and 1373 cm^{-1} [50, 51]. The minimum detectable concentration was achieved at around 5 µM. The whole dataset is shown in Figure 5A.5(a).

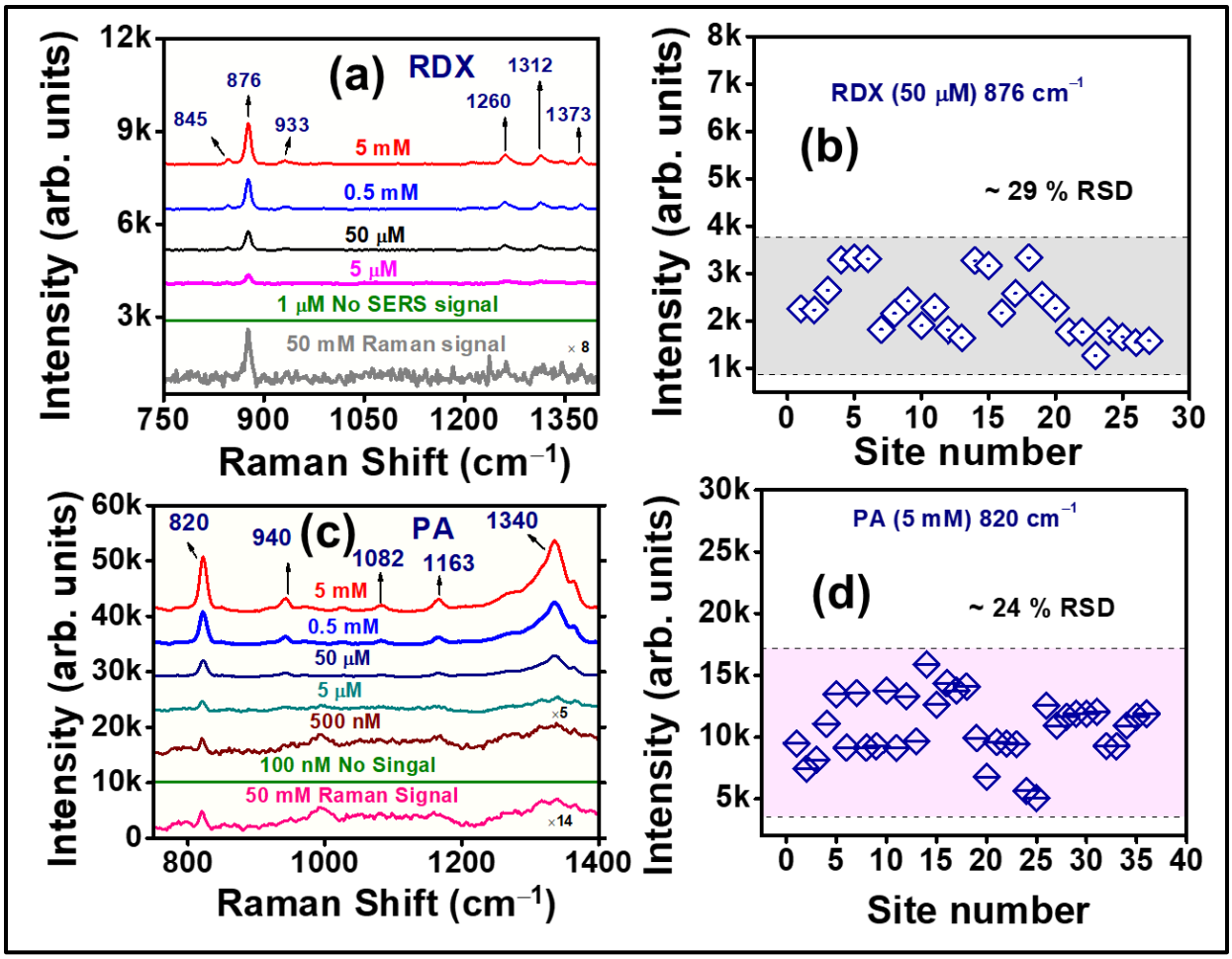

Figure 5A. 5 (a) Concentration-dependent SERS spectra of RDX using MM NAPs drop cast on unablated Ag pristine, along with pure Raman spectrum (in grey colour) of RDX (50 mM) collected from only unablated Ag pristine, (b) Reproducibility spectra (with ~29% RSD) of RDX (50 µM), (c) Concentration-dependent SERS spectra of PA using MM NAPs drop cast on unablated Ag pristine, along with pure Raman spectrum (in pink colour) of PA (50 mM) collected from unablated Ag pristine, (d) Reproducibility spectra (with ~24% RSD) of HMX (50 mM). The portable Raman acquired the complete SERS data in this figure, with the same acquisition parameters mentioned in the experimental details.

The SERS spectrum of RDX exhibited well-defined peaks. The 876 cm^{-1} band corresponds to the symmetric ring-breathing mode, while the 933 cm^{-1} band represents the combination of ring stretching and N–O deformation [51]. In addition, the 1260 cm^{-1} band is attributed to the CH_2 scissoring and N-N stretch vibration, whereas the 1312 cm^{-1} band is attributed to CH_2 wagging. The 1373 cm^{-1} band includes the υNO_2 symmetric stretching vibration and βCH_2 scissoring, which together characterize the several vibrational modes of RDX [50, 51]. In addition, the uniformity of the SERS signal was evaluated by analyzing several SERS spectra (>25), resulting in a relative standard deviation (RSD) value of around 29% [for a concentration of 50 µM RDX, as seen in

Figure 5A.5(b)]. Using the drop-casting method to identify PA, the MM NAPs were then applied onto a fresh and uncontaminated Ag substrate. The SERS spectra of PA at different concentrations, ranging from 500 nM to higher concentrations, are shown in Figure 5A.5(c). The signal-variation-plot, which demonstrates a relative standard deviation (RSD) value of around 24%, is given in Figure 5A.5(d). In the case of PA, the Raman signature peak at 820 cm^{-1} is attributed to NO_2 scissoring, whereas its presence at 1340 cm^{-1} is attributed to NO_2 symmetric stretching [52, 53]. The enhancement factors (EFs) for all trace detections produced by BB-ablated MM NAPs have been calculated using published formulas from previous works [39, 49, 54] to provide a clear representation. The calculated values for the EFs (enhancement factors) of RDX (5 µM) and PA (500 nM) are found to be 1.7×10^4 and 2.4×10^5, respectively. We have compared our findings with previous studies to provide a comprehensive overview. Almaviva et al. [50] conducted a study where they successfully detected RDX using commercially available SERS substrates. They achieved detection limits in the range of a few tens of picograms. Hatab et al. [51] successfully detected RDX in contaminated groundwater at concentrations as low as 0.15 mg/l using gold nanoparticles as SERS substrates. The enhancement factor achieved was around 6×10^4. Liyanage et al. [55] developed a highly adaptable nanosensor to assemble and accurately detect explosives like RDX. The sensor also has a high level of sensitivity in its SERS responses. In addition, Hakonen et al. [52] conducted a study on the use of hydrophobic Ag nanopillar SERS substrates for accurate detection of PA, achieving a limit of quantification (LOQ) of 0.06 ppb (parts per billion). In addition, we have provided a detailed analysis of the SERS capabilities of nanoparticles in their pure state. Moram and co-workers [56] have successfully identified explosives, namely PA (5 µM) and 2,4-Dinitrotoluene (DNT, 1 µM), using laser-ablated Ag NPs placed on filter paper in conjunction with the SERS approach. In addition, the same group successfully detected a dye, methylene blue (MB), at a concentration of 5 µM using the LAL approach. Furthermore, they generated pure Copper (Cu) and Silver (Ag) nanoparticles [57]. Elaborate SERS studies are underway, focusing on various pure and alloy nanoparticles generated by BB LAL. These investigations aim to understand the enhancement processes thoroughly, and their findings will be published separately. Based on this experiment, the MM NAPs show a similar capability to detect various explosives, including PA and RDX, when compared to earlier investigations. These examples demonstrate their great level of sensitivity and ability to adjust. These nanomaterials show great potential for use in applications that include SERS. In the future, there is a strong

likelihood of achieving even bigger improvements in the augmentation of the Raman signal by combining colloidal nanoentities with other solid nanostructures.

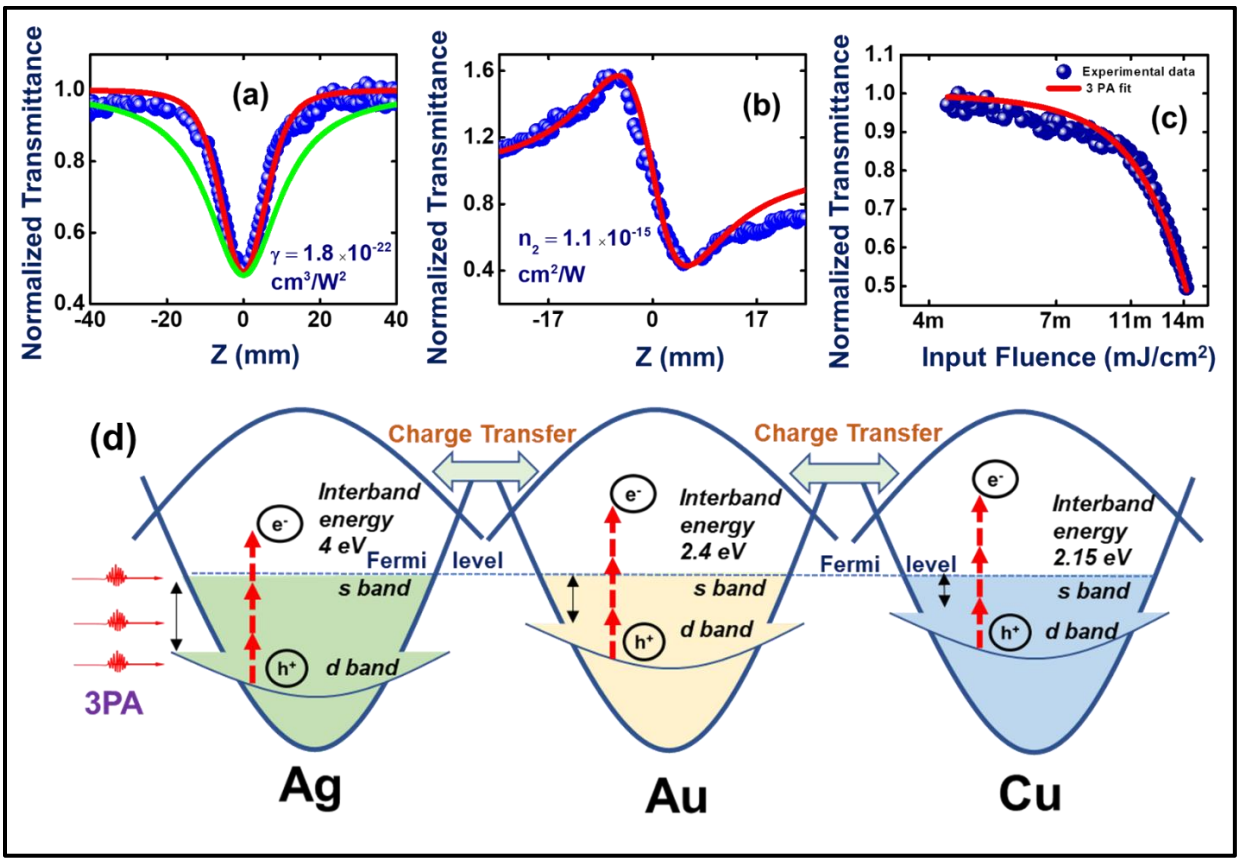

Figure 5A. 6 (a) Open aperture Z-scan curves of MM NAPs in deionized water performed with ~50 fs amplifier pulses,1 kHz, and 800 nm excitation. 3d spheres in blue represent the experimental data, whereas the solid red curve is the theoretical fit corresponding to 3PA. The yellow solid line depicts the theoretical fit for 2PA, which does not fit with the experimental data. (b) Closed aperture Z-scan data of the MM NAPs reveal the n_2 value. Similarly, 3d spheres in blue represent the experimental data, whereas the solid red curve is the theoretical fit. (c) The TEM image shows different alloyed portions of the MM NAPs. (d) Schematic energy level diagram of MM NAPs in NLO regime.

5A.3.3. Superior three-photon absorption under femtosecond NLO excitation

To investigate the behavior of these alloy nanoparticles when subjected to multi-photon excitation induced by fs pulses, NLO experiments were conducted utilizing the Z-scan method [58]. A comprehensive examination of the NAPs was conducted to investigate the influence of nanoscale alloying of the three coinage metals. The Z-scan experiment used femtosecond pulses generated by a Ti: sapphire laser amplifier (~800 nm, ~50 fs, 1 kHz). The Z-scan configuration has been elucidated in our prior investigations [58, 59], while further experimental parameters have been

elaborated upon in the section specifically devoted to experimental particulars. The Z-scan experimental setup was used to evaluate the nonlinear absorption (NLA), nonlinear refractions (NLR), and nonlinear absorption (NLA) of the colloidal alloy nanoparticles. Equation (1) describes the fundamental behavior of the transmittance impacted by multi-photon absorption in the open aperture Z-scan fit equation under tight focusing conditions [58].

$$T_{OA(nPA)} = \frac{1}{[1+(n-1)\alpha_n L(I_0/(1+\left(\frac{z}{z_0}\right)^2))^{n-1}]^{\frac{1}{n-1}}} \quad (1)$$

here, the effective length of the sample being $L_{eff}(cm^{-1}) = 1 - e^{-\alpha L}/_{\alpha}$ (corresponding to 2PA), $L'_{eff}(cm^{-1}) = 1 - e^{-2\alpha_0 L}/_{2\alpha_0}$ (corresponding to 3PA), α_n being the multi-photon absorption coefficient, γ is the 3PA coefficient (cm^2/GW^3), $z_0$is the Rayleigh range, I_0 is the peak intensity. Equation (2) may be used to fit the transmittance curve for the closed aperture [58, 59] Z-scan setup as,

$$T_{CA} = 1 \pm \frac{4\Delta\Phi\left(\frac{z}{z_0}\right)}{\left[\left(\frac{z}{z_0}\right)^2+9\right]\left[\left(\frac{z}{z_0}\right)^2+1\right]} \quad (2)$$

The NLO coefficients, namely $\Delta\Phi$ (nonlinear phase shift), n_2 (cm^2/GW), β (cm/GW), and γ (cm^2/GW^3), have been determined using the theoretical fits of the experimental data. Subsequently, the third-order nonlinear optical susceptibility χ (3) and the nonlinear absorption cross section (σ3) of the MM NAPs in question were calculated. Mathematically, multi-photon absorption cross-section (for 3PA, n = 3) is expressed as, $\sigma_n = \frac{(\hbar\omega)^{n-1}}{N}\alpha_n$, N being the concentration of nano entities. Further details have been mentioned in previous reports. Figure 5A.6(a) shows that MM NAPs exhibited pure reverse saturable absorption (RSA) behavior with a dominant 3PA process at input wavelengths of 800 nm. The plausibility of the 3PA is substantiated by the absorbance of MM NAPs, which was measured at 550 nm. Additionally, we have provided a 2PA fit that demonstrates the deviations from the experimental data. This demonstrates the successful manifestation of 3PA. The Z-scan traces in Figure 5A.6(b) depict a peak-valley pattern and demonstrate nonlinearity with a negative sign (n_2). This data provides information regarding the response of the defocusing Kerr lens effect inside the MM NAPs under fs pulse excitation. Subsequently, thorough theoretical adjustments and computations revealed several nonlinear

optics (NLO) parameters. The 3PA coefficient (γ) was determined to be 1.8×10^{-22} cm^3/W_2, while the NLR coefficient (n_2) was measured to be 1.1×10^{-15} cm^2/W. In addition, the imaginary component of the $\chi^{(3)}$ coefficient has been determined to be 7.6×10^{-14} esu. To comprehensively understand the energy levels inside the system, the 3PA cross-section (σ_3) has been calculated to be 1.9×10^{-75} cm^6/s^2. We have also calculated the initial onset of optical limiting (OL) [60] for the nanoalloys. The optical limiting threshold is the point at which the transmittance decreases to 50% of the linear transmittance, which is determined by the incident fluence. The onset optical limiting [60,61] is the minimum incident fluence required to initiate optical limiting activity [60]. The data from the OL experiment is shown in Figure 5A.6(c). The measured onset OL threshold value was 8.8 mJ/cm^2. The main source of error in estimating the NLO coefficients was the ambiguity in estimating the peak intensities, leading to an estimated inaccuracy of ±5%. In addition, we conducted measurements and estimations, which revealed that the impact of the solvent (clean distilled water) on the nonlinearity was insignificant, being at least ten times smaller. The MM NAPs exhibit an intrinsically electronic nonlinear response when subjected to 1 kHz, 50 fs laser pulses. Typically, the occurrence of RSA may be ascribed to many mechanisms, such as photo-ejection of electrons, free-carrier absorption (intraband transition), and multi-photon absorption. The photon energy corresponding to 800 nm excitation is 1.55 eV [58], which is sufficient for the interband population transition from the valence band (VB) to the conduction band (CB). Three-photon absorption (3PA) is supported by the prominent peak in the UV-visible-IR spectra between 600 and 900 nm. This peak is believed to be caused by the formation of Ag-Au-Cu alloy, which introduces new energy levels at intermediate values. Additional evidence confirming the adjustability of the surface plasmon resonance (SPR) peak of the newly created Ag-Au-Cu MM NAPs is derived from previously studied absorption peaks of the individual components, namely pure NPs. These pure NPs have been documented to exhibit absorption peaks at approximately 420 nm (for pure Ag NPs), around 525 nm (for pure Au NPs in general), and approximately 600 nm (as reported for pure Cu NPs) [43, 57]. The altered absorption surface plasmon resonance (SPR) peak of the MM NAPs, situated at 550 nm in Figure 5A.6(d), suggests the presence of new intermediate energy levels inside the complex while composed of identical pure nanoparticles. Furthermore, the magnitudes of the NLO coefficients (γ, n_2) indicate a higher level of nonlinearity demonstrated by these alloy nanoentities compared to other previously described nanoparticles.

The significant nonlinearity may be elucidated by the plasmon-enhanced model of nonlinear absorption.

5A.3.3.1. Central understandings of the MM NAPs' higher NLO response

The materials that possess prominent plasmonic properties and are well-recognized for their characteristics include copper, gold, and silver, the three metals often used in coins. The materials in the nano-regime exhibit a phenomenon called local field trapping, which is induced by the quantum confinement effects. This trapping results from the fine collective coherent free electron oscillation at the fermi surface. Some recent works [61-64] provide additional information on this topic. When high repetition rate fs pulses interact with localized surface plasmons (LSP), they may enhance the NLO response [65, 66, 67]. Understanding the basic insights is vital for correctly comprehending the energy levels of alloyed metals since they are not just the superposition of independent levels. Furthermore, apart from localized surface plasmons (LSPs), the NLO process in Ag-Au-Cu NAPs is also influenced by a greater quantity of electrons generated by ultrafast pulses. These carriers are generated by transitions such as the d-band to unfilled 's' band (valence band to conduction band inter-band transition) and the occupied s-band to unfilled 's' band (inside the conduction band, intra-band excitations). Valenti et al. [68] have extensively studied the electronic transitions associated with these coinage metal nanoparticles in this environment. It has been shown that under the stimulation of visible light. On the other hand, Au (2.4 eV) and Cu (2.15 eV) generate charge carriers with low energy levels because of inter-band (d-s) [69] population transfers [68, 70]. In contrast, Ag (4 eV) produces high-energy electrons and holes only via intra-band excitations, thanks to its larger inter-band energy gap. Within the context of MM NAPs, three-photon absorption will probably occur under intense NIR (800 nm) light. Additionally, a significant discovery from the elemental composition data [Figure 5A.2(k)] is that these nanoalloys have been shown to possess the most elevated concentration of Ag. Therefore, one should expect a larger population of high-energy electrons due to intra-band transition. These photo-excitation processes directly affect the non-linear optical (NLO) response, which also naturally regulates the density of charge carriers in the MM NAPs. Kudryashov et al. [71] have shown that metallic gold nanoparticles rapidly form unique 'superplasmonic' states when subjected to intense photo injection. This process significantly increases the number of free carriers, affecting the NLO processes. The potential charge/energy exchange among the three metallic nano-systems, which

exist in an alloyed form, might serve as an additional supporting explanation. The alloy's Ag, Au, and Cu elements facilitate charge transfer [61], significantly increasing free carriers. This, in turn, considerably enhances the probability of experiencing increased excited state absorption. Hence, the optical reaction in the nonlinear realm is intensified due to resonant energy exchanges between a system consisting of a pair of linked elements (namely, Ag, Au, and Cu in this case). Hence, the previously described ideas of charge transfer processes and plasmon-assisted amplification may be used to explain the NLO response of the MM NAPs manufactured using BB technology.

The energy level diagram shown in Figure 5A.6(d) demonstrates the 3PA process, which transfers energy from the ground state and reduces energy levels to enhance the conduction band (CB) population. Furthermore, it has been shown that the component constituents of the nanoalloys - Ag, Au, and Cu - contribute to the enhanced nonlinearity via their plasmonic response, charge transfer processes, and population generation facilitated by multi-photon absorption. Lama et al. [72] have also examined the adjustable plasmon-enhanced nonlinear optical refraction of monodisperse and polydisperse silver nanoparticles. Biswas et al. [73] recently discovered that graphene oxide–silver nanocomposites depict an improved NLO response. This enhancement is attributed to a resonant transition from surface plasmon resonance (SPR) to the conduction band. Based on their thorough nanosecond nonlinear absorption studies, the Ag-GO composite exhibited a nonlinear absorption coefficient that was 2.6 times greater than pure GO's. In addition, they have observed a roughly five-fold increase in the nonlinear refractive index in the presence of Ag. Mamidala et al. [74] studied the nonlinear refractive indices and actual and theoretical two-photon absorption strengths of Fe_3O_4 nanocubes with and without Ag nanoparticles. They observed increases in these coefficients and cross-sections of several folds. The NLO coefficients of the MM NAPs, with γ values of roughly 10^{-22} cm^3/W^2 and n_2 values of around 10^{-15} cm^2/W, indicate their significant potential in many optical applications such as optoelectronics, photonics, solar cells, optical limiting, and others. In addition, our strategy includes conducting intensity-dependent and excitation wavelength-varying Z-scan experiments to get a comprehensive and detailed knowledge of these alloy micro entities' NLO response. In addition, fs transient absorption spectroscopy was conducted to comprehend the time-resolved electron dynamics of these NAPs.

5A.3.4. Transient absorption dynamics under femtosecond laser excitation

The study examines the dynamic behavior of excited carriers by ultrafast pump-probe measurements of plasmonic nanoparticles. This behavior encompasses several substantial impacts that are often concealed in scientific inquiries. Therefore, fs TAS measurements were conducted on the colloidal dispersion of MM NAPs to understand better the interaction between the excited electrons in the conduction band (CB). The details of the experimental setup have been discussed in our previous studies [75]. Figure 5A.7(a) displays the transient absorption spectra of MM NAPs at different probe delay durations. After using a laser to excite the plasmonic band, a transitory absorption spectrum was detected on the right side of the bleached spectrum. The transient absorption spectra decreased, and the bleached spectrum returned to its original state as the time gap between the pump and probe pulses increased. When stimulated with light at a wavelength of 400 nm, a wide absorption band was seen between 480 and 570 nm. This absorption band is likely caused by the depletion of plasmon electrons [76]. The positive band found above 630 nm may be attributed to the absorption of the non-equilibrium electron distribution around the Fermi level induced by thermal stimulation. This phenomenon is called the excited state absorption (ESA) band [75, 76]. The inter-band excitation-induced plasmon (EIP) [77] is accountable for the absorption above 630 nm, specifically at 675 nm, since it has been seen to diminish at a slower rate compared to the intrinsic plasmon bleach peak (until ~20 ps). The previously described favorable band was found until around 302 picoseconds. Additional analysis of the TAS spectra revealed other noteworthy findings. The negative bleach (photo-induced bleach, PIB) initially appeared at a wavelength of 478 nm, but was shown to move towards a longer wavelength (550 nm) after being exposed for 1.2 picoseconds. The negative absorption band has also separated into two distinct peaks, one at 478 nm and another at 550 nm. The peak at 478 nm, which exhibited a blue shift, saw a faster recovery than the 550 nm peak, as seen in the TAS spectra at 2.5 ps [Figure 5A.7(a)]. The occurrence of bleach-splitting may be explained by the transfer of charge between the various components of the nanoalloy system, which is then followed by the expansion of excited electrons in distinct energy states [78, 79]. Previous investigations have provided evidence for the production of new states by illustrating a change in energy levels [80] resulting from the alloying of plasmonic nanoparticles. The time-delayed signal exhibited a blue shift in the ESA band. The zero-line spots of the various time-delayed TAS spectra [Figure 5A.7(a)] were seen to undergo a progressive blue shift. Based on the ab initio predictions of Brown et al. [81], it is seen

that in plasmonic nanoparticles, nonthermal carriers experience dephasing within a few femtoseconds after being excited. This results in the generation of carriers closer to the Fermi level. These carriers undergo thermalization by electron-electron scattering throughout several hundred femtoseconds [82], resulting in a thermal distribution with a greater temperature peak. During a brief period, known as tens of picoseconds, these thermalized carriers transfer their energy to the lattice via electron-phonon scattering [77, 79, 81, 83]. Finally, the phenomenon of phonon-phonon scattering takes over as the prevailing factor. The Surface Xplorer program was used to analyze the representative kinetics of the ESA band, notably the peak at 675 nm. The data was fitted using a triple exponential function. The data is shown in Figure 5A.7(b). For fitting the TAS data, three lifetimes were taken into account: one for electron-electron (e-e) scattering, one for electron-phonon (e-ph) scattering, and one for phonon-phonon (ph-ph) scattering processes [77, 81]. The retrieved lifetime values from the fit are as follows: the lifetime of electron-electron interactions ($\tau_{e\text{-}e}$) is 0.7±0.1 ps, the lifetime of electron-phonon interactions ($\tau_{e\text{-}ph}$) is 1.2±0.1 ps, and the lifetime of phonon-phonon interactions ($\tau_{ph\text{-}ph}$) is 47.5±8 ps. Prior research has shown that Ahmadi et al.[84] determined decay times of 2.5 and 50 picoseconds for the interactions between electrons and phonons, as well as between the phonons themselves, in 30-nanometer gold nanoparticles suspended in water. Perner et al. [85] found similar outcomes, reporting relaxation periods of 4 ps and 200 ps for 30 nm gold particles embedded in a sol-gel matrix. These timings correspond to electron-phonon and phonon-phonon interactions following stimulation at 400 nm. In the study by Link et al. [86], the electron-phonon and phonon-phonon relaxation durations for gold nanoparticles were found to be 3.1 ps and 90 ps, respectively, under 400 nm excitation. Similarly, the alloy nanoparticles' corresponding relaxation times were determined to be 3.3 ps and 86 ps. Zheng et al. [87] further exhibited silver-gold bimetallic nanoparticles' quantitative electron-phonon coupling constants. In a recent study, Engelbrekt and colleagues [2] found that the cooling rate was reduced due to prolonged lattice cooling ($\tau_{ph\text{-}ph}$). They observed that the cooling time rose from 46 ps for $Au_{100}Pt_0$ NCs to 66 ps for $Au_{70}Pt_{30}$ NCs. Furthermore, in the context of highly plasmonic nanoparticles [77, 88, 89], photo-excited plasmons are essential for sustaining the strength and density of localized surface plasmons. The plasmon charge density is thought to significantly impact the durations of electron-electron and electron-phonon scattering times [77, 81], determining the overall photophysical dynamics. Zhang et al. [77] utilized fs pump-probe technique to investigate the photoexcited system of gold NPs (diameter ~10 nm) and the impact

of conduction-band electrons produced by interband excitation on excitation dynamics. More precisely, they have shown that these stimulated electrons actively engage in plasmonic oscillations. A delay is anticipated before the relaxation of electrons generated by interband excitation and their involvement in plasmonic oscillation [77, 83]. The energetic electrons must undergo an adaptive phase/frequency adjustment and an intraband relaxation to engage in the plasmonic oscillation process. Increased interaction among plasmonic electrons is anticipated due to newly generated conduction-band electrons or an increase in their density. Therefore, the plasmonic oscillation is decelerated by the interaction of these electrons, resulting in scattering [77]. This drop in resonance frequency will result in a red-shifted resonance spectrum. Similarly, our reported MM NAPs have shown a red shift in the bleach (from 478 nm to 550 nm) during the initial time scales of 400 fs to less than 1 ps. This phenomenon may be elucidated by the inter-band transition-induced creation of a larger population of energetic charge carriers, often referred to as interband-excitation-induced plasmon (EIP). The heating of the lattices is enhanced due to the surplus energy of the hot electrons and holes, resulting in a considerably enhanced and extended phonon relaxation process [77]. The energy transfer from hot electrons or holes to the surrounding lattices occurs via the interaction between plasmonic charge carriers and phonons. This interaction is mainly responsible for heating the lattice. This enhances the phonon-scattering mechanism, increasing the electron-phonon interaction's time scale. The presence of three plasmonic substances (Ag, Au, Cu) may generate a greater number of hot charges. These nanoalloys have slightly longer relaxation time scales ($\tau_{e\text{-}e}$ = 0.7±0.1 ps, $\tau_{e\text{-}ph}$= 1.2±0.1 ps, $\tau_{ph\text{-}ph}$= 47.5±8 ps) than those reported in our previous studies on a bimetallic alloy NPs [75]. This data can also be used to rationalize the difference.

Figure 5A.8 displays the kinetic evolution data for the bleach at a wavelength of 550 nm. To get a comprehensive and detailed understanding, analyzing the bleach kinetics of these nanoalloy systems using intensity-dependent time-resolved absorption spectroscopy (TAS) and a global analytic technique is necessary. This task is to be executed, and it will fall under our upcoming strategies. In addition, TAS spectroscopy's comprehensive comprehension of charge dynamics has led to the diverse use of distinct nanoentities across several domains.

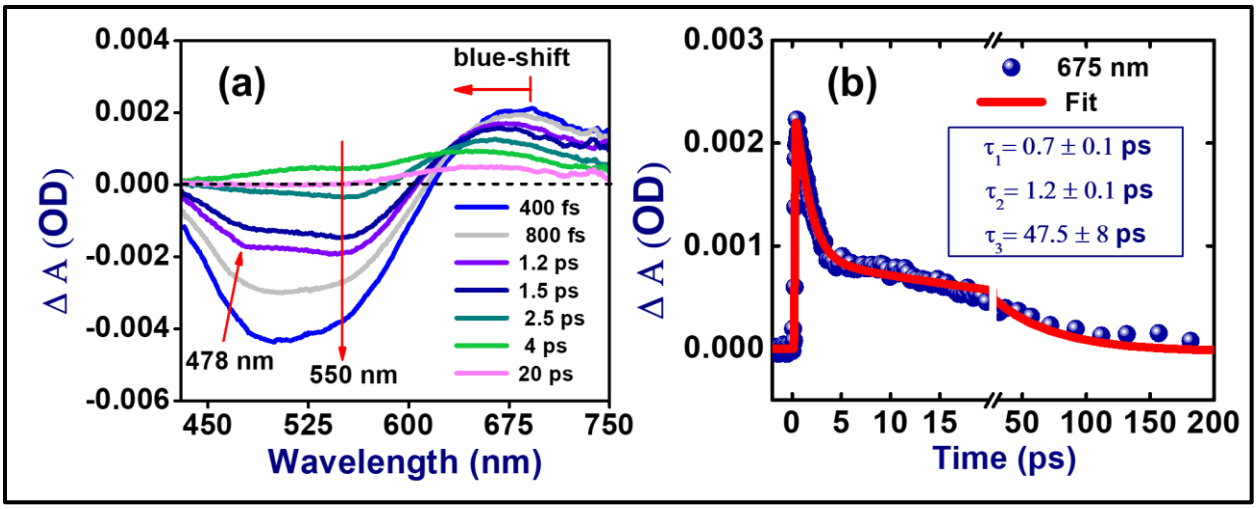

Figure 5A. 7 (a) fs transient absorption spectra of MM NAPs at a time delay increased from 0 to 20 ps for a pump wavelength of 400 nm. (b) Transient absorption time profiles of the same MM NAPs at 675 nm central peak of the ESA band with the corresponding triple-exponential fit.

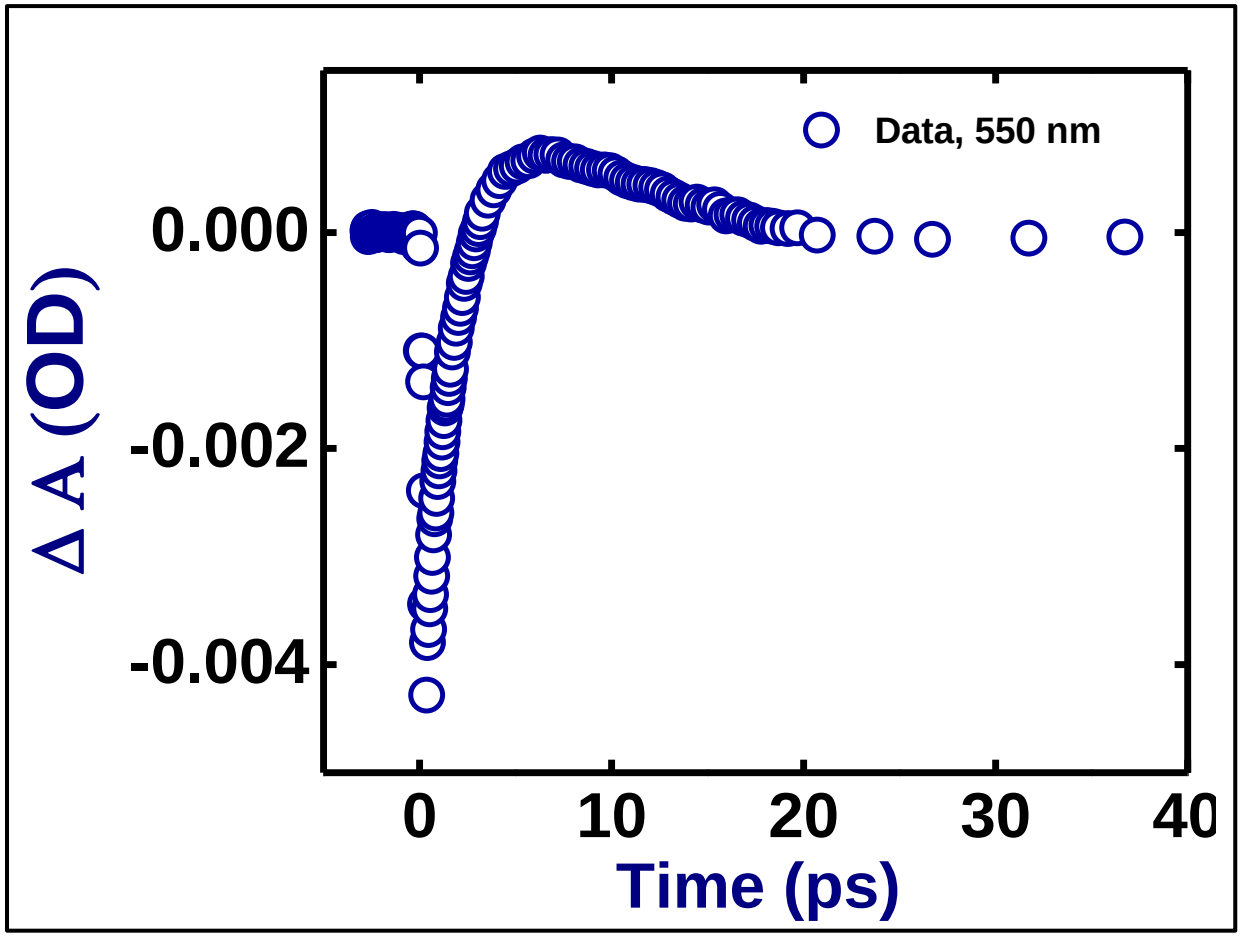

Figure 5A. 8 (a) Transient absorption time profile of the MM NAPs, corresponding to the bleach central peak at 550 nm.

Karam et al. [76] showed via transient absorption measurements that colloidal gold-silver-gold core-shell-shell nanoparticles have a notably quicker phonon-phonon scattering lifetime than gold nanospheres and nanorods. This aspect contributes to increased photothermal efficiency, useful for medicinal purposes such as selectively eliminating cancer cells. Yanagiya et al. [90] observed the transportation of hot electrons from a gold nanostructure in a multilayer film of titanium dioxide, gold nanoparticles, and a gold thin film. Soavi et al. [91] used ultrafast pump-probe spectroscopy to examine the temporary photophysical properties of graphene nanoribbons (GNRs) with a very thin and well-defined structure. The researchers demonstrated that by using GNRs as light absorbers, they observed the phenomenon of exciton-exciton annihilation, which leads to forming a radiative biexciton state with an unusually strong associated binding energy. This finding has the potential to enhance the efficiency of photovoltaic systems. Saroha et al. [92] used ultrafast transient absorption spectroscopy to assess colloidal gold nanoparticles' stability and optical properties with diameters ranging from 13 to 30 nm. The stability of Au NPs was evaluated using kinetic characteristics. It was noted that NPs with longer development durations showed increased stability, as seen by a longer average decay time. Moreover, they predicted that these plasmonic nanoparticles might be valuable in energy conversion or photocatalysis. Engelbrekt et al. [2] studied the rapid photodynamics of plasmon-mediated energy transfer to the surface of Au-Pt core-shell nanocrystals. Their research has discovered a high possibility of developing highly efficient plasmon-driven photocatalysts. The current research on fs TAS measurements of plasmonic colloids suggests that these nanoalloys possess promising prospects for several domains, such as photonics, photothermal conversion, charge-transfer-based solar cells, photocatalysis, and photoelectric conversion.

5A.4. Conclusions

Overall, this study showcases the creation of a new colloid consisting of nanoalloy particles made from several metals. The colloid is produced using a femtosecond broadband laser beam created by an axicon. This approach uses the unique properties of non-diffracting light and the versatility of alloyed nanoparticles. In this work, we have effectively synthesized colloidal dispersions of unique multi-metal (Ag-Au-Cu) nanoalloy particles. Transmission electron microscopy measurements and EDX spectra have been used for comprehensive topographical and elemental characterizations. HRTEM pictures provided an extensive examination of the newly developed

nanoalloys. In addition to conducting UV-visible-IR absorption analysis, the produced nanoalloys were used in SERS-based sensing experiments, effectively detecting minute amounts of explosive compounds of RDX (5 µM) and PA (500 nM). The calculated enhancement factors for RDX and PA were 1.7×10^{4} and 2.4×10^{5}, respectively. In addition, the NAPs were examined under fs, a nonlinear optical domain, and it was discovered that they exhibited three-photon absorption. Subsequently, thorough theoretical fits of the RSA spectrum and subsequent computations revealed the magnitudes of other NLO parameters. The coefficient for third-order NLO response, γ, has been determined to be 1.8×10^{-22} cm^3/W^2, whereas the coefficient for nonlinear refractive index, n_2, has been measured to be 1.1×10^{-15} cm^2/W. In addition, the computed value for the actual component of the $\chi^{(3)}$ is 7.6×10^{-14} esu. The cross-section for three-photon absorption (σ_3) has been calculated to be 1.9×10^{-75} cm^6/s^2. In addition, we have calculated the initial optical limiting (OL) value to be 8.8 mJ/cm^2, hence expanding the potential use of NAPs in optical limiting applications. The NLO response of the MM NAPs has been justified and explained via detailed talks on the notions of charger transfer events and plasmon-assisted amplification. In addition, we conducted fs transient absorption spectroscopy (TAS) to observe the time-dependent behavior of the electrons that were stimulated by the light in the nanoalloy system. The TAS data revealed many photoexcited processes, including electron-electron/thermalization ($\tau_{e\text{-}e}$ = 0.7±0.1 ps), electron-phonon ($\tau_{e\text{-}ph}$ = 1.2±0.1 ps), and phonon-phonon scattering ($\tau_{ph\text{-}ph}$ = 47.5±8 ps). The TAS data provided a systematic understanding of several characteristics of the nanoalloy system, including the interband-excitation-induced plasmon (EIP), the ESA band's delayed lifespan, and the bleach's splitting. In our future goal, we want to research alloy nanoentities' NLO and transient absorption spectroscopy (TAS) properties. These studies will include adjusting the intensity of the excitation wavelength and will be analyzed globally to get a comprehensive and detailed knowledge of these entities. This work has provided a comprehensive grasp of the benefits of using the BB-induced LAL method to create innovative, multi-metal plasmonic nanoalloys. In addition, we have investigated the NLO and time-resolved dynamic properties of the innovative nano-system and its use in SERS sensing. The research demonstrates that these innovative nanoalloys are promising for use in several domains, such as sensors, NLO switching, photothermal conversion, charge-transfer-based solar cells, photocatalysis, and optical limiting.

References

[1] M.B. Cortie, A.M. McDonagh, Synthesis and optical properties of hybrid and alloy plasmonic nanoparticles, Chem Rev, 111 (2011) 3713-3735.

[2] C. Engelbrekt, K.T. Crampton, D.A. Fishman, M. Law, V.A. Apkarian, Efficient Plasmon-Mediated Energy Funneling to the Surface of Au@Pt Core-Shell Nanocrystals, ACS Nano, 14 (2020) 5061-5074.

[3] A.N. Koya, J. Cunha, T.-L. Guo, A. Toma, D. Garoli, T. Wang, S. Juodkazis, D. Cojoc, R. Proietti Zaccaria, Novel Plasmonic Nanocavities for Optical Trapping-Assisted Biosensing Applications, Advanced Optical Materials, 8 (2020) 1901481.

[4] R. Borah, S.W. Verbruggen, Silver-Gold Bimetallic Alloy versus Core-Shell Nanoparticles: Implications for Plasmonic Enhancement and Photothermal Applications, J Phys Chem C, 124 (2020) 12081-12094.

[5] K. Sytwu, M. Vadai, J.A. Dionne, Bimetallic nanostructures: combining plasmonic and catalytic metals for photocatalysis, Advances in physics: X, 4 (2019) 1619480.

[6] R. Ferrando, J. Jellinek, R.L. Johnston, Nanoalloys: From Theory to Applications of Alloy Clusters and Nanoparticles, Chem Rev, 108 (2008) 845-910.

[7] V. Coviello, D. Forrer, V. Amendola, Recent Developments in Plasmonic Alloy Nanoparticles: Synthesis, Modelling, Properties and Applications, Chemphyschem, 23 (2022) e202200136.

[8] Y. Yao, Q. Dong, A. Brozena, J. Luo, J. Miao, M. Chi, C. Wang, I.G. Kevrekidis, Z.J. Ren, J. Greeley, G. Wang, A. Anapolsky, L. Hu, High-entropy nanoparticles: Synthesis-structure-property relationships and data-driven discovery, Science, 376 (2022) eabn3103.

[9] W. Tang, L. Zhang, G. Henkelman, Catalytic Activity of Pd/Cu Random Alloy Nanoparticles for Oxygen Reduction, J Phys Chem Lett, 2 (2011) 1328-1331.

[10] H. Chen, L. Shao, Q. Li, J. Wang, Gold nanorods and their plasmonic properties, Chem Soc Rev, 42 (2013) 2679-2724.

[11] G.V. Hartland, Optical studies of dynamics in noble metal nanostructures, Chem Rev, 111 (2011) 3858-3887.

[12] S.A. Jalil, B. Lai, M. ElKabbash, J. Zhang, E.M. Garcell, S. Singh, C. Guo, Spectral absorption control of femtosecond laser-treated metals and application in solar-thermal devices, Light: Science & Applications, 9 (2020) 14.

[13] L.R. Buddiga, G.R. Gajula, B.B.V. Sailaja, M.L.V.P. Ch, Visible light photocatalytic exploit of P/Zr doped TiO_2 nano particles for dye degradation of rose Bengal, Applied Surface Science Advances, 18 (2023) 100492.

[14] J. Zhang, J. Claverie, M. Chaker, D. Ma, Colloidal Metal Nanoparticles Prepared by Laser Ablation and their Applications, Chemphyschem, 18 (2017) 986-1006.

[15] A.M. Fagan, W.R. Jeffries, K.L. Knappenberger, Jr., R.E. Schaak, Synthetic Control of Hot-Electron Thermalization Efficiency in Size-Tunable Au-Pt Hybrid Nanoparticles, ACS Nano, 15 (2021) 1378-1387.

[16] V. Amendola, Laser-Assisted Synthesis of Non-Equilibrium Nanoalloys, Chemphyschem, 22 (2021) 622-624.

[17] V. Amendola, S. Scaramuzza, F. Carraro, E. Cattaruzza, Formation of alloy nanoparticles by laser ablation of Au/Fe multilayer films in liquid environment, J Colloid Interface Sci, 489 (2017) 18-27.

[18] M. Ahlawat, D. Mittal, V. Govind Rao, Plasmon-induced hot-hole generation and extraction at nano-heterointerfaces for photocatalysis, Communications Materials, 2 (2021) 114.

[19] K.K. Haldar, S. Tanwar, R. Biswas, T. Sen, J. Lahtinen, Noble copper-silver-gold trimetallic nanobowls: An efficient catalyst, J Colloid Interface Sci, 556 (2019) 140-146.

[20] K. Bhunia, S. Khilari, D. Pradhan, Trimetallic PtAuNi alloy nanoparticles as an efficient electrocatalyst for the methanol electrooxidation reaction, Dalton Trans, 46 (2017) 15558-15566.

[21] M. Kushwah, S. Bhadauria, K. Arora, M.S. Gaur, Enhanced catalytic activity of chemically synthesized Au/Ag/Cu trimetallic nanoparticles, Materials Research Express, 6 (2019) 095013.

[22] Y. Shen, S. Pidishety, I. Nape, A. Dudley, Self-healing of structured light: a review, Journal of Optics, 24 (2022) 103001.

[23] S.N. Khonina, N.L. Kazanskiy, S.V. Karpeev, M.A. Butt, Bessel beam: Significance and applications—A progressive review, Micromachines, 11 (2020) 997.

[24] T. Chen, G. Zhang, H. Zhang, J. Lv, Y. Wang, P. Qu, R. Stoian, G. Cheng, Nano-spheroid formation on YAG surfaces induced by single ultrafast Bessel laser pulses, Applied Surface Science, 604 (2022) 154360.

[25] F. Courvoisier, J. Zhang, M. Bhuyan, M. Jacquot, J.M. Dudley, Applications of femtosecond Bessel beams to laser ablation, Applied Physics A, 112 (2013) 29-34.

[26] G. Kontenis, D. Gailevičius, N. Jiménez, K. Staliunas, Optical Drills by Dynamic High-Order Bessel Beam Mixing, Physical Review Applied, 17 (2022).

[27] R. Stoian, M.K. Bhuyan, A. Rudenko, J.-P. Colombier, G. Cheng, High-resolution material structuring using ultrafast laser non-diffractive beams, Advances in Physics: X, 4 (2019) 034059.

[28] P. Wu, C. Sui, W. Huang, Theoretical analysis of a quasi-Bessel beam for laser ablation, Photonics Research, 2 (2014) 82-86.

[29] G.K. Podagatlapalli, S. Hamad, M.A. Mohiddon, S.V. Rao, Fabrication of nanoparticles and nanostructures using ultrafast laser ablation of silver with Bessel beams, Laser Physics Letters, 12 (2015) 036003.

[30] S.V. Rao, G.K. Podagatlapalli, S. Hamad, Ultrafast laser ablation in liquids for nanomaterials and applications, Journal of nanoscience and nanotechnology, 14 (2014) 1364-1388.

[31] V. Amendola, M. Meneghetti, What controls the composition and the structure of nanomaterials generated by laser ablation in liquid solution?, Phys Chem Chem Phys, 15 (2013) 3027-3046.

[32] B.K. Singh, D. Banerjee, A. Mangababu, Y. Shadangi, N.K. Mukhopadhyay, R. Rawat, A.P. Pathak, A. Tiwari, A. Tripathi, Ultra-short pulsed laser ablation of decagonal AlCoNi and AlCoCuNi quasicrystals, Journal of Alloys and Compounds, 968 (2023) 172238.

[33] D. Zhang, B. Gokce, S. Barcikowski, Laser Synthesis and Processing of Colloids: Fundamentals and Applications, Chem Rev, 117 (2017) 3990-4103.

[34] G.K. Podagatlapalli, S. Hamad, M.A. Mohiddon, S.V. Rao, Fabrication of nanoparticles and nanostructures using ultrafast laser ablation of silver with Bessel beams, Laser Physics Letters, 12 (2015) 036003.

[35] G. Krishna Podagatlapalli, S. Hamad, M. Ahamad Mohiddon, S. Venugopal Rao, Effect of oblique incidence on silver nanomaterials fabricated in water via ultrafast laser ablation for photonics and explosives detection, Applied Surface Science, 303 (2014) 217-232.

[36] Z. Lin, J. Yue, L. Liang, B. Tang, B. Liu, L. Ren, Y. Li, L.L. Jiang, Rapid synthesis of metallic and alloy micro/nanoparticles by laser ablation towards water, Applied Surface Science, 504 (2020) 144461.

[37] A.A. Nastulyavichus, S.I. Kudryashov, N.A. Smirnov, A.A. Rudenko, A.Y. Kharin, N.I. Busleev, D.A. Zayarny, A.A. Ionin, D.A. Kirilenko, P.N. Brunkov, Novel approach of controllable stoichiometric fabrication of alloyed Au/Ag nanoparticles by nanosecond laser ablation of thin bi-layered films in water, Laser Physics Letters, 16 (2019) 096002.

[38] J. Jakobi, S. Petersen, A. Menendez-Manjon, P. Wagener, S. Barcikowski, Magnetic alloy nanoparticles from laser ablation in cyclopentanone and their embedding into a photoresist, Langmuir, 26 (2010) 6892-6897.

[39] D. Banerjee, M. Akkanaboina, R. Kumar Kanaka, V. Rao Soma, Femtosecond Bessel beam induced ladder-like LIPSS on trimetallic surface for SERS-based sensing of Tetryl and PETN, Applied Surface Science, 616 (2023) 156561.

[40] K. Furusawa, K. Takahashi, H. Kumagai, K. Midorikawa, M. Obara, Ablation characteristics of Au, Ag, and Cu metals using a femtosecond Ti: sapphire laser, Applied Physics A, 69 (1999) S359-S366.

[41] J. Byskov-Nielsen, J.-M. Savolainen, M.S. Christensen, P. Balling, Ultra-short pulse laser ablation of metals: threshold fluence, incubation coefficient and ablation rates, Applied Physics A, 101 (2010) 97-101.

[42] G.K. Podagatlapalli, S. Hamad, S.V. Rao, Trace-Level Detection of Secondary Explosives Using Hybrid Silver-Gold Nanoparticles and Nanostructures Achieved with Femtosecond Laser Ablation, J Phys Chem C, 119 (2015) 16972-16983.

[43] M. Sree Satya Bharati, C. Byram, V.R. Soma, Femtosecond Laser Fabricated Ag@Au and Cu@Au Alloy Nanoparticles for Surface Enhanced Raman Spectroscopy Based Trace Explosives Detection, Frontiers in Physics, 6 (2018) 28.

[44] S. Dittrich, R. Streubel, C. McDonnell, H.P. Huber, S. Barcikowski, B. Gökce, Comparison of the productivity and ablation efficiency of different laser classes for laser ablation of gold in water and air, Applied Physics A, 125 (2019) 432.

[45] A.A. Nastulyavichus, S.I. Kudryashov, A.M. Emelyanenko, L.B. Boinovich, Laser Generation of Colloidal Nanoparticles in Liquids: Key Processes of Laser Dispersion and Main Characteristics of Nanoparticles, Colloid Journal, 85 (2023) 233-250.

[46] I.N. Saraeva, S.I. Kudryashov, A.A. Rudenko, M.I. Zhilnikova, D.S. Ivanov, D.A. Zayarny, A.V. Simakin, A.A. Ionin, M.E. Garcia, Effect of fs/ps laser pulsewidth on ablation of metals and silicon in air and liquids, and on their nanoparticle yields, Applied Surface Science, 470 (2019) 1018-1034.

[47] J. Langer, D. Jimenez de Aberasturi, J. Aizpurua, R.A. Alvarez-Puebla, B. Auguie, J.J. Baumberg, G.C. Bazan, S.E.J. Bell, A. Boisen, A.G. Brolo, J. Choo, D. Cialla-May, V. Deckert, L. Fabris, K. Faulds, F.J. Garcia de Abajo, R. Goodacre, D. Graham, A.J. Haes, C.L. Haynes, C. Huck, T. Itoh, M. Kall, J. Kneipp, N.A. Kotov, H. Kuang, E.C. Le Ru, H.K. Lee, J.F. Li, X.Y. Ling, S.A. Maier, T. Mayerhofer, M. Moskovits, K. Murakoshi, J.M. Nam, S. Nie, Y. Ozaki, I. Pastoriza-Santos, J. Perez-Juste, J. Popp, A. Pucci, S. Reich, B. Ren, G.C. Schatz, T. Shegai, S. Schlucker, L.L. Tay, K.G. Thomas, Z.Q. Tian, R.P. Van Duyne, T. Vo-Dinh, Y. Wang, K.A. Willets, C. Xu, H. Xu, Y. Xu, Y.S. Yamamoto, B. Zhao, L.M. Liz-Marzan, Present and Future of Surface-Enhanced Raman Scattering, ACS Nano, 14 (2020) 28-117.

[48] A. Mangababu, R. Sai Prasad Goud, C. Byram, J. Rathod, D. Banerjee, V. Rao Soma, S.V.S. Nageswara Rao, Multi-functional gallium arsenide nanoparticles and nanostructures fabricated using picosecond laser ablation, Applied Surface Science, 589 (2022) 152802.

[49] M. Akkanaboina, D. Banerjee, K.R. Kumar, R.S.P. Goud, V.R. Soma, S.V.S.N. Rao, Gold nanoparticles coated LIPSS on GaAs for trace detection of RDX and Tetryl, Surfaces and Interfaces, 36 (2023) 102563.

[50] S. Almaviva, S. Botti, L. Cantarini, R. Fantoni, S. Lecci, A. Palucci, A. Puiu, A. Rufoloni, Ultrasensitive RDX detection with commercial SERS substrates, Journal of Raman Spectroscopy, 45 (2013) 41-46.

[51] N.A. Hatab, G. Eres, P.B. Hatzinger, B.H. Gu, Detection and analysis of cyclotrimethylenetrinitramine (RDX) in environmental samples by surface-enhanced Raman spectroscopy, Journal of Raman Spectroscopy, 41 (2010) 1131-1136.

[52] A. Hakonen, K. Wu, M. Stenbaek Schmidt, P.O. Andersson, A. Boisen, T. Rindzevicius, Detecting forensic substances using commercially available SERS substrates and handheld Raman spectrometers, Talanta, 189 (2018) 649-652.

[53] T.S. Wang, Q.T. Zheng, A.N. Zhu, Y. Wang, X.Y. Guo, X.L. Liu, Y. Ying, Y.P. Wu, Y. Wen, H.F. Yang, Construction of Jaffe reaction-based SERS chip for determination of trace picric acid, Sensor Actuat B-Chem, 368 (2022) 132201.

[54] M. Akkanaboina, D. Banerjee, K.R. Kumar, R.S.P. Goud, V.R. Soma, S.N. Rao, Sub-70 nm surface structures on femtosecond laser irradiated GaAs in distilled water and sensing application, Optics Letters, 48 (2023) 5539-5542.

[55] T. Liyanage, A. Rael, S. Shaffer, S. Zaidi, J.V. Goodpaster, R. Sardar, Fabrication of a self-assembled and flexible SERS nanosensor for explosive detection at parts-per-quadrillion levels from fingerprints, Analyst, 143 (2018) 2012-2022.

[56] S.S.B. Moram, C. Byram, S.N. Shibu, B.M. Chilukamarri, V.R. Soma, Ag/Au Nanoparticle-Loaded Paper-Based Versatile Surface-Enhanced Raman Spectroscopy Substrates for Multiple Explosives Detection, ACS Omega, 3 (2018) 8190-8201.

[57] M.S. Satya Bharati, B. Chandu, S.V. Rao, Explosives sensing using Ag-Cu alloy nanoparticles synthesized by femtosecond laser ablation and irradiation, RSC Adv, 9 (2019) 1517-1525.

[58] D. Banerjee, S.S.B. Moram, C. Byram, J. Rathod, T. Jena, G.K. Podagatlapalli, V.R. Soma, Plasmon-enhanced ultrafast and tunable thermo-optic nonlinear optical properties of femtosecond laser ablated TiO_2 and Silver-doped TiO_2 nanoparticles, Applied Surface Science, 569 (2021) 151070.

[59] N.K. Katturi, G. Reddy, C. Biswas, S.S. Kumar Raavi, L. Giribabu, V.R. Soma, Ultrafast nonlinear optical properties and excited-state dynamics of Soret-band excited D-π-D porphyrins, Optical Materials, 107 (2020) 110041.

[60] S.K. Nayak, M.S. Ahmed, M. Velpandian, P. Meduri, J. Rathod, V.R. Soma, S.S.K. Raavi, Exotic femtosecond nonlinear optical properties of laser ablated MoS2 quantum dots, Optical Materials, 147 (2024) 114630.

[61] S. Edappadikkunnummal, S.N. Nherakkayyil, V. Kuttippurath, D.M. Chalil, N.R. Desai, C. Keloth, Surface Plasmon Assisted Enhancement in the Nonlinear Optical Properties of Phenothiazine by Gold Nanoparticle, The Journal of Physical Chemistry C, 121 (2017) 26976-26986.

[62] M. Kauranen, A.V. Zayats, Nonlinear plasmonics, Nature Photonics, 6 (2012) 737-748.

[63] B. Park, D. Lee, H.-s. Kim, Y. Cho, S. Park, C. Kim, T. Lee, D.H. Woo, J.H. Kim, Synergetic enhancement in optical nonlinearity of Au nanoparticle decorated MoS2 via interaction between excitonic and surface plasmon resonances, Applied Surface Science, 532 (2020) 147486.

[64] N. Pinçon, B. Palpant, D. Prot, E. Charron, S. Debrus, Third-order nonlinear optical response of Au:SiO_2 thin films: Influence of gold nanoparticle concentration and morphologic parameters, The European Physical Journal D - Atomic, Molecular, Optical and Plasma Physics, 19 (2002) 395-402.

[65] S.I. Kudryashov, P.A. Danilov, S.G. Bezhanov, A.A. Rudenko, A.A. Ionin, S.A. Uryupin, S.F. Umanskaya, N.A. Smirnov, Plasmon-Enhanced Two-Photon Absorption of Infrared Femtosecond Laser Pulses in Thin Gold Films, JETP Letters, 109 (2019) 382-386.

[66] X. Tian, R. Wei, D. Yang, J. Qiu, Paradoxical combination of saturable absorption and reverse-saturable absorption in plasmon semiconductor nanocrystals, Nanoscale Advances, 2 (2020) 1676-1684.

[67] H. Yu, Y. Peng, Y. Yang, Z.-Y. Li, Plasmon-enhanced light–matter interactions and applications, npj Computational Materials, 5 (2019) 45.

[68] M. Valenti, A. Venugopal, D. Tordera, M.P. Jonsson, G. Biskos, A. Schmidt-Ott, W.A. Smith, Hot Carrier Generation and Extraction of Plasmonic Alloy Nanoparticles, ACS Photonics, 4 (2017) 1146-1152.

[69] S.I. Kudryashov, A.A. Samokhvalov, S.N. Shelygina, N.I. Busleev, A.K. Ivanova, N.A. Smirnov, S.G. Bezhanov, S.A. Uryupin, A.A. Ionin, V.P. Veiko, Ultrafast Broadband Diagnostics of the Filling of the s Band at the Two-Photon Femtosecond Laser Excitation of a Gold Film, JETP Letters, 110 (2019) 250-253.

[70] C. Lee, Y. Park, J.Y. Park, Hot electrons generated by intraband and interband transition detected using a plasmonic Cu/TiO_2 nanodiode, RSC Adv, 9 (2019) 18371-18376.

[71] S.I. Kudryashov, A.A. Samokhvalov, S.N. Shelygina, V.P. Veiko, Tuning of localized plasmon resonance in colloidal gold nano-particles by ultrafast interband photoinjection of free carriers: Superplasmonic states?, Applied Physics Letters, 115, 161903 (2019).

[72] P. Lama, A. Suslov, A.D. Walser, R. Dorsinville, Plasmon assisted enhanced nonlinear refraction of monodispersed silver nanoparticles and their tunability, Optics Express, 22 (2014) 14014-14021.

[73] S. Biswas, A. Kole, C. Tiwary, P. Kumbhakar, Enhanced nonlinear optical properties of graphene oxide–silver nanocomposites measured by Z-scan technique, RSC advances, 6 (2016) 10319-10325.

[74] V. Mamidala, G. Xing, W. Ji, Surface Plasmon Enhanced Third-Order Nonlinear Optical Effects in Ag− Fe_3O_4 Nanocomposites, The Journal of Physical Chemistry C, 114 (2010) 22466-22471.

[75] K.N. Krishnakanth, B. Chandu, M.S.S. Bharathi, S.S.K. Raavi, S.V. Rao, Ultrafast excited state dynamics and femtosecond nonlinear optical properties of laser fabricated Au and Ag Au nanoparticles, Optical Materials, 95 (2019) 109239.

[76] T.E. Karam, H.T. Smith, L.H. Haber, Enhanced Photothermal Effects and Excited-State Dynamics of Plasmonic Size-Controlled Gold-Silver-Gold Core-Shell-Shell Nanoparticles, J Phys Chem C, 119 (2015) 18573-18580.

[77] X. Zhang, C. Huang, M. Wang, P. Huang, X. He, Z. Wei, Transient localized surface plasmon induced by femtosecond interband excitation in gold nanoparticles, Sci Rep, 8 (2018) 10499.

[78] S. Link, C. Burda, M. Mohamed, B. Nikoobakht, M. El-Sayed, Femtosecond transient-absorption dynamics of colloidal gold nanorods: Shape independence of the electron-phonon relaxation time, Physical Review B, 61 (2000) 6086.

[79] M. Zhou, C. Zeng, Y. Chen, S. Zhao, M.Y. Sfeir, M. Zhu, R. Jin, Evolution from the plasmon to exciton state in ligand-protected atomically precise gold nanoparticles, Nat Commun, 7 (2016) 13240.

[80] S.K. Sengar, B.R. Mehta, Govind, Size and alloying induced shift in core and valence bands of Pd-Ag and Pd-Cu nanoparticles, J Appl Phys, 115 (2014) 124301.

[81] A.M. Brown, R. Sundararaman, P. Narang, A.M. Schwartzberg, W.A. Goddard, H.A. Atwater, Experimental and Ab Initio Ultrafast Carrier Dynamics in Plasmonic Nanoparticles, Phys Rev Lett, 118 (2017) 087401.

[82] C. Voisin, D. Christofilos, P.A. Loukakos, N. Del Fatti, F. Vallée, J. Lermé, M. Gaudry, E. Cottancin, M. Pellarin, M. Broyer, Ultrafast electron-electron scattering and energy exchanges in noble-metal nanoparticles, Physical Review B, 69 (2004).

[83] T. Higaki, M. Zhou, K.J. Lambright, K. Kirschbaum, M.Y. Sfeir, R. Jin, Sharp Transition from Nonmetallic Au(246) to Metallic Au(279) with Nascent Surface Plasmon Resonance, J Am Chem Soc, 140 (2018) 5691-5695.

[84] T.S. Ahmadi, S.L. Logunov, M.A. El-Sayed, Picosecond Dynamics of Colloidal Gold Nanoparticles, The Journal of Physical Chemistry, 100 (1996) 8053-8056.

[85] M. Perner, P. Bost, U. Lemmer, G. von Plessen, J. Feldmann, U. Becker, M. Mennig, M. Schmitt, H. Schmidt, Optically Induced Damping of the Surface Plasmon Resonance in Gold Colloids, Physical Review Letters, 78 (1997) 2192-2195.

[86] S. Link, C. Burda, Z.L. Wang, M.A. El-Sayed, Electron dynamics in gold and gold–silver alloy nanoparticles: The influence of a nonequilibrium electron distribution and the size dependence of the electron–phonon relaxation, The Journal of Chemical Physics, 111 (1999) 1255-1264.

[87] H. Zheng, M.A. Tofanelli, C.J. Ackerson, K.L. Knappenberger, Composition-dependent electronic energy relaxation dynamics of metal domains as revealed by bimetallic Au144-xAgx(SC8H9)60 monolayer-protected clusters, Phys Chem Chem Phys, 19 (2017) 14471-14477.

[88] Q. Darugar, W. Qian, M.A. El-Sayed, M.-P. Pileni, Size-dependent ultrafast electronic energy relaxation and enhanced fluorescence of copper nanoparticles, The Journal of Physical Chemistry B, 110 (2006) 143-149.

[89] A. Gaál, I. Bugár, I. Capek, L. Fialová, T. Pálszegi, V. Szöcs, A. Šatka, F. Uherek, Femtosecond multicolor transient absorption spectroscopy of colloidal silver nanoparticles, Laser Physics, 19 (2009) 961-968.

[90] S. Yanagiya, T. Takahata, Y. Yoshitani, R. Kawakami, A. Furube, Steady-State and Time-Resolved Optical Properties of Multilayer Film of Titanium Dioxide Sandwiched by Gold Nanoparticles and Gold Thin Film, Chemnanomat, 5 (2019) 1015-1020.

[91] G. Soavi, S. Dal Conte, C. Manzoni, D. Viola, A. Narita, Y. Hu, X. Feng, U. Hohenester, E. Molinari, D. Prezzi, K. Mullen, G. Cerullo, Exciton-exciton annihilation and biexciton stimulated emission in graphene nanoribbons, Nat Commun, 7 (2016) 11010.

[92] J. Saroha, N.P. Lalla, M. Kumar, S.N. Sharma, Ultrafast transient absorption spectroscopic studies on the Impact of growth time on size, stability, and optical characteristics of colloidal gold nanoparticles, Optik, 268 (2022) 169759.

Intentional Blank Page

5B

Preliminary Studies Involving Femtosecond Vortex beam-metal Interaction and Its Initial Application in SERS-based Sensing

Abstract

Optical vortex beams have recently gained much attention as they offer a novel mode of laser-matter interaction. This study showcases the fabrication of silver nanostructures (NS) using an 800 nm, ~50 femtosecond (fs), 1 kHz vortex beam. The modified surface was analyzed by performing single spot ablation and a complete raster scan to investigate the VB profile imprint, which led to the development of the full NS. The intrinsic nanoscale topographical characteristics of the NS were thoroughly examined using a field emission scanning electron microscope (FESEM). The formation of spherical/ aspherical nanogrowths in the ablation lines and the irregular, immature laser-induced periodic surface structures (LIPSS) have been seen inside the ablation lines. In addition, the Ag NS generated by VB showed exceptional effectiveness when employed as a plasmonic SERS-active substrate for detecting explosives. Our investigation determined that we could identify Tetryl (an explosive molecule) at a concentration of 500 nM and ammonium nitrate (AN) at 5 μM (lowest detectable traces). The enhancement factor for detection was calculated to be around 10^4-10^5. This chapter overviews our preliminary findings on the interaction of fs VB-metal surfaces and their sensing response. A graphical abstract image of the work done in this chapter is presented in the following section.

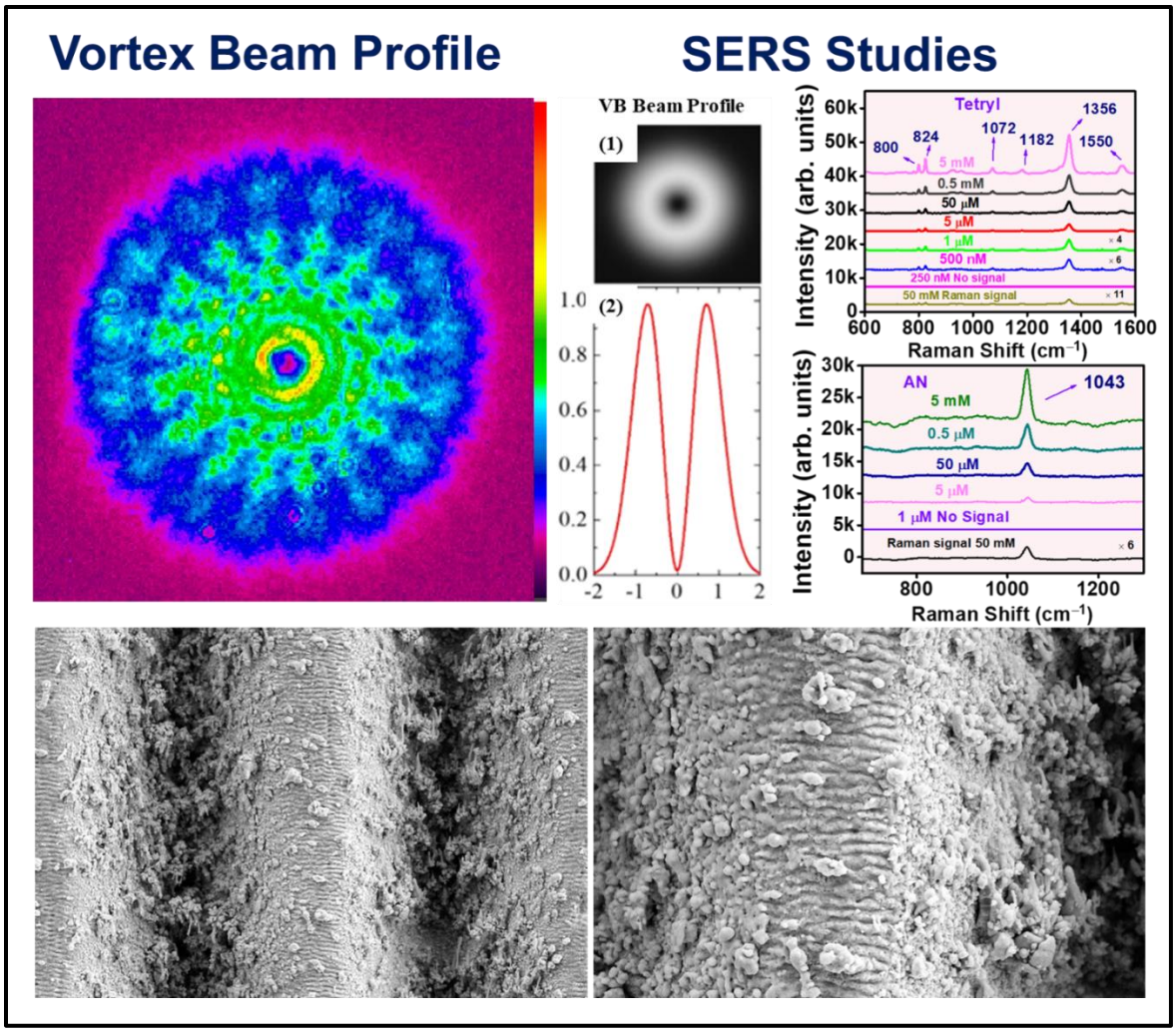

The work presented in this chapter has been published in,

1. Preliminary Studies involving Femtosecond Vortex beam-metal interaction and Its Initial Application in SERS-based Sensing (Manuscript under preparation, 2024).

5B.1. Introduction

The field of surface engineering in materials is of great importance due to the increasing interest in the micro-machining of metals, semiconductors, and insulators and their numerous applications. This interest is driven by the many applications (mentioned extensively in previous chapters) that may be achieved by manipulating the characteristics of the treated surfaces. The preceding chapters have examined the interaction of femtosecond (fs) Bessel beams and Gaussian beams with metal surfaces, resulting in LIPSS, alloy nanocolloids, and notable sensing applications based on SERS. This chapter focuses on the examination of fs vortex beams. Vector vortex beams [1] have recently been a topic of significant interest due to their potential in laser-matter interactions and associated applications [2,3]. Vortex beams possess distinct characteristics, [4,5] such as helical wavefronts[6,7], a doughnut-shaped spatial form resulting from a phase singularity [8], and orbital angular momentum [9,10], which differentiates them from standard Gaussian beams [11–17]. Due to their distinctive characteristics, VBs have garnered significant attention in several scientific domains, including optical tweezers, particle entrapment, and material processing.

Before delving into our experiments with OV beams, providing a brief overview of the existing literature about material processing utilizing this kind of VB is prudent. The capacity of the VB laser ablation has been shown in several experiments. Recently, in some reports by Hnatovsky et al. [18,19], VB beams were used in laser surface structuring and created subwavelength annular ring structures on silicon and glass. In similar studies, the formation of surface microstructures has been reported on stainless steel, silicon, and copper [13,14,16,17]. Toyoda et al. [10] observed a rotational phenomenon in metal when exposed to a VB. This rotation was induced by the transfer of helicity from the optical vortex to the melted material and was facilitated by the formation of chiral nanoneedles by ablation. In addition, manipulating the nanoneedles' chirality was achieved simply by altering the sign of the optical vortex helicity. A recent study by Ablez et al. [20] showed that aluminum (Al) might undergo nanoscale twisting when exposed to a single picosecond optical vortex pulse with low energy close to the ablation threshold. This twisting is attributed to the transfer of orbital angular momentum (OAM). The study demonstrated that the twisting needle may be readily converted into a microscale non-twisting needle by depositing overlapping optical vortex pulses. Using a high-energy laser pulse with a picosecond/nanosecond duration and at mJ energy level allowed for creating a small-scale needle. Additionally, they forecasted that the

nano/microstructure of aluminum would bring a fresh understanding of the interplay between orbital angular momentum (OAM) and materials. Furthermore, the report presented a novel approach for creating UV plasmonic devices at the nano/micro scale. Additional findings from Meier et al.'s study [21] indicated that when using nanosecond laser pulses on materials including stainless steel, brass, and copper, both azimuthal and radial polarizations are more effective in creating precise, deep holes compared to a Gaussian beam with linear or circular polarization. In a separate study, Yoo et al. [22] demonstrated that when a laser beam with a toroidal shape interacts with an amorphous silicon film on a fused silica substrate, it causes molten silicon to gather at the centre of the beam. This leads to the formation of a nano dome with a significantly greater height through a process known as thermocapillary-induced dewetting. The rapid melting and solidification process is accountable for the transition of the amorphous structure into a crystalline one [22]. Takahashi et al. [23] conducted a picosecond laser study to show the creation of a single-crystal silicon needle that was recrystallized by exposure to a picosecond vortex pulse. The height of the needle was increased by overlaying several vortex pulses over the target, resulting in a height of roughly 40 μm after 12 consecutive pulses [23]. When subjected to the fs vector field with various topological charges, the silicon surface exhibits distinct rippling patterns. These patterns consistently prefer a direction perpendicular to the laser polarization. Additionally, the surface shows the development of intricate quasi-periodic patterns. This phenomenon has been seen in previous research [17] by Lou et al.. In a recent study by Tsibidis et al. [24], the researchers examined the surface profile and periodicity of the ripples created when Nickel was exposed to radially polarized femtosecond laser pulses. The study demonstrated that the incident beam's polarization substantially impacts both the shape and size of the resulting structures. Even further, Xu et al. [25] conducted computational and experimental studies to show the formation of strong supercontinuum vortices from femtosecond vortex beams using numerous thin fused silica plates. The supercontinuum vortices were reported to maintain the vortex phase profile of the original beam over spectral components spanning from 500 nm to 1200 nm. Nivas et al. [11,26] have established a method for directly creating surface structures using femtosecond laser technology. This method utilizes optical vortex beams with varying spatial distributions of polarization states, which may be readily created using a q-plate. An array of optical vortices with distinct states of an optical vortex was used to showcase the creation of multiple regular surface patterns on silicon. The spatial characteristics of the regular rippled and grooved surface textures were linked to the

polarization state of the optical vortex beam. Nakamura et al. [27] conducted a radiation hydrodynamic simulation to illustrate the formation of microcone formations on silicon (Si) substrates by the ablation of optical vortex pulses. Single pulse irradiation on the Si substrate resulted in the formation of doughnut-shaped craters. Additionally, a twisted cone structure with a height of 3.5 µm was developed in the centre of the irradiation location by the circularly polarized optical vortex pulse.

The data presented in this chapter uses a vortex phase plate to generate a VB from 50 fs, 800 nm. 1 kHz Gaussian beam. We have performed initial studies like single spot ablation and a raster scan on the Ag surface. We attempted to explore the nanoscale topography of the NSs formed via fs VB interaction. SERS-based sensing studies were also conducted to detect traces of hazardous explosives like Tetryl and ammonium nitrate (AN).

5B.2. Experimental details

The process of femtosecond laser ablation in the air (LAA) was performed using a vortex beam profile. A vortex phase plate (VPP) [28–31] was used to convert a Gaussian beam (GB) input into a vortex beam (VB). The main purpose of this device is to adjust the phase of the beam that goes through it. The phase plate is identified by the following specifications: serial number VL-209-800-Y-A with a thickness of 3 mm, operating at a wavelength of 800 nm, has a topological charge of 1, and possesses an anti-reflective (AR) coating. The material used is fused silica, and the element size was 25.4 mm. After cleaning the silver target in an ultrasonic wash, they proceeded with the VB interacted ablation procedure. Ablation was performed using a time-limited approach, with a duration of 2 seconds and an exposure of 2000 fs pulses. This was followed by a full ablation using a laser raster scan. The procedure used two X-Y stages and a LabVIEW interfaced motion controller (ESP 300, Newport, USA). The laser ablation parameters were set to provide 3300 pulses per millimeter, with a scan speed of 0.3 millimeters per second and an inter-line spacing of 40 micrometers during the raster scan. Therefore, a sizable Ag NS region (3 mm x 3 mm) was created by VB ablation. We used a field emission scanning electron microscope (FESEM, ZEISS ULTRA 55) to examine the surface characteristics and composition of nanostructures. Additionally, we conducted energy dispersive x-ray spectroscopy (EDX) to analyze the elements present. The SERS measurements were conducted using a portable Raman system, the i-Raman

plus model from B&W Tek in the USA. The system had an excitation wavelength of 785 nm, a power output of 102 mW, and a spot size of about 90 μm. Each measurement had an accumulation period of 5 seconds and a spectral average of three.

5B.3. Results & Discussion

Before performing the fs ablation, the Gaussian beam was transformed into a vortex beam, and after aligning it, it passed through the VPP. A plano-convex lens has been used after the VPP to focus the vortex beam for ablation. The experimental setup has been depicted in Figure 5B.1(a). The beam profile has been analyzed using a beam profiler [Spiricon, Model # BGP-USB-L11059, USA]. The beam profile image has been shown in Figure 5B.1(b). The pulse energy used in the experiment was 50 μJ with a 1 kHz laser repetition rate. This generated 1.8 μJ/cm^2 peak fluence [32,33] corresponding to the VB after the VPP.

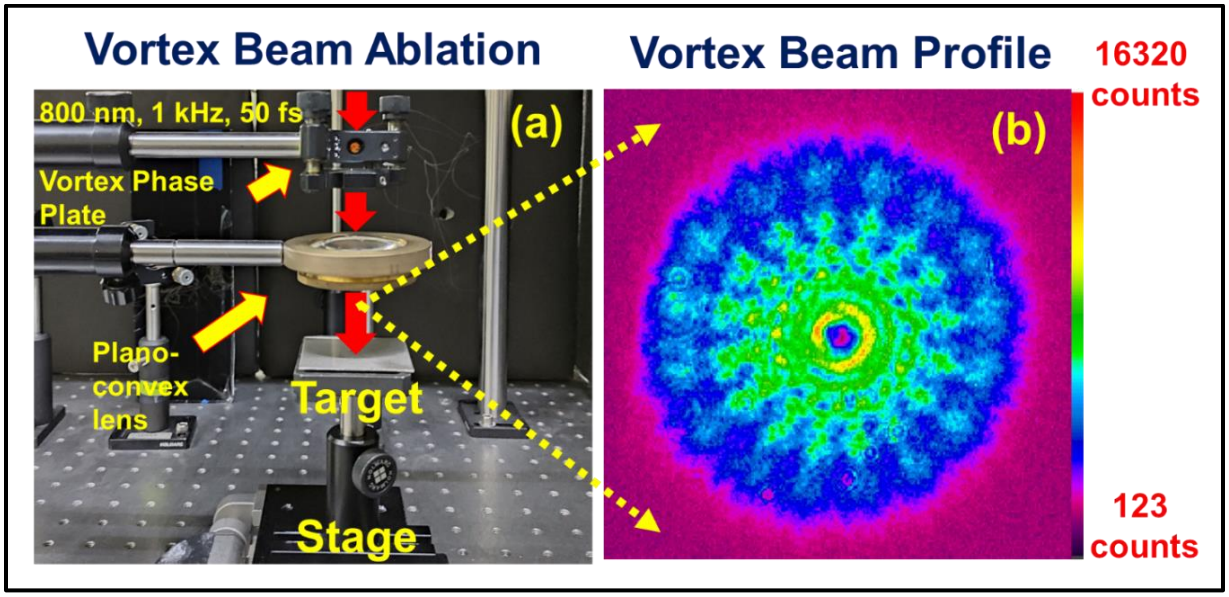

Figure 5B. 1 (a) Experimental setup engaging vortex phase plate and a plano-convex lens (b) VB profile captured in a beam profiler.

5B.3.1 Single spot ablation imprint using femtosecond vortex beam

After verifying the created vortex beam profile, we executed single-spot ablation using the same profile. A noticeable beam profile imprint was detected on the ablation site of the Ag substrate surface [Figure 5B.2(a)]. This impression was caused by around 2000 pulses (exposure time - 2 seconds) interacting with the surface. The formation of two lobes (ablated holes), with ablated

portions in between, was noticed in the FESEM image of the single spot irradiated region. The ablation spot length was found to be ~ 44 µm, taking the two lobes into account. Nivas et al. have reported the 2D map of the VB profile generated from the simulation, shown in Figure 5B.2b(1). The normalized intensity profiles along the diameter for the VB have been presented from the report mentioned above in Figure 5B.2b(2). The topographical profile of the single spot imprint matches well with the intensity profile of VB, presented in Figure 5B.2b(2). The asymmetricity of the two lobes found in Figure 5B.2(a) may be attributed to slight angular variation in the alignment. Subsequently, creating this topographical characteristic in a specific location motivated the urge to create a larger area NS with a raster scan process.

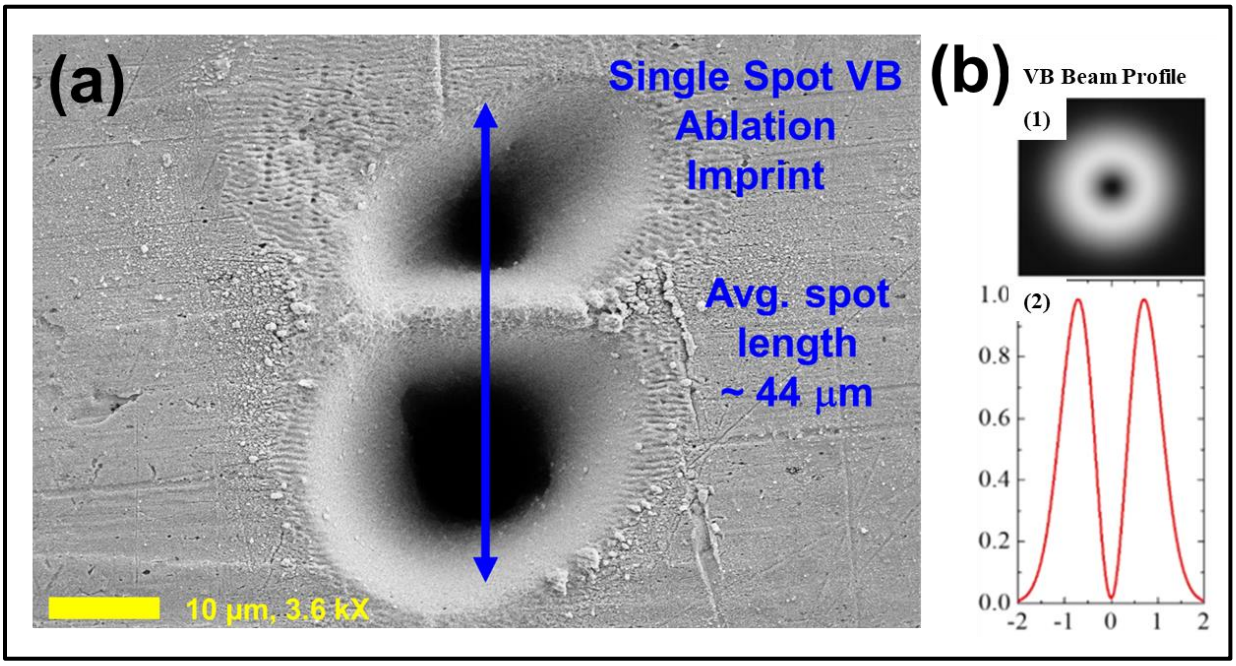

Figure 5B. 2 (a) Single spot ablation with fs VB engaging 2000 pulses for 2 seconds of exposure time (b1) 2D map of the theoretically simulated VB profile (b2) normalized intensity profiles along the diameter for the VB beam. The (b1, b2) images are adapted from Ref. 33.

5B.3.2 Nanostructure prepared using large area raster scan

After raster scanning with the focused VB, the nanoscale features of the structured surface were examined meticulously. The structured surface's nanoscale characteristics were thoroughly investigated through FESEM after raster scanning using the focussed VB. Figure 5B.3(a) displays an image of the entire structured surface, covering an area of (3 µm × 3 µm). Figure 5B.3(b) shows an enlarged portion of it. Figures 5B.3(c) and 5B.3(d) show more detailed pictures at

magnifications of 4 kX and 10 kX, respectively. Nano growths of arbitrary shapes have been seen inside the ablated lines created by the focused laser. The successive ablation performed by the two high-intensity lobes [seen in Figure 5B.2] through each ablation line can be considered the reason behind the formation of such features. Here, irregular and immature formation of Laser-induced periodic surface structures (LIPSS) patterns have been observed between two consecutive laser-ablated lines. Further studies and optimizations are required to completely understand these results, which is a part of our future plan. EDX investigations were also conducted to determine the elemental compositions and also to find out the oxidation on the NSs generated following ablation. The produced NSs exhibited a significant content of Ag (94% by weight) and Oxygen (6%). The complete EDX data is shown in Figure 5B.4.

5B.3.3. Sensing studies based on SERS

The discovery of surface-enhanced Raman scattering has marked a remarkable achievement and enabled progress in spectroscopy, analytical photonics, and sensing. [34] Various comprehensive investigations have already been carried out on the plasmon-enhanced SERS technique in the sensing field. [35–43] Our study aimed to evaluate the efficacy of the Ag NS produced by VB as on-chip SERS substrates. Hence, the primary emphasis was placed on using the SERS technique to identify explosive substances. [39,42–50], namely Tetryl (CE- 2,4,6-trinitrophenylmethylnitramine) and ammonium nitrate (NH_4NO_3) (AN). The VB-ablated Ag NS was a highly plasmonic substrate for SERS to detect trace levels of the listed hazardous substances. Figure 5B.5(a) depicts the SERS signal data for Tetryl, showing its dependence on concentration. The minimal detectable concentration is 500 nM. The molecule's distinctive Raman peaks were identified at 824 cm^{-1}, 1182 cm^{-1}, and 1356 cm^{-1} over a range of concentrations from 500 nM to 5 mM. No detectable peaks were seen at the dose of 250 nM. The main distinguishing Raman mode features of Tetryl are attributed to the non-symmetrical stretching of NO_2 at 1356 cm^{-1} and the vibrations of nitro-aromatic compounds at 824 cm^{-1} [51].

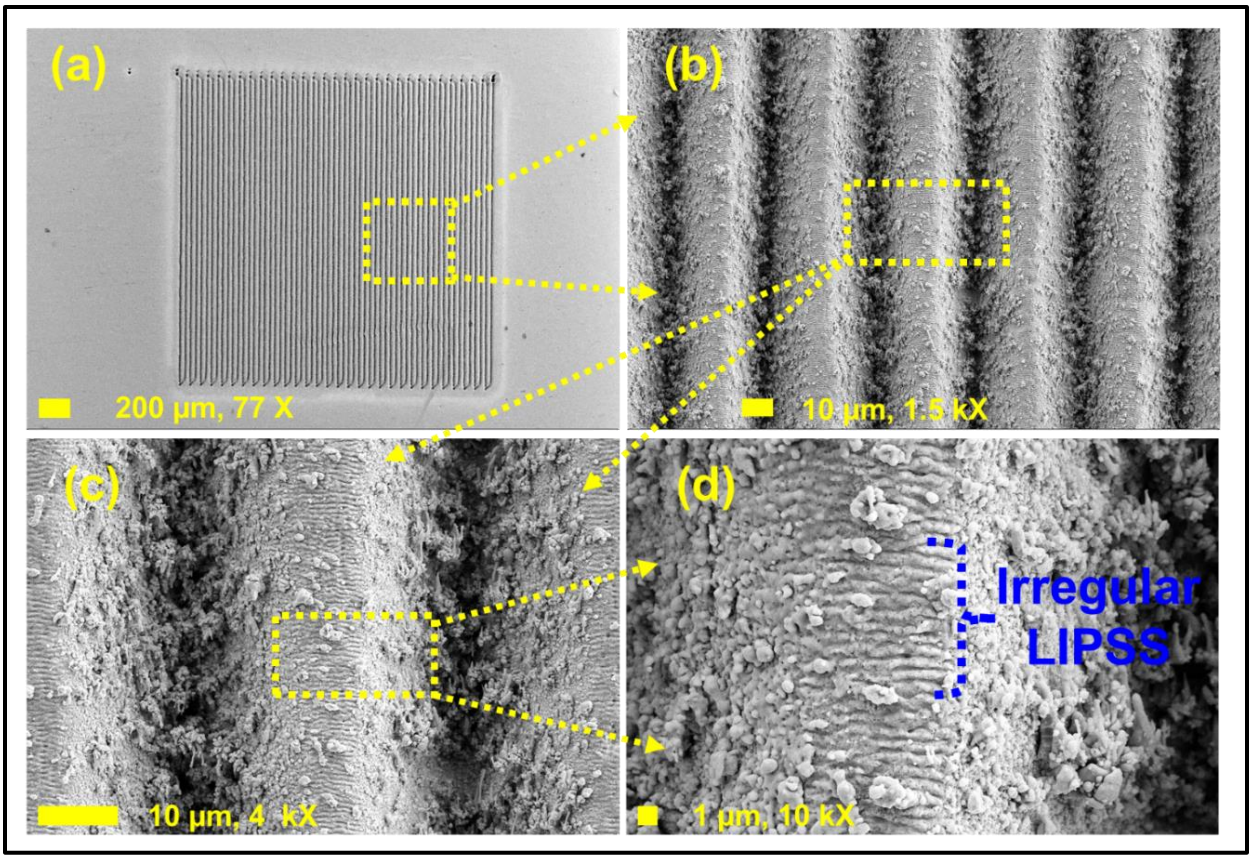

Figure 5B. 3 FESEM images of the VB ablated Ag NSs. (a) Image of the complete structure (b) lower magnification (1.5 kX) images of the NS showing the laser ablated lines. (c, d) higher magnification (4 kX, 10 kX) images showing immature LIPSS formation.

To evaluate the consistency of the SERS signal generated by the Ag NS, over 30 SERS spectra were acquired from several random positions. The RSD of the SERS signals for the 1357 cm^{-1} peak of the chemical Tetryl at a concentration of 5 µM was ~26%, according to the data presented in Figure 5B.5(b). Similarly, Figure 5B.5(c) displays the concentration-dependent SERS data of AN. The minimum detectable concentration of AN was determined to be 5 µM. AN exhibited a characteristic peak at 1043 cm^{-1}, which corresponds to the symmetric stretching mode of NO_3 [40,52,53]. The RSD of the SERS signals for the 1043 cm^{-1} peak of AN at a concentration of 5 mM was around 23% [see Figure 5B.5(d)]. Using standard calculation, the estimated enhancement factors of Tetryl (500 nM) and AN (5 'M) were 3.8×10^5 and 2.5×10^4, respectively. [54,55] These results open up the potential of these VB-structured substrates for sensing applications.

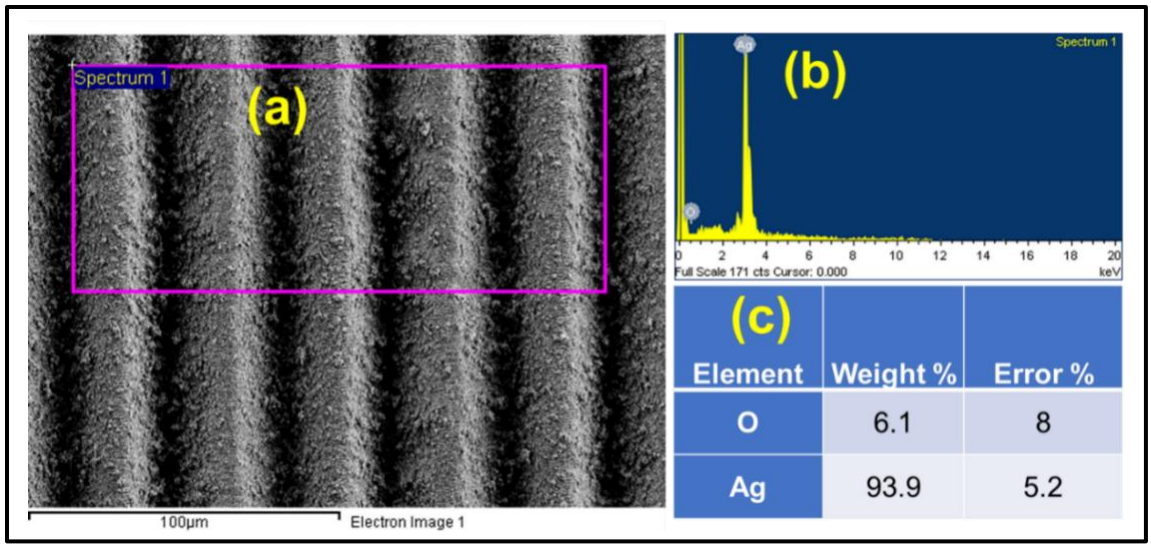

Figure 5B. 4 EDX data of the fabricated Ag NS (a, b) EDX spectra of the same showing Ag and O peaks (c) Table showing the elemental analysis.

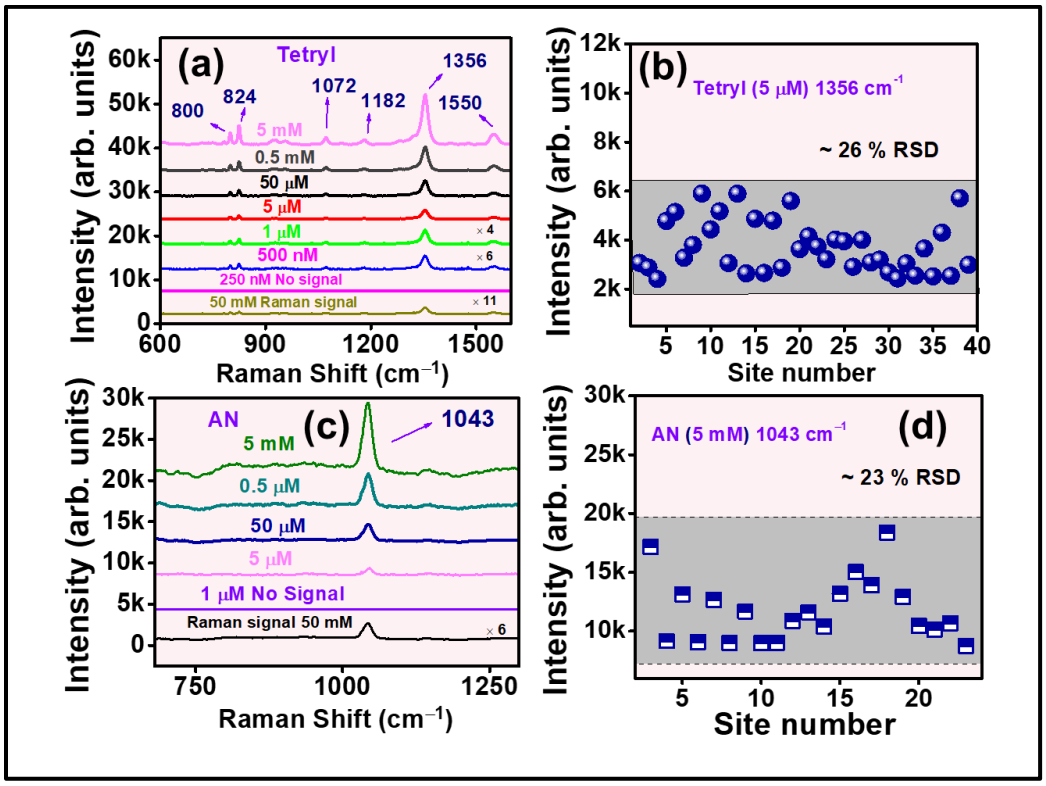

Figure 5B. 5 (a) Concentration-dependent SERS spectra of Tetryl collected by VB ablated Ag NS, along with pure Raman spectrum (in dark yellow colour) of Tetryl (50 mM) collected from unablated pristine Ag surface, (b) Reproducibility spectra (with ~26% RSD) of Tetryl (5 µM), (c) Concentration-dependent SERS spectra of AN using VB ablated Ag NS, along with pure Raman spectrum (in black colour) of AN (50 mM) collected from unablated Ag pristine, (d) Reproducibility spectra (with ~23% RSD) of AN (5 mM). The portable Raman acquired the complete SERS data in this Figure, with the same acquisition parameters mentioned in the experimental details.

5B.4. Conclusions

This work demonstrates the production of Ag NSs with a femtosecond vortex beam. The VB profile imprint on the surface was examined using single spot ablation and comprehensive raster scanning, forming the entire NS. The inherent nanoscale topographical features of the NS were extensively analyzed using FESEM. The creation of nanogrowths features within the ablation lines may be attributed to the consecutive ablation conducted by the two high-intensity lobes, as seen in Figure 5B.2. Irregular and immature LIPSS have been seen inside the ablation lines. Future experiments will be conducted to optimize these NSs better. Furthermore, the Ag NS produced by VB demonstrated remarkable efficacy when used as a plasmonic, SERS-active substrate for detecting explosives. Our analysis found that we could detect 500 nM Tetryl and 5 μM AN as the lowest trace, with enhancement factors in the range of 10^4-10^5. This chapter presents our preliminary results obtained on fs VB-metal surface interaction. Further detailed experiments are required to optimize the NSs and their SERS performance. This work on VB-metal interaction has potential applications in several scientific fields, including sensing, bio-medical applications, and nanophotonics.

References

[1] L. Marrucci, C. Manzo, D. Paparo, Optical Spin-to-Orbital Angular Momentum Conversion in Inhomogeneous Anisotropic Media, Phys. Rev. Lett. 96 (2006) 163905. https://doi.org/10.1103/PhysRevLett.96.163905.

[2] M. Duocastella, C.B. Arnold, Bessel and annular beams for materials processing, Laser Photon. Rev. 6 (2012) 607–621. https://doi.org/https://doi.org/10.1002/lpor.201100031.

[3] E.G. Gamaly, A. V Rode, Physics of ultra-short laser interaction with matter: From phonon excitation to ultimate transformations, Prog. Quantum Electron. 37 (2013) 215–323. https://doi.org/https://doi.org/10.1016/j.pquantelec.2013.05.001.

[4] F. Cardano, E. Karimi, S. Slussarenko, L. Marrucci, C. de Lisio, E. Santamato, Polarization pattern of vector vortex beams generated by q-plates with different topological charges, Appl. Opt. 51 (2012) C1–C6. https://doi.org/10.1364/AO.51.0000C1.

[5] Q. Zhan, Cylindrical vector beams: from mathematical concepts to applications, Adv. Opt. Photonics. 1 (2009) 1–57. https://doi.org/10.1364/AOP.1.000001.

[6] F. Cardano, L. Marrucci, Spin–orbit photonics, Nat. Photonics. 9 (2015) 776–778. https://doi.org/10.1038/nphoton.2015.232.

[7] L. Marrucci, E. Karimi, S. Slussarenko, B. Piccirillo, E. Santamato, E. Nagali, F. Sciarrino, Spin-to-orbital conversion of the angular momentum of light and its classical and quantum applications, J. Opt. 13 (2011) 64001. https://doi.org/10.1088/2040-8978/13/6/064001.

[8] R. Dorn, S. Quabis, G. Leuchs, Sharper Focus for a Radially Polarized Light Beam, Phys. Rev. Lett. 91 (2003) 233901. https://doi.org/10.1103/PhysRevLett.91.233901.

[9] K. Toyoda, F. Takahashi, S. Takizawa, Y. Tokizane, K. Miyamoto, R. Morita, T. Omatsu, Transfer of light helicity to nanostructures, Phys. Rev. Lett. 110 (2013) 143603.

[10] K. Toyoda, K. Miyamoto, N. Aoki, R. Morita, T. Omatsu, Using Optical Vortex To Control the Chirality of Twisted Metal Nanostructures, Nano Lett. 12 (2012) 3645–3649. https://doi.org/10.1021/nl301347j.

[11] J. JJ Nivas, S. He, A. Rubano, A. Vecchione, D. Paparo, L. Marrucci, R. Bruzzese, S. Amoruso, Direct Femtosecond Laser Surface Structuring with Optical Vortex Beams Generated by a q-plate, Sci. Rep. 5 (2015) 17929. https://doi.org/10.1038/srep17929.

[12] J. Ouyang, W. Perrie, O.J. Allegre, T. Heil, Y. Jin, E. Fearon, D. Eckford, S.P. Edwardson, G. Dearden, Tailored optical vector fields for ultrashort-pulse laser induced complex surface plasmon structuring, Opt. Express. 23 (2015) 12562–12572. https://doi.org/10.1364/OE.23.012562.

[13] K.K. Anoop, A. Rubano, R. Fittipaldi, X. Wang, D. Paparo, A. Vecchione, L. Marrucci, R.

Bruzzese, S. Amoruso, Femtosecond laser surface structuring of silicon using optical vortex beams generated by a q-plate, Appl. Phys. Lett. 104 (2014) 241604. https://doi.org/10.1063/1.4884116.

[14] K.K. Anoop, R. Fittipaldi, A. Rubano, X. Wang, D. Paparo, A. Vecchione, L. Marrucci, R. Bruzzese, S. Amoruso, Direct femtosecond laser ablation of copper with an optical vortex beam, J. Appl. Phys. 116 (2014) 113102. https://doi.org/10.1063/1.4896068.

[15] O.J. Allegre, Y. Jin, W. Perrie, J. Ouyang, E. Fearon, S.P. Edwardson, G. Dearden, Complete wavefront and polarization control for ultrashort-pulse laser microprocessing, Opt. Express. 21 (2013) 21198–21207. https://doi.org/10.1364/OE.21.021198.

[16] Y. Jin, O.J. Allegre, W. Perrie, K. Abrams, J. Ouyang, E. Fearon, S.P. Edwardson, G. Dearden, Dynamic modulation of spatially structured polarization fields for real-time control of ultrafast laser-material interactions, Opt. Express. 21 (2013) 25333–25343. https://doi.org/10.1364/OE.21.025333.

[17] K. Lou, S.-X. Qian, X.-L. Wang, Y. Li, B. Gu, C. Tu, H.-T. Wang, Two-dimensional microstructures induced by femtosecond vector light fields on silicon, Opt. Express. 20 (2012) 120–127. https://doi.org/10.1364/OE.20.000120.

[18] C. Hnatovsky, V.G. Shvedov, N. Shostka, A. V Rode, W. Krolikowski, Polarization-dependent ablation of silicon using tightly focused femtosecond laser vortex pulses, Opt. Lett. 37 (2012) 226–228. https://doi.org/10.1364/OL.37.000226.

[19] C. Hnatovsky, V.G. Shvedov, W. Krolikowski, A. V Rode, Materials processing with a tightly focused femtosecond laser vortex pulse, Opt. Lett. 35 (2010) 3417–3419. https://doi.org/10.1364/OL.35.003417.

[20] A. Ablez, K. Toyoda, K. Miyamoto, T. Omatsu, Nanotwist of aluminum with irradiation of a single optical vortex pulse, OSA Contin. 4 (2021) 403–408. https://doi.org/10.1364/OSAC.417444.

[21] M. Meier, V. Romano, T. Feurer, Material processing with pulsed radially and azimuthally polarized laser radiation, Appl. Phys. A. 86 (2007) 329–334. https://doi.org/10.1007/s00339-006-3784-9.

[22] J.-H. Yoo, J. Bin In, C. Zheng, I. Sakellari, R.N. Raman, M.J. Matthews, S. Elhadj, C.P. Grigoropoulos, Directed dewetting of amorphous silicon film by a donut-shaped laser pulse, Nanotechnology. 26 (2015) 165303. https://doi.org/10.1088/0957-4484/26/16/165303.

[23] F. Takahashi, K. Miyamoto, H. Hidai, K. Yamane, R. Morita, T. Omatsu, Picosecond optical vortex pulse illumination forms a monocrystalline silicon needle, Sci. Rep. 6 (2016) 21738. https://doi.org/10.1038/srep21738.

[24] G.D. Tsibidis, E. Skoulas, E. Stratakis, Ripple formation on nickel irradiated with radially

polarized femtosecond beams, Opt. Lett. 40 (2015) 5172–5175. https://doi.org/10.1364/OL.40.005172.

[25] L. Xu, D. Li, J. Chang, D. Li, T. Xi, Z. Hao, Powerful supercontinuum vortices generated by femtosecond vortex beams with thin plates, Photonics Res. 10 (2022) 802–809.

[26] J.J.J. Nivas, H.E. Shutong, K.K. Anoop, A. Rubano, R. Fittipaldi, A. Vecchione, D. Paparo, L. Marrucci, R. Bruzzese, S. Amoruso, Laser ablation of silicon induced by a femtosecond optical vortex beam, Opt. Lett. 40 (2015) 4611–4614.

[27] D. Nakamura, R. Tasaki, M. Kawamoto, H. Oshima, M. Higashihata, H. Ikenoue, T. Wakayama, A. Sunahara, T. Higashiguchi, Silicon twisted cone structure produced by optical vortex pulse with structure evaluation by radiation hydrodynamic simulation, Sci. Rep. 10 (2020) 20512.

[28] S.N. Khonina, A. V. Ustinov, V.I. Logachev, A.P. Porfirev, Properties of vortex light fields generated by generalized spiral phase plates, Phys. Rev. A. 101 (2020) 043829. https://doi.org/10.1103/PhysRevA.101.043829.

[29] V. V. Kotlyar, A.A. Kovalev, R. V. Skidanov, S.N. Khonina, O.Y. Moiseev, V.A. Soĭfer, Simple optical vortices formed by a spiral phase plate, J. Opt. Technol. 74 (2007) 686. https://doi.org/10.1364/jot.74.000686.

[30] T. Jankowski, N. Bennis, P. Morawiak, D.C. Zografopoulos, A. Pakuła, M. Filipiak, M. Słowikowski, J.M. López-Higuera, J.F. Algorri, Optical vortices by an adaptive spiral phase plate, Opt. Laser Technol. 176 (2024) 111029. https://doi.org/10.1016/j.optlastec.2024.111029.

[31] W. Wang, Y. Li, Z. Guo, R. Li, J. Zhang, A. Zhang, S. Qu, Ultra-thin optical vortex phase plate based on the metasurface and the angular momentum transformation, J. Opt. (United Kingdom). 17 (2015) 045102. https://doi.org/10.1088/2040-8978/17/4/045102.

[32] Y.-E. Li, J.-F. Kuo, C.-W. Cheng, A.-C. Lee, Efficient fabrication of high-quality hybrid periodic nanostructures on 4H-SiC using a single-step vector femtosecond laser processing, Opt. Laser Technol. 179 (2024) 111363.

[33] J.J. Nivas, S. Amoruso, Ultrafast laser surface structuring with Gaussian and Optical Vortex beam, Thesis submitted to Univ. Naples Federico II Italy. (2017) https://core.ac.uk/download/pdf/153401056.pdf.

[34] J. Langer, D. Jimenez de Aberasturi, J. Aizpurua, R.A. Alvarez-Puebla, B. Auguié, et al. Baumberg, Present and Future of Surface-Enhanced Raman Scattering, ACS Nano. 14 (2020) 28–117. https://doi.org/10.1021/acsnano.9b04224.

[35] A. Mangababu, R. Sai Prasad Goud, C. Byram, J. Rathod, D. Banerjee, V. Rao Soma, S.V.S. Nageswara Rao, Multi-functional gallium arsenide nanoparticles and nanostructures

fabricated using picosecond laser ablation, Appl. Surf. Sci. 589 (2022) 152802.

[36] M. Haribabu, B. Dipanjan, M.S.S. Bharati, J. Chelsea, A. Chandrasekhar, P. Kanaka raju, S. Venugopal Rao, S. Hamad, G. Krishna Podagatlapalli, Exciton-mediated surface-enhanced Raman studies of Aluminum doped platinum nano colloids, Opt. Mater. (Amst). 133 (2022) 113013. https://doi.org/10.1016/j.optmat.2022.113013.

[37] D. Banerjee, S.S.B. Moram, C. Byram, J. Rathod, T. Jena, G.K. Podagatlapalli, V.R. Soma, Plasmon-enhanced ultrafast and tunable thermo-optic nonlinear optical properties of femtosecond laser ablated TiO2 and Silver-doped TiO2 nanoparticles, Appl. Surf. Sci. 569 (2021) 151070. https://doi.org/10.1016/j.apsusc.2021.151070.

[38] M.S.S. Bharati, C. Byram, V.R. Soma, Femtosecond laser fabricated Ag@Au and Cu@Au alloy nanoparticles for surface enhanced raman spectroscopy based trace explosives detection, Front. Phys. 6 (2018) 1–13. https://doi.org/10.3389/fphy.2018.00028.

[39] G.K. Podagatlapalli, S. Hamad, S.V. Rao, Trace-Level Detection of Secondary Explosives Using Hybrid Silver-Gold Nanoparticles and Nanostructures Achieved with Femtosecond Laser Ablation, J. Phys. Chem. C. 119 (2015) 16972–16983. https://doi.org/10.1021/acs.jpcc.5b03958.

[40] M.S.S. Bharati, V.R. Soma, Flexible sers substrates for hazardous materials detection: Recent advances, Opto-Electronic Adv. 4 (2021) 1–26. https://doi.org/10.29026/oea.2021.210048.

[41] D. Banerjee, M. Akkanaboina, S. Ghosh, V.R. Soma, Picosecond Bessel Beam Fabricated Pure, Gold-Coated Silver Nanostructures for Trace-Level Sensing of Multiple Explosives and Hazardous Molecules, Materials (Basel). 15 (2022) 4155. https://doi.org/10.3390/ma15124155.

[42] G.K. Podagatlapalli, S. Hamad, M.A. Mohiddon, S.V. Rao, Fabrication of nanoparticles and nanostructures using ultrafast laser ablation of silver with Bessel beams, Laser Phys. Lett. 12 (2015) 36003. https://doi.org/10.1088/1612-2011/12/3/036003.

[43] M. Akkanaboina, D. Banerjee, K.R. Kumar, R.S.P. Goud, V.R. Soma, S.V.S.N. Rao, Gold nanoparticles coated LIPSS on GaAs for trace detection of RDX and Tetryl, Surfaces and Interfaces. 36 (2023) 102563. https://doi.org/10.1016/j.surfin.2022.102563.

[44] S.S.B. Moram, C. Byram, S.N. Shibu, B.M. Chilukamarri, V.R. Soma, Ag/Au Nanoparticle-Loaded Paper-Based Versatile Surface-Enhanced Raman Spectroscopy Substrates for Multiple Explosives Detection, ACS Omega. 3 (2018) 8190–8201. https://doi.org/10.1021/acsomega.8b01318.

[45] S.V. Rao, G.K. Podagatlapalli, S. Hamad, Ultrafast laser ablation in liquids for nanomaterials and applications, J. Nanosci. Nanotechnol. 14 (2014) 1364–1388.

[46] J. Rathod, C. Byram, R.K. Kanaka, M. Sree Satya Bharati, D. Banerjee, M. Akkanaboina, V.R. Soma, Hybrid Surface-Enhanced Raman Scattering Substrates for the Trace Detection of Ammonium Nitrate, Thiram, and Nile Blue, ACS Omega. 7 (2022) 15969–15981. https://doi.org/10.1021/acsomega.2c01095.

[47] M.S. Satya Bharati, B. Chandu, S. V Rao, Explosives sensing using Ag-Cu alloy nanoparticles synthesized by femtosecond laser ablation and irradiation, RSC Adv. 9 (2019) 1517–1525. https://doi.org/10.1039/c8ra08462a.

[48] D. Banerjee, M. Akkanaboina, R. Kumar Kanaka, V. Rao Soma, Femtosecond Bessel beam induced ladder-like LIPSS on trimetallic surface for SERS-based sensing of Tetryl and PETN, Appl. Surf. Sci. 616 (2023) 156561. https://doi.org/10.1016/j.apsusc.2023.156561.

[49] D. Banerjee, M. Akkanaboina, R.K. Kanaka, B. Ghose, V.R. Soma, Nanotubular Arrayed LIPSS Achieved with Femtosecond Bessel Beam on Silver Surface for SERS-Based Multiple Explosive Sensing, J. Phys. Chem. C. 128 (2024) 4655–4665. https://doi.org/10.1021/acs.jpcc.4c00160.

[50] A. Mangababu, R. Sai Prasad Goud, C. Byram, J. Rathod, D. Banerjee, V. Rao Soma, S.V.S.V.S. Nageswara Rao, Multi-functional gallium arsenide nanoparticles and nanostructures fabricated using picosecond laser ablation, Appl. Surf. Sci. 589 (2022) 152802. https://doi.org/10.1016/j.apsusc.2022.152802.

[51] K. Milligan, N.C. Shand, D. Graham, K. Faulds, Detection of Multiple Nitroaromatic Explosives via Formation of a Janowsky Complex and SERS, Anal. Chem. 92 (2020) 3253–3261. https://doi.org/10.1021/acs.analchem.9b05062.

[52] M.S.S. Bharati, C. Byram, V.R. Soma, M. Sree Satya Bharati, C. Byram, V.R. Soma, Femtosecond Laser Fabricated Ag@Au and Cu@Au Alloy Nanoparticles for Surface Enhanced Raman Spectroscopy Based Trace Explosives Detection, Front. Phys. 6 (2018) 1–13. https://doi.org/10.3389/fphy.2018.00028.

[53] C. Byram, S.S.B. Moram, D. Banerjee, R. Beeram, J. Rathod, V.R. Soma, Review of ultrafast laser ablation for sensing and photonic applications, J. Opt. 25 (2023) 043001. https://doi.org/10.1088/2040-8986/acbc31.

[54] M. Akkanaboina, D. Banerjee, K. Ravi Kumar, R. Sai Prasad Goud, V.R. Soma, S.V.S. Nageswara Rao, Sub-70 nm surface structures on femtosecond laser irradiated GaAs in distilled water and sensing application, Opt. Lett. 48 (2023) 5539. https://doi.org/10.1364/OL.502527.

[55] K.R. Kumar, D. Banerjee, A. Mangababu, R.S. Prasad Goud, A.P. Pathak, V.R. Soma, S.V.S. Nageswara Rao, Resistivity dependence on nanostructure formation in picosecond ablation of silicon and SERS-based sensing applications, J. Phys. D. Appl. Phys. 55 (2022) 405103. https://doi.org/10.1088/1361-6463/ac818b.

Intentional Blank Page

Chapter 6

Conclusions & Future Scope

6.1 Conclusions

In this thesis, we explored the potential of ultrafast laser ablation techniques, engaging Gaussian, Bessel, and Vortex beams to fabricate novel plasmonic nanostructures and nanoparticles. We have extensively studied the formation of laser-induced periodic surface structures (LIPSS) NSs on the trimetallic, bimetallic, and pure metal surfaces due to femtosecond (fs) Bessel beam interaction. We have also focused on fabricating alloy fs BB nano colloids and investigated their ultrafast response using a time-resolved spectroscopic technique. One of the primary objectives of the thesis was to design and manufacture plasmonic SERS substrates with significant enhancement factors, reliability, and repeatability. Additionally, the aim was to utilize a portable Raman spectrometer in conjunction with these substrates to identify several explosive molecules. We have explored femtosecond laser-matter interaction to investigate the aforementioned topics, producing colloidal nanoentities and surface nanostructures. Eight probe molecules have been identified, with the lowest detected trace concentrations as low as 50-500 nanomolar for explosives. They typically revealed enhancement factors (EF) ranging from 10^5 to 10^6. These investigations demonstrated reproducibility levels of <20% (RSD). A few significant findings derived from this thesis have been presented chapter-wise as follows,

Chapter 3: Femtosecond Gaussian beam ablation produced Ag-doped TiO_2 NPs and NSs for SERS studies

- The techniques of fs laser ablation and simultaneous laser-induced chemical reduction by irradiation were used to create titanium dioxide (TiO_2) and silver-titanium dioxide (Ag-TiO_2) nanoparticles in deionized water, respectively.
- Both Ag-doped TiO_2 and TiO_2 nanoparticles (NPs) were used in our SERS research. Here, we successfully identified the presence of RDX (100 µM) and ammonium nitrate (AN, 20 µM) in real-time using Ag-doped TiO_2 nanoparticles. Interestingly, using TiO_2 NPs alone did not provide any detectable signal.
- We fabricated a nanostructured titanium surface decorated with silver using femtosecond laser ablation and irradiation in a single-step process. Adding Ag-decorated Ti NSs led to a significant increase in the SERS signal, which was 16 times more intense than Ti NS.

Chapter 4A: Femtosecond Bessel beam generated trimetallic/ bimetallic LIPSS

- This chapter presents the production of distinct ladder-shaped trimetallic (TM, Ag-Au-Cu alloyed) LIPSS utilizing a femtosecond Bessel beam. The LIPSS were classified as LSFL I, with a period (Λ) of around (540±12) nm.
- SERS investigations demonstrated that the detection of 200 nM Tetryl, at its lowest concentration, had an enhancement factor of around 10^5. SERS mapping was performed throughout a large region of the TM NS.
- This work has provided valuable insights into the possibility of utilizing fs BB for generating LIPSS on the distinctive trimetallic surface. This is one of the first findings on the interaction between fs BB and metal.
- We have also created silver-gold bimetallic LIPSS nanostructures using femtosecond laser ablation and utilized them in SERS experiments. We could detect trace amounts of AN (10 μM) and tetryl (5 μM) effectively. The EFs were determined to be in the range of 10^3-10^4.

Chapter 4B: Nanotubular LIPSS generated on Ag surface and detection of multiple explosives

- This chapter has demonstrated the creation of nanotubular arrayed LIPSS on a silver surface utilizing a fs Bessel beam. Their period (Λ) was determined to be 575±10 nm.
- Comparative ablation experiments utilized a fs Gaussian beam with the same fluence and identical ablation parameters. These experiments revealed intriguing differences in the morphology of the resulting NSs. At this intensity, no laser-induced periodic surface structures (LIPSS) were seen for the Gaussian beam.
- The use of Ag LIPSS NSs produced by Bessel beams has shown remarkable efficacy in detecting multiple explosives. These explosives include TNT (50 nanomolar), Tetryl (50 nanomolar), RDX (500 nanomolar), and HMX (5 μM).
- Significant values of relative standard deviation (RSD < 22%) and enhancement factors, reaching ~10^6, were achieved using the same study.

- Also, in this chapter, we have effectively generated uniform LIPSS nano-structures on a Copper (Cu) surface using the fs BB LAA technique. The same NS was used in SERS tests to detect Tetryl and PETN, resulting in an enhancement factor of ~10^3.

Chapter 5A: Multi-metal Alloy Nanocolloids for Time-resolved Photonics Studies and SERS Applications

- This chapter showcases the creation of a new colloid consisting of nanoalloy particles made from several metals. The colloid is produced using a femtosecond broadband laser beam generated by an axicon.
- UV-visible-IR absorption, TEM, HRTEM measurements, and EDX spectra have been used for comprehensive topographical and elemental characterizations.
- The produced nanoalloys were used in SERS-based sensing experiments, effectively detecting minute amounts of RDX (5 µM) and PA (500 nM). The calculated enhancement factors for RDX and PA were 1.7×10^4 and 2.4×10^5, respectively.
- In addition, the alloy NPs were examined using fs pulses to evaluate their nonlinear optical (NLO) properties/coefficients. The 3PA coefficient for a third-order NLO response, γ, has been determined to be 1.8×10^{-22} cm^3/W^2, whereas the coefficient for nonlinear refractive index, n_2, has been measured to be 1.1×10^{-15} cm^2/W. Furthermore, the $\chi^{(3)}$ computed value was 7.6×10^{-14} e.s.u. The cross-section for three-photon absorption (σ_3) has been calculated to be 1.9×10^{-75} cm^6/s^2. We could also estimate the initial optical limiting (OL) value to be 8.8 mJ/cm^2, expanding the potential use of NAPs in optical limiting applications.
- The transient absorption spectroscopy (TAS) data revealed many photoexcited processes, including electron-electron/thermalization ($\tau_{e\text{-}e}$ = 0.7±0.1 ps), electron-phonon ($\tau_{e\text{-}ph}$ = 1.2±0.1 ps), and phonon-phonon scattering ($\tau_{ph\text{-}ph}$ = 47.5±8 ps).

Chapter 5B: Femtosecond vortex beam structured Ag surface for SERS-based sensing

- The final study presents our initial results involving fs Vortex beam (VB) ablation, creating NSs on a silver surface. Vortex phase plates were utilized to generate Vortex beams from a Gaussian beam. The fs BB was focused on the Ag surface to perform

surface engineering. The fabricated NSs were characterized via FESEM imaging. These NSs were employed as SERS-active substrates to detect two explosive molecules. The fs Vortex beam ablation study is to be continued to optimize the NSs and ablation parameters further. Additional molecules are to be detected in SERS studies. The summarised picture of the complete work of the thesis is presented in Figure 6.1.

6.2. Future scope of our research

The research work carried out in this thesis can be translated into some significant plans as follows,

- Several parameters, like excitation wavelength and laser spot diameter [1–6], are crucial for fabricating fine-quality LIPSS. We have determined to aim to achieve LIPSS on plasmonic NSs with high spatial frequency (HSFL) [LIPSS period to be much less than 200 nm] LIPSS by further optimizing these parameters. We aim to fabricate fs BB-induced LIPSS under 400 nm incident light, causing a shorter surface plasmon polariton decay length and a shortened incident laser diameter.
- Compared to silver and copper, gold has better stability [7] due to its less affinity towards oxidation. Hence, the fabrication of fs BB interacted LIPSS on the gold surface is one of our major plans. The ablation parameters, like scan speed, interline spacing corresponding to the overlapping of two consecutive BB ablated zones, and ablation fluence, are to be extensively optimized to achieve LIPSS on the gold surface via fs BB, which is also not yet reported. We sincerely aim to complete this investigation.
- We also wish to study the SERS performance of the BB fabricated gold LIPSS NS in terms of sensing hazardous materials and test its efficiency for the trace detection of various biomolecules [8–11] like proteins, infected cells, biohazardous molecules, and bacterial traces [12–15]. We also have plans to investigate the SERS performances of some of our already-achieved, fine-performing BB structured metal NSs (trimetallic, bimetallic LIPSS NSs) for sensing biomolecules.

- We can work towards chirality-based sensing [16–20] involving the fabricated novel plasmonic LIPSS NSs. This can ensure that the performance of the SERS-active substrates is enhanced by improving its enhancement factor.
- We have preliminarily explored the fs Vortex beam's interaction [21–25] with metals and fabricated plasmonic NSs. The fs Vortex beam ablation study is to be continued to optimize the NSs and ablation parameters further. AFM measurements must be taken to understand the depth profile of the NSs. Additional explosive molecules like HMX, PA, and RDX will be detected in SERS studies using the VB-structured NSs.
- Transient absorption studies must be performed in reflection geometry involving the solid trimetallic, bimetallic LIPSS NSs directly and probe the time-resolved dynamics of the excitation-induced plasmons. This will help us better understand the LIPSS NSs' plasmonic responses.
- Femtosecond BB ablation has turned out to be a more efficient [26] (at least 3 times higher ablation yield) technique for producing NPs with a higher yield, as we explored in our trimetallic alloy nanocolloids report. Quantification studies involving the optical density of the BB ablated pure/alloy NPs, in comparison with conventional Gaussian beam-engaged ablation technique, will be carried out in the future.

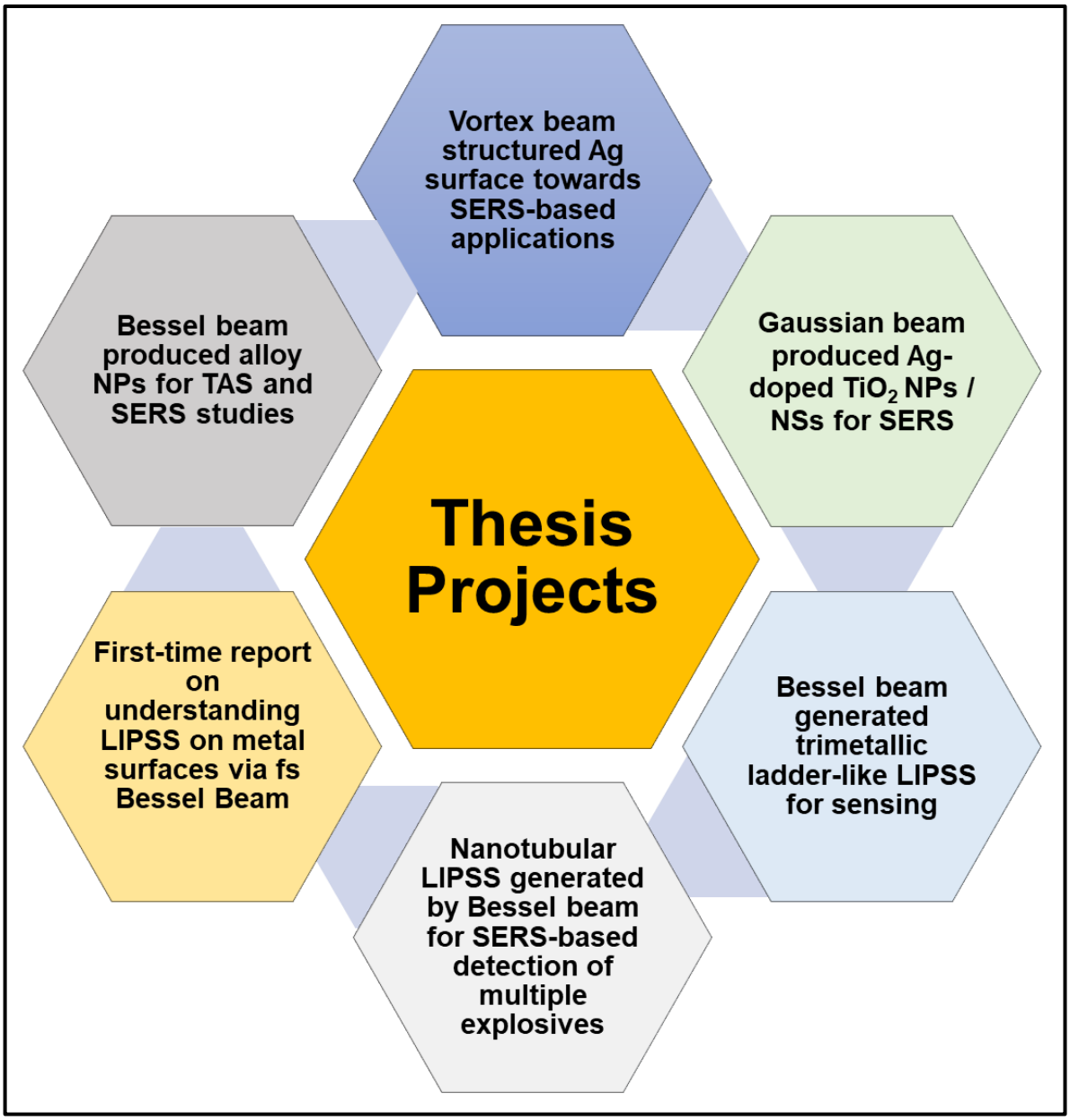

Figure 6.1 Summary of different segments of the complete thesis work

References

[1] I. Gnilitskyi, T.J.Y. Derrien, Y. Levy, N.M. Bulgakova, T. Mocek, L. Orazi, High-speed manufacturing of highly regular femtosecond laser-induced periodic surface structures: Physical origin of regularity, Sci. Rep. 7 (2017) 1–11. https://doi.org/10.1038/s41598-017-08788-z.

[2] J. Bonse, S. V. Kirner, J. Krüger, Laser-Induced Periodic Surface Structures (LIPSS), in: Handb. Laser Micro- Nano-Engineering, Springer International Publishing, Cham, 2021: pp. 1–59. https://doi.org/10.1007/978-3-319-69537-2_17-2.

[3] J. Bonse, S. Gräf, Maxwell Meets Marangoni—A Review of Theories on Laser-Induced Periodic Surface Structures, Laser Photon. Rev. 14 (2020) 1–25. https://doi.org/10.1002/lpor.202000215.

[4] J. Bonse, A. Rosenfeld, J. Krüger, On the role of surface plasmon polaritons in the formation of laser-induced periodic surface structures upon irradiation of silicon by femtosecond-laser pulses, J. Appl. Phys. 106 (2009). https://doi.org/10.1063/1.3261734.

[5] J. Bonse, Quo Vadis LIPSS?—Recent and Future Trends on Laser-Induced Periodic Surface Structures, Nanomaterials. 10 (2020) 1950. https://doi.org/10.3390/nano10101950.

[6] J. Bonse, J. Krüger, S. Höhm, A. Rosenfeld, Femtosecond laser-induced periodic surface structures, J. Laser Appl. 24 (2012) 572–579. https://doi.org/10.2351/1.4712658.

[7] C. Byram, S.S.B. Moram, D. Banerjee, R. Beeram, J. Rathod, V.R. Soma, Review of ultrafast laser ablation for sensing and photonic applications, J. Opt. 25 (2023) 043001. https://doi.org/10.1088/2040-8986/acbc31.

[8] D. Cialla, S. Pollok, C. Steinbrücker, K. Weber, J. Popp, SERS-based detection of biomolecules, Nanophotonics. 3 (2014) 383–411.

[9] Y. Li, H. Yan, R. Zhou, G. Zheng, A. He, Z. Ye, Cauliflower-like super-hydrophobic SERS substrate via two-step laser processing for acetamiprid detection, Appl. Surf. Sci. 669 (2024) 160599.

[10] C. Quezada, S. Samhitha, A. Salas, A. Ges, L.F. Barraza, D.A. Palacio, S. Esquivel, M.C. Blanco-López, G. Sánchez-Sanhueza, M.F. Meléndrez, Surface-Enhanced Raman Sensor with Molecularly Imprinted Nanoparticles as Highly Sensitive Recognition Material for Cancer Marker Amino Acids, Talanta. 278 (2024) 126465.

[11] H. Liu, C. Gao, P. Xu, Y. Li, X. Yan, X. Guo, C. Wen, X. Shen, Biomimetic Gold Nanorods-Manganese Porphyrins with Surface-Enhanced Raman Scattering Effect for

Photoacoustic Imaging-Guided Photothermal/Photodynamic Therapy, Small. 20 (2024) 2401117.

[12] S. Premachandran, S. Manickam, B. Tan, K. Venkatakrishnan, Fabrication of Isotope-Enriched Nanostructures using Ultrafast Laser Pulses under Ambient Conditions for Biomolecular Sensing, Adv. Mater. 24, (2024) 2406081.

[13] Z. Zhang, H. Li, L. Huang, H. Wang, H. Niu, Z. Yang, M. Wang, Rapid identification and quantitative analysis of malachite green in fish via SERS and 1D convolutional neural network, Spectrochim. Acta Part A Mol. Biomol. Spectrosc. 320 (2024) 124655.

[14] N. Feliu, M. Hassan, E. Garcia Rico, D. Cui, W. Parak, R. Alvarez-Puebla, SERS quantification and characterization of proteins and other biomolecules, Langmuir. 33 (2017) 9711–9730.

[15] X.-S. Zheng, I.J. Jahn, K. Weber, D. Cialla-May, J. Popp, Label-free SERS in biological and biomedical applications: recent progress, current challenges and opportunities, Spectrochim. Acta Part A Mol. Biomol. Spectrosc. 197 (2018) 56–77.

[16] W. Wu, M. Pauly, Chiral plasmonic nanostructures: recent advances in their synthesis and applications, Mater. Adv. 3 (2022) 186–215.

[17] Y. Kalachyova, O. Guselnikova, R. Elashnikov, I. Panov, J. Žádný, V. Církva, J. Storch, J. Sykora, K. Zaruba, V. Švorčík, Helicene-SPP-based chiral plasmonic hybrid structure: toward direct enantiomers SERS discrimination, ACS Appl. Mater. Interfaces. 11 (2018) 1555–1562.

[18] M. Arabi, A. Ostovan, Y. Wang, R. Mei, L. Fu, J. Li, X. Wang, L. Chen, Chiral molecular imprinting-based SERS detection strategy for absolute enantiomeric discrimination, Nat. Commun. 13 (2022) 5757.

[19] G. Wang, C. Hao, W. Ma, A. Qu, C. Chen, J. Xu, C. Xu, H. Kuang, L. Xu, Chiral plasmonic triangular nanorings with SERS activity for ultrasensitive detection of amyloid proteins in Alzheimer's disease, Adv. Mater. 33 (2021) 2102337.

[20] L. Sun, Y. Tao, G. Yang, C. Liu, X. Sun, Q. Zhang, Geometric Control and Optical Properties of Intrinsically Chiral Plasmonic Nanomaterials, Adv. Mater. 202, (2023) 2306297. https://doi.org/10.1002/adma.202306297.

[21] K. Toyoda, K. Miyamoto, N. Aoki, R. Morita, T. Omatsu, Using optical vortex to control the chirality of twisted metal nanostructures, Nano Lett. 12 (2012) 3645–3649. https://doi.org/10.1021/nl301347j.

[22] F. Takahashi, K. Miyamoto, H. Hidai, K. Yamane, R. Morita, T. Omatsu, Picosecond optical vortex pulse illumination forms a monocrystalline silicon needle, Sci. Rep. 6 (2016) 21738. https://doi.org/10.1038/srep21738.

[23] K.K. Anoop, R. Fittipaldi, A. Rubano, X. Wang, D. Paparo, A. Vecchione, L. Marrucci, R. Bruzzese, S. Amoruso, Direct femtosecond laser ablation of copper with an optical vortex beam, J. Appl. Phys. 116 (2014) 113102. https://doi.org/10.1063/1.4896068.

[24] H. Kawaguchi, R. Yasuhara, H. Yang, C. Hori, R. Miyagawa, K. Sugioka, M. Ota, H. Uehara, Femtosecond vector vortex laser ablation in tungsten: chiral nano-micro texturing and structuring, Opt. Mater. Express. 14 (2024) 424–434.

[25] D. Pavlov, A. Porfirev, S. Khonina, L. Pan, S.I. Kudryashov, A.A. Kuchmizhak, Coaxial hole array fabricated by ultrafast femtosecond-laser processing with spatially multiplexed vortex beams for surface enhanced infrared absorption, Appl. Surf. Sci. 541 (2021) 148602.

[26] D. Banerjee, M. Akkanaboina, V.R. Soma, Plasmonic alloy nanocolloids fabricated via femtosecond Bessel beam for photonic and SERS-based sensing applications, Opt. Mater. (Amst). 154 (2024) 115668. https://doi.org/https://doi.org/10.1016/j.optmat.2024.115668.

Publications/ Peer-reviewed Journal articles (related to this thesis work)

1. **Dipanjan Banerjee**, M Akkanaboina, RK Kanaka, VR Soma, Femtosecond Bessel beam induced ladder-like LIPSS on the trimetallic surface for SERS-based sensing of Tetryl and PETN, **Applied Surface Science [IF-7.4]**, 616, 156561, 2023. https://doi.org/10.1016/j.apsusc.2023.156561.
2. **Dipanjan Banerjee,** S. S. B. Moram; C. Byram; J. Rathod; T. Jena; G. K. Podagatlapalli, V. R. Soma, Plasmon-enhanced Ultrafast and Tunable Thermo-Optic Nonlinear Optical Properties of Femtosecond Laser Ablated TiO_2 and Silver-doped TiO_2 Nanoparticles, **Applied Surface Science [IF-7.4],** 569, 151070, 2021 https://doi.org/10.1016/j.apsusc.2021.151070.
3. **Dipanjan Banerjee,** A. Mangababu, Ravi Kumar Kanaka, Venugopal Rao Soma, Nanotubular Arrayed LIPSS Achieved With Femtosecond Bessel Beam on Silver Surface for SERS-based Multiple Explosives Sensing, **Journal of Physical Chemistry C [IF 3.7]** 128 (11), 4655–4665. https://doi.org/10.1021/acs.jpcc.4c00160.
4. **Dipanjan Banerjee,** A. Mangababu, Ravi Kumar Kanaka, Venugopal Rao Soma, Plasmonic Alloy Nanocolloids Fabricated via Femtosecond Bessel Beam for Photonic and SERS-based Sensing Applications, **Optical Materials [IF 3.9],** 154, 115668, 2024**.** https://doi.org/10.1016/j.optmat.2024.115668

Peer-reviewed International Conference Proceedings (related to this thesis work)

1. **Dipanjan Banerjee,** Mangababu Akkanaboina, Ravi Kumar Kanaka, Venugopal Rao Soma, Ag-Au bimetallic ladder-like nanostructures achieved with femtosecond Bessel beam for real-time sensing of tetryl and ammonium nitrate, SPIE Photonics West, Laser-based Micro-and Nanoprocessing XVII, **Proc. SPIE** 255-260, San Francisco California United States, 17 March 2023, https://doi.org/10.1117/12.2649704.
2. **Dipanjan Banerjee,** Akkanaboina Mangababu, Supriya Pradhan, and Venugopal Rao Soma, Uniform LIPSS on copper created using zeroth-order femtosecond Bessel beam for SERS-based applications, **Proc. SPIE** 13069, International Conference on Optical and Photonic Engineering (icOPEN), 130691F, 15 February 2024, Singapore https://doi.org/10.1117/12.3021658
3. **D Banerjee,** SSB Moram, VR Soma, Ag-doped TiO2 Nanoparticles Generated with Femtosecond Laser Ablation for Sensing RDX and Ammonium Nitrate, **Laser Science,** JM7A. 1, Laser Science 2023, **OSA,** Tacoma, Washington United States, 9–12 October 2023. https://doi.org/10.1364/FIO.2023.JM7A.1.
4. MSS Bharathi, **D Banerjee**, VR Soma, Femtosecond Laser Ablation Assisted Single-step Fabrication of Metal-semiconductor Interfaced SERS-active Substrate, Laser Applications Conference, JW2A. 7, **Laser Applications Conference 2023, OSA,** Tacoma, Washington United States, 8–12 October 2023. https://doi.org/10.1364/ASSL.2023.JW2A.7.

Co-authored publications (not related to thesis work)

1. Mangababu, **Dipanjan Banerjee**, Kanaka Ravi Kumar, R. Sai Prasad Goud, Venugopal Rao Soma, S.V.S. Nageswara Rao, Sub-100 nm DNA-like Surface Structures on Femtosecond Laser Irradiated GaAs in Distilled Water and Sensing Application, **Optics Letters**, 48 (21), 5539-5542. https://doi.org/10.1364/OL.502527.
2. KR Kumar, **D Banerjee**, A Mangababu, RS Prasad Goud, A Anjum, S V Rao, SVSN Rao, New Aspects of Femtosecond Laser Ablation of Si in Water: A Material Perspective, **Journal of Physics: Condensed Matter**, 36 235702, 10.1088/1361-648X/ad2f55.
3. M. Akkanaboina, **Dipanjan Banerjee**, Kanaka Ravi Kumar, R Sai Prasad Goud, Venugopal Rao Soma, SVS Nageswara Ra, Gold nanoparticles coated LIPSS on GaAs for trace detection of RDX and Tetryl, **Surfaces and Interfaces** [IF-6.8], 36, 102563, 2023. //doi.org/10.1016/j.surfin.2022.102563.
4. K.R. Kumar, **Dipanjan Banerjee**, A. Mangababu, R. Sai Prasad Goud, A.P. Pathak, Venugopal Rao Soma, S.V.S. Nageswara Rao, Resistivity Dependence on Nanostructure Formation in Picosecond Ablation of Silicon and SERS-based Sensing Applications, **Journal of Physics D**, 55(40), 5103, 2022, https://doi.org/10.1088/1361-6463/ac818b
5. M. Haribabu; **B. Dipanjan**; S. Hamad; M.S.S. Bharati; J. Chelsea; S. Venugopal Rao, Exciton mediated Surface-Enhanced Raman studies of Aluminium doped Platinum Nano colloids, **Optical Materials**, 133, 113013, 2022, https://doi.org/10.1016/j.optmat.2022.113013.
6. **Dipanjan Banerjee**, A. Mangababu, Subhasree Ghosh, Venugopal Rao Soma, Picosecond Bessel Beam Fabricated Pure, Gold-Coated Silver Nanostructures for Trace-level Sensing of Multiple Explosives and hazardous Molecules, **Materials**, 15, 12, 41552022, https://doi.org/10.3390/ma15124155.
7. R Beeram, **D Banerjee**, LM Narlagiri, VR Soma, Machine learning for rapid quantification of trace analyte molecules using SERS and flexible plasmonic paper substrates, **Analytical Methods**, 2022,14, 1788-1796, https://doi.org/10.1039/D2AY00408A.
8. BK Singh**, D Banerjee**, A Mangababu, Y Shadangi, NK Mukhopadhyay, Ultra-short pulsed laser ablation of decagonal AlCoNi and AlCoCuNi quasicrystals, **Journal of Alloys and Compounds**, 968, 172238, 2023. https://doi.org/10.1016/j.jallcom.2023.172238.
9. Allu, R., **Banerjee, D**., Avasarala, R., Hamad, S., Rao, S. V., & Podagatlapalli, G. K. (2019). Broadband femtosecond nonlinear optical properties of silver nanowire films. **Optical Materials,** 96, https://doi.org/10.1016/j.optmat.2019.109305

International Awards

1. **Selected among the top 100 candidates worldwide,** to attend the fully funded Student Leadership Conference (#SLC), Optica Annual Meeting and Frontiers in Optics (#FIO) conference organized by **Optica (formerly Optical Society of America #OSA).** This was held from 15-20 October 2022 at the Joseph A. Floreano Rochester Riverside Convention Center in **Rochester, New York, USA.**
2. **Selected as a Finalist for the Emil Wolf Student Paper Competition in the Student leadership conference** & Frontiers in Optics conference, Rochester, USA.
3. Received **Best Student Presentation International Award, 3rd position,** in the International Conference on Optical and Photonic Engineering 2023 (open), **Singapore.**

National Awards

1. Received **'BEST POSTER AND PAPER PRESENTATION'** award in National Laser Symposium 29th NLS 2021, DAE-BRNS, SVVV, Indore, Feb 12-15th, 2021.
2. Awarded **'EXCELLENCE IN PAPER PRESENTATION AWARD'** XIV Annual Symposium of the Optical Society of India, FRONTIERS IN OPTICS AND PHOTONICS (FOP21), **IIT Delhi, September 24-27, 2021.**
3. Received **'BEST POSTER AND PAPER PRESENTATION'** award in National Laser Symposium 30th NLS 2022, DAE-BRNS **National Laser Symposium (NLS-30) January 19-22, 2022,** DAE Convention Centre, Anushaktinagar, Mumbai, INDIA.
4. Received **'BEST POSTER' award in Frontiers in Physics conference,** University of Hyderabad, Hyderabad, March 3-4, 2023.
5. Received **'HIGHLIGHTED POSTER' recognition at PMRF annual symposium,** conducted by IIT Madras on February 17-18th, 2023.

Innovative, Robust Nanostructures for SERS based Hazardous Materials Sensing Realized Using Ultrafast Gaussian/Bessel/Vortex Beams

by Dipanjan Banerjee

Submission date: 16-Jul-2024 04:50PM (UTC+0530)
Submission ID: 2417720012
File name: Dipanjan_Banerjee.pdf (12.99M)
Word count: 51463
Character count: 285648

S. Venugopal Rao 16/7/24

Soma Venugopal Rao
Senior Professor
FSPIE, F.N.A.Sc., FRSC, F.Inst.Phys., FIAAM, FTAS
School of Physics & ACRHEM, DIA-CoE
University of Hyderabad
Hyderabad-500 046. Telangana, India.

Innovative, Robust Nanostructures for SERS based Hazardous Materials Sensing Realized Using Ultrafast Gaussian/Bessel/Vortex Beams

by Dipanjan Banerjee

Librarian
Indira Gandhi Memorial Library
UNIVERSITY OF HYDERABAD
Central University P.O.
HYDERABAD-500 046.

Submission date: 16-Jul-2024 04:50PM (UTC+0530)
Submission ID: 2417720012
File name: Dipanjan_Banerjee.pdf (12.99M)
Word count: 51463
Character count: 285648

Soma Venugopal Rao 16/7/24
Senior Professor
FSPIE, F.N.A.Sc., FRSC, F.Inst.Phys., FIAAM, FTAS
School of Physics & ACRHEM, DIA-CoE
University of Hyderabad
Hyderabad-500 046. Telangana, India.

Innovative, Robust Nanostructures for SERS based Hazardous Materials Sensing Realized Using Ultrafast Gaussian/Bessel/Vortex Beams

ORIGINALITY REPORT

24%	5%	21%	5%
SIMILARITY INDEX	INTERNET SOURCES	PUBLICATIONS	STUDENT PAPERS

Soma Venugopal Rao
Senior Professor
FSPIE, F.N.A.Sc., FRSC, F.Inst.Phys., FIAAM, FTAS
School of Physics & ACRHEM, DIA-CoE
University of Hyderabad
Hyderabad-500 046. Telangana, India.

PRIMARY SOURCES

1	Dipanjan Banerjee, Mangababu Akkanaboina, Venugopal Rao Soma. "Plasmonic Alloy Nanocolloids Fabricated via Femtosecond Bessel Beam for Photonic and SERS-based Sensing Applications", Optical Materials, 2024 Publication	8%
2	Dipanjan Banerjee, Mangababu Akkanaboina, Ravi Kumar Kanaka, Venugopal Rao Soma. "Femtosecond Bessel Beam Induced Ladder-like LIPSS on Trimetallic Surface for SERS-based Sensing of Tetryl and PETN", Applied Surface Science, 2023 Publication	5%
3	Submitted to University of Hyderabad, Hyderabad Student Paper	3%
4	Dipanjan Banerjee, Sree Satya Bharati Moram, Chandu Byram, Jagganath Rathod et al. "Plasmon-enhanced Ultrafast and Tunable	2%

Soma Venugopal Rao
Senior Professor
FSPIE, F.N.A.Sc., FRSC, F.Inst.Phys., FIAAM, FTA
School of Physics & ACRHEM, DIA-CoE
University of Hyderabad
Hyderabad-500 046. Telangana, Indi

Serial #s 1-4 are Students own publications.
The similarity after discarding these is < 10%.

18/7/2024

Soma Venugopal Rao
Senior Professor
FSPIE, F.N.A.Sc., FRSC, F.Inst.Phys., FIAAM, FTAS
School of Physics & ACRHEM, DIA-CoE
University of Hyderabad
Hyderabad-500 046. Telangana, India.

Thermo-Optic Nonlinear Optical Properties of Femtosecond Laser Ablated TiO2 and Silver-doped TiO2 Nanoparticles", Applied Surface Science, 2021
Publication

5	Submitted to Birla Institute of Technology Student Paper	<1 %
6	Dipanjan Banerjee, Mangababu Akkanaboina, Ravi Kumar Kanaka, Bikash Ghose, Venugopal Rao Soma. "Nanotubular Arrayed LIPSS Achieved with Femtosecond Bessel Beam on Silver Surface for SERS-Based Multiple Explosive Sensing", The Journal of Physical Chemistry C, 2024 Publication	<1 %
7	www.thorlabs.com Internet Source	<1 %
8	www.nature.com Internet Source	<1 %
9	www.researchgate.net Internet Source	<1 %
10	Dipanjan Banerjee, Mangababu Akkanaboina, Venugopal Rao Soma. "Plasmonic alloy nanocolloids fabricated via femtosecond Bessel beam for photonic and SERS-based sensing applications", Optical Materials, 2024 Publication	<1 %

Serial #s 1-4 are Students own publications.
The similarity after discarding these is
<10%. S.Venugopal Rao

S.Venugopal Rao (Soma Venugopal Rao)
Soma Venugopal Rao
Senior Professor
FSPIE, F.N.A.Sc., FRSC, F.Inst.Phys., FIAAM, FTAS
School of Physics & ACRHEM, DIA-CoE
University of Hyderabad
Hyderabad-500 046. Telangana, India.

11	www.mdpi.com Internet Source	<1 %
12	dspace.uohyd.ac.in Internet Source	<1 %
13	Jagannath Rathod, Sree Satya Bharati Moram, Byram Chandu, Paweł Henryk Albrycht, VENUGOPAL RAO SOMA. "Single-Step Fabrication of Hybrid Germanium-Gold/Silver Nanoentities by Femtosecond Laser Ablation and Applications in SERS-based Sensing", Nanotechnology, 2023 Publication	<1 %
14	www.researchid.co Internet Source	<1 %
15	Dongshi Zhang, Bilal Gökce, Stephan Barcikowski. "Laser Synthesis and Processing of Colloids: Fundamentals and Applications", Chemical Reviews, 2017 Publication	<1 %
16	K.N. Krishnakanth, Byram Chandu, M.S.S. Bharathi, Sai Santhosh Kumar Raavi, S. Venugopal Rao. "Ultrafast excited state dynamics and femtosecond nonlinear optical properties of laser fabricated Au and Ag50Au50 nanoparticles", Optical Materials, 2019 Publication	<1 %

S Venugopal Rao
18/07/2023

Serial #s 1-4 are students own publications. The similarity after discarding these is <10%. S Venugopal Rao

Soma Venugopal Rao
Senior Professor
FSPIE, F.N.A.Sc., FRSC, F.Inst.Phys., FIAAM, FTAS
School of Physics & ACRHEM, DIA-CoE
University of Hyderabad
Hyderabad-500 046. Telangana, India.

Plagiarism-free statement

This is to certify that the thesis titled "Innovative, Robust Nanostructures for SERS-based Hazardous Materials Sensing Realized Using Ultrafast Gaussian/Bessel/Vortex Beams" has been screened by the Turnitin software at the Indira Gandhi Memorial Library of the University of Hyderabad. The software shows a 24 % similarity index, of which 15 % came from the candidate's own research articles related to the thesis, which are published and available online. Thus, the effective similarity index excluding his own articles is 24% - 15% = 9 %, which is lower than 10%, according to the rule specified by the university guidelines. Therefore, this thesis may be considered free from plagiarism as per guidelines.

S Venugopal Rao 18-7-2024

Prof. Soma Venugopal Rao

PhD Supervisor,

School of Physics & ACRHEM (DIA-CoE)

University of Hyderabad

Soma Venugopal Rao
Senior Professor
FSPIE, F.N.A.Sc., FRSC,F.Inst.Phys., FIAAM, FTAS
School of Physics & ACRHEM, DIA-CoE
University of Hyderabad
Hyderabad-500 046. Telangana, India.